IMPROVED DESIGN AND PERFORMANCE ANALYSIS OF SIMILAR POLE RATIO DUAL STATOR WINDINGS FOR SIX PHASE INDUCTION MACHINES

BY

Yusuf JIBRIL

FACULTY OF ENGINEERING
DEPARTMENT OF ELECTRICAL AND COMPUTER ENGINEERING
AHMADU BELLO UNIVERSITY – ZARIA

February 2015

IMPROVED DESIGN AND PERFORMANCE ANALYSIS OF SIMILAR POLE RATIO DUAL STATOR WINDINGS FOR SIX PHASE INDUCTION MACHINES

BY

Yusuf **JIBRIL** MSc(Ukraine),1994
PhD/ENG/14582/2011-12
(jyusuf@abu.edu.ng)

A DISSERTATION SUBMITTED TO THE DEPARTMENT OF ELECTRICAL AND COMPUTER ENGINEERING, AHMADU BELLO UNIVERSITY ZARIA IN PARTIAL FULFILLMENT OF THE REQUIREMENTS FOR THE AWARD OF A DOCTOR OF PHILOSOPHY (Ph.D) DEGREE IN ELECTRICAL ENGINEERING.

DEPARTMENT OF ELECTRICAL AND COMPUTER ENGINEERING

FACULTY OF ENGINEERING

AHMADU BELLO UNIVERSITY, ZARIA

NIGERIA

FEBRUARY, 2015

DECLARATION

I, Yusuf Jibrilhereby declare that this dissertation titled **"Improved Design and Performance Analysis of Similar Pole Ratio Dual Stator Windings for Six Phase Induction Machines"** presented to the School of Post Graduate Studies of Ahmadu Bello University, Zaria is the result of my own research and it has not been presented in any form, anywhere for the award of any certificate.

All literature herein referenced and cited have been duly acknowledged. All shortcomings in this work are entirely my responsibility.

Yusuf Jibril _____ _____

Signature **Date**

CERTIFICATION

This is to certify that the PhD dissertation titled **"Improved Design and Performance Analysis of Similar Pole Ratio Dual Stator Windings for Six Phase Induction Machines"**meet the regulations governing the award of the degree of Doctor of Philosophy (PhD) in Electrical Engineering of Ahmadu Bello University, and is approved for its contribution to literary presentation.

Prof. U. O. Aliyu **Chairman, Supervisory Committee**	**Signature**	**Date**
Prof. B. G. Bajoga **Member, Supervisory Committee**	**Signature**	**Date**
Dr. M. B. Mu'azu **Member, Supervisory Committee**	**Signature**	**Date**
Dr. M. B. Mu'azu **Head of Department**	**Signature**	**Date**
Prof. A. Z. HASSAN **Dean, School of Postgraduate Studies**	**Signature**	**Date**

DEDICATION

I dedicate this work to my entire family members, friends and well-wishers.

ACKNOWLEDGEMENTS

All Praise is due to Allah, we are grateful to Him and unto Him we implore for help. We repent to Him and we seek refuge in Allah from the evils of our souls and our bad deeds. He who Allah guided no one can mislead him and he who go astray no one can guide him. I bear witness that there is no deity worthy of worship but Allah (He is alone without partner) and I bear witness that Muhammad is His servant and messenger (SAW).

I acknowledge the contributions of authors referred to in this research.`

I am very grateful for the guidance and support of the supervisory committee headed by Prof. U. O. Aliyu, supported by eminent Prof. B.G. Bajoga, and Dr. M. B. Mu'azu. The supervisory committee has worked tirelessly to ensure the success of the research. May Allah in his unique mercy reward them abundantly and give His true and continues guidance to them all. Ameen.

I remain grateful to Prof. OlorunfemiOjo who introduced me to the world of multi-phase machines and gave me the opportunity to conduct part of this research work in his laboratory at Tennesee Technological University, Cookville, Tennessee, U. S. A. The contributions of Dr. Adeola of University of Lagos and Dr. S Karugaba, with whom we worked in Prof. Ojo's Laboratory will never be forgotten. May God reward you abundantly.

My sincere appreciation goes to Prof. Nichola Bianchi (and his research assistant Dr. Luigi Alberti) for the opportunity he accorded me to conduct yet another round of research in his Electric Drive Laboratory, University of Padova, Padova, Italy.

I am also grateful to my colleagues, Dr. O. Akinsanmi, Dr. B. Jimoh, Prof. B. A. Adegboye, Dr. J. Y. Oricha, Dr. S. Garba, Malamand A. S. Musa, for their contributions. Special thanks go to Dr. S. M. Sani (the brain behind Postgraduateacademic revolution in the Department of Electrical and Computer Engineering, A. B. U.,Zaria.) for his encouragement and support.

I am highly indebted to my parents, my brothers and sisters, my wives and my children.

I would also like to appreciate the encouragement and support of all the Technical staff from the Department of Electrical and Computer Engineering, A. B. U.,Zaria, headed by Mr. F. O. Sadiku.

Finally, my sincere appreciations to three of my colleagues for their valuable contributions towards the successful completion of this research work. They are: Dr. K. A. Abubilal; Dr. Y. Sha'aban and Engr. B. Abdurrazaq. May God Almighty reward them accordingly.

I sincerely hope that this work will contribute immensely to knowledge.

You are glorified oh Allah and praise is due to You, I repent to You and I ask for Your forgiveness.

TABLE OF CONTENTS

COVER PAGE	i
TITLE PAGE	ii
DECLARATION	iii
CERTIFICATION	iv
DEDICATION	v
ACKNOWLEDGEMENT	vi
TABLE OF CONTENTS	viii
LIST OF FIGURES	xvii
LIST OF PLATES	xxi
LIST OF TABLES	xxii
ABBREVIATION AND DEFINITION	xxiii
LIST OF SYMBOLS	xxiv
ABSTRACT	xxv

CHAPTER ONE: INTRODUCTION

1.1 Background Information 1

1.2 Motivation 3

1.3 Problem Definition 4

1.4 Aim and Objectives 6

1.5 Overview of Research Methodology 7

1.6 Significance of the Research 10

1.7 Dissertation Organization 11

CHAPTER TWO: THEORETICAL BACKGROUND AND LITERATURE REVIEW

2.1 Introduction 13

2.2 Review of Fundamental Concept 13

2.2.1 Characterizations of physical features and operating modes of IM 14

2.2.2 Development of induction machine speed-torque characteristics 17

2.2.3 Motoring and braking operating regimes 19

2.2.4 Generating mode of operation of induction motor 22

2.2.5 Dual stator winding induction machine theoretical concept 23

2.2.6 Derivation of DSWIM equivalent circuit parameters and torque equation 24

2.2.6.1 Voltage equations in machine variables 25

2.2.7 Derivation of winding inductances 29

2.2.7.1 Generalized flux equation based on winding function theory 29

2.2.8 Derivation of self-inductances 34

2.2.9 Derivation of mutual inductances 35

2.2.10 Derivation of stator leakage inductance for three special cases 37

2.2.11 Derivation of mutual leakage inductance 42

2.2.12 Transformation of machine variable equations into arbitrary d-q-0 reference frame 45

2.2.13 Turns Ratio Scaling Procedure 48

2.2.14 Development of torque equation for DSWIM 50

2.2.15 Overview of multi-phase induction machine design concepts 52

2.2.16 Design optimization of multi-phase induction machine 56

2.2.17 Overview of genetic algorithm 57

2.2.18 Selection of method of field analysis for induction machines 61

2.2.18.1 Finite element method (FEM) 63

2.3 Review of Similar Works 63

2.3.1 Review of historical development of DSWIM 63

2.3.2 Review of recent publications on DSWIM design, modelling and control techniques 68

2.3.4 Research thrusts pursued in this dissertation 76

2.4 Summary 76

CHAPTER THREE: DSWIM DESIGN METHODOLOGY

3.1 Introduction 78

3.2 Generalized Description of a Dual Stator Winding Induction Machine Design Procedure 79

3.3 Magnetic Loading Characterization 83

3.3.1 Mathematical description of air-gap flux density for DSWIM 84

3.4 Computation of Total MMF in a Magnetic Circuit of Asynchronous Machine 87

3.4.1 MMF estimation for air gap considering slots on the rotor and stator surfaces88

3.4.2 Derivation of MMF of stator tooth and rotor tooth 92

3.4.3 Derivation of MMF of the stator core 94

3.4.4 Derivation of MMF for rotor core 95

3.4.5 Determination of number of stator turns per phase 97

3.4.6 Computation of magnetising current and inductance per phase 99

3.4.7 Surface current density estimation 99

3. 4.8 Calculation of stator conductor diameter 101

3.4.9 Stator conductor current density calculation 101

3.4.10 Stator winding categorization 101

3.4.11 Outline of stator winding Architecture 103

3.4.12 Quantitative description of winding arrangement in slots 103

3.4.13Winding dimension calculation 104

3.5 Analytical Calculations of DSWIM Steady State Equivalent Circuit Parameters 105

3.5.1 Stator resistance calculation 106

3.5.2 Stator leakage Inductance (Reactance) 109

3.5.2.1 Slot leakage inductance 110

3.5.2.2 End winding leakage inductance 111

3.5.2.3 Belt leakage inductance 112

3.5.2.4 Zig-zag leakage inductance 113

3.5.2.5 Skew leakage inductance 114

3.5.2.6 Total stator leakage inductance 114

3.5.3 Determination of rotor parameters 114

3.5.3.1 Rotor parameters referred to stator side 116

3.6 DSWIM Design Framework 117

3.6.1 Functional description of DSWIM design procedure 118

3.7 GA Based Optimization of DSWIM 122

3.8.1 GA solution methodology 123

3.9 Design Calculations for Similar Pole DSWIM 126

3.9.1 Specification of magnetic loading for 8/8 pole DSWIM 126

3.9.2 Calculations of total MMFs in 8/8 pole DSWIM 128

3.9.3 Power, surface current density, number of turns per phase and conductor sizing

3.9.4 Calculations of inductances and resistances for 8/8 DSWIM 129

3.10 Winding Layout Design for 8/8 DSWIM 130

3.10.1 Stator winding dimension calculation 131

3.10.2 Stator ‘a-b-c’ winding diagram 131

3.10.3 Stator ‘x-y-z’ winding diagram 132

3.10.4 Complete stator winding diagram for 8/8 pole DSWIM 133

3.11 Summary 134

CHAPTER FOUR: DSWIM MATHEMATICAL MODELING AND FINITE ELEMENT ANALYSIS

4.1 Introduction 135

4.2 Development of DSWIM Equations in d-q-0 Arbitrary Reference Frame 135

4.2.1 Functional representation of DSWIM mathematical model 139

4.2.2 Description of DSWIM Simulink model 142

4.3 Finite Element Method 146

4.3.1 Description of finite element method magnetics (FEMM) software 147

4.3.1.1 Femme.exe program 147

4.3.1.2 Simulation.exe program 148

4.3.1.3 Femmview.exe program 148

4.4 DWIM Based FEMM Analysis 149

4.4.1 Categorization of DSWIM inductances 150

4.4.2 Procedures for calculating self-inductances 153

4.4.2.1 Stator winding inductance calculation procedure 153

4.4.2.1 Rotor Equivalent winding inductance calculation procedure 154

4.4.3 Procedures for calculating mutual inductances 156

4.4.3.1 Mutual inductances due to stator phases of the same winding procedure 156

4.4.3.2 Mutual inductances due to stator phases of different winding sets procedure 156

4.4.3.3 Mutual inductances between rotor phases procedure 157

4.4.3.4 Mutual inductances between stator and rotor phases procedure 157

4.5 Determination of DSWIM Equivalent Circuit Parameters Using FEMM 158

4.5.1 No-load test FEMM simulation procedure for magnetizing inductance calculation 158

4.5.2 FEMM model based locked-rotor test procedure 159

4.5.2.1 Excitation of only stator 'a-b-c' winding set in FEMM model of DSWIM 159

4.5.2.2 Excitation of both stator winding sets (with 30^0shift) 161

4.5.2.3 Excitation of both stator winding sets (with 0^0shift) 161

4.6 Determination of Equivalent Resistance and Inductance for DSWIM 162

4.7 Summary 165

CHAPTER FIVE: RESULTS AND DISCUSSIONS

5.1 Introduction 167

5.2 DSWIM Design Consideration Results 167

5.2.1 Results of DSWIM improved classical design (ICD) approach 168

5.2.2 Results of GA optimization of DSWIM power factor and efficiency 171

5.2.3 Results of DSWIM parameter calculations based on winding function approach 175

5.2.4 Results of FEMM model of DSWIM for parameter estimations 176

5.2.4.1 Results of self- inductances stator windings 176

5.2.4.2 Results of self- inductances of rotor windings 176

5.2.4.3 Results of mutual inductances of intra-stator windings 177

5.2.4.4 Results of mutual inductances of inter-stator windings 177

5.2.4.5 Results of mutual inductances of rotor windings 178

5.2.4.6 Results of mutual inductances between stator and rotor windings 178

5.2.4.7 Results of equivalent Circuit Parameter Determinations from FEMM Model 179

5.2.4.8 Analysis of FEMM simulation results 180

5.2.5 Comparison of DSWIM Inductance Values Computed Via Three Methods 184

5.3 Results of DSWIM Simulation in MATLAB/Simulink Software 186

5.3.1 Results of Starting process and fixed loading dynamic response of DSWIM 187

5.3.2 Investigation of effects of mutual leakage inductance (L'_{ldq}) on the characteristics of similar pole DSWIM 191

5.3.2.1 Case study I 191

5.3.2.2 Case study II 191

5.3.2.3 Case study III 192

5.3 Discussion of Simulink Model Results 201

5.4 Prototype Realization of DSWIM and Experimental Results 203

5.4.1 Prototype realization of DSWIM 203

5.4.2 Experimental results 206

5.4.3 Determination of the induction machine parameters 208

5.4.3.1 DC resistance test 208

5.4.3.2 Locked- rotor test 209

5.4.3.3 No- load test 211

5.4.4 Comparison of DSWIM simulation and prototype experimental results 215

5.4.5 Comparison of results for DSWIM and standard 3-ϕ IM 216

5.4.6 DSWIM circle diagram results 220

5.4.7 DSWIM loss segregation results 221

5.5 Analyses of Experimental Results 222

5.5.1 Rotor starting torque characterization 224

5.5.2 Acceleration of DSWIM from standstill 224

5.5.3 Behavior of DSWIM near synchronous speed 225

5.5.4 DSWIM behavior during loading and breakdown 225

5.6 Summary 226

CHAPTER SIX:SUMMARY, CONCLUSIONS AND RECOMMENDATIONS 227

6.1 Introduction 228

6.2 Summary 228

6.3 Conclusion 230

6.4 Contributions to Knowledge 232

6.5 Recommendations 234

6.6 Suggestions for further work 235

LIST OF FIGURES

Figure 1.1: Generalized AC Machine Family (*Adapted from*: *Lessons in AC Circuits Vol. II-AC7*) 2

Figure 1.2: Generalized Representation of Multi-Phase Induction Machine and Phase Arrangement 4

Figure 1.3: Flowchart Overview of Research Methodology 9

Figure 1.4: Block Diagram of DSWIM in MATLAB/ Simulink Simulation Environment 10

Figure 1.5: Basic Block Diagram of Finite Element Method (FEM) 10

Figure 2.1: Synopsis of Conventional Induction Machine Salient Features and Basic Analysis 15

Figure 2.2: Functional Diagram of Poly-phase Induction Machine for Three Operating ModesTorque-Speed 16

Figure 2.3: Complete Characteristics of Multi-phase InductionMachine 17

Figure 2.4: Speed versus torque characteristics for Induction Machine Motoring Mode 19

Figure 2.5: Circle Diagram of an Induction Machine (Motoring Mode) 20

Figure 2.6: Schematic of Self Excited Induction Generator (SEIG) 22

Figure 2.7: Schematic Diagram of a Dual Stator Induction Machine with Dissimilar Pole Ratio 24

Figure 2.8: Schematic Diagram of a Dual-Winding Induction Machine 26

Figure 2.9: Dual Stator Winding Induction Machine Drive System Depicting All Self Inductances and Mutual Inductances between Stator Winding 'as' and Rotor Winding 'ar' and all other Windings 27

Figure 2.10: Relative Locations of Stator and Rotor Winding Flux Axes 27

Figure 2.11: Uniformly Distributed Winding According to Winding Function Definition for Elementary Induction Machine 30

Figure 2.12: Dual Stator Winding Phases Vector Diagrams in d-q-0 Arbitrary Reference Frame 46

Figure 2.13: Leading Dimensions of an Induction Machine Housing Structure 53

Figure 2.14: Classes of Optimization Techniques 58

Figure 2.15: Generalized Procedure of Genetic Algorithm 60

Figure 2.16: Fundamentals of FEM Concept 63

Figure 2.17: Typical Triangular Meshes Generated for a Quarter Cross-Section of an Induction Machine 65

Figure 2.18: Schematic Diagrams of Dual Stator Windings Angular Displacements 67

Figure 2.19: Single Winding dissimilar Pole Number Distribution 69

Figure 3.1: Block Diagram Representation of DSWIM Design Approach 82

Figure 3.2: Magnetic Flux Path for a Section of a Poly-phase Induction machine 86

Figure 3.3: Actual Flux Distribution within Slot Pitch 87

Figure 3.4: Air-gap Flux Distribution with Smooth Iron Surfaces 88

Figure 3.5: Air gap Flux Distribution Confined to a Tooth Width 88

Figure 3.6: Air gap Flux Distribution with a Correction Factor 89

Figure 3.7: Application of Simpson's Rule to Approximate MMF of Stator Tooth 91

Figure 3.8: Half Cross Section View of Induction Machine's Core Showing Leading Dimensions 93

Figure 3.9: Typical B-H Curves for Different Metals 95

Figure 3.10: Composite Plots of Form Factor (k_f) and Flux Density Shape Factor (α) Versus Teeth Saturation Factor Source 97

Figure 3.11: Typical Multi-turn Coil and Winding Layer Topologies 101

Figure 3.12: Generalized Steady State Equivalent Circuit of 104

Figure 3.13: Basic Illustration of Interwoven Stator conductor 105

Figure 3.14: Idealized Geometrical View of Stator Winding Coil 106

Figure 3.15: Induction Machine Leakage Fluxes 108

Figure 3.16: Physical Slot Dimensions Used in Single and Double layer Permeance Calculations 110

Figure 3.17: Basic Geometric Dimension of the Squirrel Cage Rotor: Adapted from (BoldeaandNaser, 2004) 114

Figure 3.18: Schematic Representation DSWIM Equipped with n/n Similar Pole Ratios 117

Figure 3.19: Functional Flowchart for DSWIM Analytical Design Algorithm 120

Figure 3.20: Flow Chart for the Optimization of Efficiency and Power Factor 124

Figure 3.21: The Complete Developed Winding Diagram of Phase "a" 130

Figure 3.22: The Developed Winding Diagram of ‘a-b-c’ Winding set 131

Figure 3.23: The Developed Winding Diagram of Phases ‘a’ and ‘x’ 132

Figure 3.24: The Developed Winding Diagram of the ‘x-y-z’ Winding set 132

Figure 3.25:The Complete Stator Winding Clock Diagram for 8/8 DSWIM 133

Figure 4.1:Schematic Diagram of an n/n Similar Pole Ratio Dual Winding Induction Machine 135

Figure 4.2:Equivalent Circuit of Similar Pole Dual Winding Induction Machine 137

Figure 4.3: Generalized Functional Representation of DSWIM Mathematical Model 139

Figure 4.4:Simulink Main Software Hosting DSWIM Simulation Model 143

Figure 4.5: Complete Simulink Simulation of DSWIM Model 144

Figure 4.6: Simulink Inverter Model Feeding ‘x-y-z’ Winding Set 145

Figure 4.7: Typical Geometric Drawing 147

Figure 4.8: Typical Mesh Creation 147

Figure 4.9: Magnetic Flux Contour Plot 147

Figure 4.10: Functional Flowchart for FEMM Analysis of DSWIM 148

Figure 4.11: Complete Stator Winding Clock Diagram 150

Figure 4.12: Rotor Phase ‘a’ Equivalent Winding Clock Diagram 151

Figure 4.13: Rotor Phase ‘b’ Equivalent Winding Clock Diagram 151

Figure 4.14: Rotor Phase ‘c’ Equivalent Winding Clock Diagram 151

Figure 4.15:Distribution of Magnetic Flux when only Phase ‘a’ of the Stator is Excited. 153

Figure- 4.16:Four Flux Distribution Patterns with Phase ‘a’ of Rotor Excited at Different Electrical Reference angles 157

Figure 4.17: Magnetic Flux Pattern under No Load Test 158

Figure 4.18:Different Flux Density Plots under Locked Rotor Tests with a-b-c Winding Excitedby Rated Current 159

Figure 4.19:Different Flux Density Plots under Locked Rotor Tests with both stator Winding sets Excited 160

Figure 4.18: Different Flux Density Plots under Locked Rotor Tests with Both ‘a-b-c’ and ‘x-y-z’ Winding Sets Excited by Rated Current of 3.5A at 0^o Phase Shift

Figure 4.19: Functional Block Diagram of DSWIM Based FEMM Model 169

Figure 5.1:Bar Charts of a) Flux Densities and b) MMFs in Various Magnetic Flux Paths169

Figure 5.2:3-D Plot of Normalized Induced Voltage in DSWIM Rotor as a Function of Slip, s and Frequency 169

Figure 5.3: 3-D Plot of Tooth Flux Density Spatial Distribution under One Pole of DSWIM 170

Figure 5.4 Nonlinear B-H Curve of the Iron Core 170

Figure 5.5: Optimal Values of Power Factor against Power Efficiency 172

Figure 5.6: Screen Capture of GUI for the GA Optimization in MATLAB Environment 173

Figure- 5.7: Variation of Rotor-Stator Mutual Inductance with Rotor Position 177

Figure 5.8: Variation of Magnetizing Inductance $(L_m)$with Stator Current 178

Figure 5.9: A Detailed Functional Flow Chart Used in the Implementation of FEMM Model Development for DSWIM 179

Figure 5.10: Magnetic Energy and Co-energy versus Rotor Frequency 180

Figure 5.11: Rotor Joule Losses versus Rotor Frequency 181

Figure 5.12: Torques from Maxwell Stress Tensor versus Rotor Frequency 181

Figure 5.13:Composite Plots of DSWIM Equivalent Parameters versus Rotor Frequency183

Figure 5.14: Starting Process of 8/8 Pole Dual Stator Winding Induction Machine-

(a) Speed Curve; (b) Torque Contribution by 'a-b-c' Winding; (c) Torque Contribution by 'x-y-z' Winding; & (d) Total Torque Developed 187

Figure 5.15: Quadrature and Direct Axis Voltages of the Two stator windings as a Function of Time 188

Figure 5.16:Currents of Two (a-b-c & x-y-z) Stator Windings and a-b-c Rotor Winding 188

Figure 5.17: Stator Voltages in Phase (abc & xyz) Variables as a Function of Time 188

Figure 5.18: Stator Phase 'a' and Phase 'x' Currents as a Function of Time 189

Figure 5.19 8/8 Pole Ratio DSWIM Simulation Result 191

Figure 5.20 8/8 Pole Ratio DSWIM Simulation Result 192

Figure 5.21 8/8 Pole Ratio DSWIM Simulation Results with $\pm L'_{ldq} = L_{ls}$ 192

Figure 5.22 Stator Phases 'a' and' xyz' Winding Set Currents against Time 193

Figure 5.23:d-q currents of two (abc & xyz) stator windings and abc rotor winding 193

Figure 5.24: d-q voltages of the two (abc & xyz) stator windings as a function of time 194

Figure 5.25:Stator voltages in natural (abc & xyz) variables as a function of time 194

Figure 5.26:d-q axes flux linkages stator “abc”, ”xyz” and rotor“abc” winding sets against time. 195

Figure 5.27: 8/8 Pole Ratio DSWIM Simulation Results with $\pm L'_{ldq} = L_{ls} = L_{lr}$ 195

Figure 5.28: Stator Phases ‘a’ and ‘xyz’ Winding Sets Current against Time 196

Figure 5.29:Quadrature and Direct Axis Currents of Two (‘a-b-c’ & ‘x-y-z’) Stator Winding and abc rotor winding 196

Figure 5.30: Quadrature and Direct Axis Voltages of the Two (abc & xyz) Stator Windings as a Function of Time 197

Figure 5.31: Stator Voltages in Phase (a-b-c & x-y-z) Variables as a Function of Time 197

Figure 5.32:8/8 Pole Ratio DSWIM Simulation Results with $\pm L'_{ldq} = 0$

(a) Speed Curve; (b) Torque Contribution by ‘a-b-c’ Winding; (c) Torque Contribution by ‘x-y-z’ Winding; & (d) Total Torque Developed 198

Figure 5.33: Quadrature and Direct Axis Flux Linkages Stator ‘a-b-c’, ‘x-y-z’ and Rotor ‘a-b-c’ Winding Sets against Time 198

Figure 5.34: Stator Phases ‘a’ and ‘xyz’ Winding Set Currents against Time 199

Figure 5.35: Quadrature and Direct Axis Currents of Two (‘a-b-c’ & ‘x-y-z’) Stator Windings anda-b-c’ Rotor Winding 199

Figure 5.36: d-q Quadrature and Direct Voltages of the Two (a-b-c & x-y-z) Stator Windings as a Function of Time 200

Figure 5.37:Stator Voltages in Phase (‘a-b-c’ & ‘x-y-z’) Variables as a Function 200

Figure 5.38: Schematic Representation of Experimental DSWIM Test Rig 206

Figure 5.39: DC Resistance Measurement for each Stator Winding Set 208

Figure 5.40:Connection Diagram for Locked Rotor Test on DSWIM Prototype 209

Figure 5.41:Connection Diagram for No-load Test on DSWIM Prototype 211

Figure 5.42: Comparison of DSWIM Simulated and Experimental Steady State Speed Torque Characteristics 214

Figure 5.43: Comparison of Power Factor versus Speed for Dual and 3-ϕ Induction Machine 216

Figure 5.44:Comparison of Efficiency versus Speed for Dual and 3-ϕ I.M 216

Figure 5.45:Comparison of Torque versus Speed for Dual and 3-ϕ Induction Machine 217

Figure 5.46:Comparison of Mechanical Power versus Speed for Dual and 3-ϕ Induction Machine 217

Figure 5.47:Comparison of Current versus Speed for Dual and 3-ϕ Induction Machine 218

Figure 5.48:Comparison of Torque versus Current for Dual and 3-ϕ Induction Machine 218

Figure 5.49: Key Performance Characteristics of the Dual Stator Machine 219

Figure 5.50: Constructed Circle Diagram for DSWIM Prototype 220

Figure 5.51: Full Load Loss Segregation Analysis for the Prototype DWSIM 221

LIST OF PLATES

Plate 3.1: Induction Machine Rotor Structures 113

Plate 5.1: Stator coil in their respective slots 203

Plate 5.2 Squirrel cage rotor of the machine 203

Plate 5.3: Rotor and Wound Stator Side by Side 203

Plate 5.4: Inserted Rotor within the Stator Structure 203

Plate 5.5: Complete Prototype Machine 204

Plate 5.6: The Complete Laboratory Experimental Setup 206

LIST OF TABLES

Table 2.1: Definitions of Real Power transfers and losses in Induction Machine 16

Table 2.2: Stator Winding Distribution for Unity Pitch, 60^o Phase Spread anDouble Layer 37

Table 2.3: Stator Winding Distribution for Fractional Pitch, 60^o Phase Spread and Double Layer 39

Table 2.4: Dual Stator Winding Distribution for Unity Pitch, 30^0 Phase Spread, $\xi=30^0$ and Double Layer 40

Table 2.5: Dual Stator Winding Distribution for $\frac{5}{6}$ pitch, 30^0 Phase Spread, $\gamma = 30^0$ and Double Layer 42

Table 2.6: Summary of Derived Equations for Inductances of DSWIM Using Winding Functions

Table 2.7: List of Induction Machine Design Variables 57

Table 3.1 Specified Parameters of Machine Design 81

Table 3.2: Wound Rotor Principal Equations for Calculating Leading Leakage Inductances 113

Table 3.3: Equations for Calculating Squirrel Cage Rotor Parameters Referred to Stator 115

Table 3.4 Specified Parameters of 8/8 Pole Ratio DSWIM Design 125

Table 3.5: Summary of Sample Calculations for 8/8 Pole DSWIM MMF 127

Table 3.6:Summary of Key Leading Parameters Estimated for DSWIM and Standard IM 128

Table 3.7: Summary of Calculated DSWIM Parameters 129

Table 4.1: Geometric Specifications for DSWIM's FEMM Model Development 149

Table 4.2: Summary of Meshes Generated FEMM Model for Different Locked Rotor Tests 159

Table 5.1: Design Parameters for 8/8 Pole DSWIM Case Study 167

Table 5.2: Calculated DSWIM Steady State Parameters 168

Table 5.3:Summary of GA Simulation Parameters 171

Table 5.4: Convergence in Power Efficiency and Power Factor 172

Table 5.5: Final Design DSWIM Values Based on ICD and ICD+GA Compared with 3-ϕ IM 173

Table 5.6: Calculated Parameters for a Test Case DSWIM 174

Table 5.7: Computed Rotor Referred Parameters from FEMM Model for DSWIM at Specified Frequencies 183

Table 5.8: Comparison of Computed DSWIM inductance Values by Three Different Methods 184

Table 5.9: Parameter Specifications for the Simulation of Dual Stator Winding Induction Motor (DSWIM) in Simulink/MATLAB Environment 184

Table 5.10: Summary of Final Design Parameters and Operating Data for DSWIM Prototype 204

Table 5.11: Locked Rotor Test Results with x-y-z Winding Set Open 209

Table 5.12 Locked Rotor Test Results with 'a-b-c' Winding Set Open 210

Table 5.13: No Load Test Results with 'x-y-z' Winding Set Open 212

Table 5.14: No load Test Results with 'a-b-c' Winding Set Open 213

Table 5.15: Calculated DSWIM Parameters Based on Experimental Measurements 213

Table 5.16:Comparison of Some Selected Parameters for DSWIM Model and Prototype 215

Table 5.17: Summary of the computed losses at some selected DSWIM loading Scenarios 221

Table 5.18: Fitted Polynomial Equations for DSWIM Quantities Plotted in Figures 5.42-5.46 222

Table 5.19: Fitted Polynomial Equations for DSWIM Quantities Plotted in Figure 5.48223 223

APPENDICES

Appendix A: Specific Permeance 248

Appendix B: Estimation of Stator Resistance 253

Appendix C: Determination of Rotor Parameters 255

Appendix D: Estimation of Iron Losses 260

Appendix E: Determination of Induction Machine Parameters 262

Appendix F: ATLAB Script for G.A. Optimization 267

Appendix G: Lua-Script for FEMM 269

Appendix H: Salient Steps for the Construction of a Circle Diagram 291

LIST OF SYMBOLS

SYMBOL	MEANING
J	Combined inertia of the rotor and the connected mechanical load
φ_{mr}	Mutation rate
$\bar{I}_r$	Rotor current phasor
λ_{raa}	Self-flux linkage of phase 'a'
$\mathcal{F}_g$	Magneto-motive force of air gap
$\Im_{obj}(\eta, PF)$	Objective function
T_d	Developed torque
Υ_β	Angle of displacement in electrical radian
J_R	Moment of inertia
J_s	Current density
K_w	Winding factor
L_c	Core length
L_{ldq}	Mutual leakage
L_s	Stator core axial length
N_{coil}	Number of turns per coil
P_{CONV}	Conveyor loss
T_L	Load torque
X_{ro}	Rotor leakage reactance
Z_{ph}	Number of conductors per phase
k_{cs}	Carter's coefficient
k_l	Proportionality constant depending upon the slot dimensions
$n_j(\theta)$	Turn function of j-winding
$\bar{p}$	Winding pitch
r_b	Rotor bar resistance
$\mathcal{S}_g$	Reluctance
$\bar{\zeta}$	Vector of flux linkage per second
θ_r	Rotor angle
ρ_O	Resistivity of copper conductor at 25^oc
$\bar{\varsigma}$	Maxwell stress tensor

τ_p	Pole pitch
ω_r	Rotor speed
$\phi_i(\theta)$	Flux produced due to current in i-winding
μ_0	Permeability of air
3-ϕ	Three phase
A_{CS}	Cross sectional area of stator core
B	Magnetic flux density
B_{ag}	Flux density of air gap
C_O	Input power coefficient
D_{or}	Diameter of rotor
D_{os}	Diameter of stator
E	Electromotive force
E_{ro}	Rotor induced voltage
f	Frequency
g	Air gap length
H	Magnetic flux density
h_{cs}	Stator yoke thickness
I	Current
$\mathcal{L}(x)$	Reactance matrices
N_ϕ	Number of phases
P	Pole number
pf	Power factor
P_h	Harmonic loss
P_{in}	Total power input
P_{mech}	Gross mechanical power
P_{out}	Shaft power
P_{RCL}	Rotor copper loss
P_{rotor}	Power input to rotor
P_{SCL}	Stator copper loss
P_{stator}	Power input to stator
P_{STRAY}	Stray loss
P_{TRON}	Iron loss

P_W	Windage& frictional loss
S	Slip
T_{st}	Standstill torque
V_{TH}	Thevenin equivalent voltage
W_r	Rotor slot width
Z_{TH}	Thevenin equivalent impedance
θ	Angle in degrees
β	Displacement angle
η	Efficiency
λ	Flux linkage
Φ	Flux
Ω	Angular speed
$d\theta$	Elemental angle
σ	Phase spread
ψ	Weighting factor
$k_s(\bar{p})$	Coupling factor

ABSTRACT

The desirability for new induction machines that possess the combined advantages of the well-established wound-rotor and squirrel-cage induction machines have motivated considerable research interests in the development of dual-stator induction machines. Although extensive literature survey has revealed considerable advancements in the design architecture of dual-stator winding induction machine, it is yet to attain maturity from the standpoints of optimized active material utilization, efficiency and harmonic attenuation. In pursuit of some of these critical issues, this research is primarily aimed at developing a pragmatic approach of re-designing a standard three phase induction machine into an improved dual-stator winding induction machine (DSWIM) and of its practical implementation. More specifically, a methodology which encompasses realizing a dual stator winding machine prototype based on hybrid analytical and genetic algorithm (GA) optimization as well as establishing the machine performance characteristic indices, and its experimental validations. A paramount consideration is the comprehensive characterization of such improved dual-stator winding induction machine. The adoption of DSWIM housing similar pole ratios, as opposed to dissimilar pole ratios widely studied in the literature, is to permit full winding utilization and maximization of its output power capability. In this dissertation detailed mathematical modelling, based on Park's equations in d-q-0 arbitrary reference frame, to underpin simulation of the dual stator winding in MATLAB environment and application of finite element technique to stator field distribution mapping to enable computation of machine inductances have been developed and successfully implemented. All the leading DSWIM design parameters based on the classical design and GA optimization technique are presented and comprehensively discussed. The proposed theoretical computations of dual stator winding inductances are shown to be superior to the existing technique based winding function approach. As a major goal accomplished, a prototype implementation of the DSWIM equipped with 8/8 similar pole ratio has been satisfactorily realized in the laboratory as a demonstration of the practicability of the proposed design concept. This has enabled an elaborate experimental setup which facilitated accurate measurements of fundamental parameters of the proposed dual stator winding induction machine as well as in-depth operational performance evaluations comprising its steady state and dynamic drive capabilities. Of noteworthy is the GA optimization with respect to the similar pole ratio DSWIM stator winding re-design that revealed its optimum efficiency and power factor (p.f) values respectively to be 93.43% compared with 87% and 88.02% compared with 80% for standard 3-ϕ induction machine of the same rating. The significance of the improvement in DSWIM efficiency and power factor achieved is central to the actualization of the prime goal of this research work and capable of driving future research directions. The DSWIM housing similar pole ratios has, to the best of our knowledge, remained largely unexplored. The importanceof the proposed DSWIM design consideration has also envisaged its potential application to exploiting maximum power harvest from wind turbines operating in low wind regimes prevalent in the tropical region.

CHAPTER ONE

INTRODUCTION

1.1 Background Information

As a critical operational requirement, all modern electric utilities that supply electrical appliances, industrial equipment and drives must operate at constant frequency of choice; and it is either 50 Hz or 60 Hz (chapman, 1998). It is also well known that for any electric utility, different varieties of ac machines which are the workhorses of all motorized loads constitute dominant entities within industrial, commercial and residential load compositions. From the fundamental operating principles of an alternating current (ac) machine, its speed is proportional to the frequency of input voltage and current. Consequently, all ac machines have fixed speeds when supplied from power utilities. However their speeds can be made variable to meet the needs of most industrial processes. For example, a number of modern manufacturing processes, such as machine tools, require variable speed. The expanding applications of variable speed ac motors have remained the driving force for wide range of research activities aimed at improving their operational capabilities and efficiencies. A comprehensive overview of ac machine family is illustrated in Figure 1.1.

As a matter of fact, the introduction of variable-speed drives has increased automation and productivity and, in the process, efficiency. In developed countries typified by USA, nearly 65 % of the total electric energy produced is consumed by electric motors (Krishan, 2001). Variable speed drives in the industry employ electric motors as their drive motors mainly because they enjoy several specific advantages, such as overload capacity, smooth speed control over a wide range, capability of operation in all the four quadrants of the speed-torque plane, etc.

From historical perspectives until the advent of thyristors and power converters, dc motor varieties had been very popular in the area of adjustable speed drives, even though it suffered

from the disadvantages imposed by the presence of a mechanical commutator. Power converters capable of providing variable voltage, variable frequency supplies have now made ac motors increasingly popular. Among the ac motors used in the industry, induction motor is the most dominant because of its ruggedness as well as much cheaper maintenance and control requirements. Squirrel cage and wound rotor induction motors are most common induction motors found in small to large industrial complexes. The literature is therefore replete with design concepts on the induction machines of different configurations and the emerging design concepts on, and operational characterization of, multi-phase induction machines. The magnetic design, practical realization and characterization of multi-phase induction machine, in which the stator is equipped with two sets of windings of identical number of poles and standard squirrel cage rotor, constitute the core research areas addressed herein. Of prime research interest is the optimum reductions in DSWIM losses so as to maximize efficiency and also improve p.f.

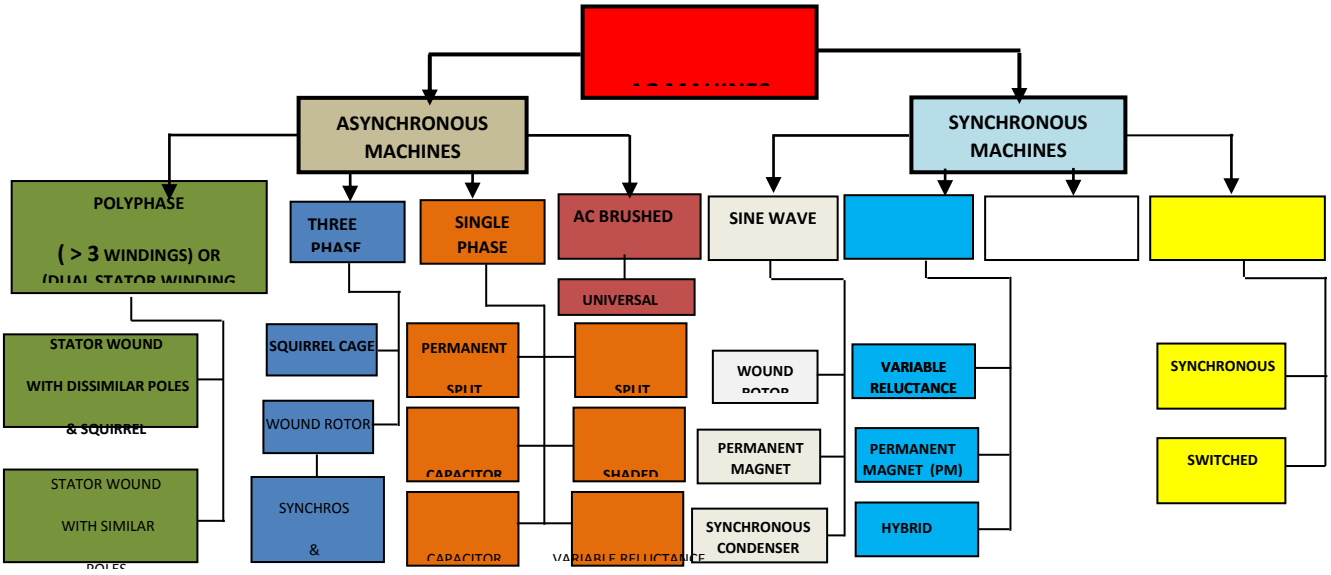


Figure 1.1: Generalized AC Machine Family (*Adapted from*: *Lessons in AC Circuits Vol. II-AC7*)

1.2 Research Justification

The conventional three phase induction motors have dominated the industrial undertaking as the workhorses of mechanized/automated processes and will continue to remain so into the foreseeable future. However with the demand for high power electric drive systems characterized by ruggedness, high energy-efficiency and reliability gave impetus to multi-phase induction machine development. Specialized applications, such as electric/hybrid vehicles, marine propulsion, aerospace applications, etc. that demand high reliability, are majorly responsible for the aforementioned demand for multi-phase induction motors. Within the last two decades therefore, multi-phase induction machines (machines equipped with phases higher than three) have been investigated by many researchers due to the following operational advantages (Alfredo and Lipo, 1998 ; Djafar et'al, 2004; Apsley and Steve 2006):

(i) Increased power ratings due to two winding design option;

(ii) Reduction in current per inverter leg ;

(iii) Increased reliability especially its fault tolerance capabilities;

(iv) Reduction in harmonic contents; and

(v) Wider scope of flexibility in the choice of control scheme.

The research effort on a multi-phase induction machine, having generalized representation of n-windings and phase configuration depicted in Figure 1.2 has not attained maturity. Yet some extremely important findings have been reported in literature indicating general feasibility of multi-phase induction machine of profound potentials. As a corollary, the prime focus of this research work is aimed at investigating design philosophy to secure improved multi-phase induction machine. The underlying design architecture and practical realization of the improved multi-phase induction machine as well as mathematical modeling

and experimental verification of its performance constitute the research thrusts embarked upon in this dissertation.

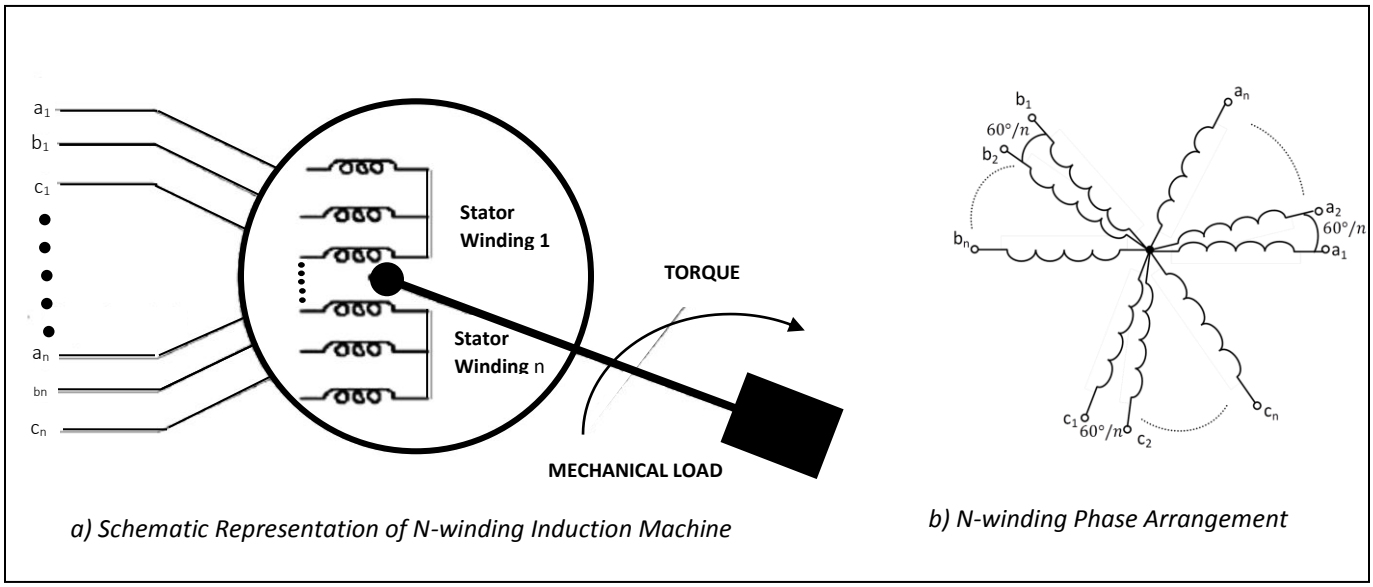


Figure 1.2: Generalized Representation of Multi-Phase Induction Machine and Phase Arrangement

1.3 Problem Definition

In recent years, multi-phase induction machines have attracted more focused attention from researchers. To date, various researchers have studied the operation of these machines as generators as well as motors with a view to analysing their performance characteristics as compared to standard three phase machines of similar ratings.

However, a comprehensive review of relevant literature: Ojo and Davidson (2000); Alfredo (1998); Munoz and Lipo (2000)) revealed that the machines either suffer from overheating due to excessive copper losses in the windings or incomplete utilization of the machine. Furthermore, the machine core performance indices such as starting torque and magnetizing current are a function of its inductances. There is therefore the need for an accurate method of determining these inductances. The conventional analytical method of determining these parameters (inductances) is anchored on the winding function approach. It assumes sinusoidal distribution of the winding but in the actual machine, the windings are not

sinusoidally distributed. This assumption therefore introduces error into the values of the inductances obtained. Consequently, performance prediction of the machine using the values of the inductances calculated by winding function method would attract appreciable modelling error.

In summary, the major unresolved research problems that have been identified with respect to dual winding induction machine to date are as follows:

- excessive copper loss in the windings by optimizing the machine's efficiency;
- partial utilization of the machine stator dual windings during running mode; and
- Inaccurate method of calculating the machine's inductances.

Against the backdrop of the foregoing, the concomitant research questions of prime interest are as follows:

- Is it possible to evolve dual stator machine re-design approach to minimize excessive copper losses in the windings?
- Is full utilization of machine stator dual winding realizable and how does it impact its architectural construction?
- Can a pragmatic analytical framework be developed to facilitate calculations of machine's inductances as superior alternative to winding function approach from the standpoint of computation accuracy?

These research questions are addressed frontally in this dissertation via specific problem definition. It seeks, in the main, to optimally redesign dual stator windings (a-b-c and x-y-z) spatially displaced by fixed angle (α degrees) and of similar number of poles to replace existing windings of standard three-phase induction machine without altering the original architecture of the squirrel cage rotor. Embedded in the problem definition are the indispensible requirements to improve efficiency and p.f. of DSWIM design, accurately

determine DSWIM parameters for its steady/dynamic state simulation studies leading finally to construction of DSWIM prototype to enable extensive experimental validations.

1.4 Aim and Objectives

The aim of this research is to design, construct and carry out performance analysis of an improved dual three-phase stator winding electric machines. (using an integrated analytical, meta-heuristic, simulation and experimental framework). Towards the realization of this aim, the following objectives are pursued:

i. Mathematical formulation of the DSWIM design based on analytical approach and GA optimization to facilitate computations of stator winding leading parameters and application of GA to specifically search for optimum DSWIM efficiency and pf.

ii. Development of a hybrid analytical and meta-heuristic framework for the optimal design of an improved dual three-phase stator winding to achieve the following:

- Minimization of excessive copper loss; and
- Enforcement of full utilization of stator windings during running mode via appropriate choice of n/n stator winding pole ratios.

iii. Derivation of necessary equations to enable accurate computations of the dual stator winding inductances and resistances that rely on the physical configurations of the stator windings and stator slot geometries, stator bore instead of the widely used winding functions in the existing relevant literature. In addition the following derivations are essential to the overall DSWIM modelling

- Fundamental derivations of the voltage equations in generalized time dependent variables and subsequent transformation into time invariant variables;
- Computations of winding mutual, self and leakage inductances with special attention given to their accurate derivations ;

- Derivation of the equivalent circuit of the dual stator winding induction machine in d-q-0 reference frame; and
- Development of software programs for the simulation of DSWIM in MATLAB environment.
- Development of finite element method (FEM) modelling of DSWIM to determine its leading inductances.

iv. Development of stator winding diagram leading to construction of a prototype 3-phase dual stator winding induction machine;

v. Setting up an experimental configured test bed rig dedicated specifically for the prototype 3-phase DWSIM to determine its wide range operational characteristics that include efficiency, torque, etc.

1.5 Overview of the Research Methodology

The research methodology roadmap is summarized in the functional flowchart of Fig. 1.3. The methodology roadmap must of necessity conform to the aim and objectives of this dissertation. For the sake of clarity, some critical research issues to be addressed are further re-iterated as follows:

1. Establishment of the current research status and milestone achievements with respect to multi-phase induction machine and therefrom identify the critical research areas deserving priority attention.
2. Derivations of generalized mathematical model and computation of necessary equivalent circuit inductances to underpin performance analyses of dual stator winding induction machine and to serve as benchmark test-bed model.
3. Development and implementation of the proposed induction machine redesign philosophy to facilitate conversion of conventional induction machine into dual stator winding induction machine of identical or dissimilar pole ratio.

4. Standard experimental test rigs configured around the redesigned dual stator winding induction machine as well as conventional three phase induction machine of the same rating for comparative evaluations of key performance indices.
5. Investigation of redesigned dual stator winding induction machine model via simulations in MATLAB Simulink as conceptualized in Fig. 1.4 and benchmarking such simulation results against equivalent experimental results for accuracy verifications.
6. Finite Element Modelling of DSWIM according to the generalized framework of Fig. 1.5 to enable determination of stator inductances and flux patterns in the machine air gap and compared with the analytical approach for inductance computations.
7. Comparative evaluations of the dual stator winding induction machine based on simulation results and experimental results.

The overall research goal is to achieve improved dual stator winding induction machine performance from standpoints of energy loss minimisation via optimum participation of the dual stator windings at different levels of mechanical loadings.

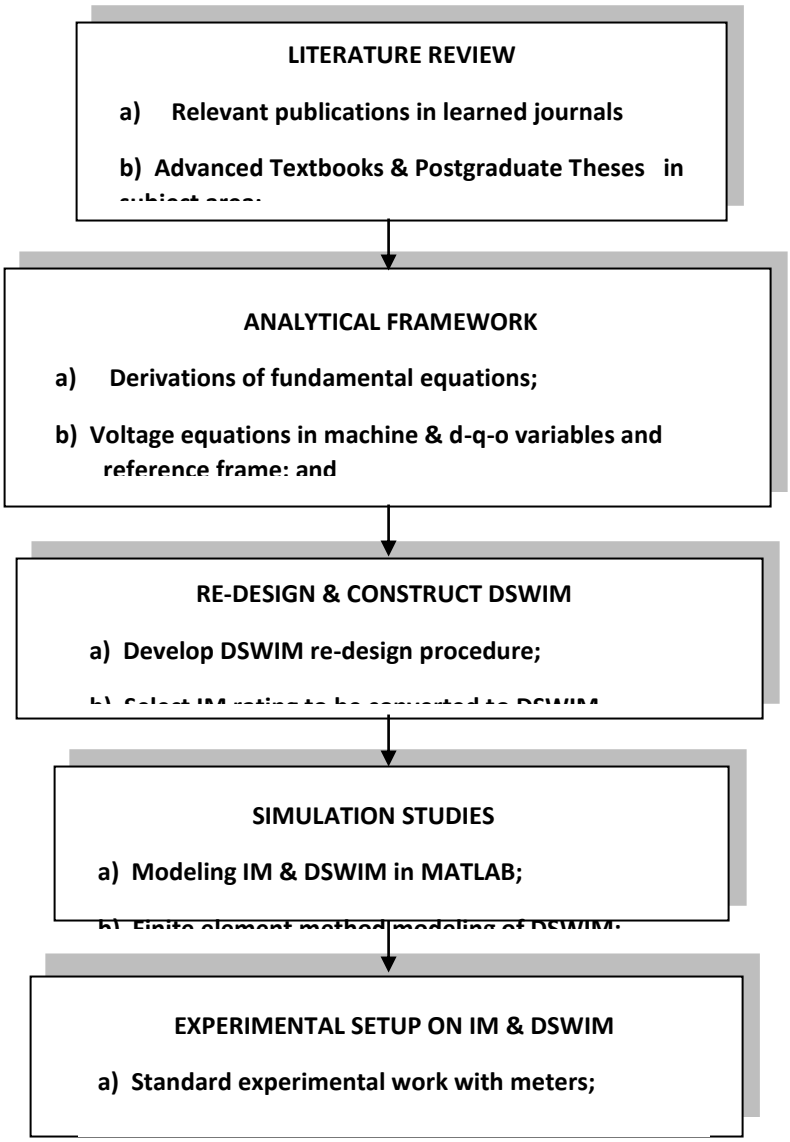


Figure 1.3: Overview of Research Methodology

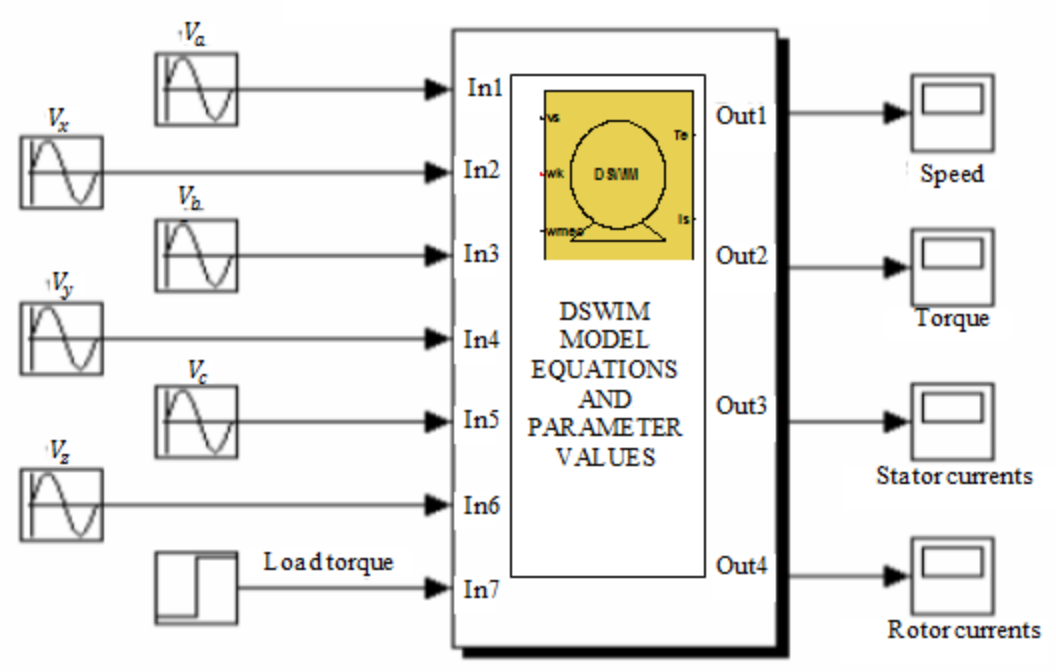


Figure 1.4: Block Diagram of DSWIM in MATLAB/ Simulink Simulation Environment

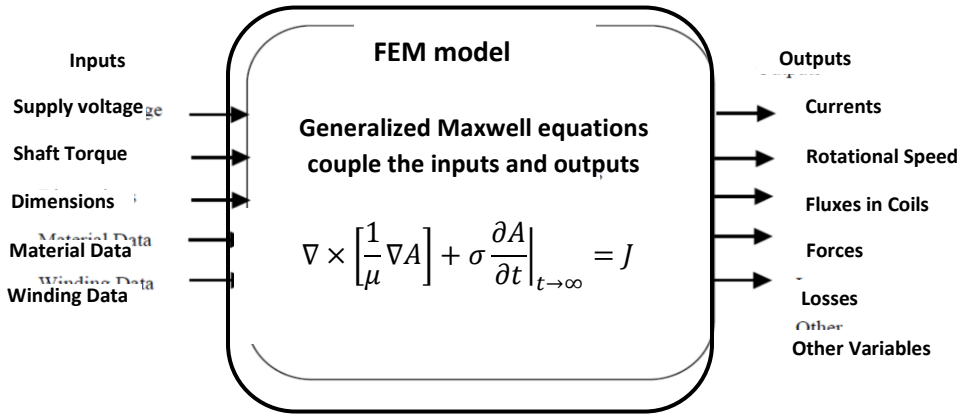


Figure 1.5: Basic Block Diagram of the Finite Element Method.

1.6 Significance of the Research

The research was concerned with design philosophy targeted at achieving improved dual stator winding induction machine in order to attract superior operational performance not attainable by existing design concepts. This is primarily driven by the global trend towards efficient energy utilisation which, in turn, called for the need to look into new design

techniques/architectures and implementation of induction machines being dominant players in industrial drive systems. For this purpose attention was herein focused more on the new class of induction machines due to some advantages they possess over other machines. Flexibility, ease of control, ruggedness and the possibility of generating voltage at any speed beyond synchronous are but a few of the inherent qualities of the induction machines. Because of the rapidly growing demand for high power drive system and more flexible operation, multiphase machines are attracting serious attention from researchers. Preliminary review of current literature has established that multi-phase induction motor design trend is yet to attain maturity. This research work is therefore an attempt to deepen maturity of multi-phase induction machine via new design concept and improved modelling strategy.

1.7 Dissertation Organization

This dissertation is divided into six chapters and supported by four appendices. Chapter one is a general introduction. In this chapter, the aim and objectives have been articulated in line with the core research problem addressed. An overview of the methodology adopted to meet the research goals is also presented in the chapter.

Chapter two has two main components: detailed review of fundamental concepts and in-depth literature review of similar works. The detailed review of fundamental concepts provide basic theoretical framework for induction machines and derivations of salient equations of relevance to dual stator winding machine design and analytical treatment. The literature review of similar works entail publications supportive of this dissertation to embark on the research direction identified.

Chapter three is dedicated to fairly extensive mathematical modelling of the dual stator winding induction machine using Park's transformation applied to its derived differential

equations in phase variables. Here, the equivalent circuits of the machine are developed and most importantly the torque equation established.

Chapter four is concerned with the design aspect of the machine based on traditional analytical approach and application of GA to optimize DSWIM efficiency. In addition, magnetic field distribution pattern via finite element analysis is set forth to determine DSWIM leading simulation parameters. A generalized winding architecture was also documented in this chapter.

Chapter five includes simulation results carried out in MATLAB/Simulink environment, results of finite element analysis applied to DSWIM, winding diagrams developed for DSWIM and its prototype realization as well as far reaching results of the experimental work done. Furthermore, comprehensive discussions of all the results obtained are contained in this chapter.

Chapter six focuses on general conclusions, and recommendations. All references duly consulted during this research work and four appendices to reinforce critical technical materials of Chapters two to four as well as two computer program listings developed are provided at the end of the dissertation.

CHAPTER TWO

THEORETICAL BACKGROUND AND LITERATURE REVIEW

2.1 Introduction

This chapter is broadly divided into two parts. The first part is concerned with the review of the fundamental background concepts on induction machine family and specific derivations of equations in respect of dual stator winding induction machines which are critical in their design philosophy. The second part presents summary of literature review of publications found relevant to the research work embarked upon in this dissertation. Of central importance is the need to reiterate the research gaps tackled in this dissertation that emanated from the current knowledge base in the literature.

2.2 Review of Fundamental Concepts

In Chapter One, a fairly comprehensive overview of ac machines was presented that focused specifically on the conventional ac machines and the emerging dual stator wound induction machines. The basic theory of all rotating machines is founded on Faraday's law ($E = BVL$) and Lorentz equation ($F = BIL$). Consequently the analysis of conventional three-phase machines is equally fundamentally valid for analyzing multi-phase induction machines of interest. More specifically, the established theoretical concept will be applied to explain braking, motoring and generating modes of induction machines. In the subsequent subsections, an attempt will be made to set forth the basic theory in respect of the identified operating modes of induction machines and proceed therefrom to derive necessary equations pertinent to DSWIM design concept.

2.2.1 Characterizations of physical features and operating modes of induction machine

The fundamental function of an electric motor is to develop an electromagnetic torque part of which is used in driving any mechanism (load) connected to its shaft. In the case of induction motor, this is achieved when alternating currents are supplied directly to its stator windings and by transformer (induction) action to the rotor. The rotor of an induction motor is of two types; the wound rotor and squirrel cage rotor. A brief synopsis of induction machine physical structure, typical loss profile and steady state equivalent circuit is depicted in composite Figure 2.1. Table 2.1 summarizes various power flows, segregated losses in multi-phase induction machines and their respective definitions as found in contemporary literature.

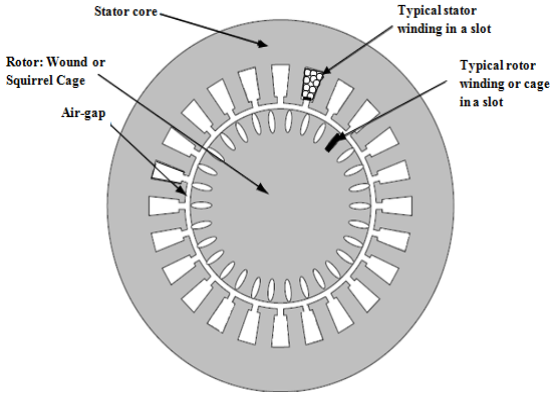
The wound rotor has distributed windings in the rotor slots and they are employed with terminals connected to insulated slip rings mounted on the rotor shaft. While the squirrel cage rotor has conducting bars embedded in the rotor slots and short-circuited at each end by conducting end rings. The rotor terminals are thus inaccessible in a squirrel cage construction, whereas they are made available through carbon brushes resting on the slip rings for the wound rotor construction.

The stator of an induction motor carries more than one winding and they are displayed in space at certain electrical degrees. The application of an alternating voltage to the stator winding results in the appearance of a rotating magnetic field within the air gap of the motor. The rotating field cuts the rotor bars and induces EMF (current) in them. The current in the bars interact with the field to produce an electromagnetic torque that rotates the rotor in the direction of the rotating field. When an induction machine operates as a motor, the rotor rotates with a speed lower than that of the rotating field. The relative speed between the rotor and the rotating field is termed slip, s. The most important performance characteristic index

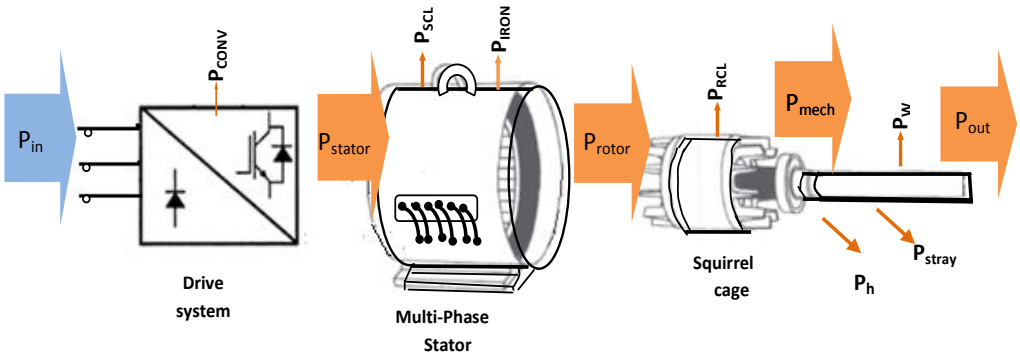
of induction motors concerns the variation in the rotor speed (slip) with torque that constitutes the so called torque-speed characteristics (Chapman, 1998). The steady state generalized representation of multi-phase induction machine is offered in Figure 2.2. Figure 2.3 depicts typical torque-speed characteristics identifying the three operating modes of multi-phase induction machine based on slip variation.



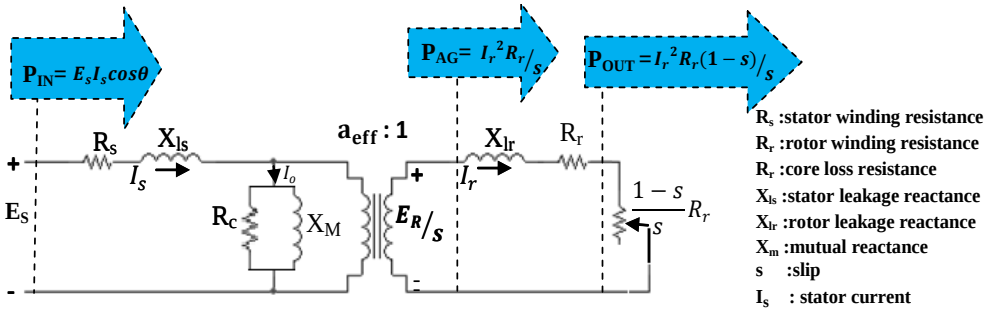
a) Assembled induction machine



b) Cross-sectional view of an induction



c) Power Balance/Loss Segregations in Multi-phase Induction Machine Drive System (*Adapted from:* Raj et. al 2009)



e) Per- phase steady state equivalent circuit for induction machine

Figure 2.1: Synopsis of Conventional Induction Machine Salient Features and Basic Analysis

Table 2.1: Definitions of Real Power transfers and losses in Induction Machine

Variables	Definitions	Calculations	Remarks
P_{CONV}	Convertor loss	$P_{CONV} = P_{in}$-P_{stator}	Essentially transistor switching + on-state losses. Typically less than 1% of the total drive system losses.
P_{SCL}	Stator copper loss	$P_{SCL} = \frac{3}{2} R_{dc} I_1^2$	R_{dc}: is stator dc resistance measured any two phases; I_1: fundamental line current; R_{dc} is temperature dependent.
P_{RCL}	Rotor copper loss	$P_{RCL} = P_{rotor} s$	Note $P_{rotor} = P_{airgap}$ and s is slip. Slip test or locked rotor test can be used to determine rotor copper loss.
P_{IRON}	Iron loss (Stator+ Rotor)	$P_{IRON} = P_{rotor} - P_{mech}$	P_{IRON} *and* P_W can be determined from IM no-load test and apply loss segregation method to determine P_W. P_{IRON}=$P_o - P_W - 3\,R_{dc} I_o^2/2$; where I_o& P_O are no load current and input power.
P_W	Windage & Frictional loss	$P_W = P_{mech} - P_{out}$	
P_{stray}	Stray loss	P_{stray}=$P_{stator} - P_{mech} - P_{IRON} - P_{SCu} - P_{RCu} - P_W$	Stray loss is the unaccounted loss between the input power and the output. Require accurate measurement of independent variables.
P_h	Harmonic loss	$P_h = P_{in} - P_{in(1)}$	$P_{in(1)}$ is the power input at fundamental frequency.
P_{in}	Total Power Input	$P_{in} = \sqrt{3} V_L I_L \cos(\theta)/2$	Measured with wattmeter setup for 3-ϕ real power measurement at converter input.
P_{stator}	Power Input to Stator	$P_{stator} = \sqrt{3} V_L' I_L' \cos(\theta')/2$	Measured with wattmeter setup for 3-ϕ real power measurement at DSWIM input.
P_{rotor}	Power Input to Rotor	$P_{rotor} = P_{airgap}$	The air-gap power can also be measured via the air torque measurement fairly accurately.
P_{mech}	Gross Mechanical Power	$P_{mech} = P_{rotor}(1 - s)$	The gross mechanical power is calculated given P_{airgap} and slip, s.
P_{out}	Shaft Power	$P_{out} = T_{out} x \omega$	The product of measured torque, T_{out} and angular speed, ω of the DSWIM
s	slip	$s = {(n_s - n_r)}/{n_s}$	n_s is rotor synchronous speed and n_r is rotor operating speed in revolutions/minute
ω	Angular speed	$\omega = 2\pi n/60$	Measured fairly accurately via digital or stroboscop

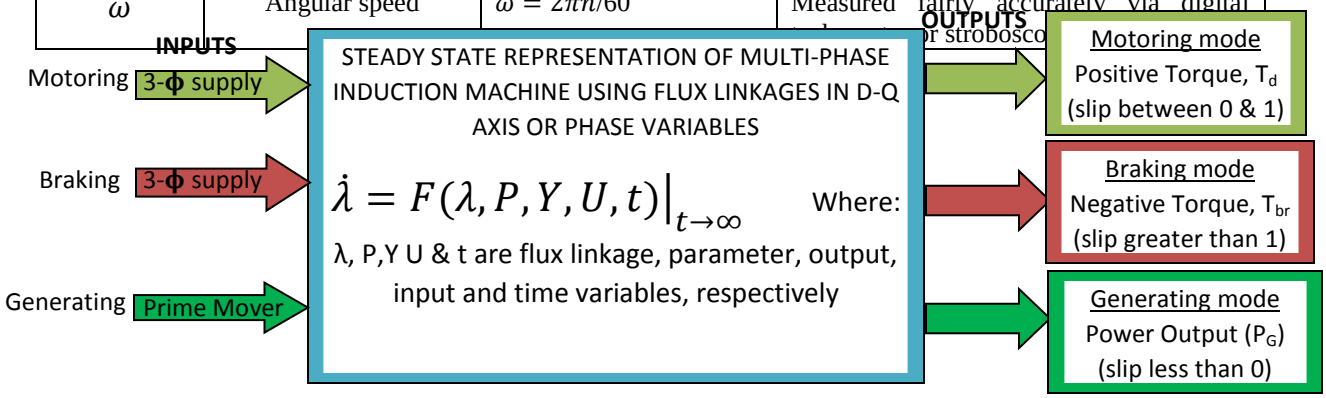


Figure 2.2: Functional Diagram of Poly-phase Induction Machine for Three Operating Modes

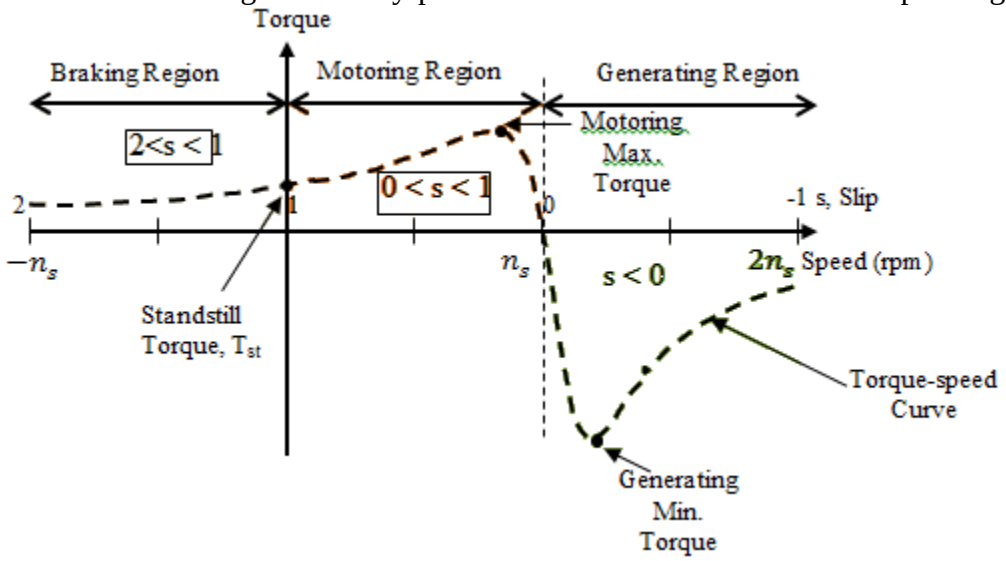


Figure 2.3: Complete Torque-Speed Characteristics of Multi-phase Induction Machine

2.2.2 Development of induction machine speed-torque characteristics

Starting from single-phase equivalent circuit of induction motor shown in Figure 2.1(e), the well-known equation for the torque developed, T_d, by an induction machine is given by (Chapman, 1998):

$$T_d = \frac{P_{AG}}{\omega_s} \tag{2.1}$$

Expressed in terms of the rotor quantities in which the, equation (2.1) becomes:

$$T_d = \frac{P_{Rcl}}{s \times \omega_s} = I_r^2 \frac{R_r}{s \times \omega_s} \tag{2.2}$$

Where the variables used in equations (2.1) and (2.2) are previously defined in Figure 2.1(d) and Table 2.1 and P is the number of poles of the induction machine.

Equation (2.2) conveys that the developed torque is a function of two variables: rotor current I_r and slip s. In order to simplify analysis the torque is expressed as a function of only one variable. To achieve it, the rotor current is substituted by the expression:

$$I_r = \frac{E_{Ro}}{\sqrt{\left(\frac{R_r}{s}\right)^2 + X_{ro}^2}} \tag{2.3}$$

Where:

$E_{Ro} \triangleq \frac{E_R}{s}$ & $X_{ro} \triangleq \frac{X_{rl}}{s}$; E_{Ro} & X_{ro} : are rotor induced voltage and rotor leakage reactance, respectively at standstill whilst E_R & X_{rl} are slip dependent variables in the rotor circuit. The intent is to transform the rotor variable speed effects into variable impedance connected across constant voltage source. This will then yield expression of the developed torque as a function of the slip as given in equation (2.4).

$$T_d = \frac{1}{\omega_s} x \frac{E_{Ro}^2 \left(\frac{R_r}{s}\right)}{\left(\left(\frac{R_r}{s}\right)^2 + X_{ro}^2\right)} \text{ (N-m)} \tag{2.4}$$

By referring the rotor circuits into the stator circuit supported by the practical assumption that $I_o \ll I'_r$ (referred to rotor current) and applying basic circuit analysis will yield the equation for the developed torque in terms of stator voltage and slip as follows:

$$T_d = \frac{R'_r}{s\omega_s} \frac{E_S^2}{\left(\left(R_S + \frac{R'_r}{s}\right)^2 + \left(X_S + X'_r\right)^2\right)} \text{ (N-m)} \tag{2.5}$$

Where:

R'_r, x'_r : are rotor quantities referred to the stator which are measurable from locked rotor tests. Although the foregoing equations are derived using single phase equivalent circuit, multiplying the right side by factor 3 convert them to values for three phase induction .machines in their respective units. An approach to evolving more accurate torque equation is to develop Thevenin equivalent circuit for the stator side represented by V_{TH} and Z_{TH} with the referred side of the rotor acting as load. It is then easily shown that (Chapman, 1998):

$$T_d = \frac{R'_r}{s\omega_s} x \frac{V_{TH}^2}{\left(\left(R_{TH} + \frac{R'_r}{s}\right)^2 + \left(X_{TH} + X'_r\right)^2\right)} \tag{2.6}$$

2.2.3 Motoring and braking operating regimes

The motoring mode of induction machine operation is the most common for all mechanical drive objectives. In this region, both torque and motion are in the same direction. A plot of T_d using typical parameters of an induction motor, popularly referred to as $\text{torque} - \text{speed}$ characteristics, is shown in Figure 2.4 at constant frequency and input voltage. The circle diagram of Figure 2.5 is essentially a locus plot of rotor current phasor, $\bar{I}_r = s_{(j)}E_{Ro}/\left(R_r + js_{(j)}X_{ro}\right)$: j = 1,2 ... 5 as slip changes for motoring mode operation. Note that at $s_{(j)} \to \infty\ \bar{I}_r = E_{Ro}/jX_{ro}$ with its magnitude being the diameter of the semi-circle. The steady state operating domain of is the induction motor is typically when the slip is in the neighbourhood of 5 percent. In this steady state analysis, space harmonics have not been considered

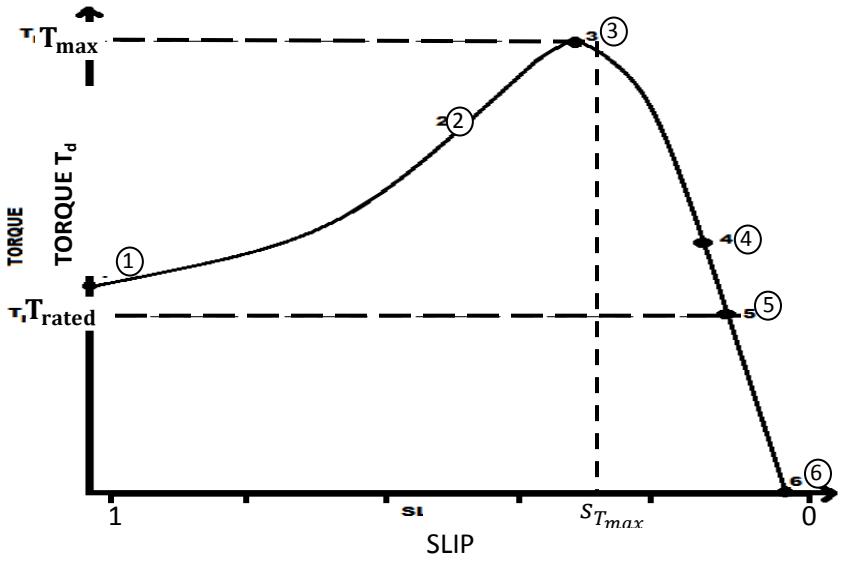


Figure 2.4: Speed versus torque characteristics for Induction Machine Motoring Mode(Chapman, 1998)

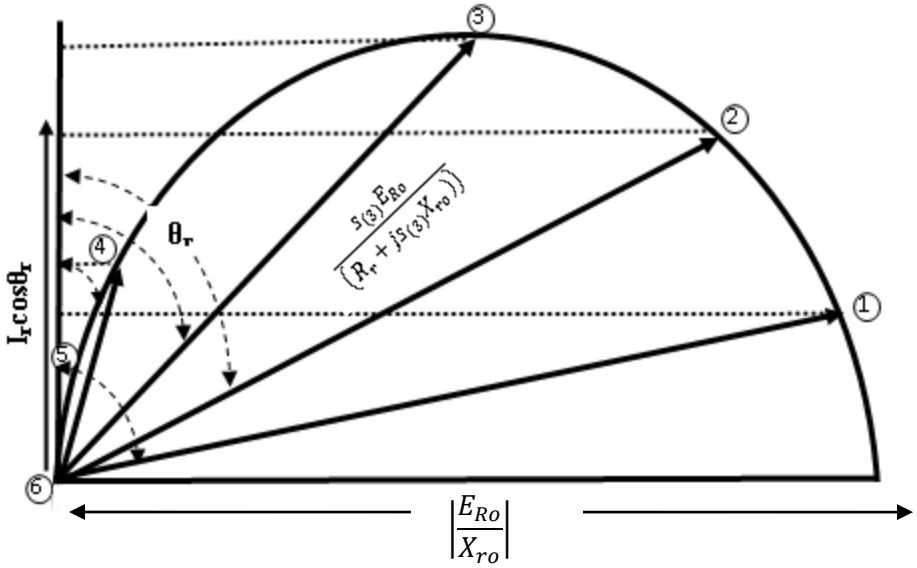


Figure 2.5: Circle Diagram of an Induction Machine in Motoring Mode (Chapman, 1998)

If the rotor is at rest, mechanical inertia prevents rotation at the instant voltage is applied to the stator; in effect, the motor behaves as though the rotor is locked. The torque developed at the locked-rotor stage is the turning moment produced by the interaction of the rotor current and the stator flux when the shaft is at rest and a voltage applied to the stator winding. This torque is called a locked-rotor or standstill torque T_{st} . It occurs at a slip $(s = 1.0)$ and substituting this value into equation 2.4 yields $T_{st} = ((R_r/\omega_r)xE_{Ro}^2)/(R_r^2 + X_{ro}^2)\ where\ \omega_r \triangleq 2\omega_s/p.$

If the load torque on the shaft is equal to or exceeds the locked-rotor torque, the motor will not start. Should this occur, and protective devices fail to isolate the machine from the line, it could lead to motor stator winding failure. Locked-rotor condition is indicated by point 1 in Figure 2.4. Assuming the load torque on the shaft is less than the locked-rotor torque, the rotor will accelerate. As the machine accelerates from its standstill position, the slip decreases causing the magnitude and phase angle of rotor current to decrease. This is shown in Figure 2.5, where the active component of rotor current, $I_r cos\theta_r$ increases from its low

value at blocked rotor to some maximum value, called the breakdown value, and then decreases again with further acceleration. Note the correlation between developed torque (T_d) and $I_r \cos\theta_r$ in Figure 2.5.

The breakdown torque is defined as the maximum torque that a motor can developed while being loaded (at rated voltage and rated frequency) without suffering an abrupt drop in speed. An expression for the maximum torque corresponding to point 3 indicated in Figure 2.3 can derived from equation 2.26 by applying maximum power transfer principle to the induction machine Thevenin equivalent circuit earlier discussed. It can then be shown that $T_{max} = (V_{TH}^2/2\omega_s)/\left(R_{TH} + \sqrt{(R_{TH}^2 + (X_{TH} + X_r')^2)}\right)$ and its correponding slip value given by $s_{T_{max}} = R_r'/\sqrt{(R_{TH}^2 + (X_{TH} + X_r')^2)}$. It can be seen from this derivation that slip $s_{T_{max}}$ is directly proportional to the R_r' and on the other hand T_{max} is independent of R_r'. It is therefore possible to control the speed at which maximum torque occurs by inserting resistor in the rotor circuit without affecting its magnitude for wound rotors only or use double squirrel cage rotor.

Within the normal operating regime of an induction motor, its rotor revolves in the same direction of rotation of the magnetic field set up by the stator currents. However in order to transfer an induction motor into the region where the slip is greater than one i.e. (s >1) will require sudden reversal of the magnetic field direction of rotation. This can be achieved practically by interchanging any two phases supplying a multi-phase induction. The practical application of this operating regime is to create an electromechanical torque T_{Br} that can bring a running induction motor to a quick stop. This, frequently referred to as braking mode of operation of an induction motor, is widely used in hoisting drives such as cranes and lifts.

2.2.4 Generating mode of operation of induction motor

When an induction machine is driven at a speed greater than the synchronous speed (negative slip) by means of an external prime mover such as wind turbine, mini-hydro turbine etc., the direction of induced torque is reversed and theoretically it starts to operate as an induction generator. To build up and maintain voltage across the generator terminals constant, excitation must be provided by some means. Broadly speaking, the induction generator can work in two modes (i.e. grid connected and isolated mode). For grid-connected mode, the induction generator can draw reactive power from the grid for its voltage support requirements. In the case of an isolated mode, there is need for a suitable capacitor bank connected across the generator terminals. This phenomenon is known as capacitor self-excitation and the induction generator is called a self-excited induction Generator (SEIG) as schematically illustrated in Figure 2.6.

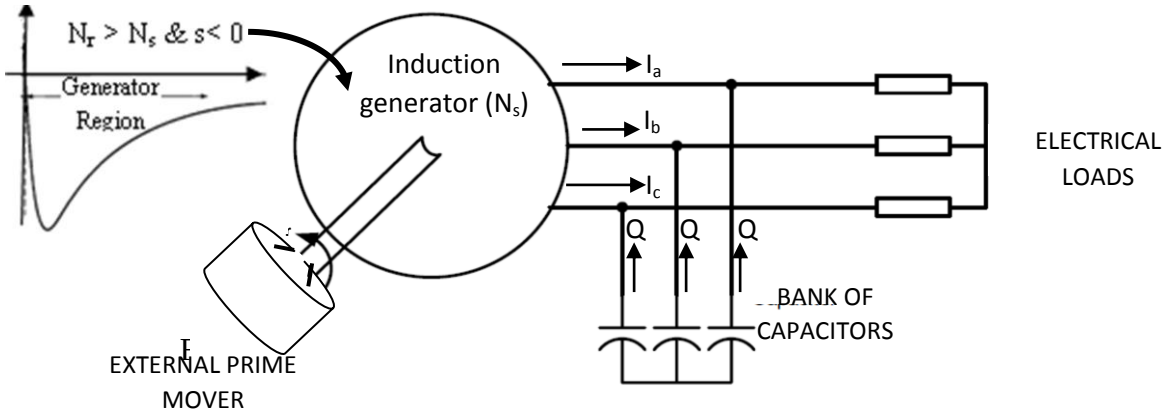


Figure 2.6: Schematic Diagram of Self Excited Induction Generator (SEIG)

When an induction generator first starts to run, the residual magnetism in the rotor circuit produces a small voltage. This produces a capacitive current flow, which increases the voltage and so forth until the voltage is fully built up. The no-load terminal voltage of the induction generator is the intersection of the generators magnetization curve with capacitor load line. The magnetization curve of the induction generator can be obtained by running the

machine as a motor at no load and measuring the armature current as a function of terminal voltage.

2.2.5 Dual stator winding induction machine theoretical concept

The operating concept of dual stator winding induction machine is basically similar to conventional induction machines dealt with in the preceding subsections. It is therefore theoretically feasible to convert any existing conventional 3-phase induction machine into n-phase machine having the same rating provided that the number of stator slots is a multiple of n as conceptualized in the generalized bock diagram and phase configuration depicted in Figure 1.2 of the preceding chapter. There are a number of ways in which multiphase machine windings can be produced. One way is to convert a single winding into a winding capable of producing two simultaneously rotating flux as proposed by (Lipo et. al, 1998).

However, to date only 6-phase (Dual-Stator Winding) machine (where n=2) has received intense research investigation as illustrated schematically in Figure 2.7 for DSWIM with dissimilar pole ratio (Alfredo and Lipo 2000). Consequently, a great deal of attention was devoted to the elaborate literature survey on the historical evolution of dual stator winding induction machine (DSWIM). It has been established, to the best of our knowledge, that for research purpose the design and construction of DSWIM almost always start from its conventional 3-phase induction machine family to actualize the desired dual winding architecture for specific operational features and capabilities.

As stated in Chapter One, and reiterated here again, the demand for high power electric drive systems characterized by ruggedness, high energy-efficiency and reliability propelled research activities in the development of multi-phase induction machine. Specialized applications, such as electric/hybrid vehicles, marine propulsion, aerospace applications, etc. that demand high reliability, are principally responsible for the aforementioned demand for

multi-phase induction motors. The research activities on multi-phase induction machines have not attained maturity. However, some far reaching findings have appeared in the literature indicating general feasibility of multi-phase induction machine.

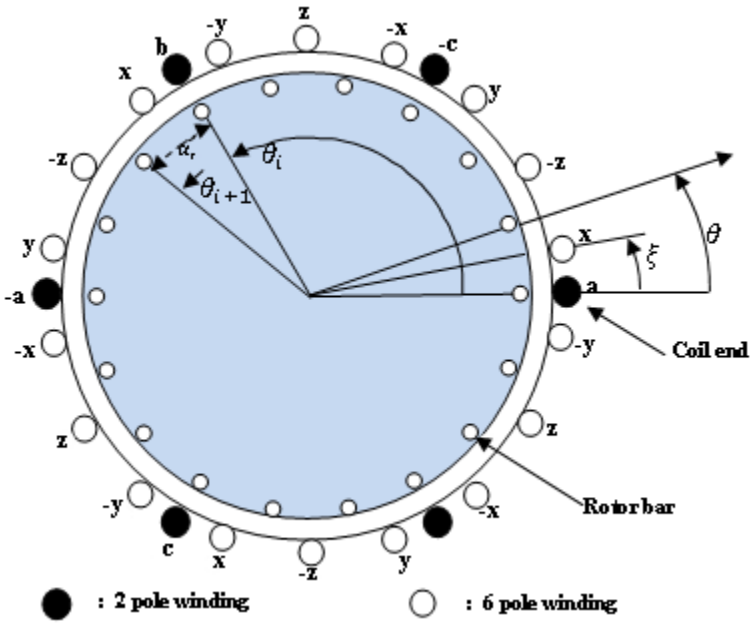


Figure 2.7: Schematic Diagram of a Dual Stator Induction Machine with Dissimilar Pole Ratio (Fuchs and Rosenberg, 1974)

2.2.6 Derivation of DSWIM equivalent circuit parameters and torque equation

This subsection is devoted to deriving an equivalent circuit and torque equation for a dual-winding induction machine. More precisely, the dual stator winding induction machine of interest in this research work has six phase windings in the stator and the rotor is modelled by three rotor phase windings. The assumptions are made as follows:

1. Two identical sets of sinusoidally distributed stator windings;
2. Each set comprises 3-phases: Set 1 is denoted by a-b-c and Set 2 is denoted x-y-z.
3. The phases in each set are displaced by an angle, $\beta=2\pi/3$.
4. The angle, ζ between corresponding phases is assumed to be the same and equals to $\pi/6$.

5. Magnetic saturation and core losses are neglected.
6. Deep rotor bar modelling and harmonics not considered.

The winding schematic representation of a dual winding induction machine is shown in Figure 2.8. It consists of two-three phase windings labelled a-b-c and x-y-z whose magnetic axes are displaced by an arbitrary angle ζ. Each three phase set consists of three identical sinusoidally distributed windings displaced by 120^o with equivalent turns of N_1 for a-b-c winding and N_2 for x-y-z winding and series resistance of r_1 for a-b-c winding and r_2 for x-y-z winding. The rotor is a standard squirrel cage with N_r equivalent turns and r_r rotor resistance per phase. Here, for simplicity of analysis a three phase rotor is assumed.

2.2.6.1 Voltage equations in machine variables

Based on the assumptions made the next step in the development of the machine's equivalent circuit is to derive expressions for the machine inductances as diagramed in Figure 2.9 and employing flux axes as defined in Figure 2.10. The voltage equations in a-b-c machine variables can be expressed in compact matrix form as:

$$V_{abc_s} = r_{abc_s} i_{abc_s} + p\lambda_{abc_s} \tag{2.7}$$

$$V_{xyz_s} = r_{xyz_s} i_{xyz_s} + p\lambda_{xyz_s} \tag{2.8}$$

$$V_{abc_r} = r_{abc_r} i_{abc_r} + p\lambda_{abc_r} \tag{2.9}$$

Where

$(f_{abc_s})^T = [f_{as}, f_{bs}, f_{cs}]$; $(f_{xyz_s})^T = [f_{xs}, f_{ys}, f_{zs}]$; $(f_{abcr})^T = [f_{ar}, f_{br}, f_{cr}]$; $p \triangleq \frac{d}{dt}$.

$f \in \{V, i, \lambda\}$; $r_{abc_s} = \text{Diagonal}(r_{as}, r_{bs}, r_{cs})$; $r_{xyzc_s} = \text{Diagonal}(r_{xs}, r_{ys}, r_{zs})$; and $r_{abc_r} = \text{Diagonal}(r_{ar}, r_{br}, r_{cr})$.

Subscripts s and r refer to variables associated with the stator and rotor windings, respectively.

The resistances in equations 2.7-2.9 form diagonal sub-matrices with non-zero elements only along the diagonals.

The flux linkages are given by the following expressions:

$$\lambda_{abc_s} = L_{abc_s}, i_{abc_s} + L_{abc_s xyz_s} i_{xyz_s} + L_{abc_s abc_r} i_{abc_r} \quad (2.10)$$

$$\lambda_{xyz_s} = L_{xyz_s}, i_{xyz_s} + L_{xyz_s abc_s} i_{abc_s} + L_{xyz_s abc_r} i_{abc_r} \quad (2.11)$$

$$\lambda_{abc_r} = L_{abc_r}, i_{abc_r} + L_{abc_r xyz_s} i_{xyz_s} + L_{abc_r abc_r} i_{abc_r} \quad (2.12)$$

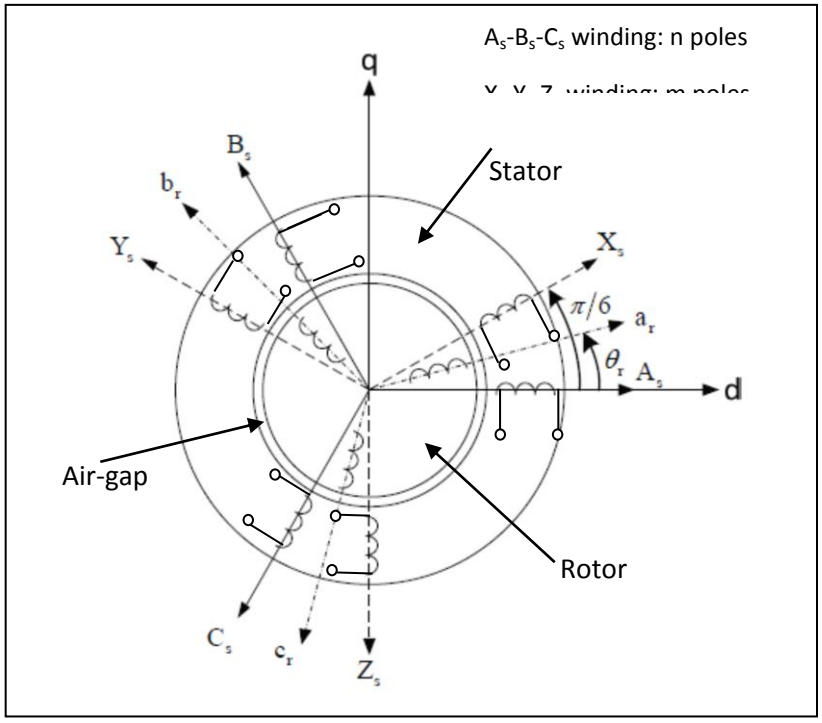


Figure 2.8: Schematic Diagram of a Dual-Winding Induction Machine

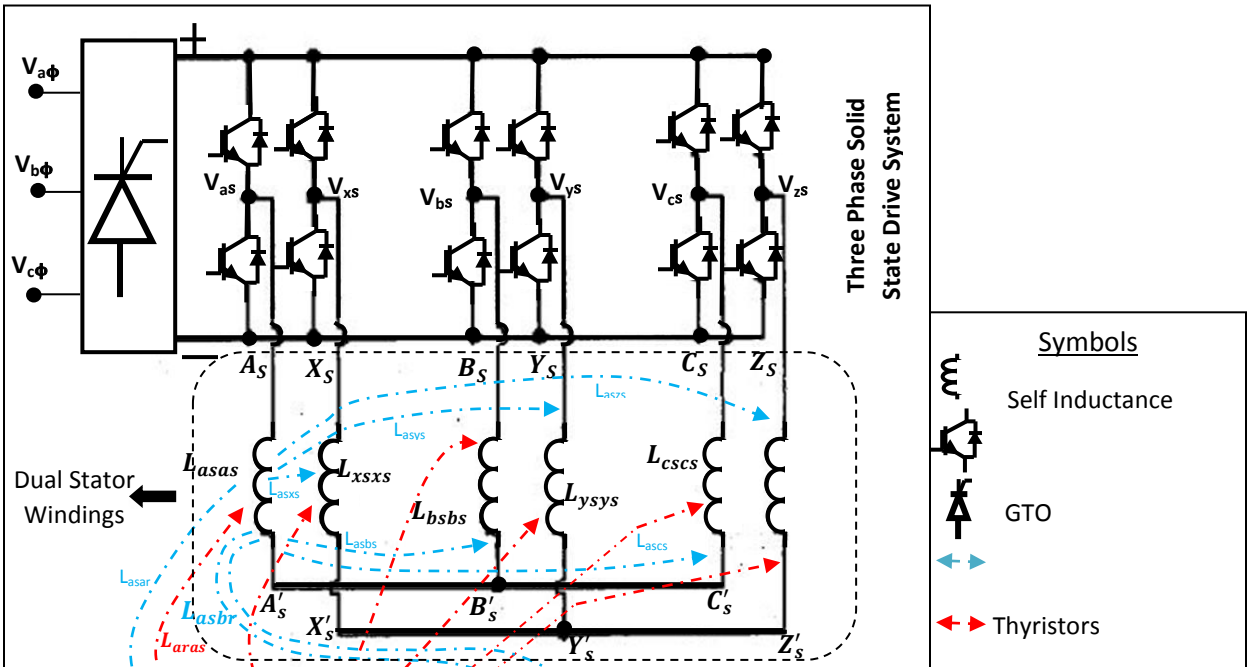


Figure 2.9: Dual Stator Winding Induction Machine Drive System Depicting All Self Inductances and Mutual Inductances between Stator Winding 'as' and Rotor Winding 'ar' and all other Windings

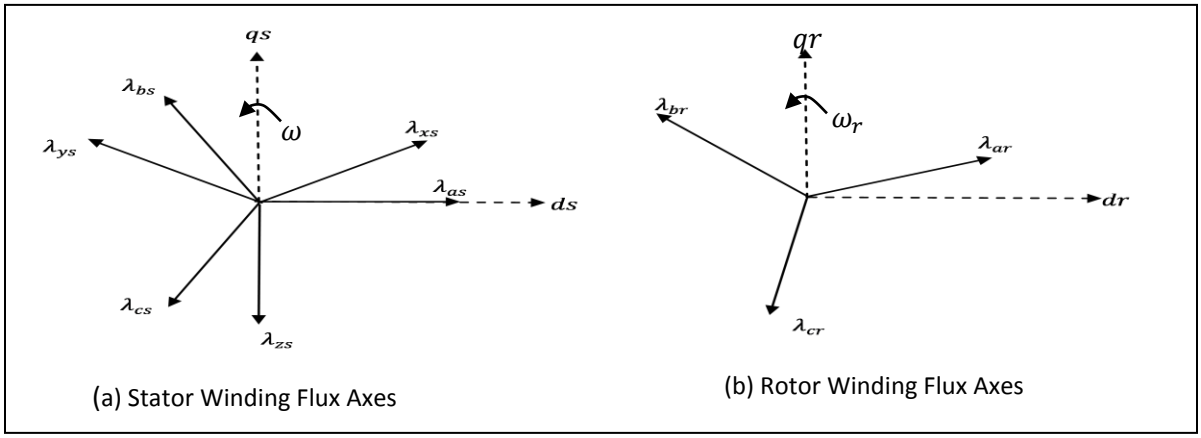


Figure 2.10: Relative Locations of Stator and Rotor Winding Flux Axes

Equations 2.10- 2.12 can now be expressed in compact matrix form thus:

$$\begin{bmatrix} \lambda_{abc_s} \\ \lambda_{xyz_s} \\ \lambda_{abc_r} \end{bmatrix} = \begin{bmatrix} L_{abc_s} & L_{abc_s xyz_s} & L_{abc_s abc_r} \\ L_{xyz_s abc_s} & L_{xyz_s} & L_{xyz_s abc_s} \\ L_{abc_r abc_s} & L_{abc_r xyz_s} & L_{abc_r} \end{bmatrix} \begin{bmatrix} i_{abc_s} \\ i_{xyz_s} \\ i_{abc_r} \end{bmatrix} \tag{2.13}$$

Where the various inductance sub-matrices of equation 2.13 are defined in equations 2.14-2.19:

$$L_{abc_s} = \begin{bmatrix} L_{lsa} + L_{asas} & L_{asbs} & L_{ascs} \\ L_{bsas} & L_{lsb} + L_{bsbs} & L_{bscs} \\ L_{csas} & L_{csbs} & L_{lsc} + L_{\mathrm{csc}\,s} \end{bmatrix} \tag{2.14}$$

$$L_{abc_s xyz_s} = \begin{bmatrix} L_{asxs} & L_{asys} & L_{aszs} \\ L_{bsxs} & L_{bsys} & L_{bszs} \\ L_{csxs} & L_{csys} & L_{cszs} \end{bmatrix} = [L_{xyz_s abc_s}]^T \tag{2.15}$$

$$L_{xyz_s} = \begin{bmatrix} L_{lsx} + L_{xsxs} & L_{xsys} & L_{xszs} \\ L_{ysxs} & L_{lsy} + L_{ysys} & L_{yszs} \\ L_{zsxs} & L_{zsys} & L_{lsz} + L_{zscz} \end{bmatrix} \tag{2.16}$$

$$L_{abc_s abc_r} = \begin{bmatrix} L_{asar} & L_{asbr} & L_{ascr} \\ L_{bsar} & L_{bsbr} & L_{bscr} \\ L_{csar} & L_{csbr} & L_{csc\,r} \end{bmatrix} = [L_{abc_r abc_s}]^T \tag{2.17}$$

$$L_{xyz_s abc_r} = \begin{bmatrix} L_{xsar} & L_{xsbr} & L_{xscr} \\ L_{ysar} & L_{ysbr} & L_{yscr} \\ L_{zsar} & L_{zsbr} & L_{zscr} \end{bmatrix} = [L_{abc_r xyz_s}]^T \tag{2.18}$$

$$L_{abc_r} = \begin{bmatrix} L_{lra} + L_{arar} & L_{arbr} & L_{arcr} \\ L_{brar} & L_{lrb} + L_{bsbs} & L_{brbr} \\ L_{crar} & L_{crbr} & L_{lrc} + L_{crcr} \end{bmatrix} \tag{2.19}$$

Because the foregoing inductances are time varying, the machine equations will be difficult to analyze in their standard form (a-b-c reference frame). To simplify analysis, transformation to arbitrary reference frame is carried out using Park's transformation. This results in parameters which are time invariant. Appropriate turns ratio scaling is then applied to the resulting arbitrary reference frame equations in order to develop an equivalent circuit. By using the machine variables and expression for the field energy, the electromagnetic torque equation of the machine is then developed. The various derivations are presented in subsequent subsections.

2.2.7 Derivation of winding inductances

In order to determine of self-inductances in equations (2.13) to (2.19), it is necessary to compute the flux linking a winding due to its own flux. Also to determine mutual inductances it is imperative to compute the flux linking one winding due to current flowing in another winding. The aim of this section is to determine the various inductances of the machine windings.

2.2.7.1 Generalized flux equation based on winding function theory

Electrical machines are normally designed so that their stator windings produce relatively good approximation of sinusoidal airgap mmf so as to minimize voltage and current harmonics. In order to establish the sinusoidal mmf waveform the stator winding must also be distributed sinusoidally. Let n_j and N_j be turns and winding functions, respectively of a sinusoidally distributed j-winding along the inner periphery of a stator core as illustrated in Figure 2.11. Then the generalized flux linkage in winding j due to current flowing in winding i is given by (Wu 1998):

$$\lambda_{ij} = n_j(\theta) x \phi_i(\theta) \tag{2.20}$$

Where,

$n_j(\theta)$: is the turn function of j-winding,

$\phi_i(\theta)$: is the flux produced due to current in i-winding,

θ : is the angular displacement along the stator circumference.

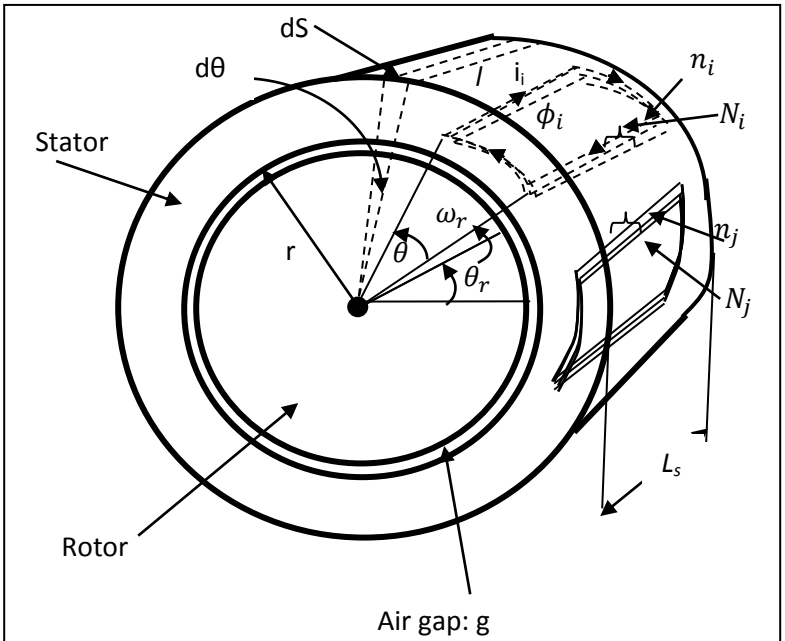


Figure 2.11: Uniformly Distributed Winding According to Winding Function Definition for Elementary Induction Machine Fu and Tang, (2002).

Due to the high permeability of the stator and rotor cores and also the short length of the air gap relative to the inside stator diameter, two additional assumptions have to be made that:

i. The magnetic fields essentially exist in the air gap

ii. The fields tend to be radial in direction.

Therefore, in the airgap the magnetic field strength (H) and the flux density (B) have a component only in the radial direction, and the magnitude is a function of the stator angle θ. The flux density and the magnetic field intensity in the air gap are related as (Wu 1998):

$$B_i(\theta) = \mu_o H_i(\theta) = \mu_o N_i(\theta) i_i g^{-1}(\theta, \theta_r) \tag{2.21}$$

Where:

μ_0: is the permeability of air,

g: is the air gap length,

θ_r: is the rotor angle as shown in Figure 3.4,

N_i: is the winding function of winding i. But

$$\phi_i(\theta) = \int B_i(\theta) ds = \int B_i(\theta) r l d\theta \tag{2.22}$$

$$ds \triangleq r L_s d\theta$$

L_s: is the stator core axial length;

r: is the radius of the inner stator circumference; and

$d\theta$: is an elemental angle defined in Figure 2.11.

Substituting equation 2.21 in equation 2.22 and using eqn. 2.20 yields:

$$\lambda_{ji} = \int_0^{2\pi} \mu_0 r L_s i_i n_j(\theta) N_i(\theta) g^{-1}(\theta, \theta_r) d\theta \tag{2.23}$$

Applying the basic definition of mutual inductance ($L_{ji} = \lambda_{ji}/i_i$) and eqn. 2.23 to obtain:

$$L_{ji} = \mu_0 r L_s \int_0^{2\pi} n_j(\theta) N_i(\theta) g^{-1}(\theta, \theta_r) d\theta \tag{2.24}$$

Following similar approach, the self-inductance is then given by:

$$L_{ii} = \mu_0 r L_s \int_0^{2\pi} n_i(\theta) Ni(\theta) g^{-1}(\theta, \theta_r) d\theta \tag{2.25}$$

As defined by Moreira and Lipo 1992, the inverse gap length is given by the following expression but for P pairs:

$$g^{-1}(\theta, \theta r) = m + n\cos(2P(\theta - \theta r)) \tag{2.26}$$

Where: m and n are defined in equations 2.21 and 2.26, respectively.

$$m = \frac{\beta}{g_1} + \frac{1-\beta}{g_2} \tag{2.27}$$

$$n = \frac{2}{\pi}\left(\frac{1}{g_1} - \frac{1}{g_2}\right)\sin(\pi\beta) \tag{2.28}$$

In equations 2.27 and 2.28: g_1 is the air gap at pole face; g_2 is the air gap between poles; and β is the pole arc/pole pitch. In the case of the machine under consideration (induction machine) the air gap is assumed constant and therefore $g_1 = g_2$ hence $n = 0$. Thus equation.2.26 reduces to:

$$g^{-1}(\theta, \theta_r) = g_o^{-1} = m \text{ or } g_o = 1/m \tag{2.29}$$

As shown by Wu 2006, whenever $g(\theta, \theta_r)$ =constant = g_o, the winding function is related to the turns function by the expression:

$$N(\theta) = n(\theta) - \langle n(\theta) \rangle \tag{2.30}$$

Where

$\langle n(\theta) \rangle$: is the average value of the turn function.

Substituting $g^{-1}(\theta,\theta r)$ and $n_j(\theta)$ in equation 2.24 by their expressions in equations 2.26 and 2.30, respectively we obtain equations 2.31 to 2.34.:

$$L_{ji} = \frac{\mu_0 r L_s}{g_0} \int_0^{2\pi} N_i(\theta)[N_j(\theta) + \langle n_j(\theta)\rangle]d\theta$$

$$= \frac{\mu_0 r L_s}{g_0}[\int_0^{2\pi} N_i(\theta)N_j(\theta)d\theta + \int_0^{2\pi} N_i(\theta)\langle n_j(\theta)\rangle d\theta] \tag{2.31}$$

$$\int_0^{2\pi} N_i(\theta)\langle n_j\rangle(\theta)\rangle d\theta = \int_0^{2\pi}[n_i(\theta) - \langle n_i(\theta)\rangle]\langle n_j(\theta)\rangle d\theta$$

$$= \int_0^{2\pi} n_i(\theta)\langle n_j(\theta)\rangle d\theta - \int_0^{2\pi} \langle n_i(\theta)\rangle\langle n_j(\theta)\rangle d\theta$$

$$= \langle n_j(\theta)\rangle \int_0^{2\pi} n_i(\theta)d\theta - \langle n_i(\theta)\rangle\langle n_j(\theta)\rangle \int_0^{2\pi} d\theta \tag{2.32}$$

$$\int_0^{2\pi} d\theta = 2\pi\langle n_j(\theta)\rangle\langle n_i(\theta)\rangle - 2\pi\langle n_i(\theta)\rangle\langle n_j(\theta)\rangle = 0 \tag{2.33}$$

$$L_{ji} = \frac{\mu_{orl}}{go} \int_0^{2\pi} N_i(\theta)N_j(\theta)d\theta \tag{2.34}$$

Since $g^{-1}(\theta,\theta r) = g_o^{-1}$ then equation 2.25 becomes

$$L_{ii} = \frac{\mu_o r L}{g_o} \int_0^{2\pi} n_i(\theta)N_i(\theta)d\theta \tag{2.35}$$

Equation (2.35) can be modified by eliminating $n_i(\theta)$ using equation 2.30. Thus

$$L_{ii} = \frac{\mu_o r L_s}{g_o} \int_0^{2\pi} [N_i(\theta) + \langle n_i(\theta)\rangle]N_i(\theta)d\theta = \frac{\mu_o r L_s}{g_o}[\int_0^{2\pi} N_i^2(\theta)d\theta + \int_0^{2\pi} \langle n_i(\theta)\rangle]N_i(\theta)d\theta \tag{2.36}$$

$$L_{ii} = \frac{\mu_o r L_s}{g_0} \int_0^{2\pi} N_i^2(\theta)d\theta \tag{2.37}$$

Equations 2.34 and 2.35 are used to calculate the mutual and self-inductances of the machine respectively. Based on the assumptions earlier made, sinusoidal distribution of the stator winding can be expressed as stated in equations 2.38-2.40 and equations 2.41-2.43 for the a-b-c and x-y-z windings, respectively:

$$N_{as} = N_{s1}\cos(p\theta) \tag{2.38}$$

$$N_{bs} = N_{s1}\cos(p\theta - \beta) \tag{2.39}$$

$$N_{cs} = N_{s1}\cos(p\theta + \beta) \tag{2.40}$$

$$N_{xs} = N_{s2}\cos(p\theta + \xi) \tag{2.41}$$

$$N_{ys} = N_{s2}\cos(p\theta + \xi - \beta) \tag{2.42}$$

$$N_{zs} = N_{s2}\cos(p\theta + \xi + \beta) \tag{2.43}$$

While for the rotor winding equations 2.44 to 2.46 apply.

$$N_{ar} = N_r\cos(p(\theta + \theta r)) \tag{2.44}$$

$$N_{br} = N_r\cos(p(\theta + \theta r) - \beta) \tag{2.45}$$

$$N_{cr} = N_r\cos(p(\theta - \theta r) + \beta) \tag{2.46}$$

Note that $N_{s1,}$ N_{s2} and N_r are the amplitudes of the sinusoidally distributed winding functions.

2.2.8 Derivation of self-inductances

The self-inductances for each of the three windings (stator a-b-c and x-y-z and rotor a-b-c) can be evaluated via equation 2.35; and thus for the stator 'as' winding we get:

$$L_{asas} = \frac{\mu_o r L_s}{g_o}\int_0^{2\pi} N_{as}(\theta)N_{as}(\theta)d\theta + L_{lsa} = \frac{\mu_o r L_s}{g_o}\int_0^{2\pi} N_{s1}^2\cos^2(p\theta)d\theta + L_{lsa}$$

$$= L_{lsa} + \frac{\mu_o r L_s}{g_o}N_{s1}^2\int_0^{2\pi}\cos^2(p\theta)d\theta \tag{2.47}$$

Equation 2.47 can now be expressed as follows:

$$L_{asas} = L_{lsa} + L_{ms1} \tag{2.48}$$

Considering integral component of equation 2.47, it can be shown that:

$$L_{msi} = \frac{\mu_o r L_s}{g_o} N_{s1}^2 \tag{2.49}$$

Equation 2.49 yields stator magnetizing inductance for the 'a-b-c' winding set. Hence self-inductance has two components: the leakage and the magnetizing components. For a given winding all the phases are identical and so their self-inductances are the same. This implies that for 'a-b-c' set:

$$L_{asas} = L_{bsbs} = L_{\mathrm{csc}\,s} = L_{ls1} + L_{ms1} \tag{2.50}$$

Likewise for 'x-y-z' stator winding set

$$L_{xsxs} = L_{ysys} = L_{zszs} = L_{ls2} + L_{ms2} \tag{2.51}$$

Equality of leakage inductances implied for each winding set as expressed in equations 2.52 and 2.53, respectively.

$$L_{ls1} = L_{lsa} = L_{lsb} = L_{lsc} \tag{2.52}$$

$$L_{ls2} = L_{lsx} = L_{lsy} = L_{lsz} \tag{2.53}$$

The resulting expression for x-y-y winding set magnetizing inductance is as follows:

$$L_{ms2} = \frac{\mu_o r l}{g_o} N_{s2}^2 \tag{2.54}$$

Similarly for the rotor winding:

$$L_{arar} = L_{brbr} = L_{crcr} = L_{lr} + L_{mr} \tag{2.55}$$

Where, L_{lr} and L_{mr} are leakage and magnetizing inductances of the rotor winding, respectively.

$$L_{mr} = \frac{\mu_o r L_s}{g_o} N_r^2 \tag{2.56}$$

2.2.9 Derivation of mutual inductances

The mutual inductances between phases of the same winding and those inductances between the phases of different windings can be evaluated using equation 2.34 in conjunction with equations2.38-2.39. Thus:

$$L_{asbs} = \frac{\mu_o r L_s}{g_o} \int_0^{2\pi} N_{as}(\theta) N_{bs}(\theta) d\theta = -\frac{1}{2} \frac{\mu_o \pi r L_s}{g_o} N_{si}^2 = -\frac{1}{2} L_{ms1} \tag{2.57}$$

In a similar manner all the remaining mutual inductances can be evaluated and are presented in matrix forms along with their corresponding mutual term definitions in equations 2.58 to 2.69:

$$L_{s1} = \begin{bmatrix} L_{ls1} + L_{A11} & -\frac{1}{2} L_{A11} & -\frac{1}{2} L_{A11} \\ -\frac{1}{2} L_{A11} & L_{ls1} + L_{A11} & -\frac{1}{2} L_{A11} \\ -\frac{1}{2} L_{A11} & -\frac{1}{2} L_{A11} & L_{ls1} + L_{A11} \end{bmatrix} \tag{2.58}$$

Where in matrix equation 2.59, we define the mutual term thus:

$$L_{A11} = L_{ms} N_{s1}^2 \tag{2.59}$$

$$L_{s2} = \begin{bmatrix} L_{ls2} + L_{A22} & -\frac{1}{2} L_{A22} & -\frac{1}{2} L_{A22} \\ -\frac{1}{2} L_{A22} & L_{ls2} + L_{A22} & -\frac{1}{2} L_{A22} \\ -\frac{1}{2} L_{A22} & -\frac{1}{2} L_{A22} & L_{ls2} + L_{A22} \end{bmatrix} \tag{2.60}$$

Where in matrix equation 2.60, we define the mutual term thus:

$$L_{A22} = L_{ms} N_{s2}^2 \tag{2.61}$$

$$L_{12} = \begin{bmatrix} L_{A12}\cos\xi & L_{A12}\cos(\xi+\beta) & L_{A12}\cos(\xi-\beta) \\ L_{A12}\cos(\xi-\beta) & L_{A12}\cos\xi & L_{A12}\cos(\xi+\beta) \\ L_{A12}\cos(\xi+\beta) & L_{A12}\cos(\xi-\beta) & L_{A12}\cos\xi \end{bmatrix} \tag{2.62}$$

Where in matrix equation 2.62, we define the mutual term thus:

$$L_{A12} = L_{ms} N_{s1} N_{s2} \tag{2.63}$$

$$L_{1r} = \begin{bmatrix} L_{1r}\cos p\theta_r & L_{1r}\cos(p\theta_r + \beta) & L_{1r}\cos(p\theta_r - \beta) \\ L_{1r}\cos(p\theta_r - \beta) & L_{1r}\cos p\theta_r & L_{1r}\cos(p\theta_r + \beta) \\ L_{1r}\cos(p\theta_r + \beta) & L_{1r}\cos(p\theta_r - \beta) & L_{1r}\cos p\theta_r \end{bmatrix} \tag{2.64}$$

Where in matrix equation 2.64, we define the mutual term thus:

$$L_{1r} = L_{ms} N_{s1} N_r \tag{2.65}$$

$$L_{2r} = \begin{bmatrix} L_{2r}\cos(p\theta_r + \xi) & L_{2r}\cos((p\theta_r + \xi) + \beta) & L_{2r}\cos(p\theta_r - \beta) \\ L_{2r}\cos(p\theta_r - \beta) & L_{2r}\cos p\theta_r & L_{2r}\cos(p\theta_r + \beta) \\ L_{2r}\cos(p\theta_r + \beta) & L_{2r}\cos(p\theta_r - \beta) & L_{2r}\cos p\theta_r \end{bmatrix} \tag{2.66}$$

Where in matrix equation 2.66, we define the mutual term thus:

$$L_{2r} = L_{ms} N_{s2} N_r \tag{2.67}$$

$$L_r = \begin{bmatrix} L_{lr} + L_R & -\frac{1}{2}L_R & -\frac{1}{2}L_R \\ -\frac{1}{2}L_R & L_{lr} + L_R & -\frac{1}{2}L_R \\ -\frac{1}{2}L_R & -\frac{1}{2}L_R & L_{lr} + L_R \end{bmatrix} \tag{2.68}$$

Where in matrix equation 2.68, we define the mutual term thus:

$$L_R = L_{ms} N_r^2 \tag{2.69}$$

2.2.10 Derivation of stator leakage inductance for three special cases

This subsection is aimed at deriving the general expression for stator phase leakage inductance. The results obtained will then be used to derive that for a six phase winding machine configuration. Three special cases considered are discussed in sequel.

Case I

The derivation is based on the assumption that the stator winding is having two layers with sixty degree phase belts. Such winding phase belts for unity pitch are illustrated in Table 2.2.

Table 2.2: Stator Winding Distribution for Unity Pitch, 60^o Phase Spread and Double Layer (Fu and Tang, (2002))

a	-c	b	-a	c	-b	a	-c	-a	C	-b	A	-c	b	-a	c
a	-c	b	-a	c	-b	a	-c	-a	C	-b	A	-c	b	-a	c

For the above winding configuration, the stator phase leakage inductance is given by:

$$L_{ls}^{3} = L_{l3} + L_{l3slot} \tag{2.70}$$

Where:

L_{l3} : are all non-slot related winding leakage inductances (this includes: end winding, zig − zag and belt leakages);

L_{l3slot}: is slot dependent leakage inductance.

Non-slot related leakage inductances are directly proportional to the square of the equivalent stator turns, N_s (Lipo, 2007) and are given by:

$$L_{l3} = k_l N_s^2 \tag{2.71}$$

Where:

k_l: is proportionality constant which depends upon the slot dimensions and the number of circuits per pole.

The slot leakage flux linkage for phase α can be expressed as:

$$\lambda_\alpha = L_{lslot} i_\alpha \tag{2.72}$$

Considering phase 'a' of Table 2.2:

$$\lambda_a = L_{lT3} i_a + L_{lB3} i_a + 2L_{lTB3} i_a \tag{2.73}$$

Where:

L_{lB3} & L_{lT3} : are slot leakage inductances per phase due to coil sides in the bottom and top of the stator slots, respectively.

L_{lTB3} : Mutual slot leakage inductance per phase between top and bottom layer coil sides in the stator slots.

It can be shown that (Munoz and Lipo 2000):

$$L_{lslot} = L_{lT3} + L_{lB3} + k_s(\overline{p})L_{lTB3} \tag{2.74}$$

Where:

$k_s(\overline{p})$: is the coupling factor; and

$\overline{p}$ = winding pitch.

Individual slot, leakage inductance components are directly proportional to the square of N_3 and inversely proportional to the number of stator slots per phase (S_3). Here, N_3 is the number of stator turns per phase which is related to N_s via winding pitch and distribution factors thus:

$$L_{lT3} = k_{sl}\frac{N_3^2}{S_3}p_T \tag{2.75}$$

$$L_{lTB3} = k_{sl}\frac{N_3^2}{S_3}p_{TB} \tag{2.76}$$

$$L_{lB3} = k_{sl}\frac{N_3^2}{S_3}p_B \tag{2.77}$$

Where:

k_{sl} : is a constant of proportionality dependent upon the number of stator circuits per pole and the number of conductors per slot.

P_T & P_B : are leakage permeances experienced by the coil sides in the top and the bottom of a stator slot, respectively.

P_{TB} : is leakage permeance between coil sides in the top and bottom half of a slot.

Each of the foregoing leakage permeances are uniquely a function of slot and machine dimensions. In a special case where the stator coil pitch is 2/3, the phase belt arrangement will be as demonstrated in Table 2.3.

Table 2.3: Stator Winding Distribution for Fractional Pitch, 60^o Phase Spread and Double Layer Fu and Tang, (2002)

a	-c	b	-a	c	-b	
-b	**a**	**-c**	**b**	**-a**	**c**	**-b**

As presented in Table 3.2, the slot leakage flux linkage for phase 'a' is given by:

$$\lambda_{aslot} = (L_{lT3} + L_{lB3})i_a - L_{lTB3}i_b - L_{lTB3}i_c \tag{2.78}$$

The above expression for a Y- connected stator can be simplified to:

$$\lambda_{aslot} = (L_{lT3} + L_{lB3} + L_{lTB3})\, i_a \tag{2.79}$$

Where:

$$i_a = -i_b - i_c \tag{2.80}$$

This equation is based on the assumption that $k_s(\tfrac{2}{3}) = 1$. It can be shown that for pitch values between 2/3 and 1 the coupling factor is linear with pitch (Fuchs 1974). Thus:

$$k_s(\bar{p}) = 3\bar{p} - 1 \;\; ; \;\; \tfrac{2}{3} \le \bar{p} \le 1 \tag{2.81}$$

The general expression for per phase leakage inductance of a three phase machine is therefore given by:

$$L_{ls}^3 = L_{l3} + L_{lT3} + L_{lB3} + (3\bar{p} - 1)L_{lTB3} \;\; ; \; \tfrac{2}{3} \le \bar{p} \le 1 \tag{2.82}$$

Case II

Here also just as in the previous case of a three phase machine, double layer winding is assumed. In addition, the corresponding phases of the two windings are assumed to have a constant displacement angle (ζ=30^0) and a variable pitch. Table 2.4 presents a winding layout

of a dual winding double layer stator with unity pitch in which the 60^0 phase spread of a three phase machine is split into two equal 30^0 phase belts, one for each three phase winding set.

Table 2.4: Dual Stator Winding Distribution for Unity Pitch, 30^0 Phase Spread, $\xi=30^0$ and Double Layer.

a	x	-c	-z	b	y	-a	-x	c	z	-b	-y	a	x	-c	-z
a	x	-c	-z	b	y	-a	-x	c	z	-b	-y	a	x	-c	-z

This winding has 2 turns per phase

$$N_6 = \tfrac{1}{2} N_3 \tag{2.83}$$

The symmetry of the winding causes self-slot leakage inductance for a-b-c (L_{ls1}) and x-y-z (L_{ls2}) winding to be equal. Thus

$$L_{ls1} = L_{ls2} = L_{l6} + L_{l6slot} \tag{2.84}$$

Where

L_{l6} : All non-slot related leakage inductance/phase of the dual winding machine; and

L_{l6slot} : self-slot related leakage inductance/phase.

Assuming the number of stator circuits per pole to remain the same as that of the three-phase winding, then:

$$L_{l6} = k_l N_1^2 \tag{2.85}$$

Where

k_l : is the same as in equation 2.71 and N_1 is the equivalent turns/phase of a-b-c or x-y-z winding.

Slot leakage in the case of dual winding can be treated similar to the three-phase winding, that is

$$L_{l6slot} = L_{lT6} + L_{lB6} + k_s(\bar{p})L_{lTB6} \tag{2.86}$$

Where

$$L_{lT6} = k_{sl}\frac{N_6^2}{S_6}P_t \tag{2.87}$$

$$L_{lB6} = k_{sl}\frac{N_6^2}{S_6}P_B \tag{2.88}$$

Case III

With unity pitch all stator slots that contain 'a' phase windings contain only phase 'a' windings both at the top and the bottom of slots, therefore $k_{xp}(1) = 0;\ k_{yp}(1) = 0;\ k_{zp}(1) = 0.$

The 30^0 phase spread dual- machine stator winding with $5/6$ pitch is illustrated in Table 2.5.

Table 2.5: Dual Stator Winding Distribution for $5/6$ pitch, 30^0 Phase Spread, $\gamma = 30^0$ and Double Layer

a	x	-c	-z	b	y	-a	-x	c	Z	-b	-y	a	x	-c	-z
-y	a	X	-c	-z	b	y	-a	-x	C	z	-b	-y	a	x	-c

Coupling factors for the winding configuration of Table 2.5 can be determined by inspection. They are: $k_{sp}(5/6) = 0;\ k_{xp}(5/6) = 1;\ k_{yp}(5/6) = -1$ & $k_{zp}(5/6) = 0.$ Similar to the 3-phase case, coupling factors vary linearly with pitch and for $5/6 \le \bar{p} \le 1,$ the applicable expressions are offered in Equations 2.89 to 2.92:

$$k_{sp}(\bar{p}) = 12\bar{p} - 10 \tag{2.89}$$

$$k_{xp}(\bar{p}) = -6\bar{p} - 6 \tag{2.90}$$

$$k_{yp}(\bar{p}) = 6\bar{p} - 6; \tag{2.91}$$

$$k_{zp}(\bar{p}) = 0 \tag{2.92}$$

In what follows, we derive mutual leakage inductances for dual stator winding inductance machine.

2.2.11 Derivation of mutual leakage inductance

The leakage flux linkage for phase **'a'** can be expressed as:

$$\lambda_{la} = L_{lax} i_x + L_{lay} i_y + L_{laz} i_z \tag{2.93}$$

Where:

L_{lax}, L_{lay} & L_{laz} : are mutual leakage inductances between phase 'a' and phases x, y and z, respectively. Similarly for the other two windings equations 2.94 and 2.95 apply:

$$\lambda_{lb} = L_{laz} i_x + L_{lax} i_y + L_{lay} i_z \tag{2.94}$$

$$\lambda_{lc} = L_{lay} i_x + L_{laz} i_y + L_{lax} i_z \tag{2.95}$$

The various current relationships in x-y-z windings are given in equations 2.96-2.99.

$$i_x + i_y + i_z = 0 \tag{2.96}$$

$$i_x = -(i_y + i_z) \tag{2.97}$$

$$i_y = -(i_x + i_z) \tag{2.98}$$

$$i_z = -(i_y + i_x) \tag{2.99}$$

Substituting equations 2.97-2.99 into equations 2.93-2.95, the following equations are obtained:

$$\lambda_{la} = L_{lax} i_x + L_{lay} i_y + L_{laz}(-i_y - i_x) \tag{2.100}$$

$$\lambda_{lb} = L_{lax}(-i_y - i_z) + L_{lay} i_y + L_{laz} i_z \tag{2.101}$$

$$\lambda_{lc} = L_{lax} i_x + L_{lay}(-i_x - i_z) + L_{laz} i_z \tag{2.102}$$

Equations 2.100-2.102, after minor simplifications, are recast as equations 2.103-2.105.

$$\lambda_{la} = L_{la}^{x} i_x + L_{la}^{y} i_y \tag{2.103}$$

$$\lambda_{lb} = L_{la}^{x} i_y + L_{la}^{y} i_z \tag{2.104}$$

$$\lambda_{lc} = L_{la}^{y} i_x + L_{la}^{x} i_z \tag{2.105}$$

From the foregoing, the explicit expressions mutual leakage inductances are given in equations 2.106 and 2.107.

$$L_{la}^{x} = L_{lax} - L_{laz} \tag{2.106}$$

$$L_{la}^{y} = L_{lay} - L_{laz} \tag{2.107}$$

The mutual leakage inductance between the two sets of windings can now be expressed in matrix form as:

$$L_{l12} = \begin{bmatrix} L_{la}^{x} & L_{la}^{y} & 0 \\ 0 & L_{la}^{x} & L_{la}^{y} \\ L_{la}^{y} & 0 & L_{la}^{x} \end{bmatrix} \tag{2.108}$$

The flux linkage equations for dual stator winding induction machine in phase variables can thus be written in compact matrix form as:

$$\lambda_{abcs} = L_{s1} i_{abcs} + [L_{l12} + L_{12}] i_{xyzs} + L_{1r} i_{abcr} \tag{2.109}$$

$$\lambda_{xyzs} = [L_{l12} + L_{12}]^{T} i_{abcs} + L_{s2} i_{xyzs} + L_{2r} i_{abcr} \tag{2.110}$$

$$\lambda_{abcr} = L_{1r} i_{abcs} + L_{2r} i_{xyzs} + L_{r} i_{abcr} \tag{2.111}$$

Because the dual stator winding induction machine a-b-c variable equations comprise time varying quantities necessitate their transformations into arbitrary d-q-0 reference frame in order to eliminate the inherent time varying quantities addressed in the next subsection. In summary, Table 2.6 provides, at a glance, the various equations derived for the DSWIM

inductances on the well known winding function analysis widely used by researchers (Wu, 1998; Munoz & Lipo, 2000).

Table 2.6: Summary of Derived Equations for Inductances of DSWIM Using Winding Functions

Inductance Classifications	Winding Sets		Symbols used	Derived Equations
Self-Inductances	stator	a-b-c x-y-z	$L_{asas}; L_{bsbs}; L_{cscs}$ $L_{xsxs}; L_{ysys}; L_{zszs}$	*Equation 2.50* Equation 2.51
	rotor	a-b-c	$L_{arar}; L_{brbr}; L_{crcr}$	Equation 2.55
Mutual Inductances	stator-stator	a-b-c ↔a-b-c x-y-z↔x-y-z	$L_{asbs}; L_{ascs}; L_{bscs}$ $L_{xsys}; L_{xszs}; L_{yszs}$	$-\frac{1}{2}$ * Equation 2.59 $-\frac{1}{2}$ * Equation 2.61
		a-b-c↔x-y-z	$L_{asxs}; L_{bsys}; L_{cszs}$ $L_{asys}; L_{bszs}; L_{csxs}$ $L_{aszs}; L_{bsxs}; L_{csys}$	Equation 2.63*$\cos\xi$ Equation 2.63 *$\cos(\xi+\beta)$ Equation 2.63 *$\cos(\xi-\beta)$
	stator-rotor	as-bs-cs↔ar-br-cr	$L_{asar}; L_{bsbr}; L_{cscr}$ $L_{asbr}; L_{bscr}; L_{csar}$ $L_{ascr}; L_{bsar}; L_{csbr}$	Equation 2.65 * $\cos p\theta_r$ Equation 2.65*$\cos(p\theta_r+\beta)$ Equation 2.65*$\cos(p\theta_r-\beta)$
Leakage Inductances	stator	a-b-c x-y-z	$L_{las}; L_{lbs}; L_{lcs}$ $L_{lxs}; L_{lys}; L_{lzs}$	Equation 2.87 Equation 2.87
	rotor	a-b-c	$L_{lar}; L_{lbr}; L_{lcr}$	Equation 2.87

2.2.12 Transformation of machine variable equations into arbitrary d-q-0 reference frame

Evaluation of each term in the voltage and flux linkage equations 2.7-2.9 and 2.10-2.12 respectively will require various self, mutual and leakage inductance matrices, some of which are time varying, derived in the preceding subsections. We define the following arbitrary reference frame widely used in the d-q-0 model development and analysis of both conventional induction machine and dual stator winding machine (Wu, 1998).

$$k(\alpha) = \frac{2}{3}\begin{bmatrix} \sin(\alpha) & \sin(\alpha - \frac{2\pi}{3}) & \sin(\alpha + \frac{2\pi}{3}) \\ \cos(\alpha) & \cos(\alpha - \frac{2\pi}{3}) & \cos(\alpha + \frac{2\pi}{3}) \\ \frac{1}{2} & \frac{1}{2} & \frac{1}{2} \end{bmatrix} \quad (2.112)$$

And its inverse given by

$$k(\alpha)^{-1} = \begin{bmatrix} \sin(\alpha) & \cos(\alpha) & 1 \\ \sin(\alpha - \frac{2\pi}{3}) & \cos(\alpha - \frac{2\pi}{3}) & 1 \\ \sin(\alpha + \frac{2\pi}{3}) & \cos(\alpha + \frac{2\pi}{3}) & 1 \end{bmatrix} \quad (2.113)$$

Where in equations 3.108 and 3.109, the angle α is defined for different windings as follows:

$$\alpha = \begin{cases} \theta & : \text{for a} - \text{b} - \text{c stator windings} \\ \theta + \xi & : \text{for x} - \text{y} - \text{w stator windings} \\ \theta - \theta_r & : \text{for a}_\text{r} - \text{b}_\text{r} - \text{c}_\text{r}\text{rotor windings} \end{cases} \quad (2.114)$$

The angular relationships between the d-q axes and the various windings in the stator and rotors are illustrated in Figure 2.12.

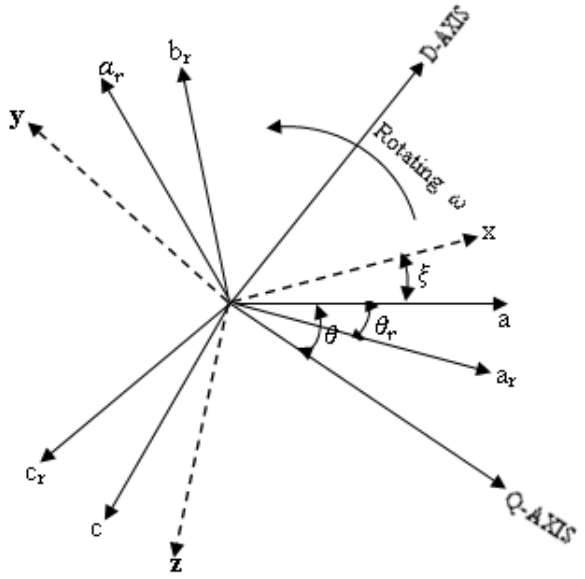


Figure 2.12: Dual Stator Winding Phases Vector Diagrams in d-q-0 Arbitrary Reference Frame

Applying transformations to the machine voltage equations we get:

$$k(\theta)V_{abc} = k(\theta)R_1 k(\theta)^{-1} i_{qd1} + k(\theta)\, p[k(\theta)^{-1}\lambda_{qd1}] \quad (2.115)$$

$$k(\theta+\xi)V_{xyz} = k(\theta+\xi)R_1 k(\theta+\xi)^{-1} i_{qd2} + k(\theta+\xi)\,p[k(\theta+\xi)^{-1}\lambda_{qd2}] \tag{2.116}$$

$$k(\theta-\theta_r)V_{abcr} = k(\theta-\theta_r)R_r k(\theta-\theta_r) i_{qdr} + k(\theta-\theta_r)\,p[k(\theta-\theta_r)^{-1}\lambda_{qdr}] \tag{2.117}$$

The foregoing equations can now be simplified to achieve the following:

$$V_{qd1} = R_1 i_{qd1} + \omega\lambda_{qd1} + p\lambda_{qd1} \tag{2.118}$$

$$V_{qd2} = R_1 i_{qd2} + \omega\lambda_{qd2} + p\lambda_{qd2} \tag{2.119}$$

$$V_{qdr} = R_r i_{qdr} + (\omega-\omega_r)\lambda_{qdr} + p\lambda_{qdr} \tag{2.120}$$

The flux linkages in d-q are obtained by applying transformation in to 2.118-2.120:

$$\lambda_{qd1} = k(\theta)L_{s1}k(\theta)^{-1} i_{qd1} + k(\theta)[L_{l12}+L_{12}]k(\theta+\xi)^{-1} i_{qd2} + k(\theta)L_{1r}k(\theta-\theta_r)^{-1} i_{qdr} \tag{2.121}$$

$$\lambda_{qd2} = k(\theta+\xi)[L_{l12}+L_{12}]^T k(\theta)^{-1} i_{qd1} + k(\theta+\xi)L_{s2}k(\theta+\xi)^{-1} i_{qd2} + k(\theta+\xi)L_{2r}k(\theta-\theta_r)^{-1} i_{qdr} \tag{2.122}$$

$$\lambda_{qdr} = k(\theta-\theta_r)L^T{}_{1r}k(\theta)^{-1} i_{qd1} + k(\theta-\theta_r)L^T{}_{2r}k(\theta+\xi)^{-1} i_{qd2} + k(\theta-\theta_r)L_r k(\theta-\theta_r)^{-1} i_{qdr} \tag{2.123}$$

Where, the various components are evaluated separately in equations 2.124-2.132 all of are expressed in compact matrix forms.

$$k(\theta)L_{s1}k(\theta)^{-1} = \begin{bmatrix} L_{ls1}+\frac{3}{2}L_{A11} & 0 & 0 \\ 0 & L_{ls1}+\frac{3}{2}L_{A11} & 0 \\ 0 & 0 & L_{ls1} \end{bmatrix} \tag{2.124}$$

$$k(\theta)L_{12}k(\theta+\xi)^{-1} = k(\theta+\xi)L_{12}^T k(\theta)^{-1} = \begin{bmatrix} \frac{3}{2}L_{A12} & 0 & 0 \\ 0 & \frac{3}{2}L_{A12} & 0 \\ 0 & 0 & 0 \end{bmatrix} \tag{2.125}$$

$$k(\theta+\xi)L_{l12}^T k(\theta)^{-1} = \begin{bmatrix} L_{lm} & L_{ldq} & 0 \\ L_{ldq} & L_{lm} & 0 \\ 0 & 0 & L_{la}^x + L_{la}^y \end{bmatrix} \tag{2.126}$$

$$k(\theta)L_{1r}k(\theta-\theta_r)^{-1}=\begin{bmatrix}\frac{3}{2}L_{1R} & 0 & 0\\ 0 & \frac{3}{2}L_{1R} & 0\\ 0 & 0 & 0\end{bmatrix} \tag{2.127}$$

$$k(\theta+\xi)L_{s2}k(\theta+\xi)^{-1}=\begin{bmatrix}L_{ls2}+\frac{3}{2}L_{A22} & 0 & 0\\ 0 & L_{ls2}+\frac{3}{2}L_{A22} & 0\\ 0 & 0 & L_{ls2}\end{bmatrix} \tag{2.128}$$

$$k(\theta+\xi)L_{2r}k(\theta-\theta_r)^{-1}=\begin{bmatrix}\frac{3}{2}L_{2R} & 0 & 0\\ 0 & \frac{3}{2}L_{2R} & 0\\ 0 & 0 & 0\end{bmatrix} \tag{2.129}$$

$$k(\theta-\theta_r)L_{1r}^{T}k(\theta)^{-1}=k(\theta)L_{1r}k(\theta-\theta_r)^{-1} \tag{2.130}$$

$$k(\theta-\theta_r)L_{2r}^{T}k(\theta+\xi)^{-1}=k(\theta+\xi)L_{2r}k(\theta-\theta_r)^{-1} \tag{2.131}$$

$$k(\theta-\theta_r)L_{r}k(\theta-\theta_r)^{-1}=\begin{bmatrix}L_{lr}+\frac{3}{2}L_{1R} & 0 & 0\\ 0 & L_{lr}+\frac{3}{2}L_{1R} & 0\\ 0 & 0 & L_{lr}\end{bmatrix} \tag{2.132}$$

The derived d-q flux linkages become:

$$\lambda_{q1}=(L_{ls1}+\tfrac{3}{2}L_{A11})i_{q1}+\tfrac{3}{2}L_{A12}i_{q2}+L_{lm}i_{q2}+L_{ldq}i_{d2}+\tfrac{3}{2}L_{1R}i_{qr} \tag{2.133}$$

$$\lambda_{d1}=(L_{ls1}+\tfrac{3}{2}L_{A11})i_{d1}+\tfrac{3}{2}L_{A12}i_{d2}-L_{ldq}i_{q2}+L_{lm}i_{d2}+\tfrac{3}{2}L_{1R}i_{dr} \tag{2.134}$$

$$\lambda_{q2}=\tfrac{3}{2}L_{A12}i_{q1}+L_{ldq}i_{d1}+L_{lm}i_{q1}+(L_{ls2}+\tfrac{3}{2}L_{A22})i_{q2}+\tfrac{3}{2}L_{2R}i_{qr} \tag{2.135}$$

$$\lambda_{d2}=-L_{ldq}i_{q1}+\tfrac{3}{2}L_{A12}i_{d1}+L_{lm}i_{d1}+(L_{ls2}+\tfrac{3}{2}L_{A22})i_{d2}+(L_{ls2}+\tfrac{3}{2}L_{A22})i_{q2} \tag{2.136}$$

$$\lambda_{qr}=\tfrac{3}{2}L_{1R}i_{q1}+\tfrac{3}{2}L_{2R}i_{q2}+(L_{lr}+\tfrac{3}{2}L_{R})i_{qr} \tag{2.137}$$

$$\lambda_{dr}=\tfrac{3}{2}L_{1R}i_{d1}+\tfrac{3}{2}L_{2R}i_{d2}+(L_{lr}+\tfrac{3}{2}L_{R})i_{dr} \tag{2.138}$$

2.2.13 Turns Ratio Scaling Procedure

The voltage and flux linkage equations derived above cannot be used in that form to develop an equivalent circuit of the machine. To facilitate the development of the equivalent circuit

the parameters of the x-y-z-winding and that of rotor are normally referred to the stator a-b-c-winding using the turns-ratio. As a starting point, let:

$$L_m = \tfrac{3}{2} L_{A11} = \tfrac{3}{2} N_1^2 L_{ms} \tag{2.139}$$

If primed quantities represent referred parameters then the referred voltages, currents, flux linkages and inductances are as expressed in equations 2.140-2.155, respectively:

$$V_{q2}^{'} = \tfrac{N_1}{N_2} V_{q2}; \tag{2.140}$$

$$V_{d2}^{'} = \tfrac{N_1}{N_2} V_{d2}; \tag{2.141}$$

$$V_{qr}^{'} = \tfrac{N_1}{N_r} V_{qr}; \tag{2.142}$$

$$V_{dr}^{'} = \tfrac{N_1}{N_r} V_{dr}; \tag{2.143}$$

$$i_{q2}^{'} = \tfrac{N_2}{N_1} i_{q2}; \tag{2.144}$$

$$i_{d2}^{'} = \tfrac{N_2}{N_1} i_{d2}; \tag{2.145}$$

$$i_{qr}^{'} = \tfrac{N_2}{N_1} i_{qr}; \tag{2.146}$$

$$i_{dr}^{'} = \tfrac{N_2}{N_1} i_{dr}; \tag{2.147}$$

$$\lambda_{q2}^{'} = \tfrac{N_1}{N_2} \lambda_{q2}; \tag{2.148}$$

$$\lambda_{d2}^{'} = \tfrac{N_1}{N_2} \lambda_{d2}; \tag{2.149}$$

$$\lambda_{qr}^{'} = \tfrac{N_1}{N_2} \lambda_{qr}; \tag{2.150}$$

$$\lambda_{dr}^{'} = \tfrac{N_1}{N_2} \lambda_{dr} \tag{2.151}$$

$$L_{ldq}^{'} = \tfrac{N_1}{N_2} L_{ldq}; \tag{2.152}$$

$$L_{lm}^{'} = \tfrac{N_1}{N_2} L_{lm}; \tag{2.153}$$

$$r_2^{'} = (\tfrac{N_1}{N_2})^2 r_2; \tag{2.154}$$

$$r_r^{'} = (\frac{N_1}{N_r})^2 r_r \tag{2.155}$$

The series leakage inductance terms are modified by mutual leakage as given in equations 2.156-2.159:

$$L_{l1} = L_{ls1} - L_{lm}^{'} \tag{2.156}$$

$$L_{l2} = L_{ls2} - L_{lm}^{'} \tag{2.157}$$

$$L_{01} = L_{ls1} - L_{la}^{x} - L_{la}^{y} \tag{2.158}$$

$$L_{02} = L_{ls2} - L_{la}^{x} - L_{la}^{y} \tag{2.159}$$

The import of this mutual coupling amongst leakage inductances will be reflected in the development of DSWIM model with similar pole ratio.

2.2.14 Development of torque equation for DSWIM

The energy stored in the coupling field of this machine may be expressed as:

$$W_f = \tfrac{1}{2}(i_{abcs})^T (L_{abcs} - L_{lsa} I) i_{abcs} + \tfrac{1}{2}(i_{xyzs})^T (L_{xyzs} - L_{lsx} I) i_{xyzs} - \tfrac{1}{2}(i_{abcs})^T L_{abcsxyzs} i_{xyzs}$$

$$+ \tfrac{1}{2}(i_{abcs})^T L_{abcsabcr} i_{abcr} + \tfrac{1}{2}(i_{xyzs})^T L_{xyzsabcr} i_{abcr} + \tfrac{1}{2}(i_{abcr})^T (L_{abcr} - L_{lr} I) i_{abcr} \tag{2.160}$$

Where: I is an identity matrix.

$$L_{lsa} = diag\begin{bmatrix} L_{lsa} & L_{lsa} & L_{lsa} \end{bmatrix} \tag{2.161}$$

$$L_{lsx} = diag\begin{bmatrix} L_{lsx} & L_{lsx} & L_{lsx} \end{bmatrix} \tag{2.162}$$

$$L_{lr} = diag\begin{bmatrix} L_{lr} & L_{lr} & L_{lr} \end{bmatrix} \tag{2.163}$$

The change dW_m in mechanical energy in this machine can be expressed as:

$$dW_m = -T_e d\theta_{rm} \tag{2.164}$$

Where, T_e is the electromagnetic torque, θ_{rm} is the mechanical angular displacement of the rotor. The electrical angular displacement of the rotor θ_r is related to θ_{rm} by the relation;

$$\theta_r = (\frac{P}{2})\theta_{rm} \tag{2.165}$$

Thus:

$$dW_m = -T_e(\tfrac{2}{P})d\theta_r \tag{2.166}$$

Where: P is the number of poles in the machine.

For a magnetically linear system the co-energy W_c=W_f. Thus if the machine is assumed to be magnetically linear then:

$$T_e = (\tfrac{P}{2})\frac{dW_f}{d\theta_r} \tag{2.167}$$

Substituting the expression for W_f in equation and also remember that L_{abcs}, L_{xyzs} and L_{abcr} are independent of θ_r electromagnetic torque T_e produced by dual stator winding induction machine can be expressed thus:

$$T_e = (\tfrac{P}{2})[(i_{abcs})^T \tfrac{dL_{asr}}{d\theta_r} i_{abcr} + (i_{xyzs})^T \tfrac{dL_{xsr}}{d\theta_r} i_{abcr}] \tag{2.168}$$

Thus electromagnetic torque component T_{e1}due to a-b-c stator windings can be expressed as follows:

$$T_{e1} = \tfrac{P}{2}[k(\theta)^{-1} i_{qdas}]^T \tfrac{d}{d\theta_r}[L_{asr} k(\theta-\theta_r)^{-1} i_{qdr}]$$

$$= (\tfrac{p}{2})[k(\theta)^{-1} i_{qdas}]^T [\tfrac{d(L_{asr})}{d\theta_r} k(\theta-\theta_r)^{-1} i_{qdr} + L_{asr} \tfrac{d(k(\theta-\theta_r)^{-1})}{d\theta_r} i_{qdr}]$$

$$= \tfrac{3}{2}(\tfrac{P}{2})\tfrac{3}{2} L_{ms}(i_{qas} i_{dr} - i_{das} i_{qr}) = \tfrac{3}{2}(\tfrac{P}{2}) L_m (i_{qas} i_{dr} - i_{das} i_{qr}) \tag{2.169}$$

Similarly electromagnetic torque T_{e2}developed in x-y-z stator windings:

$$T_{e2} = (\tfrac{P}{2})[k(\theta+\xi)^{-1} i_{qdxs}]^T \tfrac{d}{d\theta_r}[L_{xsr} k(\theta-\theta_r)^{-1} i_{qdr}]$$

$$= (\tfrac{p}{2})[k(\theta+\xi)^{-1} i_{qdxs}]^T [\tfrac{d(L_{xsr})}{d\theta_r} k(\theta-\theta_r)^{-1} i_{qdr} + L_{xsr} \tfrac{d(k(\theta-\theta_r)^{-1})}{d\theta_r} i_{qdr}]$$

$$= \tfrac{3}{2}(\tfrac{P}{2}) L_m (i_{qxs} i_{dr} - i_{dxs} i_{qr})$$

(2.170)

Finally the total electromagnetic torque is the summation of the two components of Torques produced by the two stator windings as stated thus:

$$T_e = T_{e1} + T_{e2}\,, \tag{2.171}$$

It is clear from equation 2.171 that the torque of DSWIM, if optimally designed, can be expected to be greater than its equivalent conventional three phase induction machine. The inherent reliability of DSWIM is evident due to its ability to continue to produce torque with the failure of the windings.

The electromagnetic torque, load torque (T_l) and electrical rotor speed(ω_r) are related by the expression:

$$T_e - T_l = \frac{2}{p} J \frac{d}{dt} \omega_r \tag{2.172}$$

Where:

J= moment of inertia of the rotor.

The various equations developed in subsections 2.2.6 to 2.214 are central to the development of d-q-0 models for a DSWIM which will be presented in next chapter.

2.2.15 Overview of multi-phase induction machine design concepts

The power rating of a multi-phase induction machine is majorly dependent on its leading dimensions D and L shown in Figure 2.13. The fundamental design objective with regard to induction machine is to obtain the leading dimensions that satisfy power output requirements at the desired efficiency. Considering analytical design of a generalized N-phase induction machine, the following input rating equation is essential (Say, 1970; Fu and Tang, 2002; Lipo, 2004; Harley and Duan, 2009).

$$S = N\left(2.22 f \Phi I_{ph} Z_{ph} K_w\right) x 10^{-3}\ \text{kVA} \tag{2.173}$$

For N=3, we express the input power in terms of the three-phase induction machine leading dimensions as follows:

$$S = (11B_{av}QK_w x10^{-3})D^2Ln_s = C_oD^2Ln_s \tag{2.174}$$

The various parameters used in equations 2.173 and 2.174 are defined in equations 2.175-2.178:

$$C_o = 11B_{av}QK_w x10^{-3} \tag{2.175}$$

$$B_{av} = \frac{P\Phi}{\pi DL} \tag{2.176}$$

$$f = \frac{Pn_s}{2} \tag{2.177}$$

$$Q = \frac{3I_{ph}Z_{ph}}{\pi D} \tag{2.178}$$

Where in equations 2.173-2.178:

S & C_o : input power rating of the multi-phase induction machine and input power coefficient;

f & n_s : Frequency in Hz and speed in revolutions/sec, respectively;

P & Q : Number of poles and specific electric loading, respectively;

B_{av} & Φ : Average flux density and air-gap flux per pole, respectively;

D & L : Stator bore diameter and rotor gross length, respectively; and

K_w & Z_{ph} : Winding factor and number of conductors per phase.

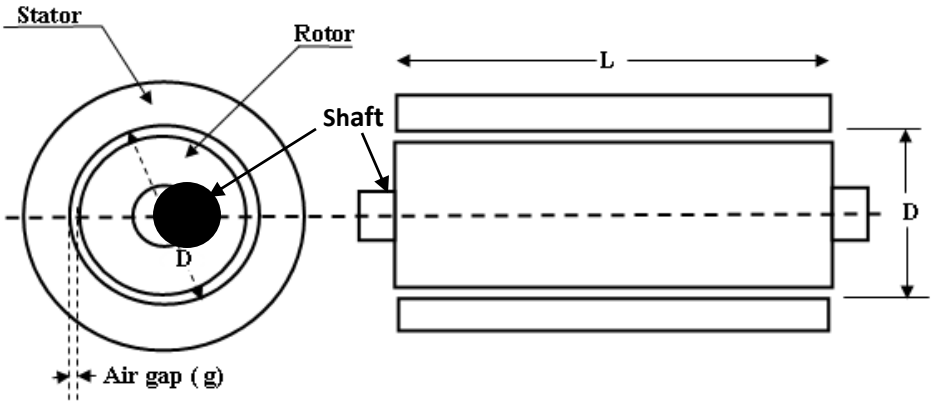


Figure 2.13: Leading Dimensions of an Induction Machine Housing Structure

The classical analytical design of multi-phase induction machine of specified rating entails determination of the stator leading dimensions, matching stator winding architecture as well as choice and specifications of rotor design details and its winding structure. The salient steps are outlined in what follows.

Step1: Determine S from the specifications of desired output power, P_{out} efficiency,η and power factor, $cos\theta$; where $S = P_{out}/(\eta\cos\theta)$.

Step 2: Compute $D^2Ln_s = S/(11B_{av}QK_w)$ based on sound engineering choices of specific magnetic loading, B_{av} and specific electric loading, Q. Optimum choices of B_{av} & Q are crucial to minimizing losses and cooling requirements.

Step 3: Select suitable ratio D/L from Tables as available in (Say, 1970) and then calculate D and L. Other empirical relationships for the separation of D and L can be found in (Fu and Tang, 2002).

Step 4: Calculate air-gap g(mm) using empirical formula such as $g = 3x10^{-3}\tau_p\sqrt{P}$ (Lipo, 2004) in which $\tau_p = \pi D/P$ is the pole pitch. Here, the pole pitch is specified in mm.

Step 5: Design the stator comprising stator core and slots. The optimum number of slots S_{ss}, slot geometry and stator outer diameter require special considerations because the operating characteristics of multi-phase induction machine are significantly influenced by them. The number of stator slots selected will determine the extent of flux leakage and magnitude of mmf harmonics. The slot geometry may be selected to be semi-open or tapered type with the latter preferred in multi-phase machine. As a compromise, the number of slots/pole/phase may be chosen as 3 or more for integral slot winding whilst 3.5 number of slots/pole/phase may be selected for fractional slot windings (Sawhney, 2011). In addition, the stator slot pitch at air-gap

surface, τ_{ss} given by $\pi D/S_{ss}$ should satisfy the following dimensional requirement $1.5cm \leq \tau_{ss} \leq 2.5cm$.

Step 6: Determine the number of turns per phase $T_{ph} \triangleq 2Z_{ph}$ from the basic equation $T_{ph} = V_{ph}/4.44f\Phi K_w$ with K_w typically selected to be 0.955 and optimum conductor cross sectional area that meets its allowable current density, J amps/mm^2. The cross sectional area of stator slots should house the conductors and maintain satisfactory slot space factor defined as (total conductor cross-sectional areas/stator slot area). Estimate accurately stator winding resistance, R_s leakage inductances $\sum L_{ls}$. Design stator winding layout/diagram.

Step 7: Select rotor type (wound or squirrel cage); select optimum number of rotor slots such that the ratio of rotor slots to stator slots combined with skewing of rotor slots to eliminate noisy vibrations, cogging problems, etc. Hence design rotor slots, windings and end rings. Estimate rotor resistance, R_r and leakage inductances $\sum L_{lr}$.

It is to be noted that the foregoing salient steps can always be modified to take care of specific design requirements that have not been captured but available in standard ac machine design textbooks.

It is noteworthy to state, at this juncture, that there is no difference in the design of the stator frame and rotor structure for either conventional three phase induction machine or the dual stator winding induction machine. However, the winding design architecture of dual stator winding induction machine is significantly different due to imposition of new set of magnetic and electric loadings. Consequently, winding design considerations for dual stator winding machine will be treated specially in the chapter three.

2.2.16 Design optimization of multi-phase induction machine

The design of multi-phase induction machine can be formulated as a nonlinear optimization problem. The generalized nonlinear problem concerns optimum selection of design variables $X = (x_1, x_2, \ldots \ldots x_i, \ldots . x_n)$ in order to minimize objective function $F(X)$ subject to specified equality and inequality constraints. This is stated mathematically as follows:

$$Min\ F(X) \text{ (Objective Function)}$$

Subject to:

$$g_i(X) = 0\ ;\ i \in \{1, m\} \text{ (Equality Constraints)}$$

$$h_k(X) \leq 0\ ;\ k \in \{1, L\} \text{ (Inequality Constraints)} \quad (2.179)$$

Where

$x_{min_j} \leq x_j \leq x_{max_j}$; $j \in \{1, n\}$: are practical limits specified for the design variables.

A comprehensive list of design variables commonly used by researchers that include electric loading, air-gap flux density, stator outer diameter, rotor gross length, etc are presented in Table 2.7. The objective function will naturally seek to improve machine efficiency, power factor and minimize overall cost. For several multi-phase induction machine design optimization problems that have appeared in the literature (Sivaraju & Devaranja, 2011; Thangaraj et al., 2010; Raj et al., 2011) meta-heuristic techniques viz. genetic algorithm (GA), particle swarm optimization (PSO), simulated annealing (SA) etc. were variously deplored as solution methodologies.

In this research work, GA has been applied to optimize the efficiency of dual stator winding induction machine after realizing its magnetic design based on pragmatic analytical approach. Thus in the next subsection, we set forth general search approach of GA and its capabilities for solving nonlinear optimization problem.

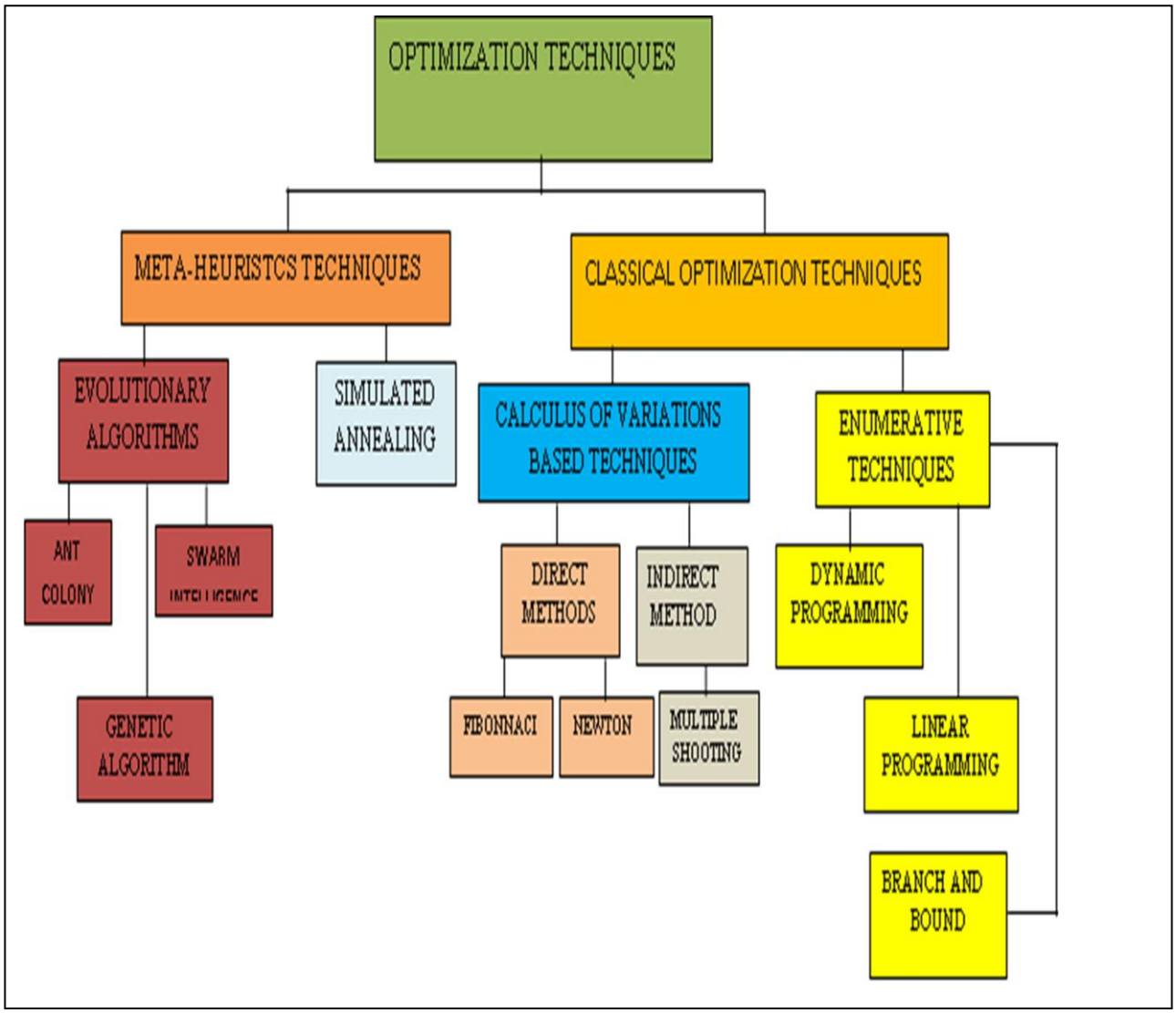
Table 2.7: List of Induction Machine Design Variables

Design Variables	Symbol	Unit
Core or stack length	L_c	mm
Inside diameter of stator	D_{is}	mm
Outside diameter of stator	D_{os}	mm
Stator yoke thickness	D_d	mm
Rotor yoke thickness	D_r	mm
Rotor current density	J_r	Amp/m^2
Stator current density	J_s	Amp/m^2
Air-gap average flux density	B_{av}	Wb/m^2
Ratio of stack length to pole pitch		-
Electric loading	Q	Ac/m
Maximum stator tooth flux density	B_{max_T}	Wb/m^2
Stator slot depth to width ratio	γ	
Stator core depth	L	mm
Power factor	pf	-
Efficiency	η	-
Pole number	P	-
Number of slots	S	-
Frequency	f	Hz
Input Voltage	V	Volts
Stator winding factor	k_w	-

2.2.17 Overview of genetic algorithm

Genetic algorithm (GA) is an optimization and search technique based on the principles of genetics and natural selection. It belongs to a class of meta-heuristic techniques in contrast with classical optimization techniques unified as classes of optimizations depicted in Figure 2.14. Broadly speaking, a GA allows an initial randomly generated population composed of many potential design solutions known as individuals to evolve under specified stochastic selection rules to a state that maximizes or minimizes a given objective function (cost function). The method was developed by John Holland (1975) and subsequently refined for solving generalized nonlinear optimization problem by Goldberg (1989). The three fundamental operators which are indispensable in the search process of a genetic algorithm

are reproduction, crossover and mutation. In essence, the GA deploys and reproduction crossover and mutation collectively to institute a random search structure.



degree

Figure 2.14: Classes of Optimization Techniques (Bharadwaj et'al, 1979b)

of fitness values $F(x)$. As a matter of necessity in the evolutionary process, reproduction ensures that the genes of the fittest individuals are preserved in all generations. The next step is to select any two individuals from the current population and perform a process referred to as crossover.

The process of selection of mating pairs can implemented in several ways-the most popular being the roulette wheel selection and stochastic tournament (Bakare, 2001). Crossover is essentially an exploitative technique, which exchanges partial genes from both parents and thereby permitting the combination of partial solutions to produce superior offspring (single point crossover). Conversely, mutation is an explorative process to primarily reintroduce genetic diversity and prevent premature convergence to local sub-optimal solution in the global search space via random exchange of bits of the parent individuals.

Central to GA algorithmic framework, every feasible solution to a nonlinear optimization problem of interest is encoded as an individual that when assembled collectively form an initial population P_0. Each individual has a fitness value, which is usually derived from one or more objective functions and is a measure of how well the solution matches objectives. In each generation, individuals with higher fitness values have a greater likelihood to be selected and reproduced in the population of the next iteration. After creating an initial population, GA will run iteratively until a termination condition is satisfied. The crossover and mutation processes have associated probabilities of occurrences. They must be carefully selected in order to achieve satisfactory global search by GA for a given nonlinear multi-objective optimization problem. The generalized algorithmic procedure of GA is depicted in Figure 2.15.

In summary, the search capabilities of a GA are as follows:

i. Can optimize with continuous or discrete variables,

ii. Does not require derivative information or detailed mathematical formulation,

iii. Simultaneously searches from a wide sampling of the cost surface,

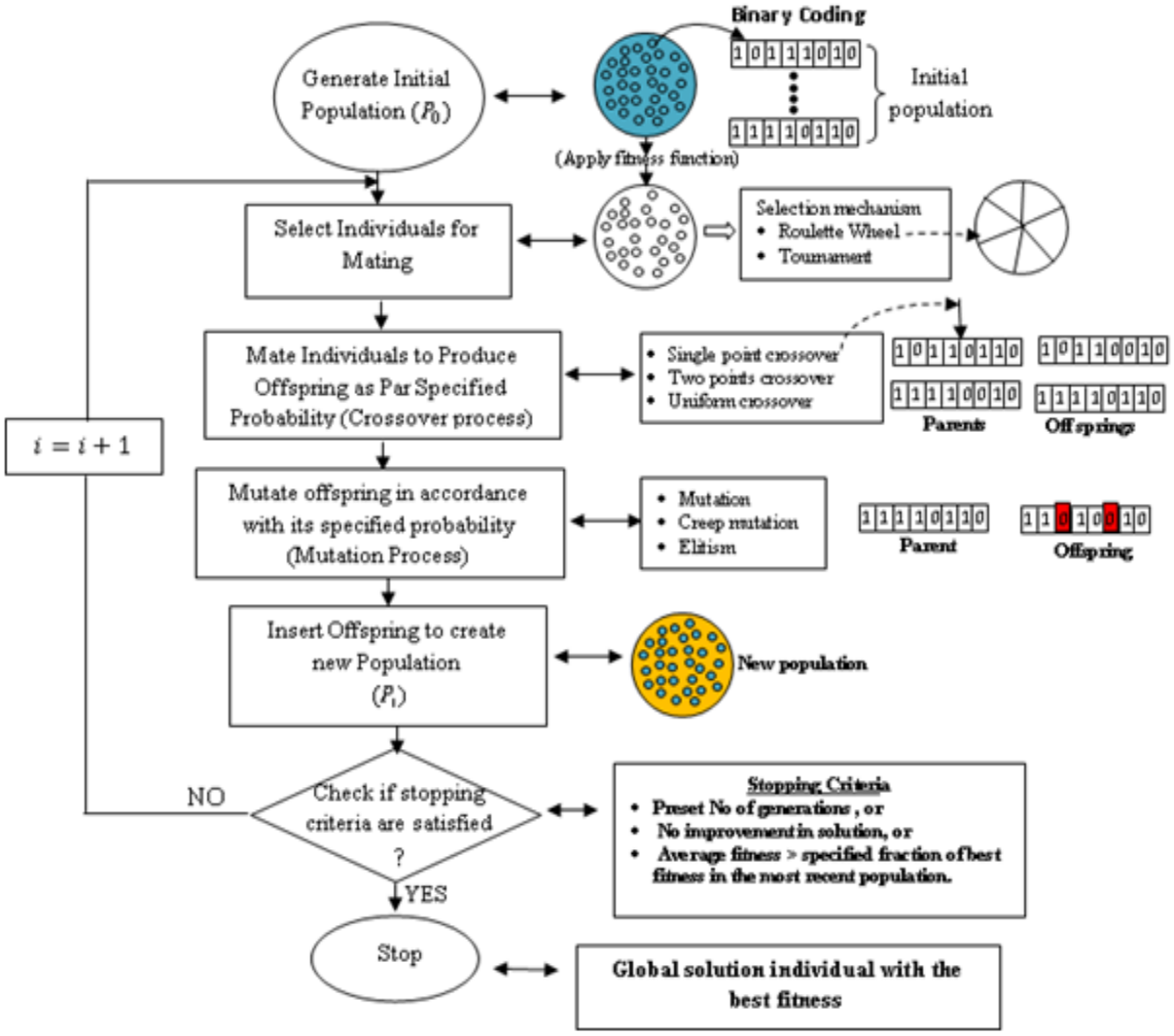


Figure 2.15: Generalized Procedure for Genetic Algorithm

iv. Can handle a large number of variables,

v. Is well suited to parallel computations,

vi. Optimizes variables with non-convex cost surfaces (they can jump out of a local minimum),

vii. Provides a list of optimum variables, not just a single solution,

viii. May encode the variables so that the optimization is done with the encoded variables, and

ix. Works with numerically generated data, experimental data, or analytical functions.

GA has continued to play a vital role in solving complex non-linear optimization problems that include machine design optimization. The adoption of GA in this research work to optimize efficiency of DSWIM is basically an extension of existing GA technique widely applied but to the design of conventional poly-phase induction machine.

2.2.18 Selection of method of field analysis for induction machines

In all engineering problems, most of the physical phenomena occurring can be described by means of partial or ordinary differential equations. The derivation of such equations may not normally pose any difficult task. However, the difficulty in most cases lies in finding the desired solutions that satisfy the set of equations derived. Over the years, numerical techniques have been developed for solving the resulting differential equations. As a result, many computing techniques have been developed.

With respect to magnetic field distribution within a specified geometric medium, three methods have been developed to solve the characteristic equations describing the physical field distribution within the geometry. These methods are:

1- Moment Method (MM)

2- Finite Difference Method (FDM)

3- Finite Element Method (FEM)

Moment and finite difference methods are basically numerical techniques for solving electromagnetic and electrostatic problems in which the original differential equations are approximated by a set of linear equations. The major drawbacks of these methods, except for conforming geometric structures such as wire or helix antennas, have to do with the computational difficulties encountered in modelling complex geometries typified by induction machine stator and rotor structures.

A finite element method (FEM) has been developed which addresses some of the drawbacks encountered in the other methods because it fits into any geometry and offers far superior approximation to the original problem. The concept is anchored on discretization of the original geometry into small elements interconnected at their nodes to form meshes. The meshes may be triangular or rectangular in shape. A triangular mesh offers the advantage of being able to fit into the shape of any complex geometrical object Dmitry and Yujing, [2013].

Electrical machines have cores of complex geometries due to stator and rotor slotting as well as the presence of teeth. This complexity of the core makes finite element method with triangular meshes a better candidate for the analysis of its field distributions in the stator, rotor and air-gap. The salient steps of finite element method are as follows:

Step 1: Discretize the solution domain into a finite number of sub-domains using triangular elements interconnected at various nodes to form meshes as conceptually illustrated in Figure 2.16.

Step 2: For i^{th} element, derive the governing equations and repeat for all elements.

Step 3: Assemble all the equations developed in step 2 with the necessary boundary conditions .

Step 4: Solve the system of equations for a specific geometric domain to obtain the desired solution.

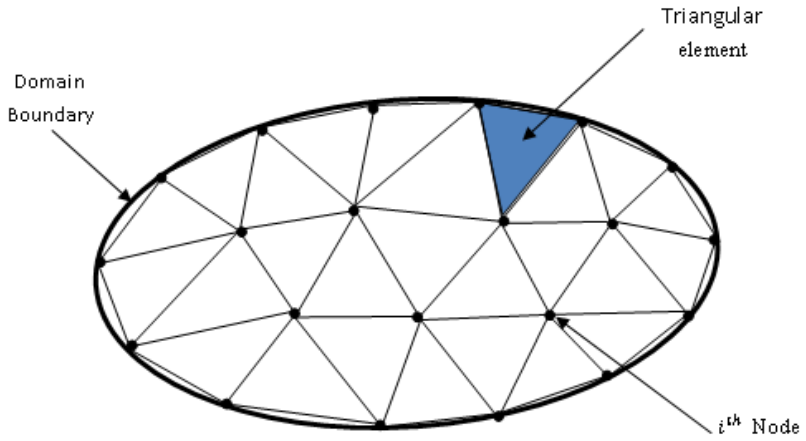


Figure 2.16: Fundamentals of FEM Concept

2.2.18.1 Finite element method (FEM)

Finite element method (FEM) is a method by means of which magnetic field problems can be analyzed. Unlike other methods, FEM has proved to be flexible, reliable and effective in the analysis and synthesis of power frequency electro-magnetic devices (Wexler, 1973). Another key advantage of this method is the availability of user friendly FEM packages that allow computation of the electromagnetic field distribution and integration of parameters that circumvent their modeling complexities (Jin, 1992). As a matter of fact, FEM has the capability to analyze electro-magnetic circuits of any shape and material (Salon, 1995). Herein, the non-linearity of any magnetic material is accounted for by introducing the magnetization characteristics of the material into the software package. There is also no need for the rigorous calculations of reluctances, leakage factors etc. normally encountered in electrical machine field calculations. This coupled with the computational qualities of the method have made it more popular in solving field problems (Bianchi, 2005).

In order to effectively understand and apply FEM, there is need for the basic understanding of the fundamentals of electro-magnetic field theory. Magneto-static problems are problems in which the fields are time invariant. These problems are such that the magnetic field intensity (H) and flux density (B) satisfy the following Maxwell's equations:

$$\nabla X \boldsymbol{H} = \boldsymbol{J} \tag{2.180}$$

$$\nabla x \boldsymbol{B} = 0 \tag{2.181}$$

$$H = \frac{B}{\mu} \tag{2.182}$$

Iron, which is the material used in electrical machine's core, has permeability, as a function of **B**. Thus equation 2.182 can be re-written as:

$$H = \frac{B}{\mu(\mathrm{B})} \tag{2.183}$$

What FEMM actually does is to find a field that satisfies the above set of Maxwell's equations via a magnetic vector potential approach (Basil and Ahmed, 2012). Herein, flux density is related to magnetic vector potential, **A** by the expression:

$$\boldsymbol{B} = \nabla \times \boldsymbol{A} \tag{2.184}$$

Equation 2.184 always satisfies equations 2.180-2.184. Hence, equation 2.78 can be re-written as:

$$\nabla \times \left(\frac{1}{\mu(B)} \nabla \times \boldsymbol{A}\right) = \boldsymbol{J} \tag{2.185}$$

Equation 2.185 is used to solve magneto-static problems with non-linear B-H curves for which the machine under consideration falls. Of special interest in this dissertation is the modeling of DSWIM using FEM to enable determination of its critical modeling parameters as dwelt upon in the next chapter. Due to modeling complexities of 3-D FEM and extraordinarily long simulation time required, in this dissertation 2-D FEM is considered adequate for the magneto-static problem developed in respect of dual stator winding machine. For this reason, attention will be focused specifically on 2-D based FEM simulation which demands much less simulation time than the 3-D even though the latter offers more information. This is because 2-D FEM software packages are readily available to researchers in this field of study.

From analytical viewpoint, FEM is essentially a numerical algorithmic framework to secure accurate solution to Maxwell's equation by subdividing the whole domain under

investigation into many smaller triangular sub-domains called elements, to form a finite element mesh (Albertiet'al, 2008). Figure 2.17 shows typical meshes generated for a quarter cross-section of a three phase squirrel cage induction machine (Vaseghi et al., 2009).

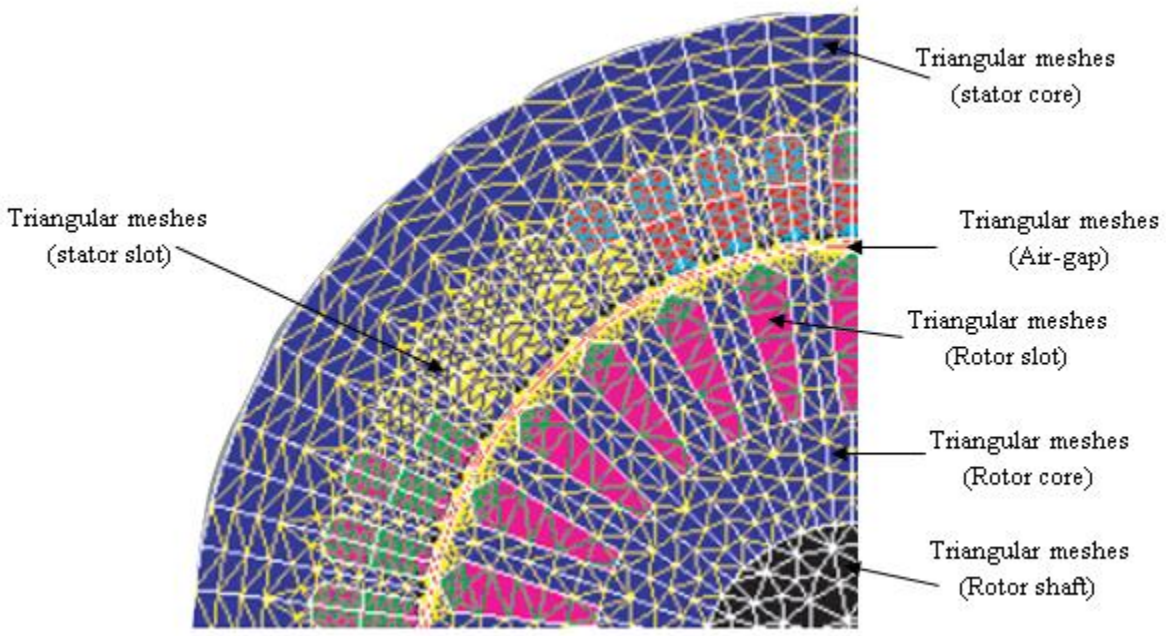


Figure 2.17: Typical Triangular Meshes Generated for a Quarter Cross-Section of an Induction Machine (Adapted from Vaseghi et al., 2009)

Three basic steps are normally followed in carrying out finite element analysis (FEA). These are:

i. Pre-processing

ii. Processing

iii. Post-processing

In the pre-processing stage, the geometry of the problem to be solved is laid out, material properties and boundary conditions are also stated here. Normally, a Dirichlet boundary condition in which null magnetic potential is assigned along the external circumference of the stator is adopted (Albertiet'al, 2011). The ampere-conductor of the circuit is also specified together with all the material blocks that are to be used in the model (copper, aluminum, iron etc).

2.3 Review of Similar Works

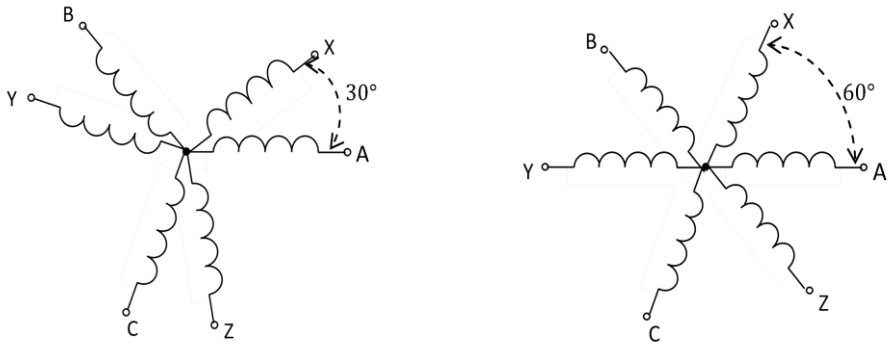
This section is devoted entirely to literature review of the existing scholarly publications on the design of dual stator winding induction machine (DSWIM) which have focused majorly on dissimilar pole ratio architecture as well as their modelling and control techniques. For the sake of completeness, historical development DSWIM is first and foremost reviewed that patently paved way for the renewed interest in this class of machines in the last two and half decades.

2.3.1 Review of historical development of DSWIM

The use of common magnetic structure to accommodate two sets of stator windings was first introduced by Hunt (1907) and Alger et al. (1930) as a way to increase the power capability of large synchronous generators. Since then dual stator machines have been used in various specialized applications such as aerospace, electric/hybrid vehicles, ship propulsion and critical drive systems. A prominent advantage of a multi-phase motor drive over a three-phase motor drive remained reliability improvement as advanced by Ward et al. (1969). The desirability for fault tolerance, to enhance reliability, is evidently one of the main reasons behind the application of six-phase (double star) and nine-phase (triple star) induction motor drives in locomotives (Nelson et al. 1974). The other main reason is that for a given motor power, an increase in the number of phases enables reduction of power per phase, which translates to a reduction of the power per inverter leg. Multi-phase machines are therefore often considered for, and applied in, high power applications.

Nelson et al. (1974) and Fuchs et al. (1974) conducted detailed studies of induction machine configurations with multiple sets of three-phase stator windings and with an arbitrary angle of displacement. They reported that in the case of a six-phase induction machine, it is advantageous to use an asymmetrical stator winding structure, with two of the three-phase windings spatially shifted by 30^0, instead of a symmetrical winding structure

with a 60^0 spatial shift between any two consecutive phases as illustrated in Fig. 2.18. The winding displacements required, however, are not necessarily the symmetrical displacements used in standard multiphase induction machines.



(a) 30° Spatial Displacement (b) 60° Spatial Displacement

Figure 2.18: Schematic Diagrams of Dual Stator Windings Angular Displacements

The rationale behind this conclusion is related to the pre-Pulse Width Modulation (PWM) era of Voltage Source Inverter (VSI) control, when 180^0 conduction mode was utilized. By using an asymmetrical six-phase machine, it became possible to eliminate the sixth harmonic from the torque ripple.

As closure of previous research activities, Klingshim (1983) posited that it is possible to improve the performance of a high phase order induction machine with appropriate winding displacements as certain characteristics of the machine are governed by phase belt angle. The renewed interest in multi-phase machines was chiefly rekindled by the possibility of reducing torque ripples in inverter fed drives (operated in 180^0 conduction mode), when compared to the three-phase case (Abbas 1984). An asymmetrical six-phase induction motor drive has continued to attract research attention.

2.3.2 Review of recent publications on DSWIM design, modelling and control techniques

This subsection provides comprehensive literature review, in the last two decades, on dual stator winding induction machine design philosophy and operational characterizations.

Lipo et al, (1991) proposed a single winding connection capable of producing two simultaneous flux distributions. Coil groups in this type of winding are interconnected and distributed in such a manner that when three phase currents flow through one set of terminals (e.g. a-b-c), they produce a rotational flux of a particular pole number. Simultaneously, when another 3 phase currents flow through the other set of terminals (in this case x-y-z), yet another rotational flux is produced having a different pole number.

A typical example of a single winding connection capable of producing two simultaneous flux distributions is shown in Figure 2.19. Coil groups in this type of winding are interconnected and distributed in such a manner that when three phase currents flow through one set of terminals (e.g. a-b-c), they produce a rotational flux of a particular pole number. Simultaneously, when another 3 phase currents flow through the other set of terminals (in this case x-y-z), yet another rotational flux is produced having a different pole number. The major drawback of this type of winding is the presence of circulating current under unbalanced operation. Another disadvantage of this kind of connection is the limitation imposed on the voltage ratio between the two sets of terminals.

The disadvantages inherent in single winding producing two simultaneous flux distributions can be overcome using n separately isolated three phase winding configuration. In addition, it also minimizes modifications with respect to standard configurations.

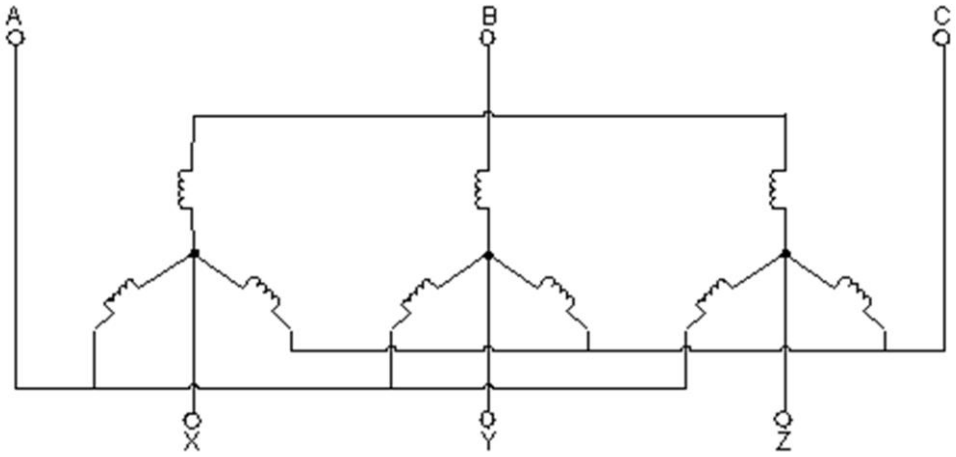


Figure 2.19: Single Winding dissimilar Pole Number Distribution

Figure 2.19: Single Winding dissimilar Pole Number Distribution

Jawad and Sharifian (1995) attempted to optimize a three phase induction motor taking efficiency as objective function. A nonlinear optimization approach for the motor design was used and the optimized design was found to compare favourably with those obtained using other optimization procedures. The results obtained in this case cannot be relied upon in view of different optimization variables and methodology used in comparison to other methods.

Zhao and Lipo (1996) applied field orientation control technique to model and control a multiphase induction machine. In order to make the field orientation a control applicable, synchronous reference frame transformation for stator current was developed. The modeling was achieved but was applied to a specific case of an open phase in the stator winding.

KaamalIdir et al. (1997) proposed a new global optimization approach for electric machine design problems. Its algorithm uses the error function between the actual cost function at a given computational step and its limit value which is lower than desired global minimum. The method suffers lack of generalized solution in the sense that it only gives a global optimum value for a given computational step.

Alfredo and Lipo (1998) gave a detailed mathematical derivation of the squirrel case induction machine d-q model. The model is based on coupled magnetic circuit theory and complex space vector notation. In this work, it was shown for the first time that in view of the symmetrical nature of the machine structure, both the stator and rotor circuits can be modeled by a simple set of only four coupled differential equations. Although the resulting equations simplified analysis of induction machines, the results obtained from the analysis are approximate due to a number of approximations and simplifications involved in the derivation.

Munoz et al. (1998) also explored the stator winding arrangement in induction drives for reliability enhancement of the drive system and reduction of space harmonics. This work essentially attempted to bridge the research gap identified in some earlier publications but did not offer any improvement in the design of dual stator winding induction.

Ojo and Innocent (1999) presented a novel usage of a dual stator winding induction machine as a stand-alone generator. The generator has one winding powering a load while the other serves as a control winding. The scheme was able to solve the problem of voltage regulation as encountered in all stand-alone induction generators. However, it is inefficient from utilization point of view to dedicate half a machine to control alone.

Alfredo and Lipo (2000) presented a model of a dual stator winding induction machine wound for a dissimilar pole numbers. The machine exhibited an improved capability to operate at very low speeds maintaining relatively high stator frequencies. This feature is particularly useful for implementation of speed sensor less schemes and adds a new degree of flexibility and standard control methods currently used in ac drives. However, the issue of optimizing the machine performance was not looked into.

Rangajaran et al. (2002) derived a transient model for an induction machine with stator winding turn faults using a reference frame transformation theory. Steady – state equivalent circuits were derived from which the sequence components of the line currents can be establish as a function of fault severity. Due to structural nature of squirrel cage rotors, it is more eretical to analyze the transient behaviour of induction machines with rotor bar faults. This work failed to consider that aspect.

Singh (2002) conducted a comprehensive survey of literature dealing with multi-phase induction machine. A number of advantages possessed by this group of machines were highlighted. They include possible elimination of some air gap flux harmonics and rotor copper losses produced by this harmonics, lower current per phase without an increase in

voltage per phase. The survey however, failed to draw a general conclusion on the practicability of multi-phase machine.

Signh (2003) presented a simple d-q model of a multiphase induction machine suitable for analyzing the transient, steady sate and dynamic behaviour of the machine under balanced operating condition. The work however, did not consider unbalanced operating conditions such as single phase, three phase short circuit etc.

Razik (2003) described a mode of a double star (six phase) induction motor with useful insight for diagnostic purposes. A special attention was paid to the rotor deflection or eccentricity this case. Although some encouraging results were obtained the issue of calculating current due to common connection between the neutral points was not addressed in the work.

Djafar et al (2004) presented modeling and design of a dual-stator winding AC machines to minimize circulating harmonics currents. The machine windings were fed through voltage source inverter. The results of the design revealed that a full pitched winding has the effect of increasing mutual leakage inductance which has led to reduction in circulating harmonics currents. The work did not consider the effect of slot-shapes in reduction of harmonics currents.

Roberts, (2005) outlined methods to evaluate the magnetic loading of a brushless doubly fed induction machine. In the first method, the peak values of flux densities set up by individual winding set. This method has the shortcoming that it only considered a single value of flux density i.e. peak value. The second method considered the vector sum of the flux densities from the two winding sets. Although this method gives a better result than the previous, it still fails to address the issue of saturation in the core of the machine.

Singh et al (2005) presented a simple and straightforward approach to develop an indirect field-oriented control (FOC) scheme for a six phase induction machine. The machine has an

arbitrary displacement between the two sets of the three-phase windings. The scheme used in this work has advantage of eliminating the unbalanced current sharing that exists between the two sets of three-phase windings normally observed in other schemes. However, the advantage of using arbitrary displacement between the two winding sets was not made obvious in the work.

Wu et al (2005) investigated the use of dual stator winding squirrel cage induction machine for generating dc power. The scheme uses series or parallel connected ac-dc PWM rectifiers. The concept of nonlinear input-output linearization was used for the regulation of the dc voltage. Connecting a dc-ac inverter in series or parallel with the load provides variable reactive power in the process of which both the load voltage magnitude and frequency are effectively regulated. Unfortunately, these remedial schemes inject harmonics into the load current and voltage waveforms.

Kim et al (2005) proposed a reduction of stator copper losses and core including harmonic losses by optimal selection of stator slot design. Finite element method (FEM) was used to design the slot as a result, core and winding losses reduced by 2.22%. However, this technique cannot be applied to an existing design since it involves modification of active core material.

Cunkas and Akkya (2006) applied genetic algorithm (GA) to optimize a three-phase induction machine design. The results of the optimization revealed a 25% reduction of the total material cost. Although the method succeeded in reducing the total cost of active materials, it, however, cannot be applied to a design where material cost is explicitly not one of the constraints.

Judith and Steve (2006) showed how the techniques of generalized harmonic analysis may be used to simulate the steady-state behaviour of a multiphase cage induction motor with any form of open-circuit or short circuit fault in the stator winding. An analytical model

developed for the purpose of simulation was verified using experimental results proved the effectiveness of the technique, transient analysis was not considered in the work. It is a well-known fact that faults could be more severe under transient conditions.

Wu and Ojo (2006) developed a model of a dual stator winding induction machine in which the space harmonics of the stator and rotor windings are accounted for. The air gap-field calculation was carried out using coupled circuit model simulation. The machine inductances arising from the model were estimated using the winding function method. However, the simulation results obtained were only approximate since the simulation was carried out using the values of inductances obtained from an inaccurate method-winding function method.

Juan and Ojo (2008) attempted to optimize air-gap flux density of a dual stator winding induction machine. To avoid saturation in the machine the fluxes generated by both windings were synchronized using a flux positioning algorithm. However, the model proposed in this work is limited to only magnetically unsaturated machine. It is a well-known fact that electrical machines operate most of the times with saturated cores.

Krishnamoorthy and Dharmalingam (2009) presented a literature study of GAs used in general in electrical machine design. The optimized design results obtained in the literature were also presented. In general, the various research works considered in this work, compared GA with other conventional techniques in solving one optimization problem or another. The general conclusion is that GA appeared to have an edge over other methods. The advantages of GA over others include; (1) Ga carries out more iterations, (2) GA focuses on finding global optimum. Despite the advantages of GA, the direct search method improves convergence speed with greater accuracy in electric motor design.

Chendrasekaran and Maniganda (2011) considered design and effective operation of a dual-stator winding reluctance motor. The efficiency and power factor of the motor were taken as objective functions. Improvement in the efficiency and the power factor was

achieved by introducing some design modifications in the active materials of the machine. Even though the power factor was increased from 0.55 to 0.78 and the torque of the new motor designed rose by 1.6 per unit (pu), the cost of getting such improvement was prohibitive.

Alberti et al (2011) described a finite element (FE) procedure suitable for the prediction of a controlled induction motor (IM) performance. The FE analysis is carried out in the rotor flux reference frame so that only magneto static FE simulations are used thereby reducing computational time. The proposed procedure is suitable for both the analysis and design of IM, allowing for the prediction of the drive performance during the various design steps. The method also has the advantage of including the saturation effects in all the machine parts during all computations. However, the analysis was done for a specific machine. A general procedure was not included.

Thangaraj et al (2012) presented the design optimization of a squirrel cage induction motor using differential evolution (DE) algorithm. The proposed algorithm was applied to induction motor selected as the driving power of spinning machines in the textile industry. The work considered operating cost as the one of the objective functions. However, power factor penalty imposed on industries which constitutes an appreciable cost of operation was not captured in the model.

Rodrigo et al (2013) proposed and implemented a modified topology of a dual stator winding induction generator with standard squirrel cage rotor. The generator design includes a two-dimensional finite elements analysis to investigate the magnetic field distribution. A prototype was developed and tested to verify the validity of the design. However, the machine was designed for a dissimilar pole numbers (2 and 6 poles). To avoid excessive rotor copper loss one stator winding was made power and the other control winding. This led to incomplete utilization of the machine.

Fireteanu et al (2013) studied the effects of the short-circuit fault in the stator winding of an induction motor and the influence of this fault on the magnetic field outside the motor. The study was based on a time domain finite element analysis of the electromagnetic field. The unbalanced electromagnetic force acting on the rotor due to faulty motor (short circuit fault) was found to be about 1500 times higher than what is obtainable with a healthy motor. Even though the results obtained were quite revealing, the work did not consider extending the analysis to multiphase machines with high fault tolerance.

2.3.4 Research thrusts pursued in this dissertation

It is worthy of note, from the reviewed literature, that most researchers have concentrated on dual winding induction machines having dissimilar pole ratios to exploit the advantages of zero circulating currents under unbalance supply voltages as well as low harmonic generations. However, for the fact that the rotor speed is fixed, excessive copper losses will occur due to partial utilization of the machine stator dual windings during running mode. A dual stator winding having similar pole ratios and two separate three phase stator windings housed in a common stator magnetic core is pursued in this research work. This design approach offers the possibility of using either of the windings at light loads thereby increasing the machines efficiency. Another advantage of same pole ratio DSWIM is the possibility of reconnecting the machine winding to operate as a conventional three phase induction machine for higher power capacity. The foregoing will not be possible for a machine wound with dissimilar pole ratios ($n \neq m$). Thus, the prime focus of this research work is aimed at pragmatic design philosophy to facilitate improved multi-phase induction machine for similar number of poles ($n=m$). The underlying design architecture and practical realization of such improved multi-phase induction machine constitute the main thrust of this work.

2.4 Summary

This chapter has developed some relevant theoretical concepts and provided comprehensive literature review of several publications that bear direct relevance to the core research work reported in this dissertation. The theoretical concepts covered are central to actualizing the goals of this research work as pursued further in the subsequent chapters. The fairly large number of publications in reputable journals reviewed is a testimony to the nascent and aggressive research focus on the dual stator winding induction machine and the postulation that this research area is yet to attain maturity. This has justifiably motivated this research work to embark on hybrid analytical and GA based design approach of DSWIM that focuses attention on similar pole ratios winding structure with the following additional goals pursued:

- DSWIM d-q-0 arbitrary reference frame modelling and simulation in MATLAB/Simulink environment as well as 2D-FEM characterization; and
- Its prototype realization to enable theoretical and experimental validations.

CHAPTER THREE

DSWIM DESIGN METHODOLOGY

3.1 Introduction

The overall design philosophy of a dual stator winding induction machine relied upon in this dissertation is presented in this chapter. As pointed out in the preceding chapter, the research work on DSWIM to date has always focused largely on sound design of two sets of stator windings having desired pole ratios but housed in standard stator frame and rotor structure assumed to be judiciously selected a-priori. Within this framework, dual stator windings capable of establishing the requisite flux in the machine are usually designed. It involves determination of number of stator turns per phase, magnetizing current, amongst others. A two stage design procedure is therefore proposed in this research work involving analytical approach and genetic algorithm based parameter optimization. More specifically, the analytical approach is deplored to calculate the leading machine parameters and pragmatically tuned by application of genetic algorithm to optimize its power factor and output efficiency.

The theoretical framework is premised on magnetic circuit design to meet desired machine specifications. The key objective remains optimal magnetic design of dual stator winding to be housed in the slots of preselected conventional three-phase induction machine stator having squirrel cage rotor without violating its original design specifications. Starting from the generalized formulation of DSWIM design philosophy, the ensuing sub-problems identified are then subjected to in-depth analytical characterizations. Herein, mathematical derivations and analyses of the constituent components of the overall objective function are explored to enable the development of pragmatic solution methodology that respect various specified equality and inequality constraints. In the subsequent sections, the various functional descriptions and mathematical derivations in respect of DSWIM design are outlined in sufficient detail.

3.2 Generalized Description of a Dual Stator Winding Induction Machine Design Procedure

It has been established that all electric machine design philosophies are anchored on fundamental electromagnetic principles. This implies that special considerations must be given to both magnetic and electrical aspects while designing an electrical machine for specific application. Because DSWIM is a member of the electromechanical conversion family, its design requirements are strictly guided by the well-established electromagnetic principles. The complete DSWIM design problem comprises design of its stator frame/rotor sub-problem and design of its magnetically coupled stator windings sub-problem to meet all operational requirements and associated constraints.

Nonlinear optimization problem targeted at designing a dual stator winding induction machine based on a generalized multi-objective function can be cast as follows:

1. Optimize Nonlinear Objective Function

$$F = \sum\big[G_1\big(B_g, \bar{\eta}\big) + G_2\big(\theta, B_{abc}, B_{xyz}\big) + G_3\big(B_g, \ell_g\big) + G_4(\mathcal{F}_1, \mathcal{F}_2, \mathcal{F}_3) + G_5(I_m, \phi_m, E) + \quad G_6(P_m, N_c, J) + G_7(d, J_c) + G_8(\tau, q, y_c) + G_9(r, L, s)\big] \tag{3.1}$$

Where:

$G_1\big(B_g, \bar{\gamma}\big)$: Available information on physical dimensions($\bar{\gamma}$) and allowable magnetic loading B_g of a standard induction machine to be converted into DSWIM;

$G_2\big(\theta, B_{abc}, B_{xyz}\big)$: Generalized mathematical description of the spatial distributions of fluxes amongst dual phase windings (a-b-c and x-y-z);

$G_3(B_g, \ell_g)$: Generalized formulation of air-gap flux density for optimum machine performance;

$G_4(\mathcal{F}_1, \mathcal{F}_2, \mathcal{F}_3)$: Generalized magneto-motive force distributions in the air-gap considering machine rotor and stator slots;

$G_5(I_m, \phi_m, E)$: Generalized description of the stator winding optimizing function;

$G_6(P_m, N_c, J)$: Generalized stator turns/phase and Power rating optimizing function;

$G_7(d, J_c)$: Generalized conductor sizing and current density optimizing function;

$G_8(\tau, q, y_c)$: Generalized optimizing function for stator winding architecture; and

$G_9(r, L, s)$: Generalized DSWIM model parameter estimation function.

Subject to the following equality and inequality constraints:

2. Equality Constraints:

$$\bar{\gamma} = \bar{\gamma}_{specified}$$ (Parameter specifications for machine design)

$$\bar{\gamma} \triangleq \left[L_c, D_{is}, D_{is}, pf, \eta, P, S_1, S_2, f, V, k_1, \ell_g\right]^T$$

$B = B_{optimum}$ (Air gap magnetic flux density at the knee point)

$$S_1 - S_2 = \begin{cases} \pm 2 \\ or \\ \pm(P \pm 1) \\ or \\ \pm(P \pm 2) \end{cases}$$ (To avoid excessive vibrations or noise according to Lipo, 2004)

$S_1 - S_2 = mP\ ; m = 0, 1, 2, \ldots$. (To avoid cogging problem or synchronous torques)

(3.2)

3. Inequality Constraints:

$S_2 \leq 1.25 S_1$ (To limit asynchronous harmonic torque)

$$\bar{X}_{min} \leq \bar{X} \leq \bar{X}_{max}$$ (3.3)

$\bar{X} \triangleq [x_1, x_2, x_3, \ldots\ldots x_n]^T$(Some constants to be selected within their respective specified limits)

Equations (3.1) to (3.3) constitute the generalized mathematical formulation that describes global design of DSWIM encompassing the search for optimum specifications in respect of the stator frame, rotor structure and stator winding. The nonlinear multi-objective optimization problem can be decomposed into two interacting sub-problems thus: Stator frame and rotor structure optimization design and stator winding optimization to satisfy the magnetic and electrical loading constraints imposed by the former until convergence is achieved. Although this approach is mathematically elegant, the resulting stator frame and rotor structure design to house optimized stator winding of DSWIM cannot be practically realized due to its prohibitive cost for research purpose. In view of the foregoing, a well-established pragmatic approach adopted by research activities on DSWIM globally is to choose appropriate stator frame and rotor structure a-priori from a large population of existing conventional 3-**ϕ** induction machines. Of course, the choice is premised on the knowledge of the desired power output, P_{out} operating frequency, f and supply voltage V_{ph}. Note that for a well designed stator frame and rotor structure that emerged from such choice, some pertinent equality constraints and inequality constraints of equations 3.2 and 3.3 will be intuitively met. The problem is then reduced to designing the dual winding of specified pole ratio to be housed in the selected stator frame and rotor type (cage or wound) without violating critical parameters such as air-gap flux density, electrical and magnetic loadings.

Against this backdrop, the analytical approach entertained is to design an optimized 3-**ϕ** induction machine dual winding from first principles considering leading parameter specifications for the DSWIM design of interest. As a follow up on the analytical design procedure, genetic algorithm (GA) has been selected for the optimization of power efficiency

and power factor due to the numerous advantages it possesses as highlighted in the preceding chapter.

In summary, the generalized formulation of a dual stator winding induction machine tackled in this research assumed the availability of a conventional 3-ϕ induction machine stator frame having squirrel cage rotor and certain specified parameters that include power rating, stator slot numbers, rotor slot numbers, etc. This is due to readily available number of manufactured 3-ϕ cage induction machines covering wide range of power ratings, voltages and speeds from which researchers worldwide can easily source standard stator frame with matching squirrel cage rotor to house optimized design of dual winding for maximum operational performance. It is intuitively clear that having selected the most suitable stator frame and cage rotor for DSWIM design objective; its leading parameters presented in Table 3.1 can readily be determined. A conceptual block diagram representation of the DSWIM stator winding design approach is shown in Figure 3.1.

Table 3.1 Specified Parameters of Machine Design

Parameter Description	Symbol	Unit
Core length	L_c	Mm
Inside diameter of stator	D_{is}	Mm
Outside diameter of stator	D_{os}	Mm
Diameter of rotor	D_{or}	Mm
Power factor	pf	-
Efficiency	η	-
Pole number	P	-
Number of stator slots	S_s	-
Number of rotor slots	S_r	-
Stator slot depth	d_s	Mm
Rotor slot depth	d_r	Mm
Frequency	f	Hz
Input Voltage	V_{ph}	Volts
Stator winding factor	k_w	-

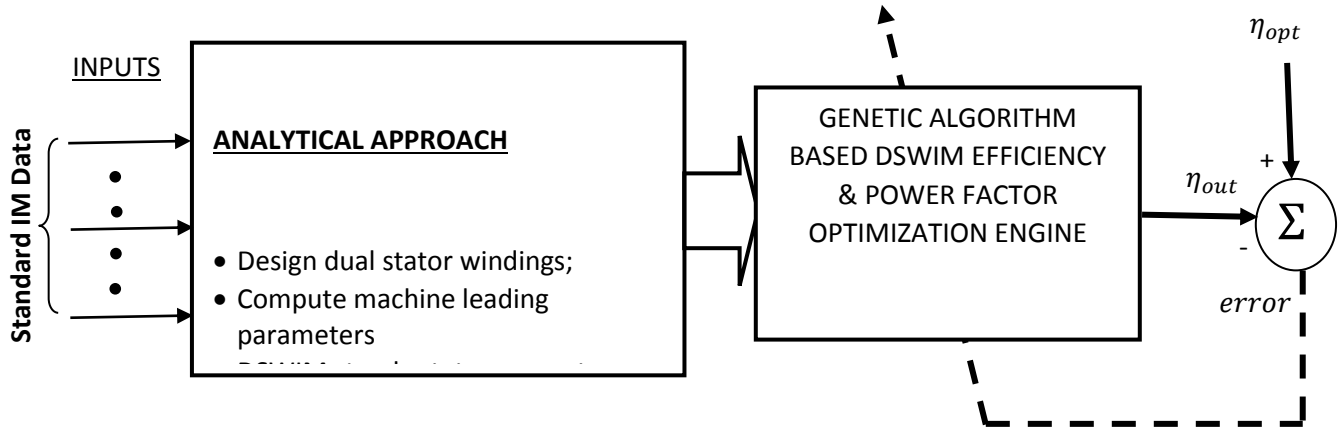


Figure 3.1: Block Diagram Representation of DSWIM Design Approach

3.3 Magnetic Loading Characterization

One of the most important aspects of design in electrical machine is the proper choice of magnetic loading. It is defined as the total flux existing around the air gap periphery of a given machine. From design point of view, air gap flux density or specific magnetic loading provides more useful information than magnetic loading. Specific magnetic loading is defined as total flux around the air gap per unit area of flux path at the air gap of a machine. This is also referred to as air gap flux density per pole of a machine. If a low value of air gap flux density is chosen, then the iron part of the machine will be operating in the linear region of the magnetization curve. This will result in small value of magnetizing current and by implications a higher power factor. But the volume of the machine will be higher.

On the other hand, if a high value of air gap flux density is selected, the iron part will be saturated thereby producing increased magnetic losses and poor power factor, even though the volume of the machine will be lower. It is thus necessary to select an optimum value of air gap flux density in electric machine design.

3.3.1 Mathematical description of air-gap flux density for DSWIM

With reference to DSWIM architecture, the distinguishing features are two independent sets of stator windings share a common magnetic structure. These winding sets, produce two separate magneto-motive force (MMF) distributed along the air gap periphery of the machine. These MMFs also set up two air gap flux densities. The problem to be addressed here, is therefore finding the value of air gap flux density produced by each winding set such that no magnetic saturation occurs in the core of the dual-stator winding machine.

Broadway, 1974 has offered the procedure for finding the two air gap flux densities for a brushless cascade alternator. However, this procedure failed to draw conclusion on how to find the flux densities in other types of machines. Roberts, 2005 outlined three methods to evaluate the magnetic loading of a brushless doubly fed machine. In the first method, the peak values of flux densities set up by individual winding set. Thus;

$$B_{dual_p} = B_{abc_p} + B_{xyz_p} \tag{3.4}$$

Where

B_{abc_p} and B_{xyz_p} : are the peak values of the flux densities of 'a-b-c' and 'x-y-z' winding sets, respectively.

This method has the short coming that it only considered a single value of flux density i.e. peak value. Moreover, critical analysis of the results obtained by this method was shown (Munoz, 2000) to be too conservative since the peak value occurs at two points per cycle. The second method defines the combined magnetic loading as:

$$B_{dual} = \sqrt{\left(B_{abc}^2 + B_{xyz}^2\right)} \tag{3.5}$$

Although this method gives a better result than the previous, it still fails to address the issue of saturation in the core of the machine.

The third method referred to as a new generalized method evaluates the value of the flux density of any induction machine by the mean absolute flux per pole expressed as:

$$B = \lim_{T\to\infty} \int_0^T \frac{1}{2\pi} \int_0^{2\pi} |B(\theta)| d\theta dt \tag{3.6}$$

The magnetic field in the dual stator winding induction machine can be expressed as:

$$B = B_1 \cos(\omega_1 t - P_1\theta) + B_2 \cos(\omega_2 t - P_2\theta + \gamma) \tag{3.7}$$

Where

1 and 2: are subscripts referring to a-b-c and x-y-z winding sets, respectively;

B_1 and B_2: are windings 1&2 flux density magnitudes, respectively;

ω: angular frequency in revolutions per second;

P_1 & P_2: Dissimilar number of pole pairs respectively;

γ : Angle between the corresponding phases of the two winding sets and

θ : Stator reference angle.

For convenience, the magnetic field of the dual stator winding machine is referred to rotor reference frame and cast as follows:

$$B_r = B_1 \cos(\omega_{s1} t - p_1\phi) + B_2 \cos(\omega_{s2} t - P_2\phi + \gamma) \tag{3.8}$$

Where

ω_{s1}& ω_{s2} : are the slip frequencies of the two winding sets, respectively.

Equation (3.8) constitutes the combined magnetic loading for a dual machine housing two independent sets of windings.

The aforementioned third method has been confirmed by previous DSWIM researchers (Alfredo et al, 1998) to yield accurate values of magnetic loading. However, the values obtained are for the two windings together. There is therefore a need to find a method that gives separate values of the magnetic loading for each winding set. In designing the loading of each winding set, saturation of the core shall be avoided. This can be achieved by ensuring

that the peak magnetic loading due to the combined effect of the two MMFs produced by the two winding sets is made the same as that of the equivalent single stator winding machine. In other words, the peak flux density in the air gap as well as the maximum flux density per pole must be constrained to be the same in both single stator winding and dual stator winding designs.

If the dual stator winding is assumed to be wound for a similar number of pole pairs, P then the flux density distribution in the air gap can be expressed as:

$$B_{gp|p(\theta)} = B_{11}[\cos(P\theta) - \varphi_1 \cos(P\theta + \delta_1)] \tag{3.9}$$

Where the magnitude of the flux density induced by the a-b-c winding set is equal to B_{11}, the ratio of the magnitudes of the flux densities induced by the two winding sets is φ_1 and the phase angle between the two flux densities, which may be a time varying quantity, is δ_1. The peak value of B_g will be obtained at a particular value of stator angle θ that will make $\cos(P\theta)$ to have a maximum value of unity assuming the delay angle δ_1 is zero (Juan, 2008). Thus equation (3.9) becomes:

$$B_{gP|P}(\theta) = B_{11}(1 - \varphi_1) \tag{3.10}$$

The flux distribution of the original P pole-pairs single stator winding machine is given by:

$$B_{gP}(\theta) = B_0 \cos(P\theta) \tag{3.11}$$

Where

B_0 : is the peak value of flux density of the single stator winding machine.

As mentioned earlier, in order to keep saturation of both designs at the same level, the peak flux density of the dual winding design must be the same as that of the single winding design. Hence,

$$B_0 = B_{11}(1 - \varphi_1) \tag{3.12}$$

With regards to DSWIM having similar pole ratio architecture, the quantity φ_1 is 0.5 and thus the ratio B_o/B_{11}will also be 0.5.

3.4 Computation of Total MMF in a Magnetic Circuit of Asynchronous Machine

The key purpose of magnetic circuit computation is to determine the total MMF required to establish the necessary magnetic flux within the magnetic circuit. For this purpose, the circuit is divided into a number of sections in series having the same cross-sectional area. The flux density is calculated in every section and magnetic intensity H is found from their respective B-H curves. The summation of the products of H and ℓ for all the sections gives the total MMF. Figure 3.2 shows a typical magnetic flux path (magnetic circuit) for a portion of an induction machine for illustrative purpose. As can be seen from this figure, the flux traverses two air gaps, two stator and two rotor teeth, a part of the stator and a part of the rotor cores considering a pair of poles.

Applying Ampere's law to this case yields:

$$2\mathcal{F}_p = 2\mathcal{F}_g + 2\mathcal{F}_{ts} + 2\mathcal{F}_{tr} + \mathcal{F}_{cs} + \mathcal{F}_{cr} \tag{3.14}$$

Where

Subscripts 'g', ts', 'tr', 'cs' and 'cr' denote air-gap, the stator tooth, the rotor tooth, the stator and rotor cores, respectively.

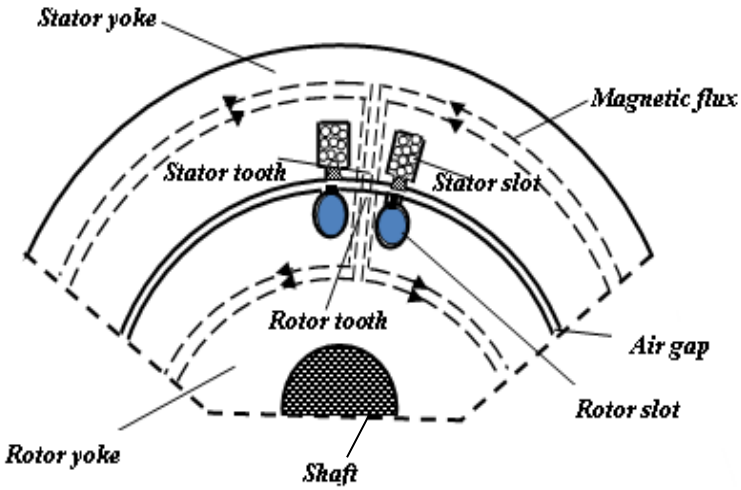


Figure 3.2: Magnetic Flux Path for a Section of a Poly-phase Induction machine

The next step in the magnetic circuit development involves the calculation of each component on the right-hand side of equation 3.14. These are treated analytically in the subsequent subsections based on realistic engineering assumptions made.

3.4.1 MMF estimation for air gap considering slots on the rotor and stator surfaces

The MMF required for air gap having an air gap length ℓ_g is given by the expression:

$$\mathcal{F}_g = \frac{B_{ag}}{\mu_0}\ell_g \tag{3.15}$$

Where

ℓ_g: is the air-gap length and

B_{ag} : is air-gap flux density.

Owing to the presence of slots on the stator and rotor surfaces of the induction machine, the iron surfaces around the air-gap are not smooth. This causes some fringing of flux around the teeth edges resulting in flux penetrating down the slot as shown in Figure 3.3. For the sake of clarity τ_s is the slot pitch defined as sum of slot width W_s and tooth width W_t.

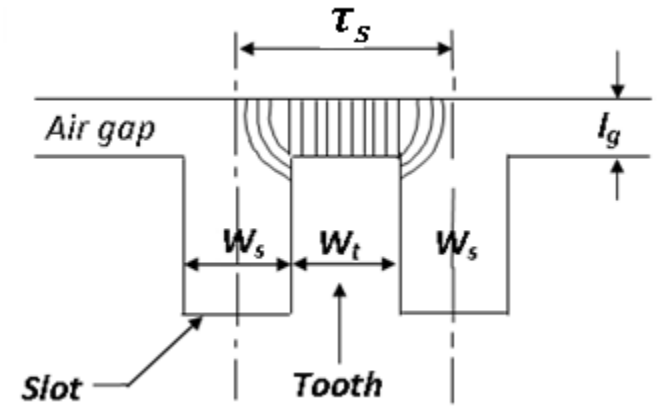


Figure 3.3: Actual Flux Distribution within Slot Pitch

The reluctance of the air-gap thus becomes higher from a magnetic viewpoint as compared to a case of smooth iron surfaces as shown in Figure 3.4.

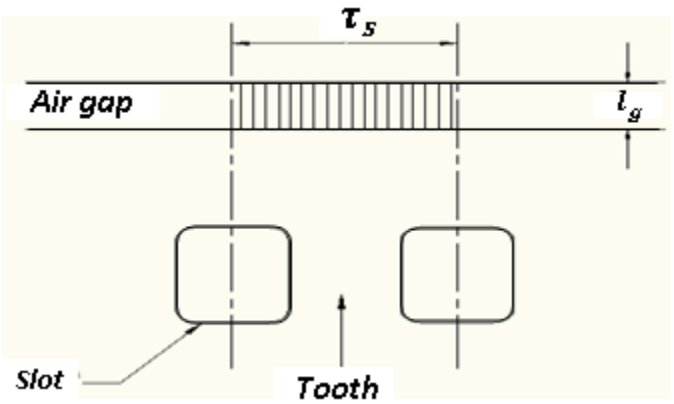


Figure 3.4: Air-gap Flux Distribution with Smooth Iron Surfaces

The reluctance of the air-gap over one slot pitch, τ_S with a smooth iron surface is:

$$\mathcal{S}_g = \frac{\ell_g}{\mu_0 A} = \frac{\ell_g}{\mu_0 L_s \tau_s} \tag{3.16}$$

On the other hand if the flux in a slotted armature is assumed to be confined within a tooth as shown in Figure 3.5, then the effective tooth width becomes:

$$y_s' = W_t = \tau_s - W_s \tag{3.17}$$

The reluctance in this case is then given as:

$$\mathcal{S}_g = \frac{\ell_g}{\mu_0 y_s' L_s} = \frac{\ell_g}{\mu_0 L_s (\tau_s - W_s)} \tag{3.18}$$

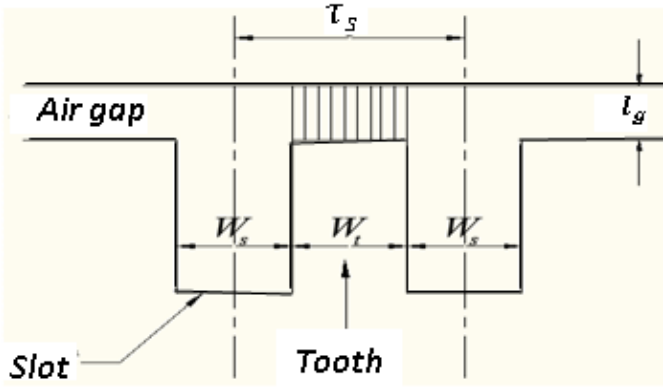


Figure 3.5: Air gap Flux Distribution Confined to a Tooth Width

The actual reluctance of the air gap however lies between these two extreme cases offered by equations 3.17 and 3.18. In order to calculate the reluctance in this case the air gap flux is assumed to be uniformly distributed over the whole slot pitch minus a fraction (δ) of slot width as illustrated in Figure 3.6.

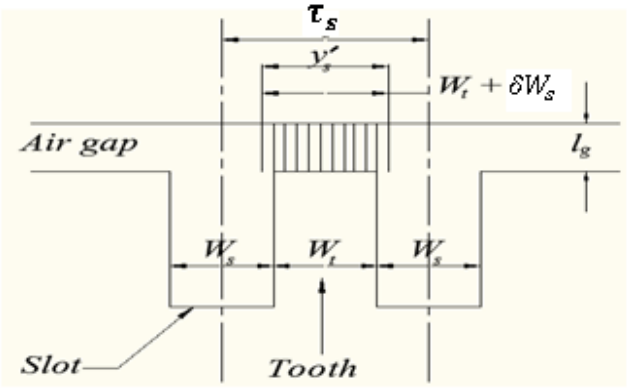


Figure 3.6: Air gap Flux Distribution with a Correction Factor

The fraction depends upon ratio of slot width to air gap length (Sawhney, 2011). The flux of one slot pitch is therefore distributed over a total pitch $W_t + \delta W_s$ as shown in Figure 3.6. The effective tooth width then becomes:

$$y_s' = W_t + \delta W_s = W_t + W_s + \delta W_s - W_s$$
$$= \tau_s - (1-\delta)W_s \quad = \tau_s - k_{cs}W_s \tag{3.19}$$

Where

$k_{cs} \triangleq 1 - \delta$: is the Carter's gap co-efficient, whose value is a function of the ratio of slot width to air-gap length.

The simplified Carter's coefficient, yet reasonably accurate, (Shariafian et al., 2009) applied in this dissertation is given in equation 3.20.

$$k_{cs} = 1 - \frac{2}{\pi}\left(tan^{-1}\chi - \frac{1}{\pi} log\sqrt{1+\chi^2}\right) \tag{3.20}$$

Where

$$\chi = \frac{W_s}{2l_g} \tag{3.21}$$

Therefore the reluctance of air-gap with slotted stator is given as:

$$\mathcal{S}_g = \frac{\ell_g}{\mu_0 y_s' L_s} = \frac{\ell_g}{\mu_0 L_s(\tau_s - k_{cs} W_s)} \tag{3.22}$$

The ratio of the reluctance of air-gap of slotted machine to that of smooth machine is therefore:

$$k_{gs} = \frac{\tau_s - W_s}{\tau_s - k_{cs} W_s} \tag{3.23}$$

Where k_{gs} : is referred to as gap contraction factor for slots on the stator.

The MMF of the air gap of the induction machine with a slotted armature can then be found as:

$$\mathcal{F}_g = k_{gs} \frac{B_{ag}}{\mu_0} \ell_g \tag{3.24}$$

If the rotor slot openings are also considered, another contraction factor can be introduced as $k_{gr} = (\tau_r - W_{r)}/(\tau_r - k_{cr} W_r)$ to account for their effects on the air-gap reluctance, where k_{cr} – the Carter's coefficient is computed based on the ratio of rotor slot width W_r and air-gap ℓ_g. Equation 3.24 is modified to account for the rotor slots on the flux density as follows:

$$\mathcal{F}_g = k_{gr} k_{gs} \frac{B_{ag}}{\mu_0} \ell_g \tag{3.25}$$

In the case of squirrel cage rotor with closed slot type, k_{cr} is unity and k_{gr} is also unity. In the computation of MMF for air-gap, the maximum value of sinusoidal flux density distribution is needed. Because the actual flux density distributions in ac machines have flattened sine wave, Lee, (1961) has been shown by that a value of 30^o from the maximum is a realistic choice for machine design purpose. Thus the amplitude of flux density at the point

of 30^o shift from its peak value B_{max} is $B_{ag} = (\sqrt{3}/2)B_{max}$; where B_{max} is a selected design parameter.

3.4.2 Derivation of MMF of stator tooth and rotor tooth

There are two major problems associated with the calculation of MMF necessary to maintain the required value of flux in the stator teeth. Each slot has two parallel sides, thereby making the teeth on either side to be tapered. As a result, the area of flux path along a tooth is not constant. This makes the value of flux density over a tooth length not to be constant.

The permeability of the iron around the teeth is very low because saturation occurs around that region. This makes an appreciable portion of the flux to go down the portion of the slots, thereby creating two parallel paths: one through air (slot) and the other through iron (tooth). The aforementioned difficulties can be overcome using the Simpson's rule. The rule is based on the assumption that the curve relating MMF per meter, H and flux density is a parabola. Based on this method, values of MMF per meter are obtained at three equidistant points; the two ends of the tooth and its centre. The mean value of MMF per meter is then given by;

$$H_{ts} = \frac{1}{6}\left(H_{ts1} + 4H_{ts2} + H_{ts3}\right) \tag{3.26}$$

Where $H_{ts1}, H_{ts2}, \& H_{ts2}$: are ampere turns per meter for the three sections shown in Figure 3.7.

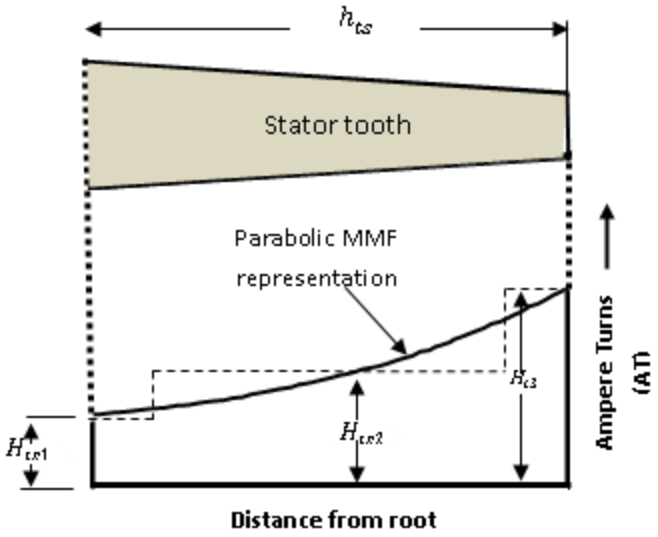


Figure 3.7: Application of Simpson's Rule to Approximate MMF of Stator Tooth (Sawhney,2011)

Finally, the MMF of the stator tooth is found as

$$\mathcal{F}_{ts} = H_{ts}h_{ts} \tag{3.27}$$

Where h_{ts} : is the height of the stator tooth.

A similar exercise for the rotor tooth under similar assumption yields the following:

$$\mathcal{F}_{tr} = H_{tr}h_{tr} \tag{3.28}$$

Where

$\mathcal{F}_{tr}$: MMF of the rotor tooth;

H_{tr} : Mean value of MMF/m determined using Simpson's rule; and

h_{tr} : is the height of the rotor tooth.

The computation of H_{tr} is as follows:

$$H_{tr} = \frac{1}{6}(H_{tr1} + 4H_{tr2} + H_{tr3}) \tag{3.29}$$

Where H_{tr1}, H_{tr1} & H_{tr1} : are the ampere turns per meter values for the three section approximations of parabolic representation of MMF of the rotor tooth.

3.4.3 Derivation of MMF of the stator core

The magnetic flux in the stator core is half of the air gap flux Φ neglecting flux leakages. This results in a stator core flux density given by

$$B_{sc} = \frac{\Phi}{2A_{cs}} \tag{3.30}$$

Where A_{cs}: is the cross sectional area of the stator core and is given by

$$A_{cs} = h_{cs} L_{cs} \tag{3.30}$$

Where

L_{CS} : is the stator core or stack length, and

h_{CS} : is the stator yoke thickness calculated from other dimensions as shown in Figure 3.8 to be follows :

$$\mathrm{h}_{\mathrm{cs}} = \frac{D_{os} - D_{is}}{2} - h_{ts} \tag{3.31}$$

Where

D_{os} & D_{is} : are the outer and inner diameters of the stator respectively

h_{ts} : is the height (depth) of the stator tooth shown in Figure 3.8.

At this point, B-H curve for the material of the stator core is utilized to obtain the MMF per meter H_{cs}. The MMF of the stator core is then computed using equation 3.32.

$$F_{cs} = H_{cs} L_{cs} \tag{3.32}$$

Referring to Figure 3.8, stator slot pitch τ_{ts} is defined as $\pi D_{is}/S_s$ where S_s is the number of stator slots and rotor slot pitch τ_{tr} is defined as $\pi D_{ir}/S_r$ where S_r is the number of stator slots.

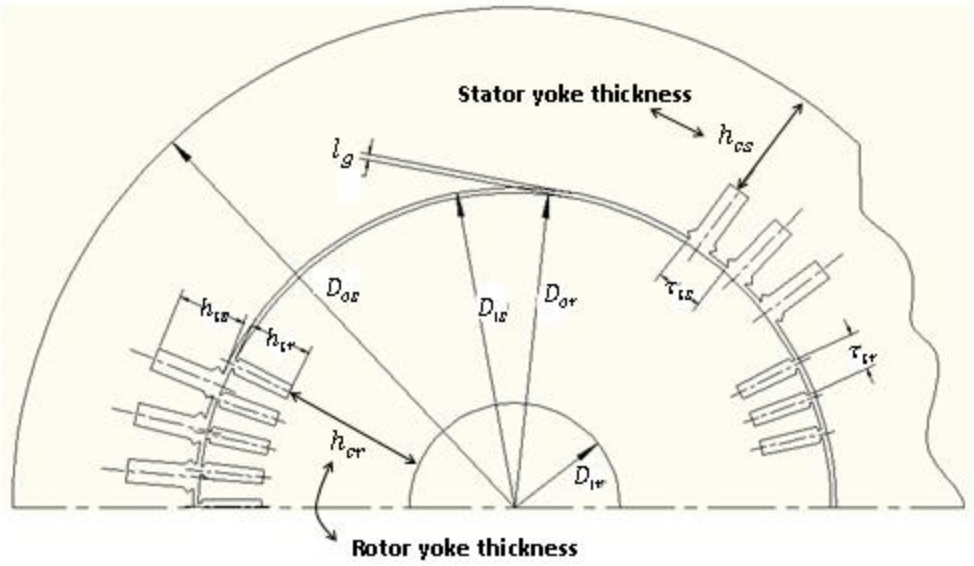


Figure 3.8: Half Cross Section View of Induction Machine's Core Showing Leading Dimensions

3.4.4 Derivation of MMF for rotor core

The flux in the rotor core is also half that in the air gap. This implies that the rotor core flux density is given as

$$B_{cr} = \frac{\Phi}{2A_{cr}} \tag{3.33}$$

Where A_{cr} : is the cross-sectional area of the rotor core and calculated using equation 3.34.

$$A_{cr} = h_{cr} L_{cr} \tag{3.34}$$

Where

L_{cr} : is the length of the rotor core;

h_{cr} : is the thickness of the rotor yoke derived in terms of other dimensions of Figure3.8 thus:

$$\mathrm{h_{cr}} = \frac{D_{or} - D_{ir}}{2} - h_{tr} \tag{3.35}$$

Where

D_{or} & D_{ir} : are the rotor core outer and inner diameters respectively;

h_{tr} : is the height of the rotor tooth as shown in Figure 3.8.

The value of B_{cr} determined via equation 3.33 is then used to find MMF/m of the rotor core with H_{cr} obtained from the appropriate B-H curve.

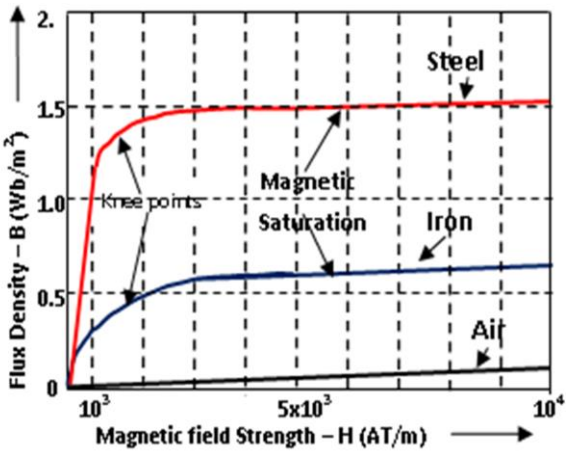
The MMF of the rotor core is then found as;

$$F_{cr} = H_{cr} L_{cr} \tag{3.36}$$

The total MMF drop around the magnetic circuit is obtained by summing up the individual MMF drops around the entire magnetic circuits two air-gaps, two stator teeth, two rotor teeth, stator yoke and rotor yoke. The required MMF per pole to produce the specific air-gap flux density is:

$$\mathcal{F}_p = k_{gr} k_{gs} \frac{B_{ag}}{\mu_0} \ell_g + H_{ts} h_{ts} + H_{tr} h_{tr} + \frac{1}{2}(H_{cr} L_{cr} + H_{cs} L_{cs}) \tag{3.37}$$

The computation of the total MMF $\mathcal{F}_p$ is crucial in the design of dual stator winding machine and would entail specifications of allowable flux densities in air-gap, stator & rotor cores, stator and rotor teeth as well as B-H curves for their respective ferromagnetic materials. Figure 3.9 shows typical family of B-H curves of well-known ferromagnetic materials and air that form essential parts in the magnetic circuit of an induction machine.



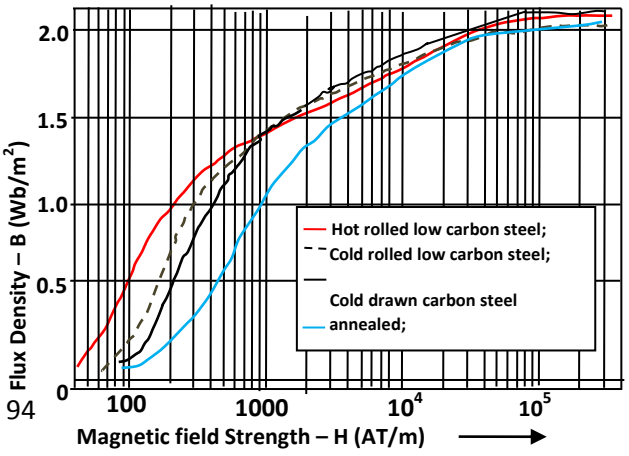


Figure 3.9: Typical B-H Curves for Different Metals (Adapted from Metals Handbook, 8th edition, 1996)

3.4.5 Determination of number of stator turns per phase

Having found the required magnitude of the flux densities and the necessary MMF for their (flux densities) establishment, the next step is to determine the number of series connected turns per phase to produce the required flux in the machine. This can be achieved by using the expression of the EMF, E generated in the armature windings. Thus:

$$E = 4fk_f k_w N_s \phi_m \tag{3.38}$$

Where

ϕ_m : is the magnetic flux per pole;

N_s : is the number of series connected turns per phase;

f: is the supply frequency and k_1 is the stator winding factor; and

k_w & k_f : are winding factor and form factor, respectively.

Such that $k_w = k_d x k_p$ where k_d & k_p: are distribution factor and pitch factor, respectively and form factor is typically 1.11 for unsaturated teeth but is in general dependent on teeth saturation factor ($1 + k_{st} = 1 + (\mathcal{F}_{ts} + \mathcal{F}_{tr})/\mathcal{F}_g$) (Boldea and Nasar, 2001 and Pyrhoren et al. 2008) as shown in Figure 3.10. Note $k_{st} \cong 0$ if $\mathcal{F}_g \gg (\mathcal{F}_{ts} + \mathcal{F}_{tr})$.

The flux per pole can be found from the following expression

$$\phi_m = \mathrm{B_{ag}}\left(\alpha \frac{\pi D_{is} L_s}{P}\right) = \mathrm{B'_{ag}}\left(\frac{\pi D_{is} L_s}{P}\right) \tag{3.39}$$

Where: $D_{is}, L_s,$ $\mathrm{B_{ag}}$ & P parameters are previously defined and α flux density shape factor depicted in Figure 3.10 as a function of teeth saturation factor; and $\mathrm{B'_{ag}} \triangleq \alpha \mathrm{B_{ag}}$.

In equation (3.38), the only unknown is N_s. It can therefore be evaluated as:

$$N_s = \frac{E}{4k_f k_w f \phi_m} \tag{3.40}$$

Now define the back EMF factor $k_e$as follows (Fu and Tang, 2002):

$$k_e = \frac{E}{V} \tag{3.41}$$

Where $(0.85 \leq k_e \leq 0.95)$ and V : is the machine supply voltage per phase.

Thus using equation 3.41 to eliminate E from equation 3.40 yields the following:

$$N_s = \frac{k_e V}{4 f k_f k_w \phi_m} \tag{3.42}$$

And eliminating ϕ_m using equation 3.39, we obtain

$$N_s = \frac{k_e V P}{4 \alpha k_f k_w f \pi D_{is} L_s B'_{ag}} \tag{3.43}$$

For two stator winding sets having the same number of poles housed in stator frame, stator turns per phase N_s is therefore the same for both winding sets.

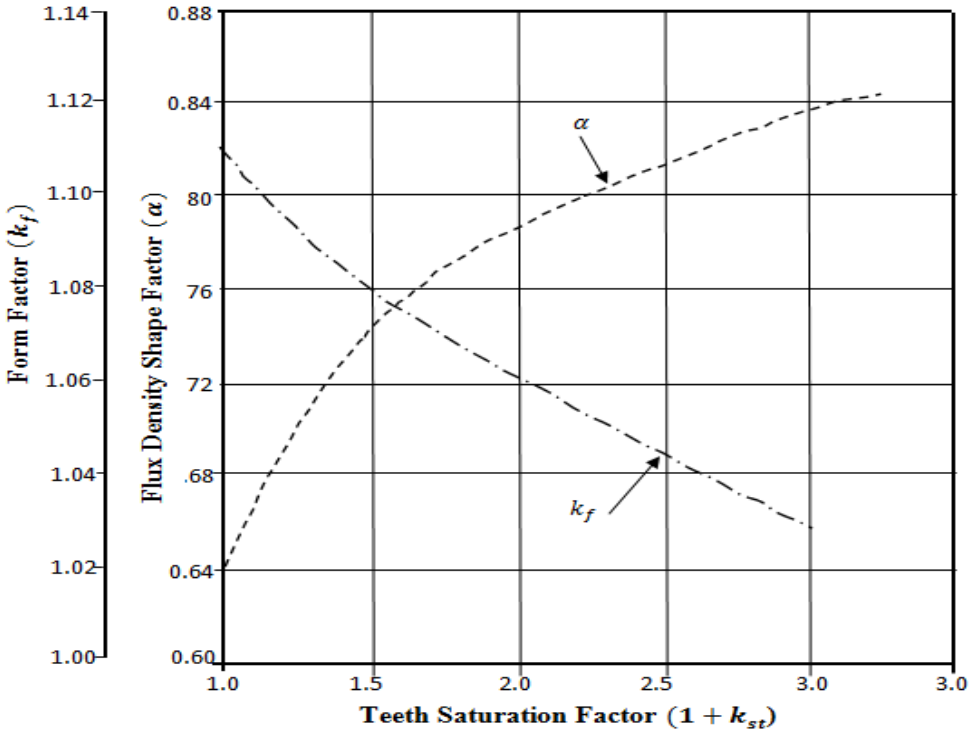


Figure 3.10: Composite Plots of Form Factor (k_f) and Flux Density Shape Factor (α) Versus Teeth Saturation Factor Source (Boldea and Nasar, 2001)

3.4.6 Computation of magnetising current and inductance per phase

The magnetising current flowing in the stator winding establishes the flow of flux in the core of the machine. The magnetizing current is calculated from the magnetic circuit of DSWIM presented in the preceding subsections. Relying on the total ampere turns of the magnetic circuits comprising stator yoke, stator teeth, air gap, rotor teeth and rotor yoke, the magnetizing current in m-phase machine can be calculated using equation 3.38 (Pyrhoren et al. 2008).

$$I_m = \frac{\pi P}{2m\sqrt{2}k_w N_s}\mathcal{F}_p \tag{3.45}$$

Pyrhoren et al. (2008) derived the magnetizing inductance for an m-phase machine as follows:

$$L_m = \frac{4mD_{is}L_s}{\pi P^2 l_{geff}}\mu_o(k_w N_s)^2 \tag{3.46}$$

Where l_{geff}: is effective air-gap axial length calculated using Carter's coefficients as follows:

$$l_{geff} = k_{cr}k_{cs}l_g \tag{3.47}$$

Equations 3.45 and 3.46 are used to calculate magnetizing current and inductance for DSWIM equipped with similar pole ratios. The foregoing magnetic circuit design approach adopted herein is not only computationally superior but simpler than the traditional technique widely used in ac machine design (Boldea and Nasar, 2001). The iron core loss is specially treated in

Appendix D from which the estimation of R_c is arrived at that included other stray losses.

3.4.7 Surface current density estimation

In the traditional design of electrical machines, in general, their desired power ratings are usually specified. The well-known generalized power equation referred to as Essen's rule in (Lipo, 2004) that relates power and other machine parameters is then applied to calculate the

main dimensions (stator inner diameter, D_{is} and effective length of the stator core, L_s of the machine. In DSWIM redesign case, however, the main dimensions as well as the power of each stator winding set are known. Thus generalized power equation (Essen's rule) deployed to determine the surface current density denoted as J_s in root mean square (rms) is specified by the following equation:

$$\mathrm{P_{out}} = \left(\frac{\sqrt{2}\pi^2}{120}\right) \mathrm{n_s k_f k_w \left(D_{is}^2 L_s\right) B'_{ag} J_s \eta \cos\phi} \tag{3.48}$$

Where,

The only unknown quantity is the surface current density J_s and is given by:

$$J_s = \frac{\mathrm{P_{out}}}{\left(\frac{\sqrt{2}\pi^2}{120}\right)\mathrm{n_s k_f k_w \left(D_{is}^2 L_s\right) B'_{ag} \eta \cos\phi}} \tag{3.49}$$

The surface current density essentially characterizes the ability of the cooling system to dissipate the heat generated in the stator winding given the temperature limit of the winding insulation. Expectedly, the surface current density in DSWIM should be the same or less than the one in the standard single stator winding induction machine. More explicitly, the current density of the 'a-b-c' winding denoted as J_s^{abc} and 'x-y-z' winding denoted as J_s^{xyz} can be expressed as:

$$J_s = J_s^{abc} + J_s^{xyz};\ J_s^{abc} = w_1 J_s;\ J_s^{xyz} = w_2 J_s \tag{3.50}$$

Where w_1 and w_2: are weighting factors such that $w_1 + w_2 = 1$; $w_1 = w_2 = 0.5$ for DWSIMs with similar pole ratios and $w_1 \neq w_2$ for DSWIMs with dissimilar pole ratios. It is implied therefore that the weighting factors are the same for the two winding sets of DSWIM equipped with similar pole ratio as a key design objective in this dissertation. The power output of a DSWIM (P_{DM}) can be written as follows:

$$P_{DM} = P_{abc_\phi} + P_{xyz_\phi} = \left(\frac{\sqrt{2}\pi^2}{120}\right) \mathrm{n_s k_f k_w \left(D_{is}^2 L_s\right) \eta \cos\phi}$$

$$\left(B_{ag}^{\prime abc} J_s^{abc} + B_{ag}^{\prime xyz} J_s^{xyz}\right) \quad (3.51)$$

For DSWIM of same pole ratio: $P_{abc_\phi} = P_{xyz_\phi} \Rightarrow B_{ag}^{\prime abc} J_s^{abc} = B_{ag}^{\prime xyz} J_s^{xyz}$; in equation 3.51.

3. 4.8 Calculation of stator conductor diameter

Recall that the number of series connected conductors per phase is given by equation 3.43. If the number of coils per phase is N_c then the number of turns per coil is;

$$N_T = \frac{N_s}{N_c} \quad (3.52)$$

Therefore the diameter of the stator conductor is determined from the relationship

$$d = 2\left(\sqrt{\frac{A_s x K_{fill}}{\pi x N_T}}\right) ; k_{fill} = N_T x \frac{a_c}{A_s} \quad (3.53)$$

Where A_s is the cross sectional area of the slot and K_{fill} is fill factor which takes into account that the slot is not entirely filled by the conductors. Here, we have assumed single layer winding for illustrative purpose.

3.4.9 Stator conductor current density calculation

The current density of the stator conductor is given by;

$$J_{con} = \frac{N_{sl} I_s}{a_s} \quad (3.54)$$

Where, N_{sl} is the number of conductors per slot, I_s is current through a conductor and a_s is the cross-section area of a conductor. We can now define specific electric loading $ac = 2mN_s I_s/\pi D_{is}$.

3.4.10 Stator winding categorization

A conductor, as far as armature winding is concerned refers to that part of an electrical wire that participates in electromechanical energy conversion. Two conductors placed in two different slots and connected in series are said to form a turn. A coil is made up of one more

turns connected in series in a later case is referred to as multi-turn coil. Part of a coil that does not take part in energy conversion is called an overhang.

The length of a coil that is inserted in slot is called a coil side. If the coil sides of a coil are spaced one pole–pitch apart they are said to be of full pitch. In most cases coil sides are spaced less than a pole pitch, in which case they are described as short-pitch or chorded. If in a particular type of an armature winding, a coil side occupies a whole slot depth, such a winding is called a single- layer winding. In most designs two coil sides occupy a slot, in which case the winding is described as double layer winding. For added clarity, Figure 3.11 depicts the various winding and stator slot topologies commonly used in induction machines

Normally chording is associated with a double layer winding. In any double layer winding, a coil side of a given coil occupies upper half of (top layer side) of a slot while the other coil side of the same coil occupies the lower half (bottom layer side) of another slot. The next two subsections describe further the general layout or architecture of an ac machine winding.

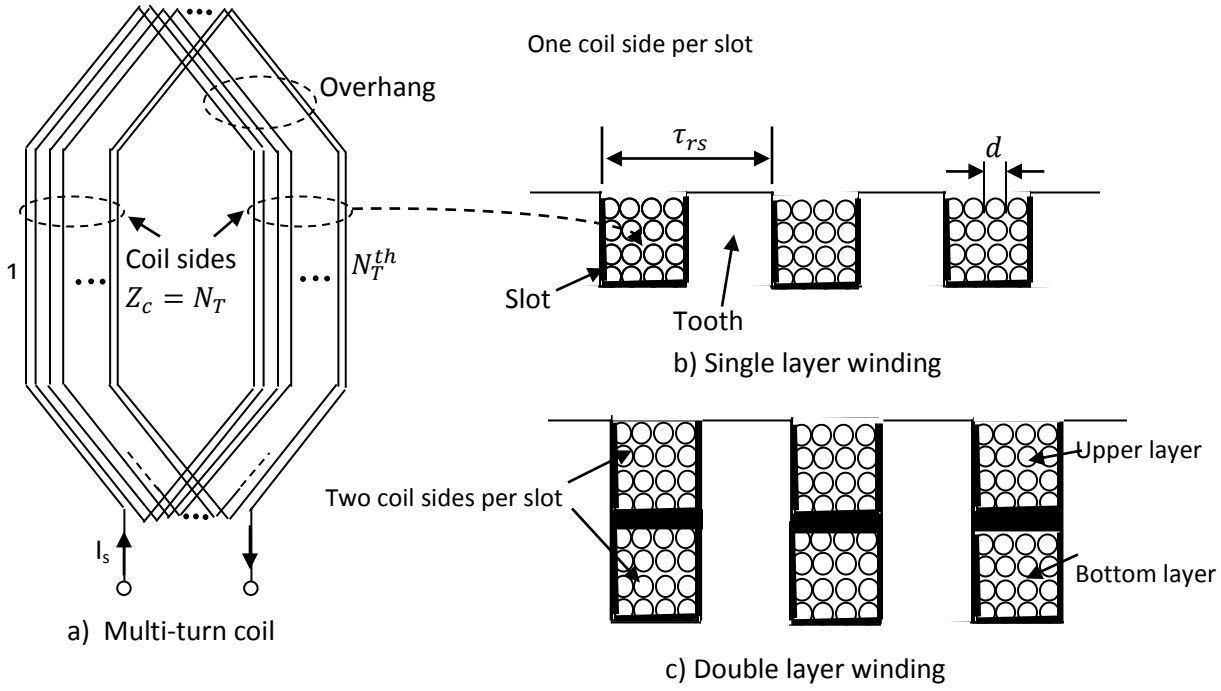


Figure 3.11: Typical Multi-turn Coil and Winding Layer Topologies

3.4.11 Outline of stator winding Architecture

In general, a poly-phase machine armature winding has "m" number of phases. These phases will be designed in such a manner that the e. m. f. s produced by each phase have:

i. Equal magnitude;

ii. Identical wave forms;

iii. Same frequency; and

iv. Angle of displacement in electrical radian displacement given by

$$\Upsilon_{\beta} = \frac{2\pi}{m} \tag{3.55}$$

These conditions can be satisfied if all the phases of a given winding have similar pole-phase groups. Furthermore, in order to ensure all phases of a stator winding are symmetrical, the spread of each phase under each pole, known as phase spread, must be met. The mathematical expression for the phase spread is given by

$$\sigma = \frac{\pi}{m} \tag{3.56}$$

In the case DSWIM stator winding design, the phase spreads for 'a-b-c' winding and 'x-y-z' winding are essential to realizing to its prototype winding diagram development. It is noteworthy that phase spreads for the two independent stator windings are equal due to similar number of poles design requirement. Note also that the different phase spreads were considered in the development of winding function analysis for DSWIM presented in Chapter Two.

3.4.12 Quantitative description of winding arrangement in slots

For a complete design of an armature winding the following data need to be specified:

i. Total number of armature slots, S_s; and

ii. Total number of poles for which the armature is to be designed, P.

A single layer winding would require coils equal to half the total number of slots. While a double layer winding requires as many coils as there are number of slots. A number of coils belonging to a phase under a pair of poles is known as a coil group.

The manner in which coil group belonging to a phase are interconnected to form a phase depends on the requirements imposed on the winding. For example when windings are required for large currents and low e.m.f.s, the entire groups of a phase will not be connected in series; but rather they will be split up into a number of sections called parallel paths or circuits each containing the same number of similar coil groups which are then paralleled to form a phase winding.

3.4.13 Winding dimension calculation

Usually a coil side lies under a north pole and the other side under a south pole. The distance between a north and a south pole called pole pitch is given by:

$$\tau_p = \frac{\pi D_{is}}{P} \tag{3.57}$$

The distance between two coil sides of a given coil is called a coil span or a coil width denoted by y_c. This distance in a single layer winding is also the same as pole pitch. In a double layer winding in which chording is employed, the coil span is usually less than the pole pitch. Thus;

$$y_c \leq \tau_p \tag{3.58}$$

The width of a coil is normally measured in terms of the number of slots. The number of slots per pole per phase which fixes the coil group is given by

$$q = \frac{S_s}{Pm} \tag{3.59}$$

If q is an integer, then the winding is referred to as an integral-slot winding otherwise it is called fractional slot winding. Both integral-slot winding and fractional slot winding are admissible in the DSWIM winding design procedure depending on its power rating. The phase belt can be shown to be $\sigma = q * \gamma$; where the stator slot pitch angle γ is given by $\pi/(\ S_s/P)$.

3.5 Analytical Calculations of DSWIM Steady State Equivalent Circuit Parameters

The parameters of the equivalent circuit of the induction machine play a critical role in the evaluation of the machine performance. The performance indices commonly determined are:

- Machine maximum torque (pull–out–torque);
- Machine starting torque;
- Efficiency; and
- Operating power factor.

Undoubtedly, if the parameters of an induction machine are not known then the performance of the machine cannot simply be assessed analytically via simulation approach. It is therefore imperative to determine these parameters. The parameters of interest specifically for DSWIM equipped with dissimilar pole ratios are as follows:

i. The stator winding resistances of 'a-b-c' and 'x-y-z' denoted as R_s^a & R_s^x , respectively and referred rotor resistance R_r';

ii. The stator winding leakage reactances of 'a-b-c' and 'x-y-z' denoted as X_{ls}^a & X_{ls}^x , respectively and referred rotor leakage reactance X_{lr}';

iii. The core loss resistance R_c and magnetizing reactance X_m.

The generalized steady state equivalent circuit developed for a DSWIM is shown in Figure 3.12. The next task is on analytical procedures to enable calculations of the relevant parameters based on the physical dimensions of the stator frame, stator slots, stator windings, rotor slot structure, etc. In the subsequent subsections, the various analytical procedures employed are set forth.

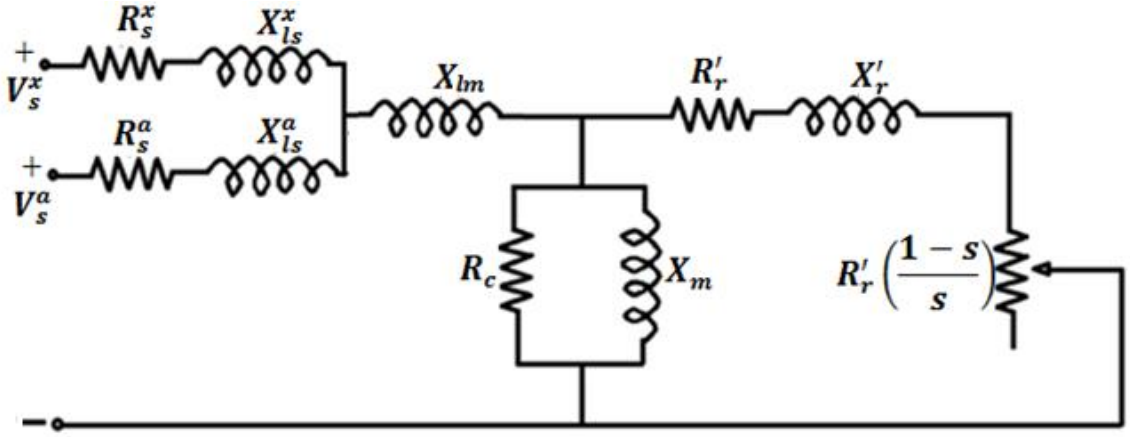


Figure 3.12: Generalized Steady State Equivalent Circuit of DSWIM

3.5.1 Stator resistance calculation

In view of the alternating current flowing in the windings of the stator associated with skin effect, albeit small at power frequency, a straight forward formula used in dc resistance calculation cannot be used without modification. However, if some modifications are made right from the manufacturing stages of the winding, the skin and eddy current effects are drastically reduced. Here two practical techniques are employed. Firstly, the conductors forming the winding are divided into sub units called strands each of which is electrically insulated. Secondly, strands are interwoven in such a way that each strand occupies all possible positions along the entire length of the conductor to reduce the effects of eddy current. This is illustrated schematically in Figure 3.13 for a conductor comprising three

strands only. In general, if a multi-strand conductor has N sub-conductors and overall length of L_T, it will require N-1 transpositions over L_T/N span lengths for each strand to occupy all possible positions.

With adequate strands and transpositions, we can neglect skin and eddy current effects in the calculation of stator winding resistance per phase. Starting from an idealized geometry of stator winding coil shown in Figure 3.14 with appropriate dimensions indicated, the procedure for calculating the stator resistance per phase is outlined in sequel (Wu, 1998).

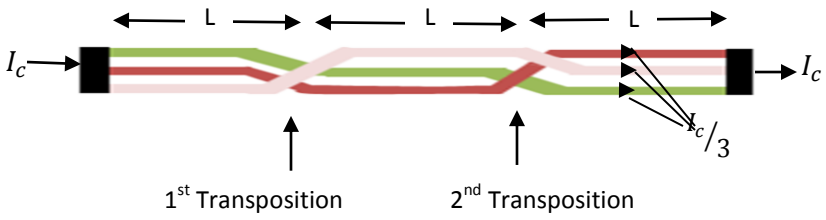


Figure 3.13: Basic Illustration of Interwoven Stator conductor

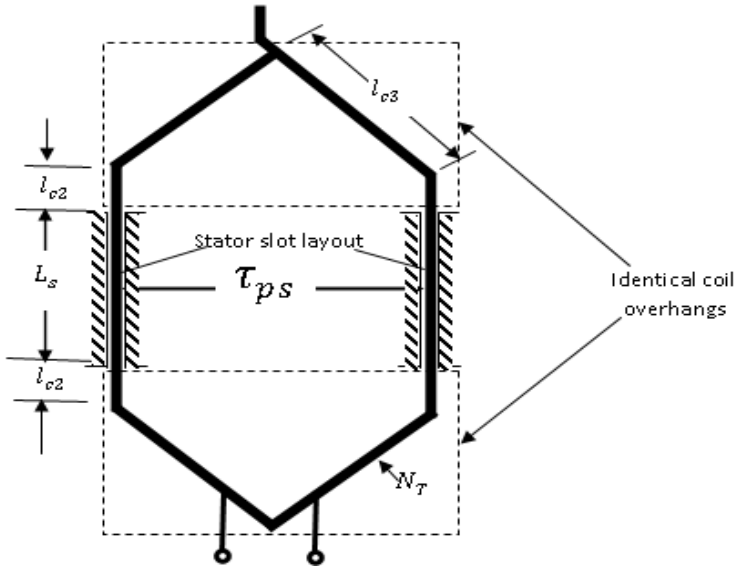


Figure 3.14: Idealized Geometrical View of Stator Winding Coil

The average length of a coil is found as:

$$l_{ave} = 2L_s + 4l_{c2} + 4l_{c3} \tag{3.60}$$

Where

L_s : is the effective stack length of the stator conductor;

l_{c2}& l_{c3} : are two lengths that represent the dimension of each overhang or end winding.

Recall the number of turns per phase is denoted as N_s. For the sake of generality, it is assumed that DSWIM comprised M_C parallel circuits per stator winding phase. For this general case and relying on appropriately dimensioned coil overhang structure, it is derived in Appendix B that net stator resistance per phase R_s is given in equation 3.61.

$$R_s = \frac{1}{M_c}\left(\rho_O \frac{N_c l_{ave}}{a_s}\right) k_R k_T \tag{3.61}$$

Where

ρ_O: Resistivity of copper conductor at 25^{o}C;

k_R : Ratio between ac and dc values, denoted as $R_{s,ac}$ & $R_{s,dc}$ respectively, of the stator phase winding resistance due to skin effect;

k_T : Temperature correction factor for stator winding resistance at other specified temperature, T_2 and is equal to $((1/\alpha_0) - T_2)/((1/\alpha_0) - T_1)$; α_0 is conductor temperature coefficient at specified benchmark temperature T_1.

Ostovic, (1994) has shown that for conductors in a stator slot without transposition the skin effect can be accounted as follows:

$$k_R = \frac{R_{s,ac}}{R_{s,dc}} = \varphi \frac{sinh2\varphi + sin2\varphi}{cosh2\varphi - cos2\varphi} \tag{3.62}$$

Where $\varphi \triangleq h/\delta$: h is slot height housing conductors and δ is skin depth defined as $\sqrt{2\rho/2\pi f\mu}$; ρ, f and μ : Conductor resistivity, frequency and conductor permeability, respectively. For the sake of correct usage, equation 3.62 is only admissible in the case of large capacity ac machines having φ greater than 1.4 (Ostovic, 1994). However for small to medium rated capacity ac machines generally of research interest$-$ $k_R \approx 1$.

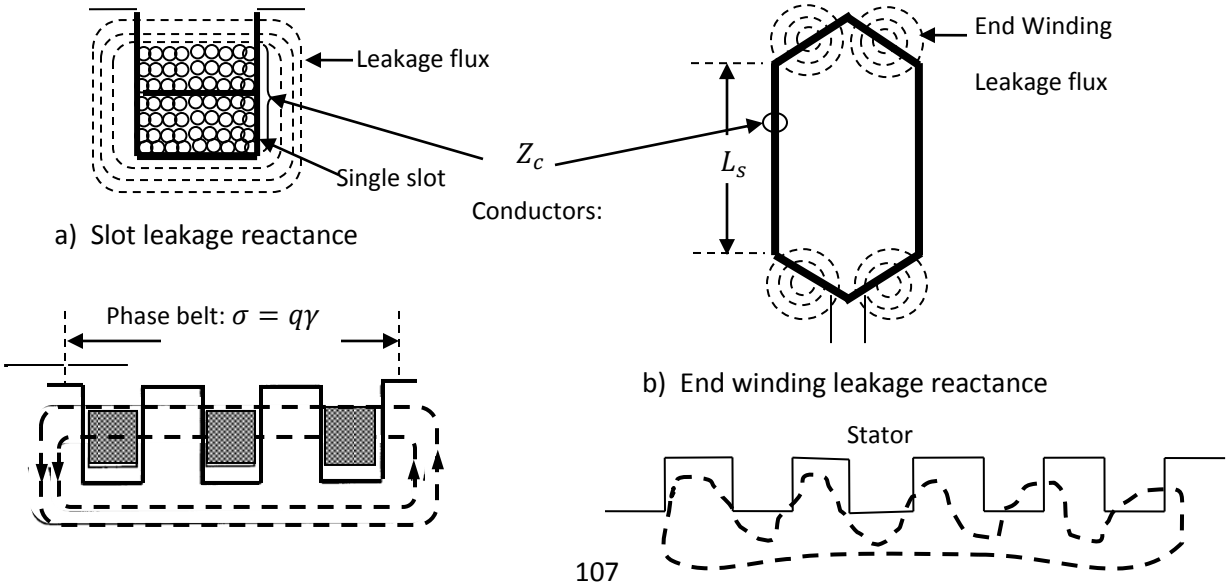
3.5.2 Stator leakage Inductance (Reactance)

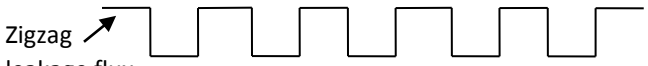
In this subsection, we present fairly detailed determination of stator leakage inductance for induction machines which is equally applicable to DSWIM. Basically, leakage inductance (reactance) represents leakage flux from circuit analysis standpoint. Electrical machines are energy conversion devices which take place due to magnetic fluxes set up by currents flowing in both their stator and rotor windings. Ideally, all fluxes produced by the currents in the two windings are expected to link both windings. In practical machines, this is not so. The flux usually has two components:

a) A portion (usually very large) that links both windings and which is responsible for energy conversion is called useful flux;
b) The remaining flux (usually very small) links with only one winding and therefore does not participate in the energy conversion process referred to as leakage flux.

If a flux links with only stator winding then that flux is termed stator leakage flux and to it, is associated stator leakage inductance L_{ls} or stator leakage reactance $X_{ls} = \omega L_{ls}$.

In an induction machine, the stator leakage flux has four components: slot leakage flux; end winding leakage flux; belt leakage flux, zig-zag leakage flux and skew leakage flux. Figure 3.15 illustrate diagrammatically various flux leakages of an induction machine. It is imperative to determine the inductances (reactances) associated with the four aforementioned leakage fluxes as presented in the subsequent subsections.





c) Belt leakage reactance

d) Zigzag leakage reactance

Figure 3.15: Induction Machine Leakage Fluxes

3.5.2.1 Slot leakage inductance

Consider an induction machine having either a single layer or double layer winding. This implies correspondingly that there is either one coil side per slot or two coil sides per slot. As derived in Appendix A, leakage inductance per slot is given by

$$L_{slot} = \begin{cases} n_s^2 L_s P_{s1} : \text{single layer} \\ \quad or \\ n_s^2 L_s P_{s2} : \text{double layer} \end{cases} \tag{3.63}$$

Where P_{s1}& P_{s2} : are the specific slot permeances for the single and double layer winding, respectively composed of a number of components given in equation 3.64.

$$P_s = \begin{cases} \mathrm{P_{s1}} = \mathrm{P_0^{(1)}} + \mathrm{P_1^{(1)}} + \mathrm{P_2^{(1)}} + \mathrm{P_3^{(1)}} : \text{ single layer} \\ \quad \text{or} \\ \mathrm{P_{s2}} = \mathrm{P_0^{(2)}} + \mathrm{P_1^{(2)}} + \mathrm{P_2^{(2)}} + \mathrm{P_3^{(2)}} + \mathrm{P_4^{(2)}} : \text{double layer} \end{cases} \tag{3.64}$$

Where the specific permeance components derived in Appendix A for single layer and double layer slot configurations shown respectively in Figure 3.16 are summarized in equation 3.65:

$$\mathrm{P_0^{(1)}} = \mu_0 \frac{\mathrm{d_3}}{3\mathrm{b_s}};\ \mathrm{P_1^{(1)}} = \mu_0 \frac{\mathrm{d_2}}{\mathrm{b_s}};\ \mathrm{P_2^{(1)}} = \mu_0 \frac{2\mathrm{d_1}}{\mathrm{b_s}+\mathrm{b_0}};\ \mathrm{P_3^{(1)}} = \mu_0 \frac{\mathrm{d_0}}{\mathrm{b_0}}$$

$$\mathrm{P_0^{(2)}} = \mu_0 \frac{2\mathrm{d_4}}{3\mathrm{b_s}};\ \mathrm{P_1^{(2)}} = \mu_0 \frac{\mathrm{d_3}}{4\mathrm{b_s}};\ \mathrm{P_2^{(2)}} = \mu_0 \frac{\mathrm{d_2}}{\mathrm{b_s}};\ \mathrm{P_3^{(2)}} = \mu_0 \frac{2\mathrm{d_1}}{\mathrm{b_s}+\mathrm{b_0}};\ \mathrm{P_3^{(2)}} = \mu_0 \frac{\mathrm{d_0}}{\mathrm{b_0}}$$

(3.65)

After giving due consideration to the number of turns per phase (N_s) and total stator slots $(S_s = qmP)$, the derived stator leakage inductance per phase for single layer or double layer winding stator is as follows:

$$L_{lsl} = \begin{cases} 12\frac{N_s}{S_s}L_s P_{s1}: \text{single layer} \\ \text{or} \\ 12\frac{N_s}{S_s}L_s P_{s2}: \text{Double layer} \end{cases} \quad (3.66)$$

The leakage slot inductance per phase is then found when the values of N_s, L_s, $P_{s1} or\ P_{s2}$ and S_s are substituted in equation 3.66 depending on whether it is single or double layer winding.

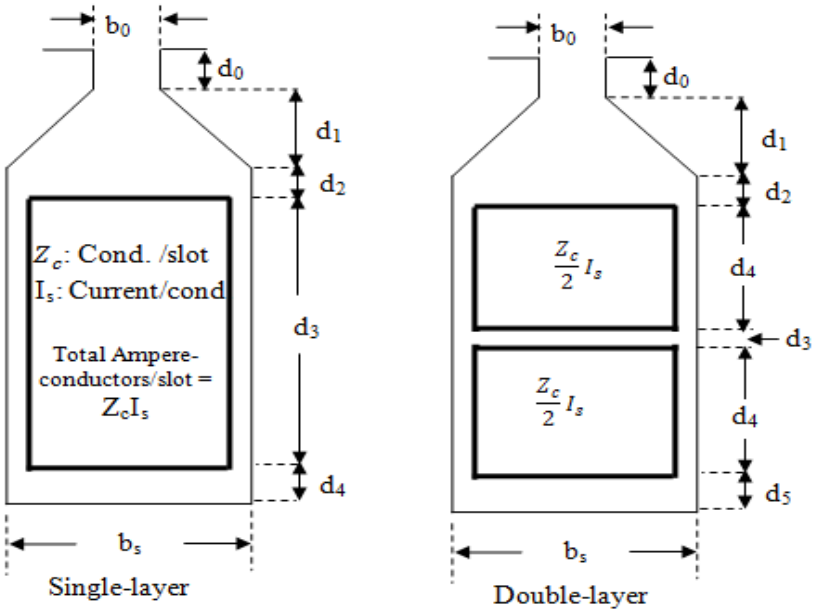


Figure 3.1 6 Physical Slot Dimensions Used in Single and Double layer Permeance Calculations

3.5.2.2 End winding leakage inductance

In electrical machines not all parts of a conductor carrying current participate in energy conversion. The only portion or length of the conductor that takes part in the energy conversion is referred to as effective length L_s the remaining parts of the conductor is called end-winding or overhang. This portion of a conductor or winding is associated with an inductance termed end-winding leakage inductance. Relying on the approach of (Liwschitz-Garik, 1961) for the calculation of this inductance, based partly on theoretical derivation and partly on experimental results, the total end winding leakage per phase is expressed thus:

$$L_{ewl}^{(s)} = 4\frac{(k_d k_p N_s)^2}{P}(2.4\mu_0)\left(l_{c2} + \frac{l_{c1}}{2}\right) \quad (3.67)$$

Where: the lengths l_{c1} and l_{c2} are shown in Figure B1. It is noteworthy that several empirical formulae are available in (Boldea and Nasar, 2001) for end winding leakage inductance calculation; as well as the attempt by (Alger, 1970) to model this inductance rigorously but without significant improvements over that given by equation 3.67.

3.5.2.3 Belt leakage inductance

This type of leakage arises as a result of the discrete number of stator coils. The belt leakage inductance is usually ignored for induction machine equipped with squirrel cage rotor because it is shorted. However, it is considered in wound rotor structure due to spatial distribution differences in the mmfs of the stator and rotor windings thereby causing harmonic leakage fluxes. The belt leakage inductance can be calculated as follows:

$$\mathrm{L_{bsl}} = \begin{cases} 0 & \text{Stator /Squirrel cage rotor structure} \\ & \text{or} \\ \sigma_{\mathrm{bts}}\mathrm{L_m} & \text{Stator/ Wound rotor structure} \end{cases} \tag{3.67}$$

Where: L_m is magnetising inductance given in equation 3.46 and σ_{bts} is ratio that captures all the space harmonics of significant values relative to fundamental harmonic and is given by (Boldea and Nasar, 2001): $\sigma_{bts} = \sum_{v\neq 1}[(k_{wsv}^2/k_{ws1}^2)\,(k_s/k_{sv})]$; k_{wsv} & k_{ws1}: are stator winding factors for v^{th} harmonic and 1st harmonic, respectively and k_s & k_s: are saturation factors for fundamental and v^{th}, respectively. Note that belt leakage inductance is an integral component of the differential leakage inductance, the other component being the zig-zag leakage inductance discussed in what follows.

3.5.2.4 Zig-zag leakage inductance

The stator winding consists of coils placed in slots. The shape of the flux wave in the air gap will therefore not be sinusoidal. This effect produces mmf of higher harmonics which gives rise to leakage inductance referred to as zig-zag leakage inductance. Using modified

expression in (Zhu, 1997), the zig-zag leakage inductance is calculated in this work as follows

$$L_{zzl}^{(s)} = \frac{12N_s^2}{S_s} L_s P_{zzs} \tag{3.68}$$

Where, P_{zzs} is specific permeance associated with zig-zag leakage inductance and defined as follows:

$$P_{zzs} = \frac{\mu_o w_s w_r (w_s^2 + w_r^2)}{6 l_g \tau_{sp}^3} \tag{3.69}$$

w_s & w_r: are the stator and rotor teeth width respectively; l_g is the length of air gap and τ_{sp} is the stator pole pitch. For the sake of analytical simplicity, it is assumed in this work that $w_s = \tau_{ts}/2$ & $w_r = \tau_{tr}/2$.

3.5.2.5 Skew leakage inductance

Recall that skewing of rotor slots in machine design is aimed at reducing $m.m.f.$ harmonics. However, the skewing rotor slot has associated leakage flux and its calculation is based on the assumption that the rotor slots are skewed half stator angular pitch (Zhu, 1998). The skew leakage inductance is given by:

$$L_{skl}^{(s)} = L_m \left\{1 - \left[\frac{\sin(\theta_{ts}/2)}{\theta_{ts}/2}\right]^2\right\} \tag{3.70}$$

Where θ_{ts}: is the angular stator slot pitch in radian and is equal to $2\pi/S_s$.

3.5.2.6 Total stator leakage inductance

The total stator leakage inductance per phase L_{ls}calculated via analytical approach is sum of all the leakage inductances outlined in subsections 3.5.2.1-3.5.2.5. Equation 3.71 offers essentially the summation of such leakage inductance components.

$$L_{ls} = L_{lsl} + L_{ewl}^{(s)} + L_{bsl} + L_{zls} + L_{skl} \tag{3.71}$$

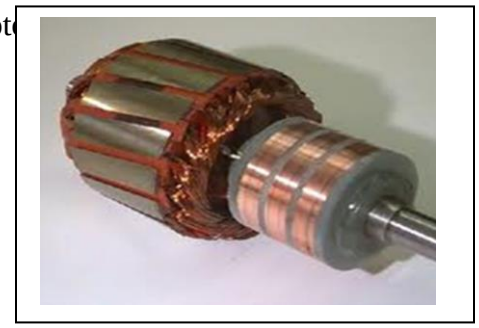
The equivalent stator leakage reactance X_{ls} is given by

$$X_{ls} = 2\pi f L_{ls} \tag{3.72}$$

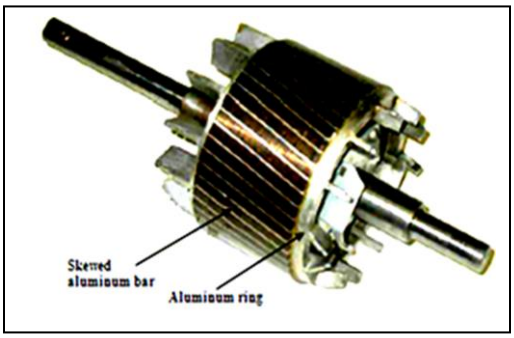
In the DSWIM design of interest, the leakage reactances for a-b-c and x-y-z winding configurations are to be calculated in accordance with equation 3.72. Later in this Chapter, sample calculation of this parameter for similar pole ratio dual stator windings housed in stator and rotor cage structure will be presented.

3.5.3 Determination of rotor parameters

`Structurally, the rotor of induction machines are of two types: the wound rotor and the squirrel cage rotor as shown in Plate 3.1. The difference is basically due to the architectural design of its respective rotor windings. In wound rotor machines, the winding is designed in the same way as the stator winding and thus the parameter determination in such winding will be similar to that explained in subsection 3.5.2. For the sake of completeness, Table 3.2 provides the principal equations for the calculations of parameters with respect to wound rot



Wound rotor type



Squirrel cage rotor

Plate 3.1: Induction Machine Rotor Structures

Table 3.2: Wound Rotor Principal Equations for Calculating Leading Leakage Inductances

Parameter Definitions	Symbols	Principal Equations
Slot leakage inductance	L_{lrl}	$\begin{cases} 12\frac{N_r}{S_r}L_rP_{r1}: \text{single layer} \\ 12\frac{N_r}{S_r}L_rP_{r2}: \text{Double layer} \end{cases}$ Where: N_r, S_r, L_r and $P_{r1,2}$ are rotor parameters corresponding to defined parameters for stator slots.

End winding leakage inductance	$L_{ewl}^{(r)}$	$4\frac{\left(k_{dr}k_{pr}N_r\right)^2}{P}(2.4\mu_0)\left(l_{r2}+\frac{l_{r1}}{2}\right)$
Belt leakage inductance	L_{brl}	$\sigma_{\mathrm{btr}}\mathrm{L_m}$; $where\ \sigma_{btr}=\sum_{v\neq1}[(k_{wrv}^2/k_{wr1}^2)\,(k_r/k_{rv})]$
Zig-zag leakage inductance	$L_{zzl}^{(r)}$	$\frac{12N_r^2}{S_r}L_rP_{zzr}$; where $P_{zzr}=\frac{\mu_o w_s w_r\,(w_s^2+w_r^2)}{6l_g\tau_{rp}^3}$
Skew leakage inductance	$L_{skl}^{(r)}$	$L_m\left\{1-\left[\frac{\sin(\theta_{tr}/2)}{\theta_{tr}/2}\right]^2\right\}$ where
Total rotor leakage inductance	L_{lr}	$L_{\,lrl}+L_{ewl}^{(r)}+L_{brl}+L_{zs}L_{zzl}^{(r)}+L_{skl}^{(r)}$

However, the squirrel cage induction machine has its rotor made up of conducting bars which run axially in the skewed rotor slots. The bars are effectively shorted at both ends by another conducting material called end rings. The portion of the end ring between two bars is termed end ring segment. The detailed calculations of the rotor parameters can be found in Appendix C. Anchored on the fundamental rotor cage slot configuration of Figure 3.17, the basic analytical equations for calculating equivalent rotor resistance and leakage inductance are highlighted in Table 3.3. Some of the basic equations used were those derived by Wu, (1997).

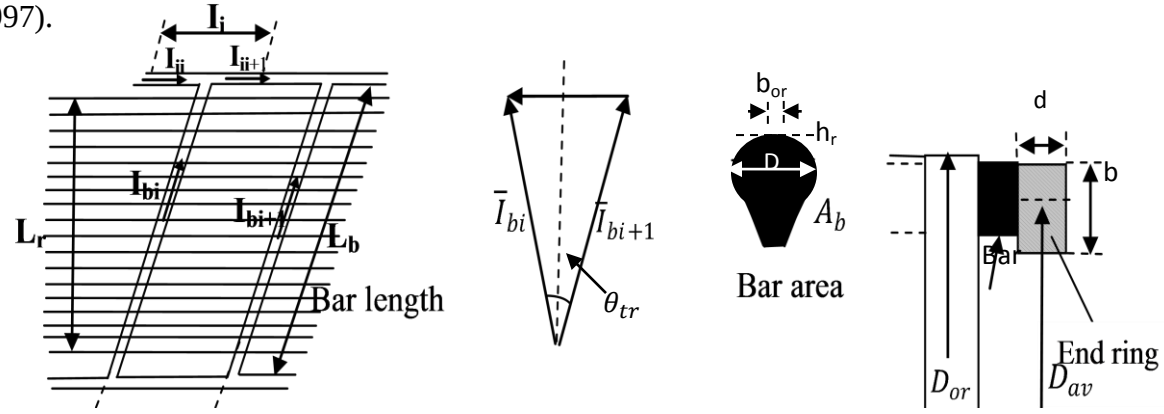


Figure 3.17: Basic Geometric Dimension of the Squirrel Cage Rotor: Adapted from (Boldea and Naser, 2004)

Table 3.3: Equations for Calculating Squirrel Cage Rotor Parameters Referred to Stator

Parameter Definitions	Symbols	Principal Equations
Rotor bar resistance	r_b	$r_b = \rho L_b/A_b$: Where $A_b \triangleq b_{0r}h_r + \pi D_{rs}^2/4$ & $L_b = (L_r + 2l_{be})/cos\theta_{tr}$
End ring resistance per average rotor slot pitch	r_e	$r_e = \frac{\rho\tau_{tr}}{A_r}$: Where $A_r \triangleq bd$ for rectangular cross-section of end ring
Rotor slot specific permeance	P_{slr}	$P_{slr} = \mu_0\big((\pi/6) + (5/16\pi)\big)$
Rotor bar leakage inductance	L_{br}	$L_{br} = N_r^2 L_b' P_{slr}$: Where $L_b' = L_r/cos\theta_{tr}$
Rotor pole pitch	$\tau_{pr,ave}$	$\tau_{pr,ave} = \pi(D_{or} - 2h - D_{rs})/P$
End ring leakage inductance per segment	L_{er}	$L_{er} = 4\mu_0\big(l_{be} + k_r\tau_{pr,ave}\big)/9$; Where k_r is rotor winding factor

It is shown in Appendix C that the effective rotor resistance and rotor leakage inductance are given in equations 3.72 and 3.73, respectively:

$$r_{be} = r_b + \frac{r_e}{2sin^2\left(\frac{\pi P}{2S_r}\right)} \tag{3.72}$$

$$L_{be} = L_{br} + \frac{L_{er}}{2sin^2\left(\frac{\pi p}{2S_r}\right)} \tag{3.73}$$

Where, all the dependent variables are previously defined or defined in Table 3.3.

3.5.3.1 Rotor parameters referred to stator side

In the development of induction machine steady state analysis, there is need to refer rotor leakage reactance and resistance into stator circuit. The rotor equivalent circuit presented in

Appendix C is mesh circuit in which each rotor bar and end ring segment form branches. Thus, the resistance and inductance per rotor mesh are expressed in equations 3.74 and 3.75.

$$r_r = 2r_{be} \tag{3.74}$$

$$L_r = 2L_{be} \tag{3.75}$$

The equivalent rotor resistance and inductance referred to stator are given in equations 3.76 and 3.77, respectively on based on equal losses and energy storage criteria.

$$r_r' = \left(\frac{4m}{S_r}\right)\left(\frac{k_{w1}N_s}{k_{wr}}\right)^2 r_r \tag{3.76}$$

$$L_r' = \left(\frac{4m}{S_r}\right)\left(\frac{k_{w1}N_s}{k_{wr}}\right)^2 L_r \tag{3.77}$$

The goal, of course, is to extend the generalized induction design procedure to calculate DSWIM leading parameters. In the next section, DSWIM design concept is addressed by applying the analytical design framework to determine dual winding specifications that meet magnetic and electric loading constraints imposed by the choice of stator frame and rotor structure.

3.6 DSWIM Design Framework

In this section, theoretical framework of the preceding section has been applied to develop an algorithmic functional DSWIM design methodology. It is worthy of reiterating again that the DSWIM of interest is equipped with dual stator windings having similar pole number. Its schematic representation is shown in Fig. 3.18 where n is the pole number to be specified. The design task is aimed at specifying the magnetic and electric parameters for dual three phase stator windings to be housed in standard stator frame and rotor structure of known specifications. It is intuitively clear that having selected the most suitable stator frame and rotor type as central to actualizing DSWIM design objective; its leading parameters earlier

presented in Table 3.1 can then be readily determined. In the next subsection, the salient steps of algorithmic functional DSWIM design procedure are presented.

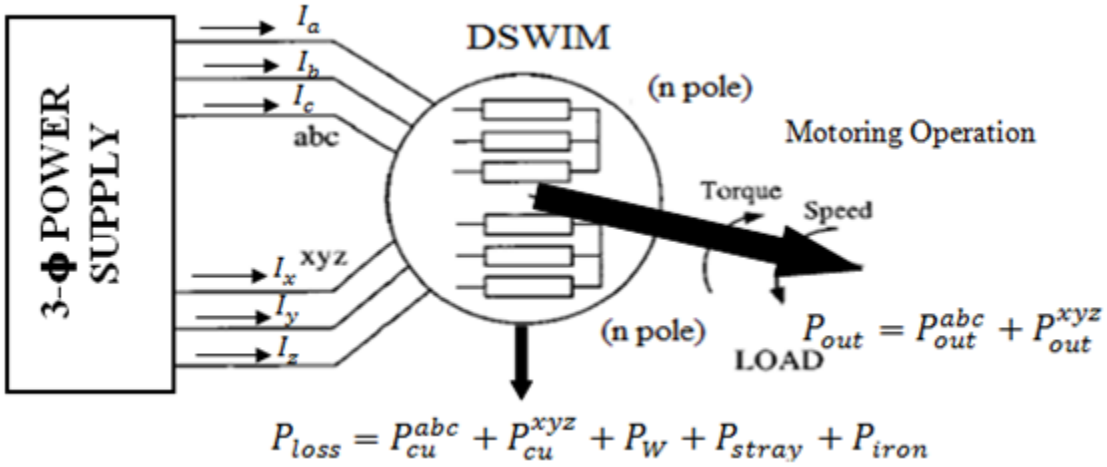


Figure 3.18: Schematic Representation DSWIM Equipped with n/n Similar Pole Ratios

3.6.1 Functional description of DSWIM design procedure

Attention is focused on the development and implementation of pragmatic induction machine redesign philosophy to facilitate conversion of conventional induction machine into dual stator winding induction machine of identical or similar pole ratio. The overall research goal is to achieve improved dual stator winding induction machine performance from standpoints of energy loss minimisation via optimum participation of the double stator windings whilst satisfying the desired magnetic and electric loadings. The analytical equations developed in the preceding sections are pertinent to the DSWIM design strategy. In this regard, the salient steps for DSWIM design algorithmic flowchart development are summarized in sequel.

Step 1: Select standard three induction machine for conversion into dual stator winding machine. Obtain its leading parameters as specified in Table 3.1. Repeat this step for several standard 3-ϕ induction machines and select the most suitable for the specified DSWIM design objectives that satisfy the equality and inequality equations 3.2 and 3.3.

Step 2: Carry out magnetic loading calculations to optimize permissible air-gap flux density B_g typically in the range $0.3 \leq B_g \leq 0.6$ Tesla. Thus select optimum air-gap flux density based on equations 3.4 to 3.12, to avoid magnetic saturation and insure 'a-b-c' and 'x-y-z' dual stator winding machine optimum performance.

Step 3: Develop detailed mathematical formulation for the air-gap flux density to be below DSWIM specified saturation level otherwise return to step 2.

Step 4: Compute total $m.m.fs$ comprising the following: air gap considering slots on stator and rotor; stator and rotor cores using equations 3.14 to 3.37. This is to enable computation of magnetizing current of the induction machine with reliance on B-H curves and accurately calculated magnetic path lengths.

Step 5: Carry out generalized stator winding design to determine optimum: (i) Number of stator turns/phase and (ii) Magnetizing current for the magnetic circuits. Equations 3.38 to 3.47 enable relevant calculations to be carried out in this step.

Step 6: Estimate specific electric loading (AC) via the following quantities: (i) Surface current density using equation 3.49; (ii) Stator conductor diameter from equations3.51 & 3.52 and (iii) stator conductor current density according to equation 3.54.

Step 7: Design dual stator winding architecture to satisfy: (i) Identical conditions for all phases; (ii) Specified winding taxonomy; (iii) Optimum winding arrangement in armature slots given slot numbers and poles; and optimum determination of winding dimensions. This step relies on equations 3.55 to 3.59 to execute the basic computational requirements.

Step 8: Estimations of machine steady parameters: (i) Magnetizing reactance & core resistance via equation 3.46 & Appendix D; (ii) Resistance of each dual stator phase winding ('a-b-c' and 'x-y-z') using equation 3.61; (iii) Stator total leakage reactance

per phase using equations 3.63 to 3.71; (iv) Rotor total resistance per phase based on equation 3.76 and (v) Rotor leakage reactance per phase as given in equation 3.77.

Step 9 Compendium of specific case study DSWIM leading design values to: (i) Develop DSWIM Steady state equivalent model of Figure 3.15 to enable GA engine optimize DSWIM power factor and efficiency; (ii) Re-adjust DSWIM parameters after GA convergence and check if either electrical or magnetic loading is violated return to step 2 otherwise stop; (iii) Develop dual Stator winding Layout; and (iv) Implement DSWIM prototype design.

The foregoing salient steps of the generalized design procedure for DSWIM are further depicted in the functional flowchart of Figure 3.19 so as to elucidate the computational procedure. The application of GA to optimize DSWIM's efficiency (η) and power factor (PF) with $obj(\eta, PF)$ as objective function subject to magnetic loading ($B_{ag} \leq B_{max}$) and electric loading ($ac \leq ac_{max}$) inequality constraints is comprehensively treated in the next section.

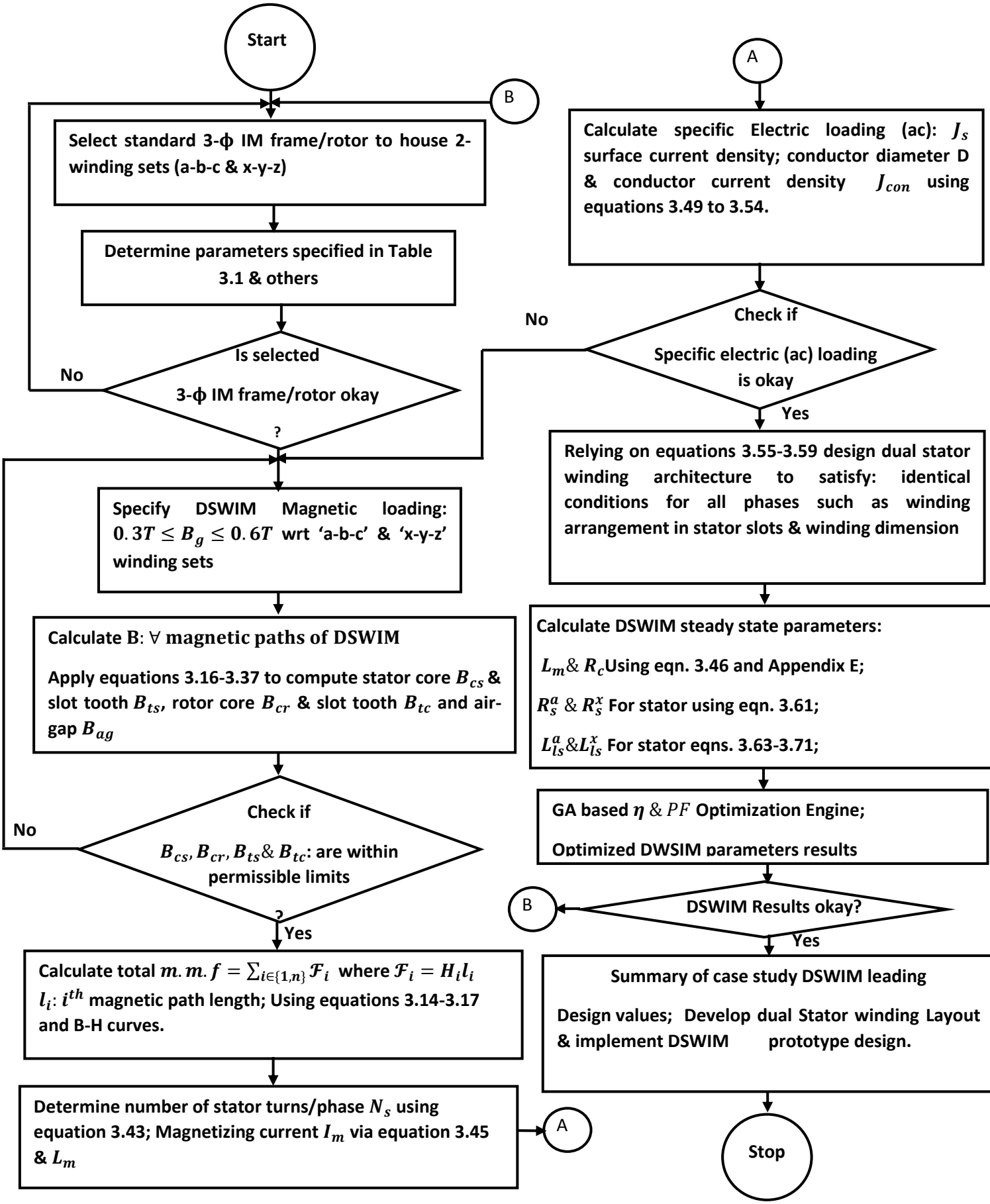

Start
B
Select standard 3-ϕ IM frame/rotor to house 2-winding sets (a-b-c & x-y-z)
Determine parameters specified in Table 3.1 & others
Is selected 3-ϕ IM frame/rotor okay ?
No
Specify DSWIM Magnetic loading: $0.3T \leq B_g \leq 0.6T$ wrt 'a-b-c' & 'x-y-z' winding sets
Calculate B: ∀ magnetic paths of DSWIM
Apply equations 3.16-3.37 to compute stator core B_{cs} & slot tooth B_{ts}, rotor core B_{cr} & slot tooth B_{tc} and air-gap B_{ag}
Check if B_{cs}, B_{cr}, B_{ts} & B_{tc}: are within permissible limits ?
No
Yes
Calculate total $m.m.f = \sum_{i\in\{1,n\}} \mathcal{F}_i$ where $\mathcal{F}_i = H_i l_i$
l_i: i^{th} magnetic path length; Using equations 3.14-3.17 and B-H curves.
Determine number of stator turns/phase N_s using equation 3.43; Magnetizing current I_m via equation 3.45 & L_m
A
A
Calculate specific Electric loading (ac): J_s surface current density; conductor diameter D & conductor current density J_{con} using equations 3.49 to 3.54.
Check if Specific electric (ac) loading is okay
No
Yes
Relying on equations 3.55-3.59 design dual stator winding architecture to satisfy: identical conditions for all phases such as winding arrangement in stator slots & winding dimension
Calculate DSWIM steady state parameters:
L_m & R_c Using eqn. 3.46 and Appendix E;
R_s^a & R_s^x For stator using eqn. 3.61;
L_{ls}^a & L_{ls}^x For stator eqns. 3.63-3.71;
GA based η & PF Optimization Engine;
Optimized DWSIM parameters results
DSWIM Results okay?
B
Yes
Summary of case study DSWIM leading Design values; Develop dual Stator winding Layout & implement DSWIM prototype design.
Stop

Figure 3.20: Functional Flowchart for DSWIM Analytical Design Algorithm

3.7 GA Based Optimization of DSWIM

This section deals with optimization of the DSWIM efficiency and power factor using Genetic Algorithm (GA) to tune its magnetic loading and specific electric loading. The problem statement can now be stated formally thus: Given the power output P_{out} as par equation 3.51 and leading geometric dimensions of the selected standard stator frame and its matching rotor cage, provided a priori, for housing analytically designed 'a-b-c' and 'x-y-z' winding sets; it is required to find optimal values of the DSWIM's efficiency and power factor subject to satisfying inequality constraints on magnetic and electric loadings. Being a subset of the generalized multi-objective optimization of section 3.2, the explicit problem formulation at hand can now be cast mathematically as follows:

Objective Function:

$$\Im_{obj}(\eta, PF) = Min\{\psi_1(1-\eta/100)^2 + \psi_2(1-PF)^2\} \tag{3.78}$$

Where $\Im_{obj}(\eta, PF), \psi_1 \& \psi_2$: are the objective function and weighting factors, respectively whilst other variables have been previously defined.

Equality Constraints:

i) DSWIM power output equation

$$P_{out}^{DM} = P_{abc_\phi} + P_{xyz_\phi} = \left(\frac{\sqrt{2}\pi^2}{120}\right) \mathrm{n_s k_f k_w (D_{is}^2 L_s) \eta PF} \left(B_{ag}'^{abc} J_s^{abc} + B_{ag}'^{xyz} J_s^{xyz}\right) \tag{3.79}$$

ii) DSWIM efficiency equation

$$\eta = \frac{P_{out}^{DM}}{P_{out}^{DM} + SCL_{DM} + SIL + RCL + F_{W+S}} * 100 \tag{3.80}$$

iii) DSWIM full load power factor

$$PF = \frac{P_{out}^{DM} + SCL_{DM} + SIL + RCL + F_{w+S}}{S_{3-\phi}^{abc} + S_{3-\phi}^{xyz}} \quad (3.81)$$

Where: $S_{3-\phi}^{abc}$ & $S_{3-\phi}^{xyz}$: are the kVA ratings of the a-b-c and x-y-z winding sets, respectively.

Where in equations 3.79-3.81: P_{DM} – DSWIM power output; SCL_{DM}-Stator copper loss = $3(I_s^{a\,2}R_s^a + I_s^{x\,2}R_s^x)$; SIL – Stator iron losses =$3E^2/R_c$; RCL – Rotor copper loss =$3I_r^2R_r$; and F_{W+S} – Frictional & Stray losses=$\zeta(SCL_{DM} + SIL + RCL); 0 \leq \zeta \leq 0.05$; i.e. frictional and stray losses are assumed to be about 5% of the other total segregated DSWIM losses.

Inequality Constraints

Magnetic Loading: $B_{min} \leq B \leq B_{max}$

Electric Loading: $ac_{min} \leq ac \leq ac_{max}$

(3.82)

Note that other equality and inequality constraints $x_j = b_j; \forall\, j \in \{1, M_1\}$ and ($x_{min_i} \leq x_i \leq x_{max_i}; \forall\, i \in \{1, M_2\}$ associated with the design of a new stator and rotor structure for DSWIM have been suppressed. The choice of a standard stator frame and rotor cage insured that the foregoing equality and inequality specifications are already satisfied. The resulting multi-objective optimization problem for two winding sets concern the optimal tuning of magnetic and electric loadings to maximize DSWIM's efficiency and power factor. The solution approach adopted in this work is via genetic algorithm. It is recalled, to notify interested readers, that the fundamental theoretical concept of GA is comprehensively discussed in Chapter Two. The unresolved task is GA's solution methodology presented in what follows.

3.8.1 GA solution methodology

It is instructive to reiterative that the choice of GA is anchored on its ability to search for global optimum solution without recourse to use of function derivatives. However, the underlying basic operations comprising reproduction, crossover and mutation earlier treated

in Chapter Two need specifications of fitness function for selecting individuals with higher probability to participate in reproduction process; followed by specifications of probabilities for crossover and mutation processes. The probability for mutation is usually selected to be very small so as to prevent local minimum trap. The fitness function chosen is given by:

$$.fitness = \frac{1}{\left(1+\Im_{obj}(\eta,PF)\right)} \tag{3.83}$$

The binary or floating point implementation of genetic algorithm is targeted at minimizing the objective function of equation 3.78 or conversely maximizing the fitness function. Every generation has feasible set of solutions from which a set of new solutions are evolved. Relying on reproduction selection, crossover and mutation operators new generations emerge with new solutions that, after N successive generations, converge to the desired global solution.

The flowchart depicted in Figure 3.20 offers algorithmic sequence of events required in determining the optimal values of the power factor and efficiency of the DSWIM by employing a genetic algorithm (multi objective pareto search). The salient step- by- step procedure for the optimization process is summarized below:

i. Define the leading constants of the DSWIM such as number of poles, angular frequency, main dimensions, etc.

ii. Select the decision making variables with the view of redesigning the dual winding sets 'a-b-c' and 'x-y-z' (stator parameters are thus chosen as decision making variables that include magnetic and electric loadings).

iii. Generate initial population of feasible solutions via analytical design procedure code each feasible solution using either binary code or real code structure where the initial population of M feasible solutions as follows:

$$\left\{X_0^{(i)} = \left[x_1^{0(i)}, x_2^{0(i)}, \ldots . x_i^{0(i)}, \ldots x_n^{0(i)}\right]^T;\ \forall\, i = \{1, M\}\right\}$$

iv. Evaluate the objective function cast in terms of quadratic efficiency η and power factor PF as stated in equation 3.78 and apply fitness function to select individuals for reproduction.

v. Carryout crossover operation at rate of φ_{cr} and the mutation at rate of φ_{mr} , to form new generation.

vi. Check if the optimal value of the objective function is reached yielding optimized DSWIM design parameters and/or if pre-set number of generations is reached; otherwise return to step ii to continue GA optimization process.

vii. Save the optimized DSWIM design parameters and for new scenario study return to step ii.

The implementation of GA based DSWIM will be pursued further in Chapter Five.

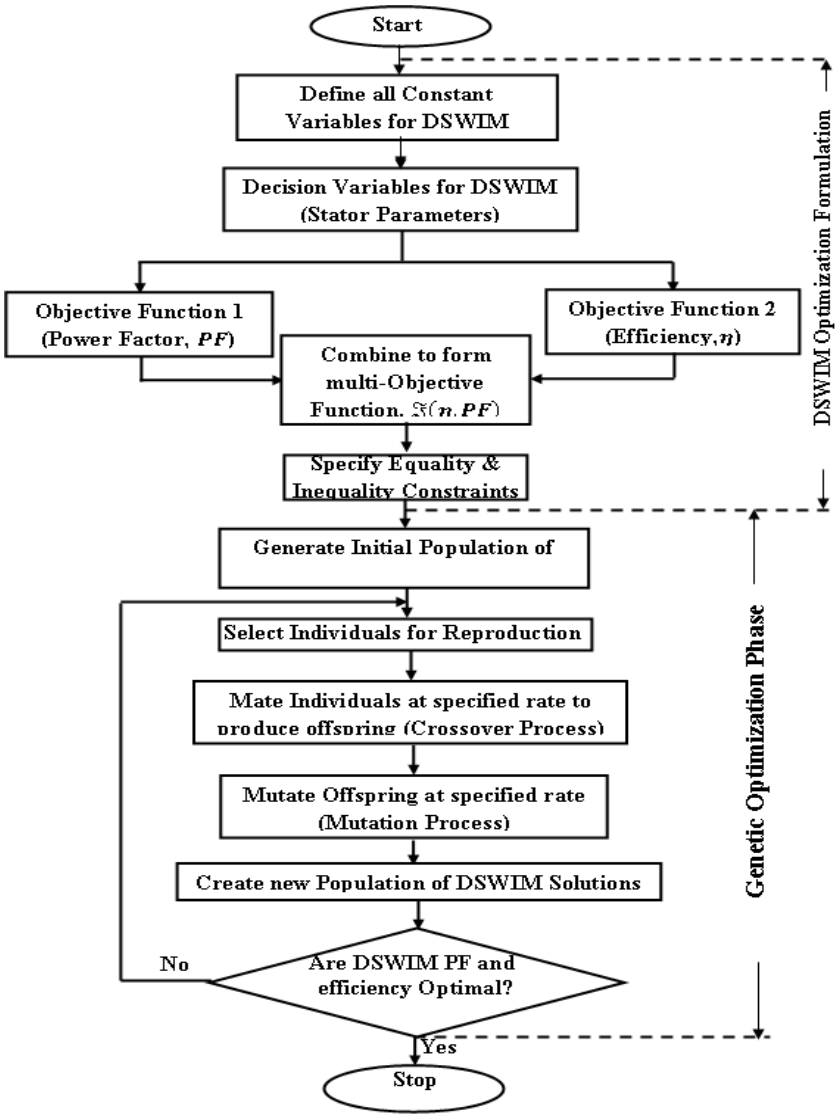


Figure 3.20: Flow Chart for the Optimization of Efficiency and Power Factor

3.9 Design Calculations for Similar Pole DSWIM

The algorithmic analytical framework presented in the preceding section for redesign of a conventional 3- ϕ machine as a dual stator winding induction machine need to be demonstrated for a specific case study. In order to satisfy this objective, a standard 8-pole, 6kW, 3-phase squirrel cage induction machine with 48 stator slots and 42 rotor slots has been carefully selected as a case study in this research work. The original 3-phase 8-pole stator winding of this machine is to be converted to 6-phase ('a-b-c' & 'x-y-z') each of 8-pole stator winding set. The squirrel cage rotor of the original machine is not altered.

This section is therefore devoted entirely to carrying out analytical calculations in respect of DSWIM having identical pole ratios n/n where n is specifically chosen to be 8. It would be recalled that the rationale for research focus on similar pole dual winding configuration was justified in Chapter One. The standard 3-ϕ induction machine to be converted into 8/8 pole dual stator winding induction machine has initial specified parameters presented in Table 3.4. In the subsequent subsections, specific calculations situated within the analytical framework of the Section 3.7 are made; starting with its magnetic characterization to fundamental calculations of its various parameters needed to construct its steady state equivalent circuit and as inputs into GA optimization process.

3.9.1 Specification of magnetic loading for 8/8 pole DSWIM

For an 8/8 pole dual machine, its magnetic loading in relation to that of the standard 8-pole 3-ϕ induction machine is given by:

$$B_{g8|8}(\theta) = B_{g8}(1 - k_1) \tag{3.84}$$

Recall that $k_1 = 0.5$ due to similar pole configuration, the peak values of the air-gap densities of two stator winding sets of the dual induction machine are:

Table 3.4 Specified Parameters of 8/8 Pole Ratio DSWIM Design

Parameter Description	Symbol	Value	Unit
Stator length	L_s	100	mm
Rotor length	L_r	100	mm
Inside diameter of stator	D_{is}	150	mm
Outside diameter of stator	D_{os}	206	mm
Outside diameter of rotor	D_{or}	149	mm
Power factor	pf	-	-
Efficiency	η	-	%
Pole number	P	8	-
Number of stator slots	S_s	48	-
Stator slot dimensions	h_s& b_{os}	17.4*7	mm
Number of rotor slots	S_r	42	-
Rotor slot dimensions	h_r& b_{or}	13*4.75	mm
Air gap	l_g	0.5	mm
Frequency	f	50	Hz

Input Voltage	V	240	Volts
Power Rating	S	6.5	kVA
Stator winding factor	k_w	0.955	-

$$B_{g/abc} = B_{g/xyz} = 0.5B_{g/8} \tag{3.85}$$

The maximum value for tooth flux density B_t in Tesla is typically in the range $B_t \epsilon \{1.55, 2.0\}$ for common steel whilst the flux density B_c in the stator or rotor core normally falls within the range$\{1.0, 1.4\}\, Tesla$. Because the width of a tooth is nearly half of the slot pitch, it then implies that the maximum value of $B_{g/8}$ is typically in the range from 0.75 to 1.0 Tesla (Lipo, 2007). Broadly speaking, small machines (< 10 kW) typically have lower value of air gap flux density than large machines; thus the peak fundamental air gap flux density $B_{g/8_{max}}$ for the 8-pole induction machine is chosen to be 0.85 Tesla. Consequently, the initial magnetic loading for the 8/8 pole dual stator winding sets are given in equation 3.85

$$B_{abc_{max}} = 0.425 \text{ Tesla}$$

$$B_{xyz_{max}} = 0.425 \text{ Tesla} \tag{3.86}$$

3.9.2 Calculations of total MMFs in 8/8 pole DSWIM

The calculations of $mmfs$ in 8/8/pole DSWIM involve evaluations of magnetic paths and field strengths via B-H curve in air-gap, stator core and tooth as well as rotor core and tooth. Here, each magnetic path length needs to be calculated by relying on the geometrical dimensions of the stator frame, stator slots and rotor structure. Table 3.5 presents summary of sample calculations for 6.0kW rated 3-ϕ stator frame /squirrel cage rotor with necessary dimensions provided in Table 3.4 utilized.

Table 3.5: Summary of Sample Calculations for 8/8 Pole DSWIM MMF

Section	Path Length (mm)	Flux Density (Tesla)	H (AT/m) From B-H Curve	MMF Components (Amp-Turns)

Air gap	$2l_g = 1.0$	$B_{ag} = 0.425x\frac{\sqrt{3}}{2} = 0.368$	H_{ag} = 48 000	AT_{ag} = 48.00
Stator core	$\frac{D_{os} - D_{is}}{2} - h_{ts} = 10.6$	B_{sc} =1.25	H_{sc} = 280	AT_{sc} =2.968
Stator tooth	$2h_{ts} = 34.8$	$B_{ts} = 1.35$	H_{ts} = 1200	AT_{ts} = 41.76
Rotor core	$\frac{D_{or} - D_{ir}}{2} - h_{ts} = 6$	$B_{cr} = 1.20$	H_{cr} = 250	AT_{cr} = 1.50
Rotor tooth	$2h_{tr} = 26$	$B_{tr} = 1.30$	H_{tr} = 1500	AT_{tr} = 39

The total mmf per pole is then given by $\sum AT_i\ /2$. We can then compute the MMF for 'a-b-c' and 'x-y-z' winding each identically wound 8-pole as $mmf_{abc} = mmf_{xyz} = 4\sum AT_i = 532.92AT$.

3.9.3 Power, surface current density, number of turns per phase and conductor sizing estimations

Using the data for the standard 3-ϕ, 8-pole IM provided in Table 3.4, the calculated key parameters for a-b-c and x-y-z windings are presented in Table 3.6. Note that the equations used to calculate these quantities are provided to avoid any computational ambiguity.

Table 3.6: Summary of Key Leading Parameters Estimated for DSWIM and Standard IM

DSWIM Parameters	Equations Used	Calculated Values for DSWIM	Values for the standard IM
.'a-b-c' winding Power in kW	3.51	3.0	6.0
'x-y-z' winding Power in kW	3.51	3.0	6.0
'a-b-c' winding surface current	3.50	35 000	52 000

density J_{abc} in AC/cm			
'a-b-c' winding surface current density J_{xyz} in AC/cm	3.50	35 000	52 000
Number of Turns per phase ('a-b-c' winding)	3.43	240	480
Number of Turns per phase ('x-y-z' winding)	3.43	240	480
Conductor diameter ('a-b-c' winding)	3.53	1.25	0.95
Conductor diameter ('x-y-z' winding)	3.53	1.25	0.95

3.9.4 Calculations of inductances and resistances for 8/8 DSWIM

The sample calculations of the various inductances and resistances associated with stator 'a-b-c' and 'x-y-w' windings as well as the squirrel cage rotor have been carried out. The enabling equations and calculated values for the various parameters are presented in Table 3.7.

Table 3.7: Summary of Calculated DSWIM Parameters

DSWIM Part Identifier	Parameters		Equations Used	Calculated Values in specified units
	Definitions	Symbols		
Magnetic circuit	Magnetizing Inductance	L_m	equation 3.46	0.12H

Core Loss	Core Resistance	R_c	Appendix D	223Ω
'a-b-c' winding (Stator)	Leakage Inductance*	L_{ls}^{a}	equations 3.63-3.71	14.2mH
	Resistance	R_s^a	Equation3.61	1.5Ω
'x-y-z' winding (stator)	Leakage Inductance*	L_{ls}^{x}	equations 3.63-3.71	14.2mH
	Resistance	R_s^x	Equation 3.61	1.5Ω
Rotor	Leakage inductance	L_{lr}	Equation 3.77	0.05H
	Resistance	R_r	Equation 3.76	0.63Ω

***** Require calculations of various leakage inductance components

3.10 Winding Layout Design for 8/8 DSWIM

The 'a-b-c' and 'x-y-z' windings constitute six winding 8/8 pole machine that occupy the same magnetic space as the standard 3-ϕ, 8-pole induction machine. Since the standard stator frame has 48 slots and of single layer configuration, it is desired to retain the same architecture for the 8/8 DSWIM whilst the 'a-b-c' winding group is displaced from 'x-y-z' winding group by 30^o (electrical degrees). This is essential to maintaining balanced spatial leakage distribution. For the single layer, full pole pitch and 8 pole structure adopted in this design, the following basic calculations are essential to winding diagram construction:

$$\tau_{p/8} = \frac{S_{s/8}}{P} = \frac{48}{8} = 6 \text{ slots /pole} \rightarrow 30^o \text{(electrical degrees per slot)} \tag{3.87}$$

This implies slot pitch of 6 slots per pole and 2 slots per pole per phase.

3.10.1 Stator winding dimension calculation

The coil width in terms of stator slots also known as coil span is given by the expression:

$$y_w = \frac{S_s}{P} \tag{3.88}$$

This means that the four coils belonging to any of the phases (say phase "a") can be arranged in slots as follows:

Assume that the slots are numbered from 1 to 48 then

1st coil ↔ 1 side will occupy slot no.1 and the other side slot no. 1+6=7;

2nd coil ↔ 1 side will occupy slot no.13 and the other side slot no 13+6=19;

3rd coil ↔ 1 side will occupy slot no.25 and the other side slot no 25+6=31; and

..

This constitutes the template for the construction of winding diagram for the two winding sets.

3.10.2 Stator 'a-b-c' winding diagram

The developed winding diagram of phase "a" is shown in Figure 3.21. Once the first slot for any given phase is identified then the arrangement will be similar to the one described above.

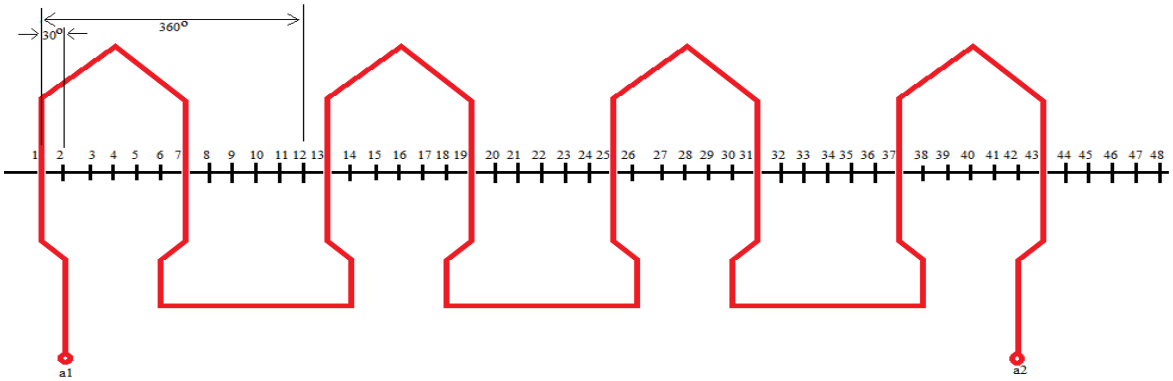


Figure 3.21: The Complete Developed Winding Diagram of Phase "a"

For example, to find the first slot for phase "b" (which supposed to be at 120 electrical degree away from phase "a"), the slot angle, α_s must be calculated. Thus;

$$\alpha_s = \frac{P*180^0}{Q_s} = 30^0 \qquad (3.89)$$

This implies that to get the required 120^0 between the two phases, phase "b" must start from the fifth slot. The same argument as above holds for phase "c". The complete developed winding diagram for the 'a-b-c' winding set is shown in Figure 3.22.

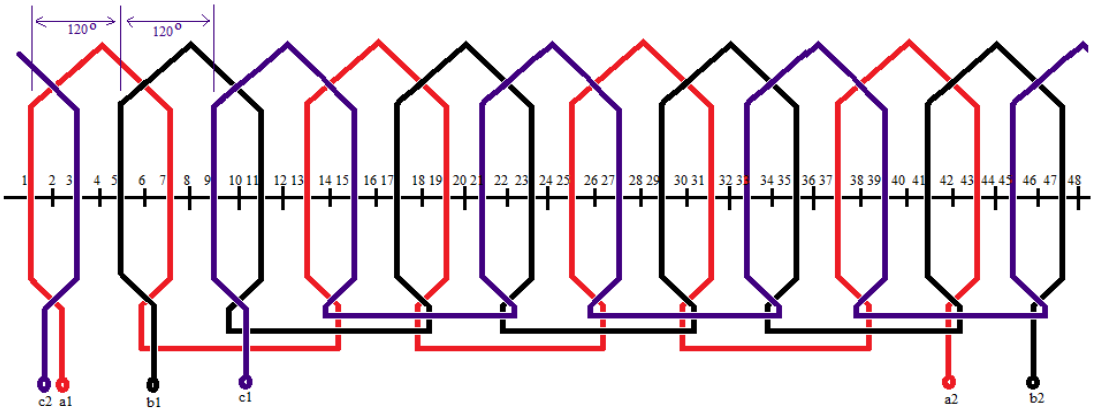


Figure 3.22: The Developed Winding Diagram of 'a-b-c' Winding set.

3.10.3 Stator 'x-y-z' winding diagram

In the case of 'x-y-z' winding set, the arrangement is as follows: The angle between phases "a" and "x" is constraint to be 30^0. This means that the first coil of phase "x" must start at a slot next to that of phase "a". The first coil of phase "x" shall thus start at slot number 2. The developed winding arrangement for phases "a" and "x" is shown in Figure 3.23. The remaining phases of 'x-y-z' winding set are inserted in slots similar to that done for a-b-c winding set. The complete arrangement of 'x-y-z' winding set is then depicted in Figure 3.24.

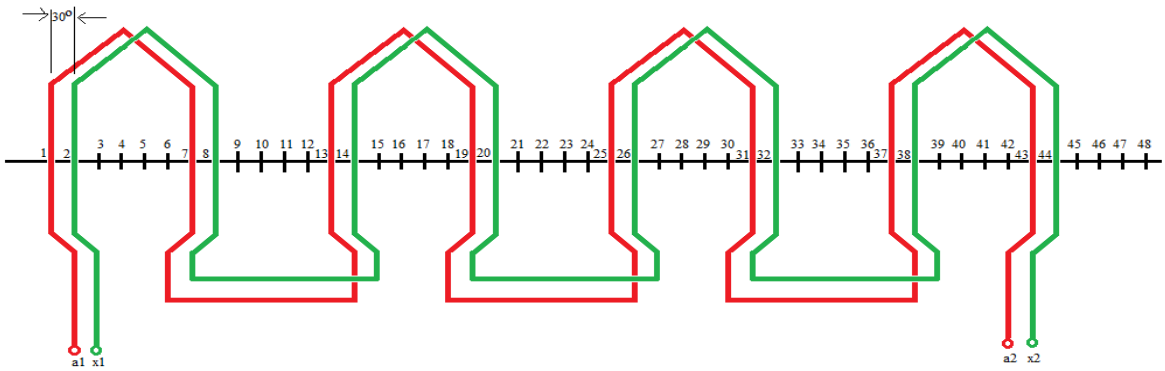


Figure 3.23: The Developed Winding Diagram of Phases 'a' and 'x'

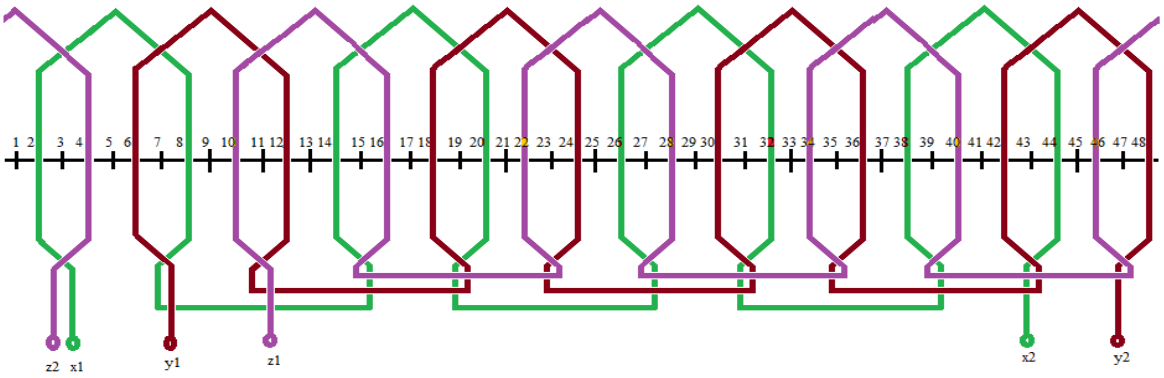


Figure 3.24: The Developed Winding Diagram of the 'x-y-z' Winding set

3.10.4 Complete stator winding diagram for 8/8 pole DSWIM

The 'a-b-c' and 'x-y-z' winding sets need to housed in the slots of the stator. The systematic procedure of winding diagram construct set forth can be generalized and applied to other winding architecture. Finally, the complete stator winding arrangement for 8/8 pole DSWIM to house two winding sets in 48 slot stator frame is shown in Figure 3.25.

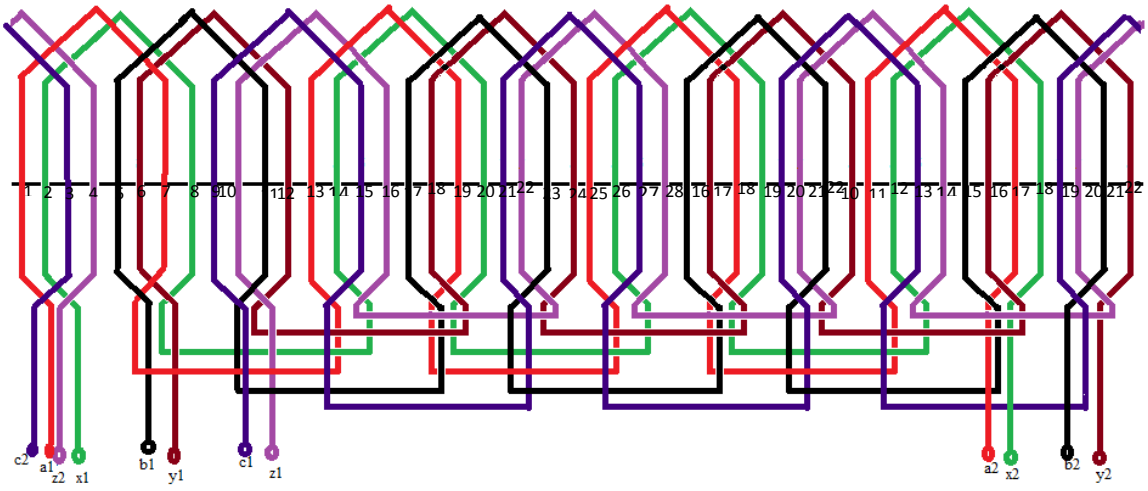


Figure 3.25: The Complete Stator Winding Clock Diagram for 8/8 DSWIM

3.11 Summary

This chapter has documented the analytical design framework specifically targeted at DSWIM magnetic and electric loading calculations to meet imposed physical constraints.

The developed analytical design framework is computationally superior to the traditional design procedure most especially with respect to the estimations of magneto-motive force in the various magnetic paths as well as DSWIM modelling parameters. In this regard, special attention was given to detailed calculations of leakage inductances that have profound effects on the DSWIM steady state performance. In pursuit of optimized DSWIM parameters, GA optimization process has been developed to achieve the prime goal of maximizing its efficiency and power factors. For the sake completeness, a sample analytical calculations for an 8/8 pole DSWIM has been carried out and finally its winding diagram developed to support its prototype implementation. In the next chapter, attention will be focused on the development of mathematical model in arbitrary reference frame for, and the application of finite element method (FEM) to model, DSWIM.

CHAPTER FOUR

DSWIM MATHEMATICAL MODELING AND FINITE ELEMENT ANALYSIS

4.1 Introduction

Mathematical modelling and finite element analysis of dual stator winding induction machine are the main subject matters treated in this chapter. The existing modelling techniques generally focused on multi-phase machines with dissimilar number of poles. In this work, detailed mathematical modelling of a dual stator winding induction machine equipped with the similar number of poles per winding is developed. More specifically, the mathematical model being developed in d-q-0 arbitrary reference frame is to be deplored subsequently to evaluate the transient operational performance of this class of DSWIM under different loading scenarios and to validate the steady state operational performance of its laboratory prototype realization. Finally, the finite element method (FEM) model considered herein is applied to calculate the inductances of DSWIM and to enable its other steady state operational characterization.

4.2 Development of DSWIM Equations in d-q-0 Arbitrary Reference Frame

In Chapter Two, we treated, in sufficient detail, theoretical concept on winding function in which equations, derived in phase variables with time varying inductances, for DSWIM were transformed into arbitrary reference frame. For the sake of convenience, Figure 2.8 is repeated here as Figure 4.1 to depict schematic representation of DSWIM but for a similar n/n pole ratio. Of noteworthy is the application of arbitrary reference frame to evaluate each term in the voltage and flux linkage equations that gave rise to the transformed inductance matrices derived in Subsection 2.2.6 of Chapter Two. Emerging therefrom are voltage equations 4.1-4.8 in d-q-0 axes for dual stator winding induction machine having identical

pole numbers. Note that the similar pole ratio case is enforced by same parameter values for ‘a-b-c’ and ‘x-y-z’ windings.

$$V_{q1} = r_1 i_{q1} + \omega\lambda_{d1} + p\lambda_{q1} \tag{4.1}$$

$$V_{d1} = r_1 i_{d1} - \omega\lambda_{q1} + p\lambda_{d1} \tag{4.2}$$

$$V_{01} = r_1 i_{q1} + p\lambda_{01} \tag{4.3}$$

$$V_{q2} = r_1 i_{q2} + \omega\lambda_{d2} + p\lambda_{q2} \tag{4.4}$$

$$V_{d2} = r_1 i_{d2} - \omega\lambda_{q2} + p\lambda_{d2} \tag{4.5}$$

$$V_{02} = r_1 i_{q2} + p\lambda_{02} \tag{4.6}$$

$$V_{qr}^{'} = r_r^{'} i_{qr}^{'} + (\omega - \omega_r)\lambda_{dr}^{'} + p\lambda_{qr}^{'} \tag{4.7}$$

$$V_{dr}^{'} = r_r^{'} i_{dr}^{'} - (\omega - \omega_r)\lambda_{qr}^{'} + p\lambda_{dr}^{'} \tag{4.8}$$

$$V_{or}^{'} = r_r^{'} i_{0r}^{'} + p\lambda_{or}^{'} \tag{4.9}$$

Where: in equations 4.1-4.9 $p \triangleq \frac{d}{dt}$; Subscripts ‘1’and ‘2’ denote ‘a-b-c’ and ‘x-y-z’ windings, respectively and subscript ‘r’ for rotor winding assumed to be three-phase.

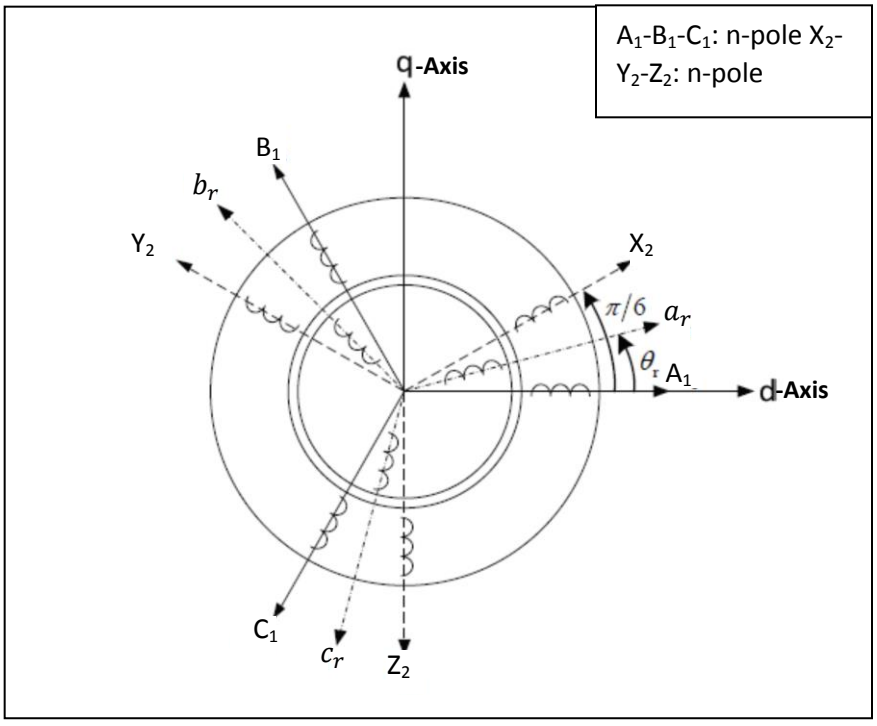


Figure 4.1: Schematic Diagram of an n/n Similar Pole Ratio Dual Winding Induction Machine

The expressions for the flux linkages taking into account the turn ratios, as found in Subsection 2.2.14, and zero sequence components can be written as follows:

$$\lambda_{q1} = (L_{l1} + L_{lm} + L_m)i_{q1} + (L_{lm} + L_m)i_{q2} + L_{ldq}i_{d2} + L_m i'_{qr} \quad (4.10)$$

$$\lambda_{d1} = (L_{l1} + L_{lm} + L_m)i_{d1} + (L_{lm} + L_m)i_{d2} - L_{ldq}i_{q2} + L_m i'_{dr} \quad (4.11)$$

$$\lambda_{01} = L_{01}i_{01} + \left(L_{la}^{x} + L_{la}^{y}\right)(i_{01} + i_{02}) \quad (4.12)$$

$$\lambda_{q2} = (L_{lm} + L_m)i_{q1} + L_{ldq}i_{d1} + (L_{l1} + L_{lm} + L_m)i_{q2} + L_m i'_{qr} \quad (4.13)$$

$$\lambda_{d2} = -L_{ldq}i_{ql} + (L_{lm} + L_m)i_{d1} + (L_{l1} + L_{lm} + L_m)i_{d2} + L_m i'_{dr} \quad (4.14)$$

$$\lambda_{02} = L_{02}i_{02} + \left(L_{la}^{x} + L_{la}^{y}\right)(i_{01} + i_{02}) \quad (4.15)$$

$$\lambda'_{qr} = L_m i_{q1} + L_m i_{q2} + (L'_{lr} + L_m)i'_{qr} \quad (4.16)$$

$$\lambda'_{dr} = L_m i_{d1} + L_m i_{d2} + (L'_{lr} + L_m)i'_{dr} \quad (4.17)$$

$$\lambda'_{0r} = L'_{lr} i_{or} \quad (4.18)$$

The transformed stator and rotor voltages and flux linkages in arbitrary reference frame as stated in equations 4.1-4.18 are used to develop equivalent circuit for a similar pole ratio dual stator winding machine. The DSWIM equivalent circuits so developed are shown in Figure 4.2 for d, q and zero axes. More specifically, the mutually coupled equivalent circuits in the quadrature and direct axes have been developed along with the zero axis equivalent circuits so as to admit balanced and unbalanced analysis of DWSIM. The arrows associated with $\pm L_{ldq}$ represent mutual leakage coupling between the windings they designate.

Starting from the generalized torque equation set forth in Subsection 2.2.14, it can be shown that the electromagnetic torque produced by the DSWIM comprising two torque components (T_{e1}& T_{e2}) is given by:

$$T_e = T_{e1} + T_{e2} = \frac{3}{2}\left(\frac{P}{2}\right)\left(\frac{L_m}{L'_r}\right)[\lambda'_{dr}\left(i_{q1} + i_{q2}\right) - \lambda'_{qr}(i_{d1} + i_{d2})] \quad (4.19)$$

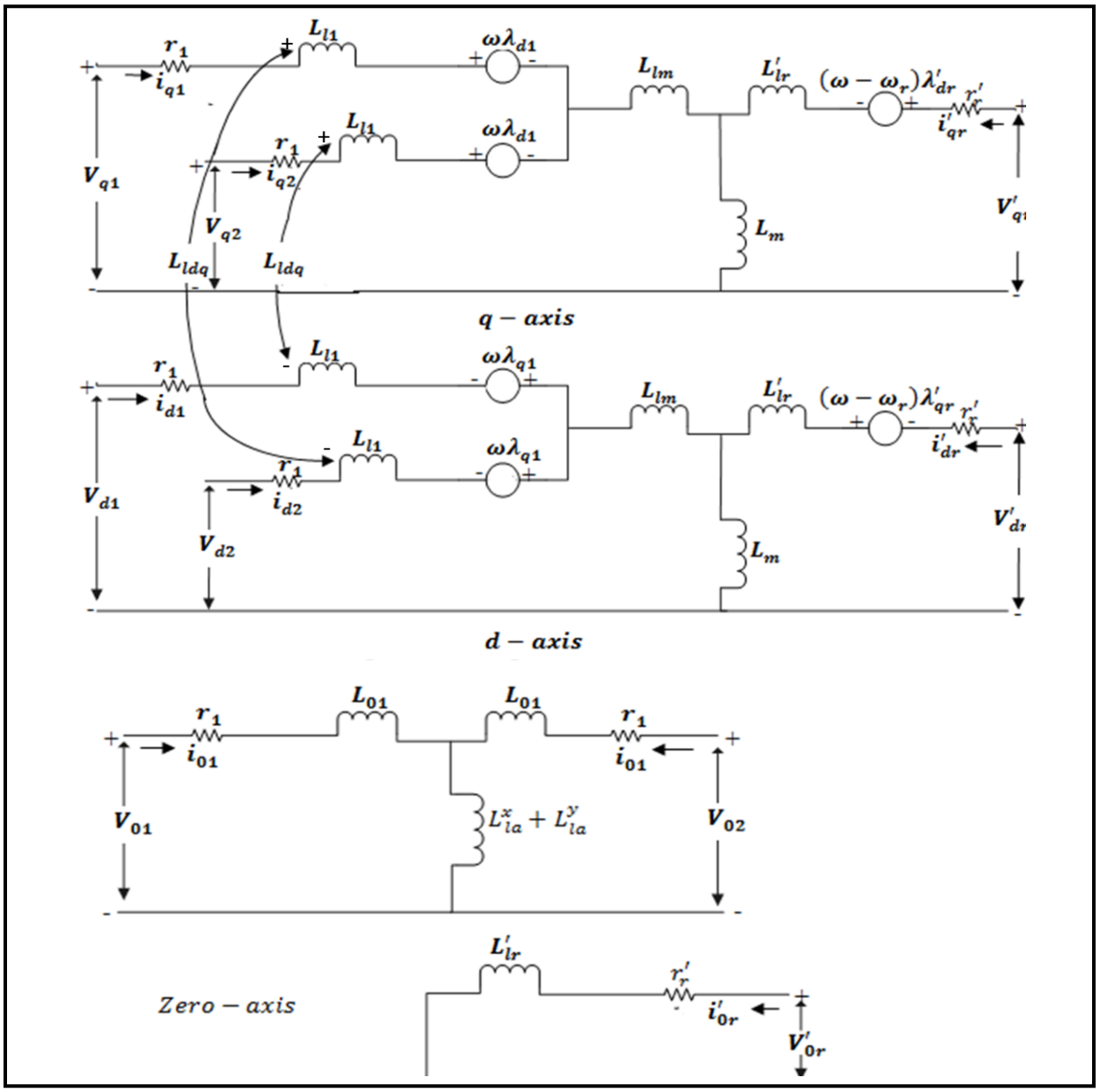


Figure 4.2: Equivalent Circuit of Similar Pole Dual Winding Induction Machine

Where, $L'_r = L_m + L'_{lr}$: is the equivalent inductance seen from the rotor circuit terminals with 'a-b-c' and 'x-y-z' stator windings open circuited. Finally, the rotor dynamical equation relates electromagnetic torque, load torque (T_L) and rotor speed (ω_r) as follows:

$$p\omega_r = \frac{d\omega_r}{dt} = \left(\frac{P}{2}\right)\left(\frac{1}{J}\right)(T_e - T_L) \tag{4.20}$$

Where, : is the combined inertia of the rotor and the connected mechanical load.

In this research work, equations 4.1-4.18 are used to model the electrical dynamics of DSWIM equipped with identical poles whilst its rotor dynamics is represented by equations 4.19 and 4.20. In the next subsection, the functional representation of DSWIM is described from mathematical standpoint to pave way for its detailed Simulink model on MATLAB platform.

4.2.1 Functional representation of DSWIM mathematical model

The overall functional representation of DSWIM model is shown in Figure 4.3 which provides a generalized mathematical framework for the development of its Simulink model in MATLAB environment. The need for the development of DSWIM model will be evident in Chapter Five as tool for its simulation. Herein, the generalized nonlinear mathematical description of DSWIM is cast in compact differential algebraic equation matrix form as follows:

$$\dot{\bar{X}} = F(\bar{X}, \bar{\zeta}, \bar{U}, t); \;\; G(\bar{X}, \bar{\zeta}, \bar{U}) = 0 \tag{4.21}$$

Where, $\bar{X}, \bar{\zeta}\ and\ \bar{U}$: are appropriately dimensioned vectors of flux linkage per second as independent state variables , current variables and voltage input variables defined as follows:

$$\bar{X} = \left[\psi_{q1}, \psi_{d1}, \psi_{01}, \psi_{q2}, \psi_{d2}, \psi_{02}, \psi'_{qr}, \psi'_{dr}, \psi'_{0r}\right]^T$$

$$\bar{\zeta} = \left[i_{q1}, i_{d1}, i_{01}, i_{q2}, i_{d2}, i_{02}, i'_{qr}, i'_{dr}, i'_{0r}\right]^T$$

$$\bar{U} = \left[V_{q1}, V_{d1}, V_{01}, V_{q2}, V_{d2}, V_{02}, V'_{qr}, V'_{dr}, V'_{0r}\right]^T$$

(4.22)

The explicit matrix differential equation constructed from equations 4.1-4.9 is expressed thus:

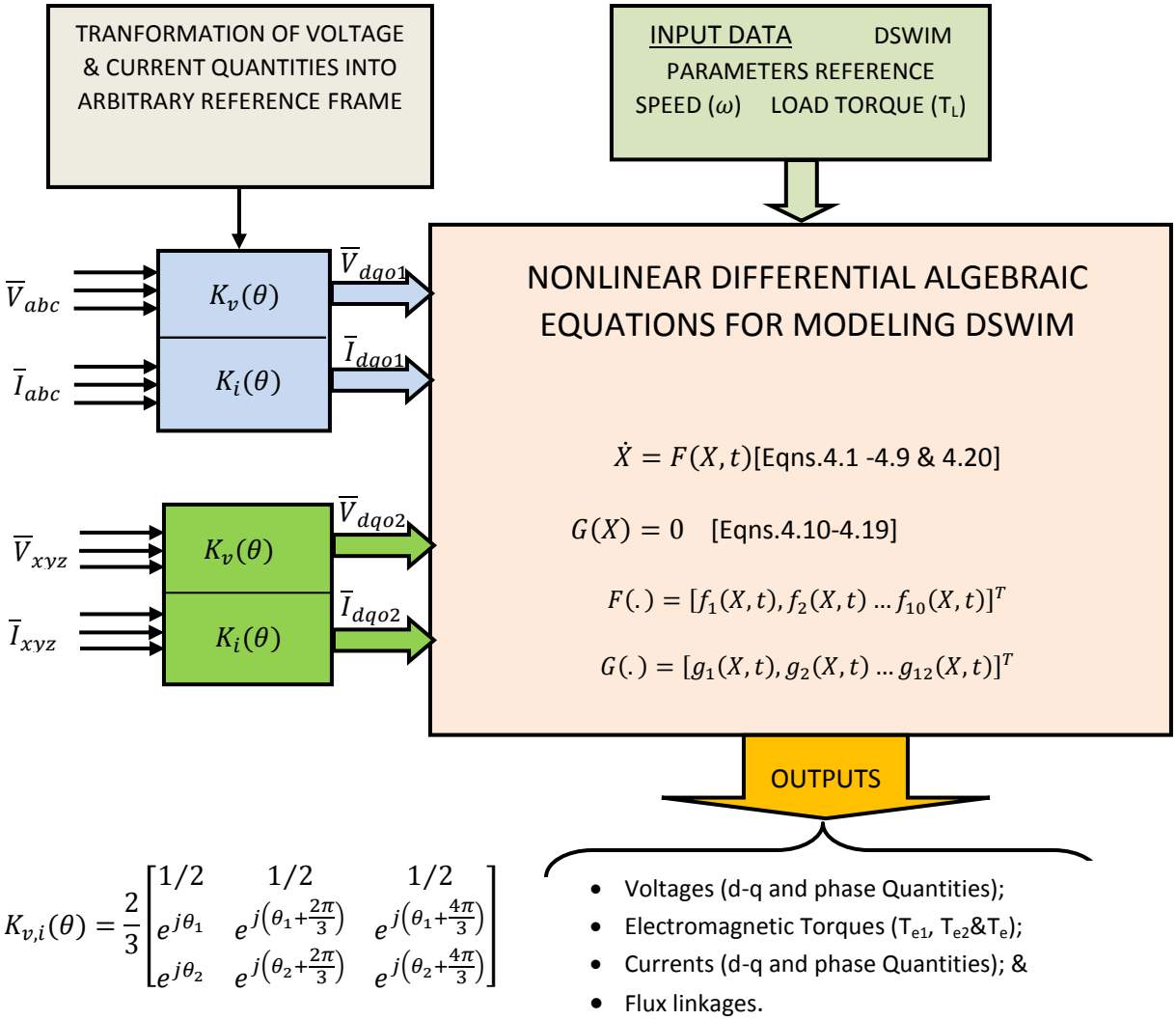
$$p\bar{X} = A(\omega)\bar{X} + C(r)\bar{\zeta} + B\bar{U} \tag{4.23}$$

Where: $A(\omega)$: is $9x9$ matrix with the following non-zero entries $A(1,2) = A(4,5) = \omega/\omega_b$; $A(2,1) = A(5,4) = \omega/\omega_b$; $A(7,8) = -(\omega - \omega_r)/\omega_b$; $A(8,7) = (\omega - \omega_r)/\omega_b$;

C(r) : is $9x9$ diagonal matrix with diag.$[-r_1, -r_1, -r_1, -r_1, -r_1, -r_1, -r_r', -r_r', -r_r']$;

B : is $9x9$ identity matrix; and

ω_b : is base angular velocity for converting inductances into reactances (Krause, et al. 1995).



$$K_{v,i}(\theta) = \frac{2}{3}\begin{bmatrix} 1/2 & 1/2 & 1/2 \\ e^{j\theta_1} & e^{j\left(\theta_1+\frac{2\pi}{3}\right)} & e^{j\left(\theta_1+\frac{4\pi}{3}\right)} \\ e^{j\theta_2} & e^{j\left(\theta_2+\frac{2\pi}{3}\right)} & e^{j\left(\theta_2+\frac{4\pi}{3}\right)} \end{bmatrix}$$

Figure 4.3: Generalized Functional Representation of DSWIM Mathematical Model

Similarly equations 4.10-4.18, after multiplying each equation by ω_b, can expressed in compact matrix form as follows:

$$\bar{\zeta} = \mathcal{L}(x)\bar{X} \tag{4.24}$$

Where $\mathcal{L}(x)$: is $9x9$ reactance matrix.

Using equation 4.24 to eliminate current vector from equation 4.23 yields DSWIM equation in compact matrix form with flux linkages per second as the independent state variables:

$$p\bar{X} = A'(\omega, r, y)\bar{X} + B\bar{U} \tag{4.25}$$

Where, $A'(.) \triangleq [A(\omega) + C(r)\mathcal{L}(x)^{-1}]$: is a derived matrix for DSWIM 'a-b-c' and 'x-y-z' windings wound for similar poles. The matrix $\mathcal{L}(x)$ is explicitly defined thus:

$$\mathcal{L}(x) = \begin{bmatrix} a_{11} & 0 & 0 & a_{14} & a_{15} & 0 & a_{17} & 0 & 0 \\ 0 & a_{22} & 0 & a_{24} & a_{25} & 0 & 0 & a_{28} & 0 \\ 0 & 0 & a_{33} & 0 & 0 & a_{36} & 0 & 0 & 0 \\ a_{41} & a_{42} & 0 & a_{44} & 0 & 0 & a_{47} & 0 & 0 \\ a_{51} & a_{52} & 0 & 0 & a_{55} & 0 & 0 & a_{58} & 0 \\ 0 & 0 & a_{63} & 0 & 0 & a_{66} & 0 & 0 & 0 \\ a_{71} & 0 & 0 & a_{74} & 0 & 0 & a_{77} & 0 & 0 \\ 0 & a_{82} & 0 & 0 & a_{85} & 0 & 0 & a_{88} & 0 \\ 0 & 0 & 0 & 0 & 0 & 0 & 0 & 0 & a_{99} \end{bmatrix} \tag{4.26}$$

Where $a_{11} = a_{22} = a_{44} = a_{55} \triangleq x'_{ss}; a_{33} = a_{66} \triangleq x'_{0s}; a_{14} = a_{41} = a_{25} = a_{52} \triangleq x_s^m; a_{15} = -a_{24} = a_{42} = -a_{51} \triangleq x_{sdq}; a_{17} = a_{28} = a_{47} = a_{58} = a_{74} = a_{25} = a_{82} = a_{85} \triangleq x_m; a_{36} = a_{63} \triangleq x_{0s}^{xy};\ a_{77} = a_{88} \triangleq x'_{rr}; a_{99} \triangleq x'_{lr};$

$$x'_{ss} \triangleq \omega_b(L_{l1} + L_{lm} + L_m); x'_{0s} \triangleq \omega_b\left(L_{01} + L_{la}^x + L_{la}^y\right); x_{sm} \triangleq \omega_b(L_{l1} + L_{lm});\ x_m \triangleq \omega_b L_m;$$

$$x_{sdq} \triangleq \omega_b L_{ldq}; x_{0s}^{xy} \triangleq \omega_b\left(L_{la}^x + L_{la}^y\right);\ x'_{0s} \triangleq \omega_b\left(L_{01} + L_{la}^x + L_{la}^y\right); x'_{rr} \triangleq \omega_b\left(L'_{lr} + L_m\right);$$

$x'_{lr} \triangleq \omega_b L'_{lr}$.

With $\mathcal{L}(x)$ inverted, the derived matrix $A'(.)$ can now be expressed in terms of the actual design parameters of DSWIM. Hence, equation 4.25 augmented by torque and rotor speed equations- equations 4.19 and 4.20 constitute the dynamical simulation model for DSWIM which can be simulated in MATLAB/Simulink environment.

The salient steps of the algorithmic simulation procedure of DSWIM in MATLAB/Simulink environment are as follows:

Step 1: Specify the leading parameters for DSWIM with similar poles which are obtainable from its design values outlined in Chapter Three. The design parameters are $L_m,\ L_{ls},\ R_s, L'_{lr},\ R'_r, T_L, \omega_b, P\ \&\ J$. Convert all the inductances into their respective reactances using the specified base angular velocity,

Step 2: Choose the appropriate reference frame for DSWIM simulation i.e. stationary, synchronous or rotor reference frame depending the nature of study. For balanced DSWIM simulation study, synchronous or stationary reframe is widely used. For balanced studies, zero axis currents will be zero and can therefore be suppressed in the DSWIM simulation.

Step 3: Transform the 3-ϕ supply voltages for 'a-b-c' and 'x-y-z' windings: $V_a, V_b\ \&\ V_c$ and $V_x, V_y\ \&\ V_z$ into their respective d-q-0 axes. Determine DSWIM steady state full load currents $I_a, I_b\ \&\ I_c,\ I_x,\ I_y\ \&\ I_z$ and $I_{ar}, I_{br}\ \&\ I_{cr}$ and then transform into d-q-0 axes. Use equation 4.24 to determine steady state values of flux linkages per second.

Step 4: Setup the dynamic simulation model for DSWIM equations 4.19, 4.20 and 4.25 with all the initial conditions specified. Specify the simulation time duration T_f and integration time step ΔT.

Step 5: Solve the DSWIM dynamical simulation equations numerically

Step 6: If $T_i \geq T_f$ go to step 7 otherwise increment time $T_i = T_{i-1} + \Delta T$ and return to step 5.

Step 7: Select all the variables to be plotted and plot them.

Step 8: End Simulation or go to step1 to run another simulation scenario for DSWIM.

In the next subsequent, a generalized representation of MATLAB/Simulink model for DSWIM is described from the standpoint of its functional block diagram implementation.

4.2.2 Description of DSWIM Simulink model

A Simulink is a software component hosted by MATLAB that enables complex simulation model to be built from basic functional blocks resident in its library. It is a popular tool widely used by researchers in the simulations of both DC and AC machines due to wide range of flexible capabilities that include interfaced displays. Simulink tool is adopted herein as a platform for the simulation of DSWIM.

In realization of the simulation task at hand, Figure 4.4 depicts a generalized functional block diagram of DSWIM model in MATLAB/Simulink environment with all the descriptive model equations in compact matrix forms inserted in the main subsystem. In order to enable Simulink software display capability, two scopes are incorporated for capturing the transient variation of flux linkages associated with the dual windings ('a-b-c' & 'x-y-z') and the electromagnetic torques developed by each stator winding set as well as the combined torque. The complete simulation model of DSWIM is depicted in Figure 4.5 which is embedded in Figure 4.3 to realize the underlying dynamical simulation equations. MATLAB differential solver is deployed to solve the resulting differential equations of the flux linkages of the two stator winding sets and a rotor winding set as well as the rotor equations. For added simulation flexibility, the 'x-y-z' winding set is fed from a constant dc source via a voltage source inverter. This has the advantage of providing variable voltage, variable frequency supply for experimental investigation.

Figure 4.6 is a detailed block diagram description of the inverter subsystem feeding 'xyz' winding set of Figure 4.5. As shown in the figure, a sine wave pulse width modulation (PWM) technique has been employed in which a modulation signal is compared with a triangular (carrier) signal. Several scopes are incorporated in the model to capture waveforms of a number of quantities such as currents, voltages and flux linkages in both 'd-q' and 'a-b-c' reference frames.

The DSWIM model tool developed in MATLAB/Simulink environment will be utilized in Chapter Five to investigate its dynamic and steady state performances. The goal, in the main, is to generate extensive simulation results that would allow meaningful comparisons with results of experimental work on the DSWIM prototype realization. There will be need, of course, to validate the developed DSWIM simulation model on comparative basis with other similar existing DSWIM simulation results in the literature. For the avoidance of doubt, it is reiterated again that DSWIM design parameters obtained from its design methodology of Chapter Three will be used along other relevant operating data of its standard three phase induction machine to drive its model in MATLAB/Simulink platform. In the next section, Finite Element Method (FEM) is admitted to emulate DSWIM model and secure its leading parameters.

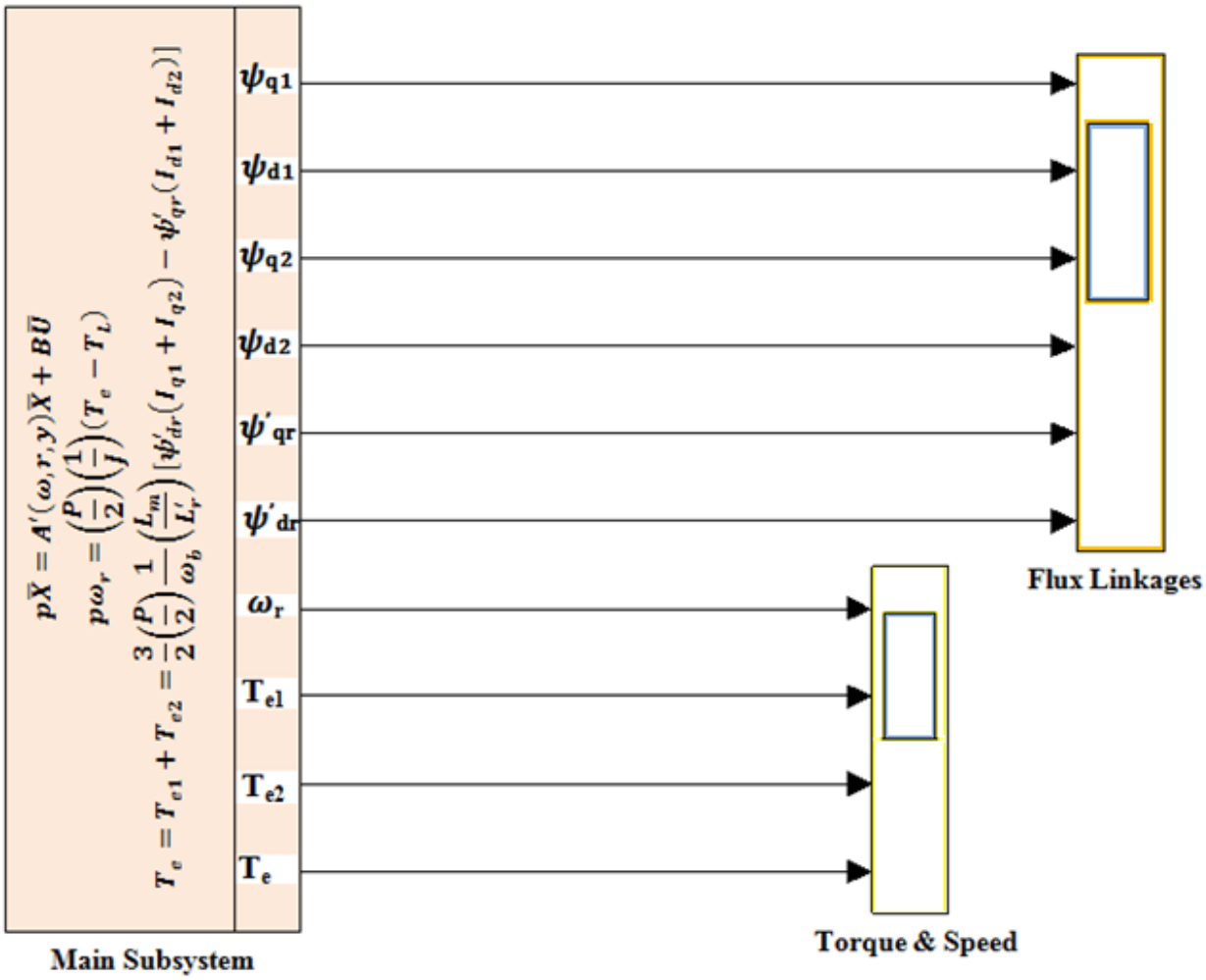


Figure 4.4: Simulink Main Software Hosting DSWIM Simulation Model

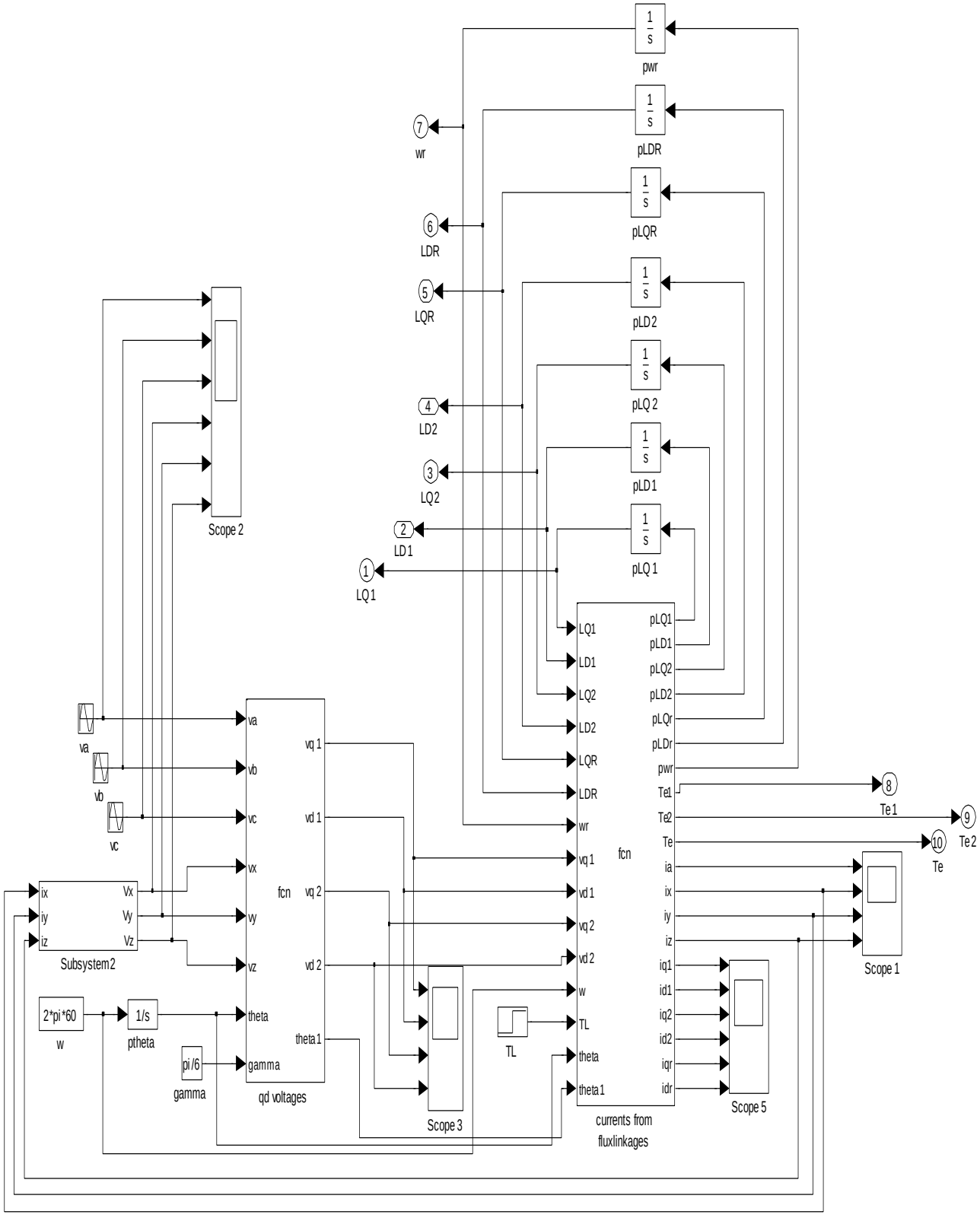


Figure 4.5: Complete Simulink Simulation of DSWIM Model

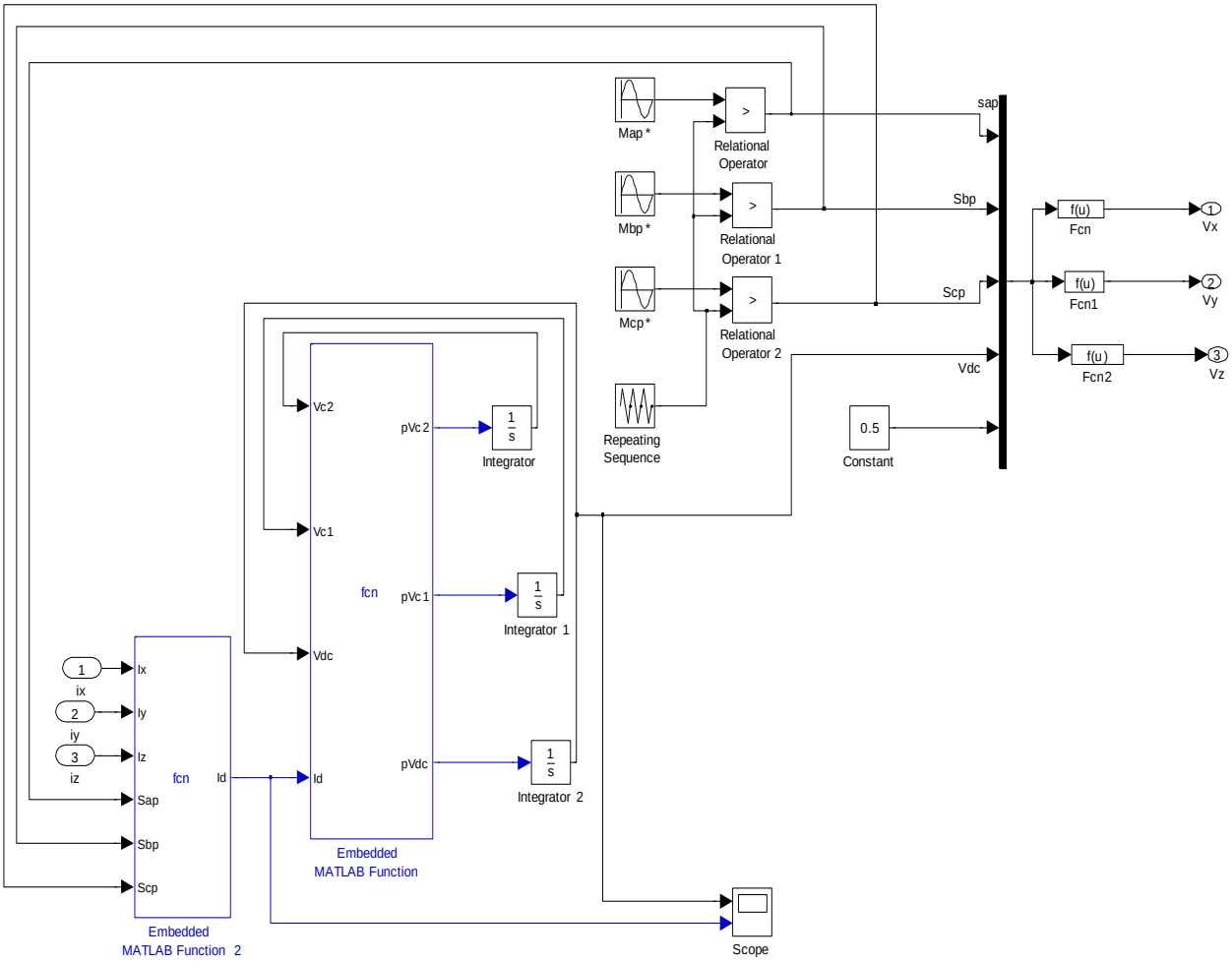


Figure 4.6: Simulink Inverter Model Feeding ‘x-y-z’ Winding Set.

4.3 Finite Element Method

The fundamental concepts of finite element method have been presented in Subsection 2.2.18 of Chapter 2. The main concern of this present section is therefore directed at the application FEM to model DSWIM equipped with similar pole ratios. Recall that FEM has been described as a powerful tool available to researchers to carry out magnetic field analysis based on Maxwell’s celebrated equation. Consequently, FEM has become indispensible in the analysis and synthesis of power frequency electro-magnetic devices, such as DSWIM characterized by complex stator and rotor geometries. As previously mentioned, FEM constructs the model of an electromagnetic device of interest by dividing it into small triangular meshes, each bounded by three corners referred to as nodes.

Fortunately, FEM software packages in 2-D and 3-D perspectives abound that are user friendly whilst offering capabilities such as menu driven geometric drawing, mesh formation, material property specifications and electrical circuits to magnetic circuits coupling. Furthermore, taking advantage of DSWIM symmetry, its FEM modelling and computational solution methodology can be confined to 25% of its cross-sectional area (Buyukbas, 2004). The magneto static problem formulation for DSWIM entertained herein is recast again in equation 4.27 in terms of magnetic vector potential A , permeability μ and current density J in a defined domain Ω.

$$\frac{\partial}{\partial x}\left(\frac{1}{\mu}\frac{\partial A}{\partial x}\right)+\frac{\partial}{\partial y}\left(\frac{1}{\mu}\frac{\partial A}{\partial y}\right)=-J \tag{4.27}$$

The search for efficient numerical solution to this problem engendered the acquisition of 2-D FEM software described in the next subsection.

4.3.1 Description of finite element method magnetics (FEMM) software

Here the field distribution of a dual-stator wir ding induction machine is studied using Finite Element Method Magnetics (FEMM) software. As previously explained in Chapter Two, it is essentially a numerical solution to Maxwell's equation in which three basic steps of pre-processing, processing and post-processing are sequentially implemented via femme.exe, simulation.exe and femmview.exe executable routines, respectively as further highlighted in what follows.

4.3.1.1 Femme.exe program

The femme.exe routine, that constitutes the pre-processing phase, draws DWSIM geometry to be solved as well as specifications of material properties and boundary conditions. An example of such geometric drawing is depicted in Figure 4.7. Normally, a Dirichlet boundary condition in which null magnetic potential is assigned along the external circumference of the stator is adopted. If a quarter of cross-sectional area of DSWIM model is utilized so as to reduce computational efforts, a second boundary condition known as anti-

cyclic or anti-periodic must be imposed at two side boundaries. The ampere-conductor of the circuit is also specified together with all the material blocks to be used in the model.

4.3.1.2 Simulation.exe program

Once the data has been entered, the next is to run the simulation.exe program referred to as the processing stage. At this point the mesh is generated automatically for a quarter-model typically illustrated in Figure 4.8. A solver takes a set of data files that describe the problem and solves the relevant Maxwell's equations to obtain values for the vector magnetic potential, A_z throughout the solution domain.

4.3.1.3 Femmview.exe program

Finally, femmview.exe that forms the core of post-processing phase is essentially a graphical program that displays the resulting fields in the form of contour and density plots as shown in Figure 4.9. The program also allows the inspection of field at arbitrary points, as well as evaluates a number of different integrals and plots for various quantities of interest.

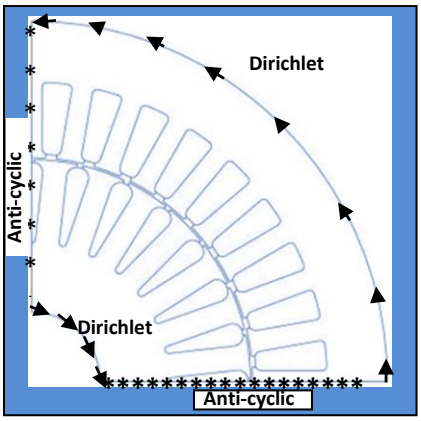


Figure 4.7: Typical Geometric Drawing

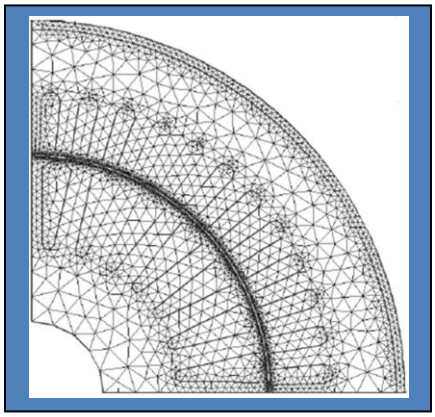


Figure 4.8: Typical Mesh Creation

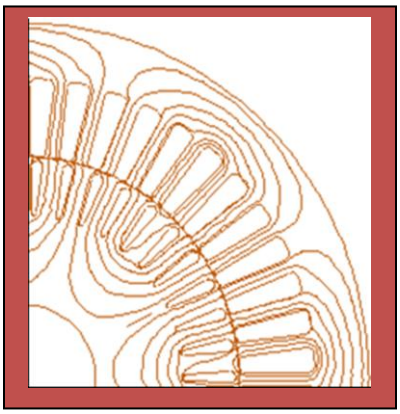


Figure 4.9: Magnetic Flux Contour Plot

4.4 DWIM Based FEMM Analysis

In this section, finite element method has been applied to determine the machine inductances. The geometric dimensions/data required to start FEMM analysis of DSWIM under consideration are presented in Table 4.1. The functional flowchart for FEMM analysis of DSWIM is depicted in Figure 4.10. The proposed flowchart is essentially a summary of the

FEMM description presented in the preceding section mainly applied in this research to calculate DSWIM inductances according to procedures set forth in the following subsections.

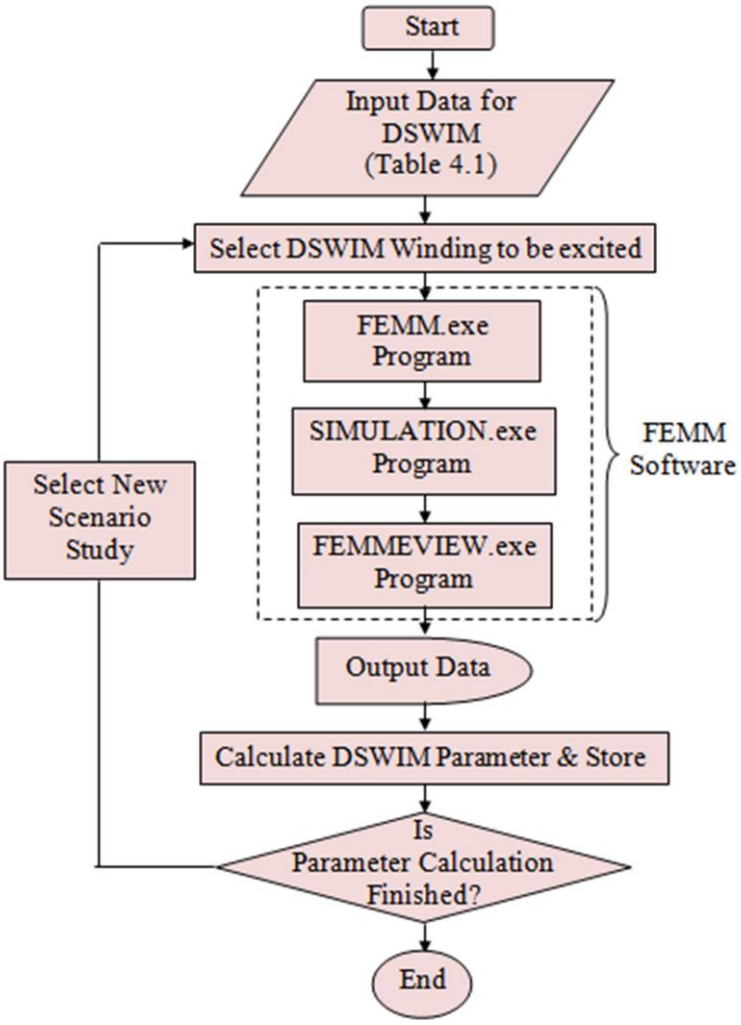


Figure 4.10: Functional Flowchart for FEMM Analysis of DSWIM

Table 4.1: Geometric Specifications for DSWIM's FEMM Model Development

DSWIM Components	Symbols	Values
Stator core external diameter	D_{os}	206 mm
Stator core internal diameter	D_{is}	150 mm
Rotor core external diameter	D_{or}	149 mm
Rotor core internal diameter	D_{ir}	111 mm
Stator axial length	L_c	100 mm

Number of stator slots	S_s	48
Number of rotor slots	S_r	42
frequency	f	50Hz
Number of Poles	P	8
Number of Phases	N_ϕ	6
Number of Conductors/stator slot	Z_c	60

4.4.1 Categorisation of DSWIM inductances

The stator and rotor winding clock diagrams developed for the complete DSWIM stator winding and each of the phases of its rotor squirrel cage are shown in Figures 4.11 to 4.14. The squirrel cage rotor is assumed to have an equivalent three phase winding-electrically displaced by 120^o. The inductances that need to be determined for DSWIM are categorized as follows:

i) Self-Inductances

These are winding inductances due to their own respect currents and they comprise:

$L_{asas};\ L_{bsbs};\ L_{cscs};\ L_{xsxs};\ L_{ysys};\ L_{zszs};\ L_{arar};\ L_{brbr};\ L_{crcr}.$

Where

abc_s – Stator 'abc' winding set; xyz_s – Stator 'xyz' winding set;

abc_r – Rotor 'abc' winding set;

ii) Mutual inductances

These are inductances of a phase due to current in another phase. They comprise the following:

Phase 'as': $L_{asbs};\ L_{ascs};\ L_{asxs};\ L_{asys};\ L_{aszs};\ L_{asar};\ L_{asbr};\ L_{ascr}$

Phase 'bs': $L_{bsas};\ L_{bscs};\ L_{bsxs};\ L_{bsys};\ L_{bszs};\ L_{bsar};\ L_{bsbr};\ L_{bscr}$

Phase 'cs': L_{csas}; L_{csbs}; L_{csxs}; L_{csys}; L_{cszs}; L_{csar}; L_{csbr}; L_{cscr}

Phase 'xs': L_{xsas}; L_{xsbs}; L_{xsas}; L_{xsys}; L_{xszs}; L_{xsar}; L_{xsbr}; L_{xscr}

Phase 'ys': L_{ysas}; L_{ysbs}; L_{yscs}; L_{ysxs}; L_{yszs}; L_{ysar}; L_{ysbr}; L_{yscr}

Phase 'zs': L_{zsas}; L_{zsbs}; L_{zscs}; L_{zsxs}; L_{zsys}; L_{zsar}; L_{zsbr}; L_{zscr}

Phase 'ar': L_{aras}; L_{arbs}; L_{arcs}; L_{arxs}; L_{arys}; L_{arzs}; L_{arbr}; L_{arcr}

Phase 'br': L_{bras}; L_{brbs}; L_{brcs}; L_{brxs}; L_{brys}; L_{brzs}; L_{brar}; L_{brcr}

Phase 'cr': L_{cras}; L_{crbs}; L_{crcs}; L_{crxs}; L_{crys}; L_{crzs}; L_{crar}; L_{crbr}

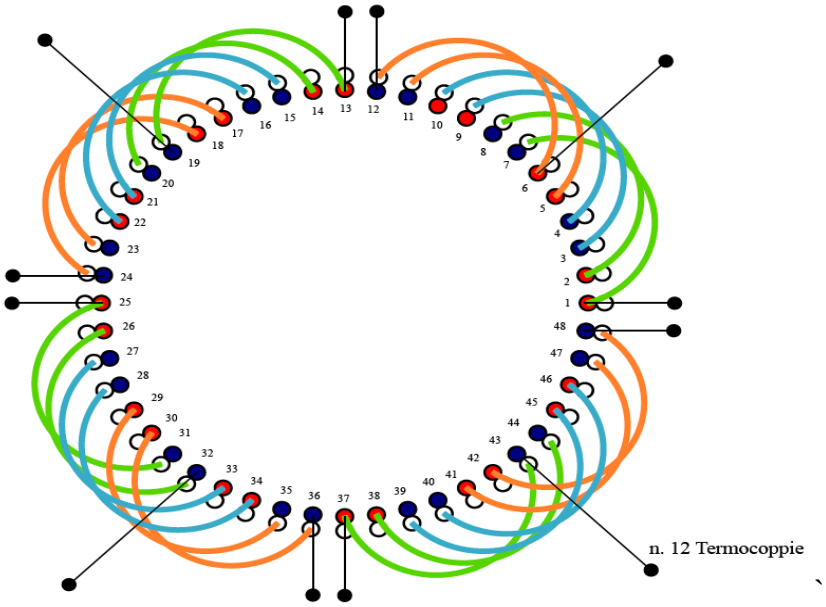


Figure 4.11: Complete Stator Winding Clock Diagram

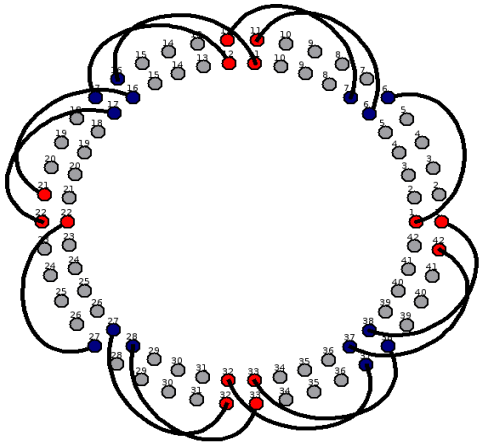


Figure 4.12: Rotor Phase 'a' Equivalent Winding Clock Diagram

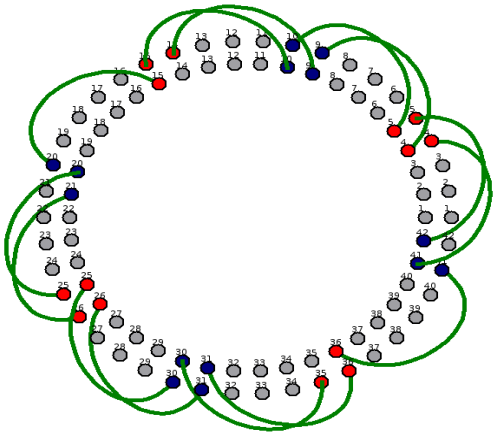


Figure 4.13: Rotor Phase 'b' Equivalent Winding Clock Diagram.

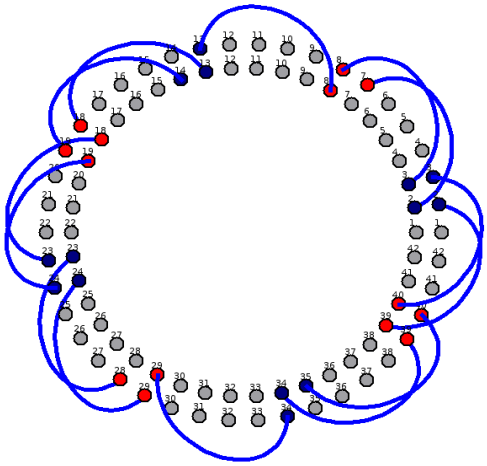


Figure 4.14: Rotor Phase 'c' Equivalent Winding Clock Diagram

4.4.2 Procedures for calculating self-inductances

The magnetic flux passing through a given surface, S is defined thus:

$$\phi = \int_{s} B \bullet n dS = \oint_{ls} A_z \bullet \tau dl \tag{4.28}$$

Where;

B: Vector magnetic flux density;

n: Unit vector normal to the surface of integration;

A_z : Vector magnetic potential; and

τ : Unit vector tangential to the line of integration.

The flux linking n conductors is then given by:

$$\lambda = n.\phi \tag{4.29}$$

If this is applied to a stator slot having Z_c conductors then the flux linking the conductors is:

$$\lambda_c = Z_c.\phi \tag{4.30}$$

The average value of magnetic potential in a slot with cross-section S_{slot}, is given by:

$$A_{av.slot} = \frac{1}{S_{slot}} \int_{Sslot} A_z dS \tag{4.31}$$

Since current enters through one slot and returns through another, then the average value of magnetic potential for a coil is given as:

$$A_{av.coil} = A_{av+} + (-A_{av-}) \tag{4.32}$$

4.4.2.1 Stator winding inductance calculation procedure

For a DSWIM with stator winding clock diagram of Figure 4.11, there are 4 coils in each phase. Thus the flux linkage of 'a' phase is found by applying equation 4.30 in conjunction with equations 4.28 and 4.32. Therefore

$$\lambda_{phase} = 4.Z_c.L_{ss}.A_{av.coil} \tag{4.33}$$

A_{av+} and A_{av-} are found by running the FEMM simulation in accordance with the flow chart of Figure 4.10;whilst in equation 4.33, L_{ss} is the inductance to be determined. Once the field solution is achieved, equation 4.32 can then be applied to find the inductances of the phases. In view of identical nature of the architecture of dual machine windings, all stator self-inductances are the same. This equally applies to the rotor winding. A typical flux distribution generated by FEMM software when only phase 'a' of stator winding is excited is shown in Figure 4.15. The FEMM mesh arrived at in this simulation has 38909 elements and 19592 nodes with excitation current at 50Hz.

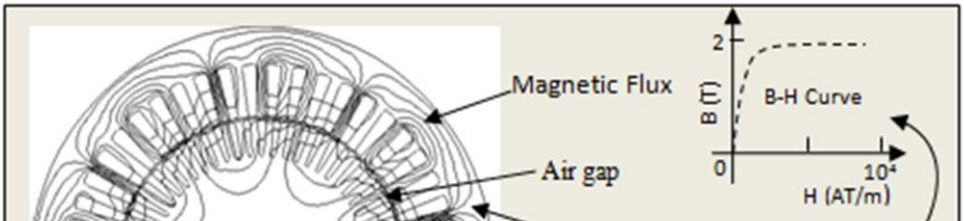


Figure 4.15: Distribution of Magnetic Flux when only Phase 'a' of the Stator is Excited

4.4.2.2 Rotor Equivalent winding inductance calculation procedure

The equivalent three phase winding of the rotor (Figures 4.12-4.14) is such that in some slots a phase may occupy a whole slot while occupying only half a slot in others. This fact has to be taken into consideration in order to accurately calculate the magnetic flux linkages of the rotor. In order to insure systematic calculation, circuits are assigned positive currents I_{p1} and I_{p2} respectively to those slots (under say north poles) completely filled up and half filled up by the conductors of phase 'a'. Similarly, negative currents I_{n1} and I_{n2} are assigned for south poles. Thus for phase 'a' from Figure 4.12: slots 1, 6, 11, 12, 16, 17, 22, 27, 32, 33, 37 and 38 are fully occupied by the conductors of the phase while occupying only half of slots 7, 21, 28 and 42. The current distribution among the slots of phase 'a' when excited, for example, by 1A will be as follows:

- I_{p1}- Slots: 1, 11, 12, 22, 32 & 33;
- I_{p2}- Slots: 21 & 42;
- I_{n1}- Slots : 6, 16, 17, 27, 37 & 38; and
- I_{n2}- Slots: 7 & 28.

The value to be assigned to total current conductors per slot I_s is given by the expression:

$$I_s = \left(\frac{current}{conductor}\right) x\ (number\ of\ slots)\ x\ \left(\frac{number\ of\ conductors}{slot}\right) \quad (4.34)$$

Hence,

I_{p1}= +1 * 6 * 68 = +408AC

I_{p2} =+1 * 2 * 34 = +68AC

I_{n1}= -1 * 6 * 68 = -408AC

I_{n2} =-1 * 2 * 34 = -68AC

The self-flux linkage of phase 'a' is therefore given by:

$$\lambda_{raa} = \frac{n_{cr}}{2} * L_{rr} * \begin{bmatrix} A_1 * 2 - A_6 * 2 - A_7 + A_{11} * 2 + A_{12} * 2 \\ -A_{16} * 2 - A_{17} * 2 + A_{21} \end{bmatrix} * 2 \quad (4.35)$$

Note that conductors in slots 6, 7, 16 and 17 provide return path for currents and thus are taken as negative. Also only half i.e. 2 pole pairs is computed and the results multiplied by 2 in view of symmetry of the phase winding about two pole pairs.

4.4.3 Procedures for calculating mutual inductances

The mutual inductances of the machine listed completely in subsection 4.4.1 are further categorized into:

i Mutual inductances due to stator phases of the same winding set.

ii Mutual inductances due to stator phases of different winding sets.

iii Mutual inductances between stator and rotor phases.

4.4.3.1 Mutual inductances due to stator phases of the same winding procedure

These inductances are calculated when only a particular stator phase of one winding set is excited and the flux linking the other stator phases of the same winding set are computed. The procedure for the calculations of the mutual inductances will call for multiple simulations of FEMM software to enable estimations of flux linkages.

4.4.3.2 Mutual inductances due to stator phases of different winding sets procedure

Here the inductances are calculated when only a particular stator phase of one winding set is excited and the flux linking the stator phases of the other winding set are computed. The procedure is to apply FEMM to calculate the mutual flux linkages from which the mutual inductances are computed.

4.4.3.3 Mutual inductances between rotor phases procedure

These inductances are computed in a similar manner as outlined in Section 4.4.3.1. As should be expected, it will also engender multiple simulations FEMM software to facilitate calculations of flux linkages and desired mutual inductances.

4.4.3.4 Mutual inductances between stator and rotor phases procedure

Unlike the cases considered in the previous subsections here the inductances, strictly speaking, are a function of rotor position. Thus the computation should be carried out at different rotor positions assuming reference or zero position to be at that point where the magnetic axes of stator and rotor phase "a" are aligned. If phase 'a' of the rotor winding is excited by a dc current (f=0 Hz) and the rotor is rotated over a pair of poles and the flux linkages of the stator phase 'a' computed via equation 4.35 at an interval of 30 electrical degrees. For illustrative purposes, the flux distribution patterns at some selected rotor angular positions are shown in Figures 4.16. The FEMM simulations created meshes that have elements within 70036 and 70158 with corresponding nodes in the range of 35153 and 35214. A careful look at the flux distribution patterns of Figure 4.16 will reveal some inherent differences causing variations in associated mutual inductances for different discrete angular positions of the rotor relative to the stator winding. The results of mutual

inductance calculations based on FEMM simulations at specific rotor angular positions, uniformly spaced between 0 and 2π will be presented and discussed in the next chapter.

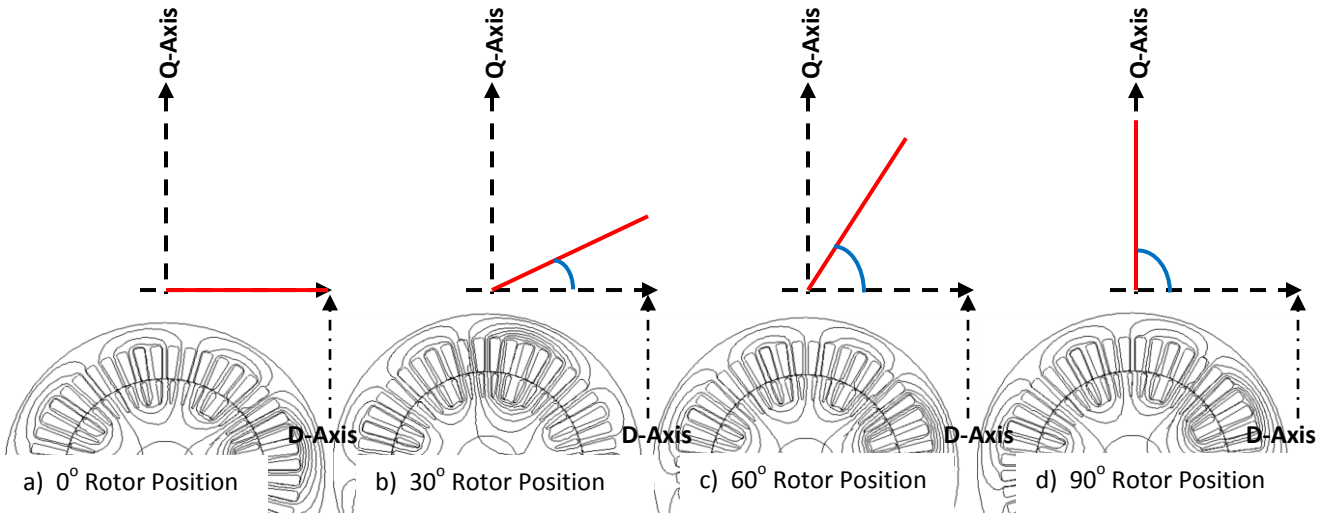


Figure 4.16: Four Flux Distribution Patterns with Phase 'a' of Rotor Excited at Different Electrical Reference angles

4.5 Determination of DSWIM Equivalent Circuit Parameters Using FEMM

In this section finite element method is used to simulate the parameters of the equivalent circuit of the machine under consideration. Two tests need to be carried out namely no-load or open circuit and blocked rotor or short circuit tests as done by Fireteanu and Romary, 2013 but for a different induction machine winding configuration.

4.5.1 No-load test FEMM simulation procedure for magnetizing inductance calculation

Under no-load test, the FEMM simulations of DSWIM are carried out at zero frequency with rotor reference frame assumed. This corresponds to a rotor slip s equals to zero. This scenario

problem in FEMM simulation environment has been referred to as magneto-static field problem by Virgiliu and Marcel, (2013). It is possible to develop a program interfaced with FEMM that automatically computes the flux linkages when the stator current is varied. The magnetizing inductance for each value of stator current is then calculated when the flux linkage is divided by its corresponding current. A representative example of magnetic flux pattern generated by FEMM under no load test is depicted in Figure 4.17. This is achieved via DSWIM cross-sectional area mesh created by FEMM comprising 70028 elements and 35149 nodes.

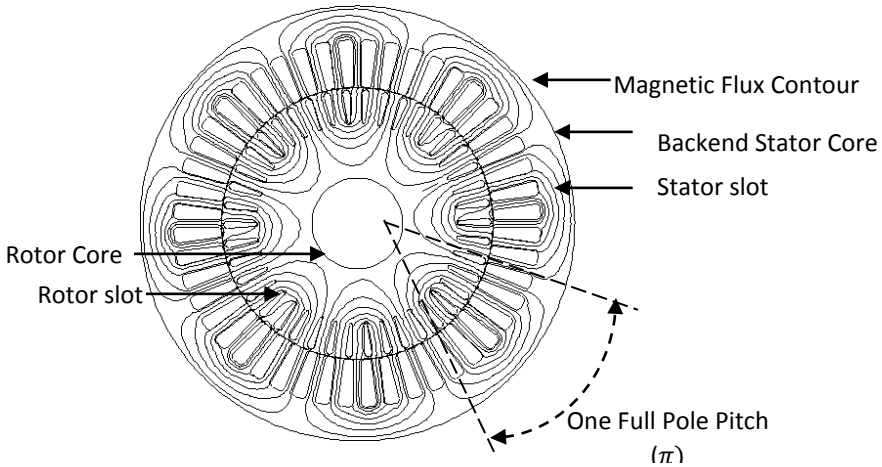


Figure 4.17: Magnetic Flux Pattern under No Load Test

4.5.2 FEMM model based locked-rotor test procedure

In all the locked rotor tests, the rotor is blocked corresponding to stationary reference frame parameterized by ω=0. Three different tests are considered in this subsection thus:

1. Firstly, only the stator 'a-b-c' winding set or 'x-y-z' winding set is supplied with rated excitation current, at specified frequency, to the FEMM model of DSWIM.
2. Secondly similar procedure is repeated but for two winding sets ('a-b-c' & 'x-y-z') having 30 electrical degrees shift between them.
3. Finally, the two stator winding sets are excited together but in this case the windings bearing zero electrical degree shift between them.

Each of the aforementioned is further expatiated upon in the subsequent subsections that follow.

4.5.2.1 Excitation of only stator 'a-b-c' winding set in FEMM model of DSWIM

In this test the stator 'a-b-c' winding set is supplied with rated current at five different values of frequency (10Hz; 20Hz; 30Hz; 40Hz and 50Hz) and as in the case of no-load test, the inductance is computed corresponding to particular values of current and frequency. The flux density plots during the locked rotor test at different frequencies but the same current are grouped together and shown in Figure 4.18 so as to facilitate comparison at a glance. The respective meshes generated by FEMM model in respect of each flux density plot are provided in Table 4.2.

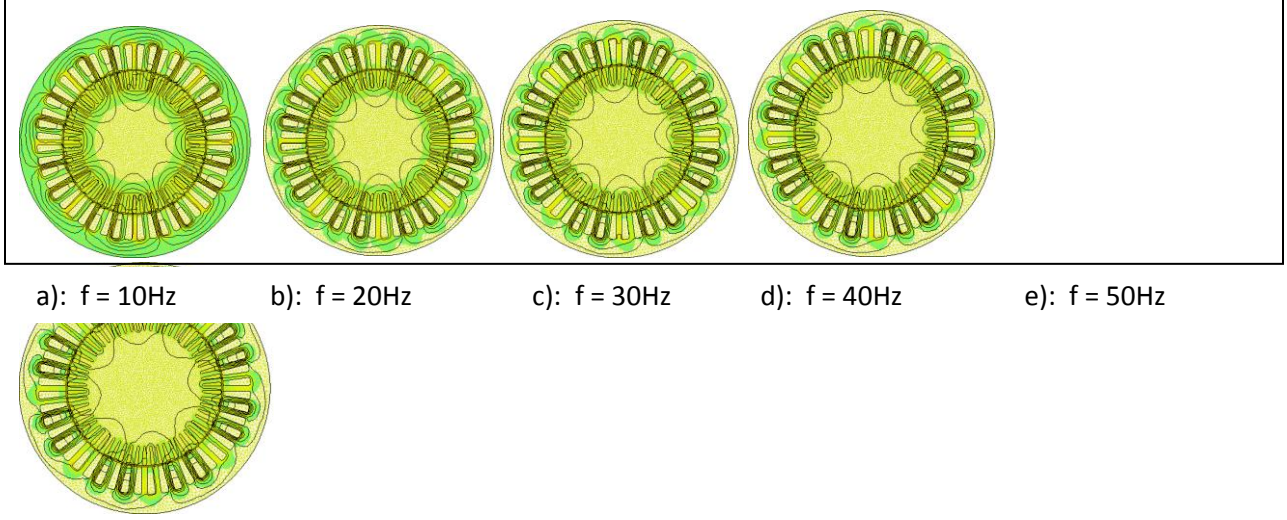


Figure 4.18: Different Flux Density Plots under Locked Rotor Tests with a-b-c Winding Excited by Rated Current.

Table 4.2: Summary of Meshes Generated FEMM Model for Different Locked Rotor Tests

FEMM Model for Locked Rotor Tests		Excitation of 'a-b-c' winding by fixed current of 3.5A at the frequency				
		10Hz	20Hz	30Hz	40Hz	50Hz
Mesh	Elements	19592	19592	19592	19592	19592
	Nodes	38909	38909	38909	38909	38909

Simulation Results	Figure 4.18	(a)	(b)	(c)	(d)	(e)

Recall that DSWIM designed in Chapter Three is equipped with similar pole ratios. This implies that the two stator winding sets 'a-b-c' and 'x-y-z' are identical but displaced electrically by 30^o. Consequently, similar results are expected to be obtained if the same experiments are repeated with only 'x-y-z' winding excited. This has been verified through several experimentations comparative analyses of magnetic flux plots for 'a-b-c' and 'x-y-z' windings, respectively. Expectedly, the magnetic flux plots for both stator windings are similar that should enable calculations of similar parameter for the two stator windings.

4.5.2.2 Excitation of both stator winding sets (with 30^0shift)

The above process is repeated with the two stator winding sets ('a-b-c' and 'x-y-z') supplied with the same (rated) current. This is equivalent to six phase system. The composite magnetic flux plots for different values of frequency are shown in Figure 4.19. Note that all the plots of figure 4.18 were also derived from the same mesh data specifications summarized in Table 4.2.

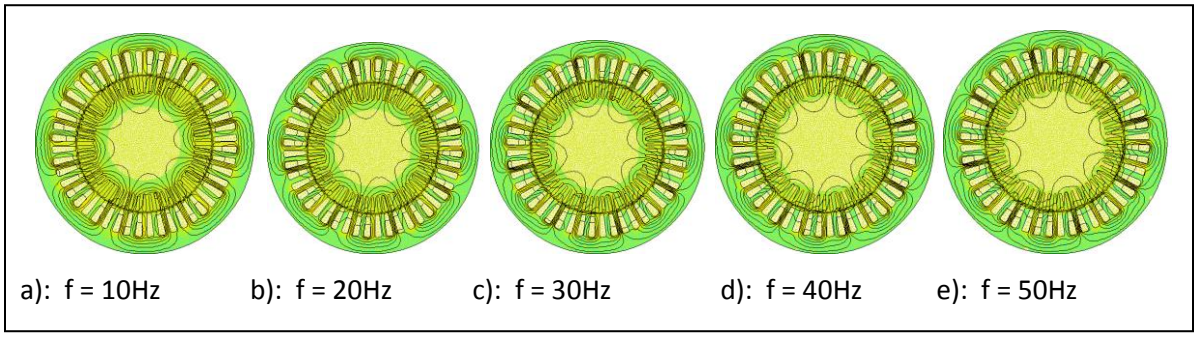


Figure 4.19: Different Flux Density Plots under Locked Rotor Tests with a-b-c Winding Excited by Rated Current with 30^o Phase Shift.

4.5.2.3 Excitation of both stator winding sets (with 0^0shift)

The two stator winding sets are excited the same way as in previous section the only difference being that here there is no phase shift between the two phases. This is equivalent

to a three phase machine with two parallel paths. The magnetic flux density plots for different frequencies but same rated current excitation condition are presented all together in Figure 4.19 to permit visual comparative analysis. Again the plots of Figure 4.18 were generated from multiple FEMM simulations based on the same mesh data specifications of Table 4.2.

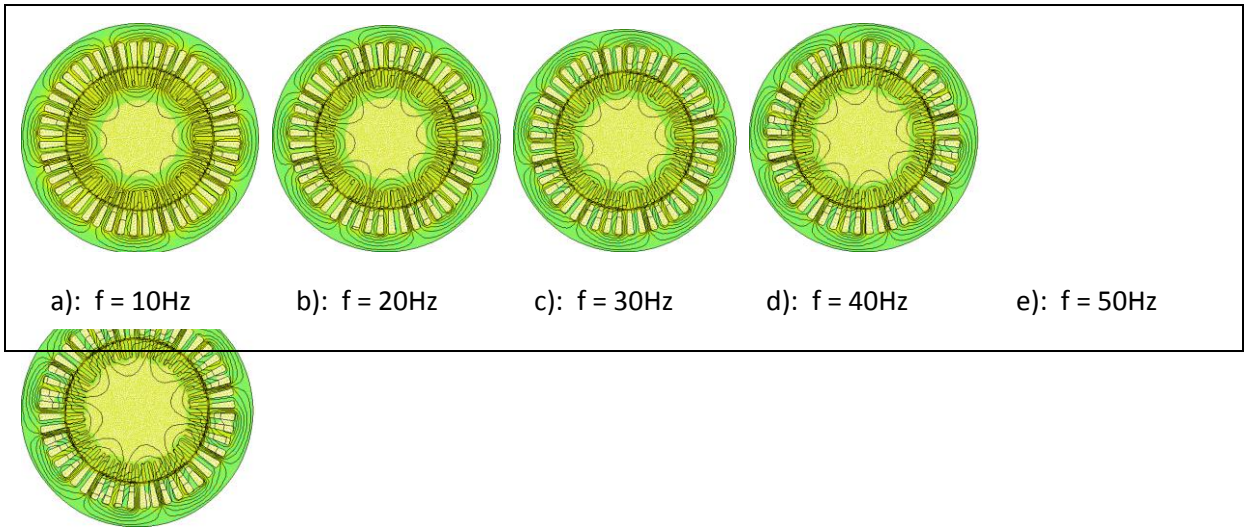


Figure 4.20: Different Flux Density Plots under Locked Rotor Tests with Both 'a-b-c' and 'x-y-z' Winding Sets Excited by Rated Current at 0^o Phase Shift.

All the flux density plots generated from the simulations of FEMM model specifically developed for DSWIM investigations under different locked rotor test scenarios constitute database needed to determine equivalent parameters for the dual stator winding induction machine having similar pole ratios. The determination of the equivalent resistance and inductance is anchored patently on the analysis of flux linkage to facilitate determination of the desired parameters. Undoubtedly, FEMM model so developed for similar pole DSWIM is aimed at determining its leading equivalent parameters. The next section will deal with the

computation of equivalent parameters for similar pole ratio DSWIM within the simulation framework of its FEMM model.

4.6 Determination of Equivalent Resistance and Inductance for DSWIM

Maxwell stress tensor has become a mathematical tool available within finite element analysis suite to facilitate accurate calculation of magnetic forces torque. Relying on the fundamental derivations in (Stanley, 2012;), the general force Law is given by:

$$F = \frac{1}{\mu_o} \iint dA\, \bar{\varsigma}.\boldsymbol{n} \tag{4.36}$$

Where **n:** Is a unit vector pointing out of surface dA and the quantity $\bar{\varsigma}$ is the Maxwell stress tensor for magneto-static fields given in Cartesian coordinates thus:

$$\varsigma = \frac{1}{\mu}\begin{bmatrix} B_x^2 - B^2/2 & B_xB_y & B_xB_z \\ B_yB_x & B_y^2 - B^2/2 & B_yB_z \\ B_zB_x & B_zB_y & B_z^2 - B^2/2 \end{bmatrix} \tag{4.37}$$

Where $B^2 = B_x^2 + B_y^2 + B_z^2$ and now considering 2-dimensional plane and using polar coordinates, equation 4.37 yields a radial stress component ς_r and tangential stress component ς_φ in equations 4.38 and 4.39 (Rodriguez, 2007):

$$\varsigma_r = \frac{1}{2\mu_o}(B_r^2 - B_\varphi^2) \tag{4.38}$$

And

$$\varsigma_\varphi = \frac{1}{\mu_o} B_r B_\varphi \tag{4.39}$$

Where B_r and B_φ are the radial and tangential components of the magnetic flux density in the air gap. The electromagnetic torque can then be calculated as follows (Vaseghi, et al. 2009):

$$T_e = \frac{D_{or}L_c}{\mu_o}\oint(B_r\, xB_\varphi)ds \tag{4.40}$$

FEMM is applied to calculate the torque in accordance with equation 4.40. Herein, The Maxwell stress tensor is computed along a line within the air-gap of DSWIM being investigated. It should be recalled that torque is also proportional to the air gap power.

For a given rotor structure of DSWIM with known current density J known in every elemental volume, its rotor Joule losses are given by:

$$P_{jr} = \iiint \rho \frac{J^2}{2} dV \tag{4.41}$$

The estimation of P_{jr} using FEMM model of DSWIM is implied from locked rotor simulations earlier discussed. Further, the magnetic energy stored in DSWIM can be calculated from the following expression.

$$W_m = \frac{1}{2}\iint HdBdl = \iint JdAdl \tag{4.42}$$

The computation of W_m according to equation 4.42 will engender the use of FEMM locked rotor model of DSWIM to estimate accurately the current distribution in the rotor structure. With P_{jr} and W_m determined from several simulations of FEMM model developed for the DSIM, the equivalent parameters can be calculated and in addition, their frequency dependency investigated.

The electromagnetic torque $T_e$and rotor Joule losses P_{jr} are related via synchronous speed ω_s (Baradoet'al, 2013). Thus:

$$T = \frac{P_{jr}}{\omega_s} = \frac{P_{jr}}{(4\pi f/P)} \tag{4.43}$$

Where f is the frequency adopted in the simulation and P is the number of poles. Note that 2πf/p is the synchronous speed of each simulation of FEMM locked rotor model.

Finally, with rotor Joule lossesP_{jr} and total magnetic energy W_m accurately determined via several simulations of FEMM model developed, the equivalent resistance and inductance of DSWIM can be calculated from the expressions:

$$R_{eq} = \frac{P_{jr}}{3I^2} \tag{4.44}$$

$$L_{eq} = \frac{2W_m}{3I^2} \tag{4.45}$$

Where R_{eq} and L_{eq} are the equivalent resistance and inductance, respectively.

The main objective of DSWIM based FEMM model is symbolized in the functional block diagram shown in Figure 4.19. It is worth mentioning that FEMM model developed has provided an avenue for determination of critical parameters for DSWIM to facilitate its detailed performance evaluation and control synthesis. It is essential that the performance characteristics of the dual stator winding induction machine so obtained must closely match the original three phase machine.

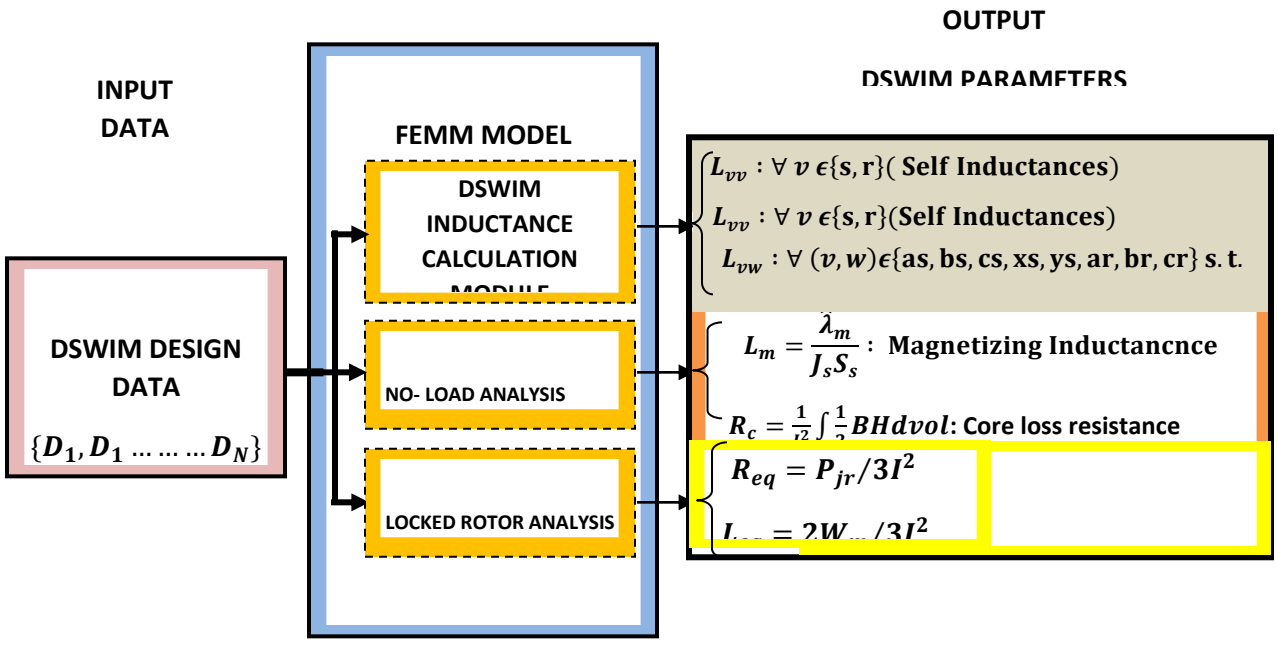


Figure 4.21: Functional Block Diagram of DSWIM Based FEMM Model

4.7 Summary

This chapter has developed a detailed simulation model for DSWIM, equipped with similar pole ratios, in MATLAB/Simulink environment using arbitrary dq0 reference frame. The inclusion of zero-axis component in the DSWIM simulation model has opened the possibilities to accommodate unbalanced investigation of similar pole DSWIM under different loading scenarios. The modelling complexity of DSWIM has considered mutual coupling between 'a-b-c' and 'x-y-z' windings housed in the stator frame. In addition, the application of FEM to model DSWIM has been developed with the framework of its detailed magneto-static analysis in 2-D space. The FEM modelling effort made in respect of similar pole DSWIM design has enabled estimations of its steady state parameters. The next chapter will be concerned with:

1. Detailed evaluation of the mathematical simulation of similar pole DSWIM within MATLAB/Simulink platform to generate meaningful results; and
2. Comparisons of parameters determined via its finite element method modelling against DSWIM parameters determined from its design approach as well as prototype realization.

In the next chapter, we will present all the results and their comprehensive discussions so as to illuminate the main achievements of this research work.

CHAPTER FIVE

RESULTS AND DISCUSSIONS

5.1 Introduction

This chapter is devoted wholly to presentations of all far-reaching results obtained as well as their extensive and in-depth discussions to illuminate the achievements of the cardinal goals pursued in this dissertation. In order to enhance clarity of presentations of numerous results and comprehend their attendant discussions in straightforward manner, the chapter is organized sequentially into three broad sections. Section 5.2 presents the pertinent outcomes of all design considerations (winding functions, improved classical design and GA optimization) specifically focused on similar pole DSWIM and demonstrated for 8/8 pole ratios as case study. In section 5.3, extensive simulation results of 8/8 pole DSWIM in Simulink/MATLAB environment are contained therein along with FEMM model characterizations of the same dual stator winding machine. Finally, several experimental results on the prototype 8/8 pole DSWIM can be found in Section 5.4.

5.2 DSWIM Design Consideration Results

In this section, significant results that emerged in respect of DSWIM based design activities carried out in this research work are set forth. The results are further split into subsections so as to facilitate their logical and meaningful discussions. This is put to effect by presenting in the subsequent subsections dedicated to the results of:

i. DSWIM improved classical design approach;

ii. GA based power factor/power efficiency optimisation;

iii. Winding function based DSWIM parameter calculations; and

iv. FEMM model of DSWIM for its parameter determinations.

5.2.1 Results of DSWIM improved classical design (ICD) approach

This subsection presents the results of improved classical design approach entertained for magnetic design and also determination of leading parameters of DSWIM. Relying on the algorithmic computational procedure of Chapter Three, the machine design results are presented in Tables 5.1 and 5.2. As mentioned earlier the design affects only the stator winding alone. The stator frame and squirrel cage rotor (including the rotor bars) remain unaltered. Therefore the results obtained and summarized in Table 5.1 are as a result of electromagnetic calculations carried out on the stator frame of a standard to house the new dual winding sets in which the prescribed magnetic and electric loading constraints are satisfied.

Table 5.1: Design Parameters for 8/8 Pole DSWIM Case Study

Components/Parameters	**Symbols**	**Values**
Stator core external diameter	D_{os}	206 mm
Stator core internal diameter	D_{is}	150 mm
Rotor core external diameter	D_{or}	149 mm
Rotor core internal diameter	D_{ir}	111 mm
Stator axial length	L_c	100 mm
Number of stator slots	S_s	48
Number of rotor slots	S_r	42
frequency	f	50Hz
Number of Poles	P	8/8
Magnetizing current	I_m	1.67A
Surface current density	J_s	$3X10^4$ AC/m
Number of turns per coil	N_{coil}	60
Conductor diameter	d	0.72mm
Stator current density	J_s	$3.5A/mm^2$

Stator winding resistance	r_s	1.5Ω
Stator winding leakage inductance	L_s	13.8mH
Magnetizing inductance	L_m	0.12H

Table 5.2: Calculated DSWIM Steady State Parameters

DSWIM Unit Identifier	**Parameters**		**Calculated Values (Ω)**
	Definitions	**Symbols**	
Magnetic circuit	Magnetizing Reactance	X_m	37.68
Core Loss	Core Resistance	R_c	253
'a-b-c' winding (Stator)	Leakage Reactance	X_{ls}^a	4.33
	Resistance	R_s^a	1.50
'x-y-z' winding (stator)	Leakage Reactance	X_{ls}^x	4.33
	Resistance	R_s^x	1.50
Rotor winding	Leakage Reactance	X_{lr}	15.38
	Resistance	R_r	0.63

Figure 5.1 depicts magnetic flux density and magneto-motive force (MMF) bar charts in various magnetic flux paths of similar pole ratio DSWIM. Note, in particular, that the flux magnetic densities in various ferromagnetic paths met the imposed constraints. It is worth mentioning that similar computations carried out by Wu (1998), albeit for dissimilar pole ratio DSWIM, corroborated with the results presented herein. Consequently, the magnetic and electric loadings computed for the DSWIM (see Table 5.2) did not exceed the design values for the original standard 3-ϕ IM. The correlation between flux density and corresponding magneto-motive is evident from cursory look at Figure 5.1. Inspired by earlier work in (Ostovic, 1994), variational calculations in respect of induced voltage normalized by its supply voltage, specifically for similar pole ratio DSWIM, are shown in Figure 5.2 as 3-D plot with the slip, s and supply frequency, f as x- and y- axis, respectively.

The import of this figure is to An illustrative 3-D plot has been done in Figure 5.2 for spatial distribution of flux density in stator under one pole of DSWIM case study.

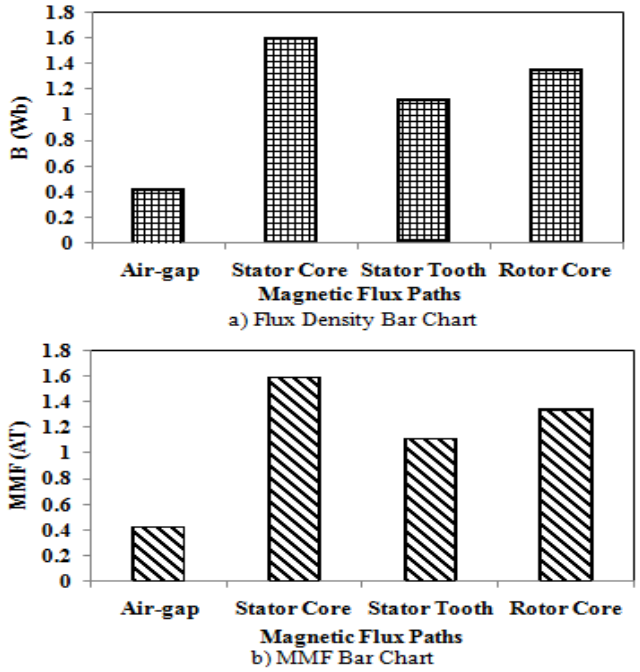


Figure 5.1: Bar Charts of a) Flux Densities and b) MMFs in Various Magnetic Flux Paths

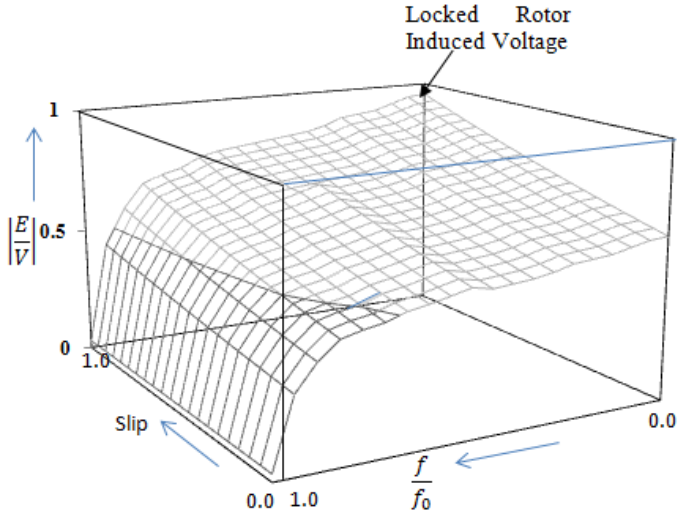
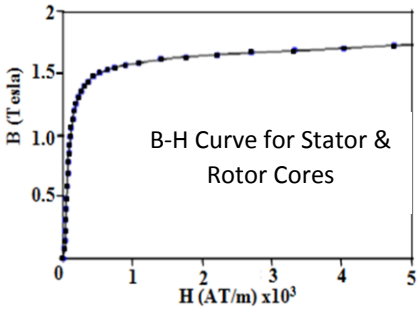


Figure 5.2: 3-D Plot of Normalized Induced Voltage in DSWIM Rotor as a Function of Slip, s and Frequency



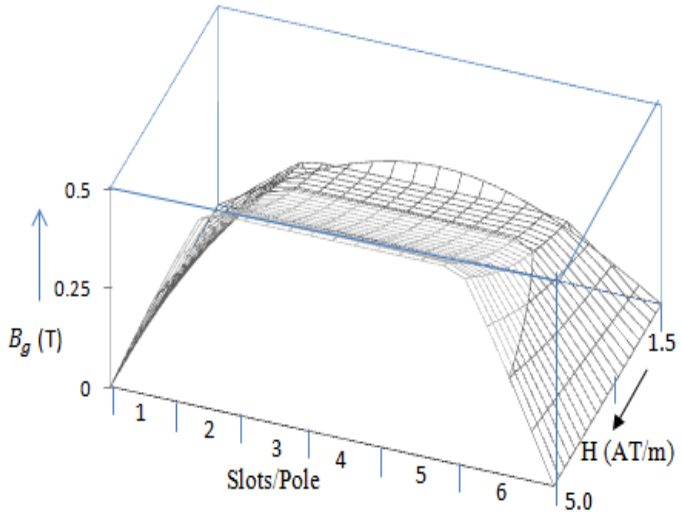


Figure 5.3: 3-D Plot of Tooth Flux Density Spatial Distribution under One Pole of DSWIM
Figure 5.4: Nonlinear B-H Curve of the Iron Core

5.2.2 Results of GA optimization of DSWIM power factor and efficiency

The flow chart of Figure 3.21 has offered the sequence of algorithmic steps of GA to be implemented in order to determine the optimal values of the power factor and efficiency of the DSWIM. Note that the decision variables (power factor and efficiency) have been introduced into the expressions of the objective function given in. equation 3.78 and as equality constraints in equations 3.80 and 3.81. A program has been developed in MATLAB environment and the resulting code listings provided in Appendix F. The DWSIM physical data inputs into GA program derive from Tables 5.1 to 5.3 that also included upper and lower limits on the decision variables as well as electric and magnetic loadings. The critical GA parameters utilized in the developed software to search optimum power factor and efficiency for DSWIM are presented in Table 5.3. MATLAB GA toolbox was used to generate the initial population size in conjunction with the 'seed' feasible solutions generated from the classical DSWIM design approach. Herein situates the DSWIM design goal which is to hybridize classical design approach and GA optimization technique to achieve improved magnetic and electric loadings for the case study.

Table 5.3 Summary of GA Simulation Parameters

Parameters	Values
Population Size	20
Cross over Rate	.02
Mutation Rate	0.8
Maximum Number of Generations	100

Table 5.4 shows the simulated multi-objective functions that enabled the optimal values of the power efficiency and power factor for the 8/8 pole DSWIM case study to be obtained from several runs. The power factor and power efficiency for several runs are presented in Table5.6 along with their corresponding objective function value. A cursory look at this table of various optimal values of the power efficiency and power factor reveals the optimal convergence occurred at run 4 to run 6. This informed the basis for the selection of power efficiency of 0.934 and power factor of 0.8802. Figure 5.5 shows the convergence characteristics plot in PF-η plane. Figure 5.6 is a 'screen capture' of the pictorial display of the MATLAB multi-objective GA solver component that optimized the power efficiency and power factor objective functions for the DSWIM case study. The final DSWIM design results that emerged from hybridized classical design approach and GA optimizer are presented in Table 5.5. For comparative evaluation purpose, the parameters for the standard 3-ϕ IM are summarized in Table 5.5. The improvement in DSWIM efficiency over its equivalent conventional 3-ϕ IM is evident at full load.

Table 5.4: Convergence in Power Efficiency and Power Factor

Numbers of Huns	**Power Efficiency**	**Power Factor**

Run1	0.8561	0.9396
Run2	0.8327	0.9661
Run3	0.8568	0.9389
Run4	0.934	0.8802
Run5	0.934	0.8802
Run6	0.934	0.8802
Run7	0.9136	0.8805

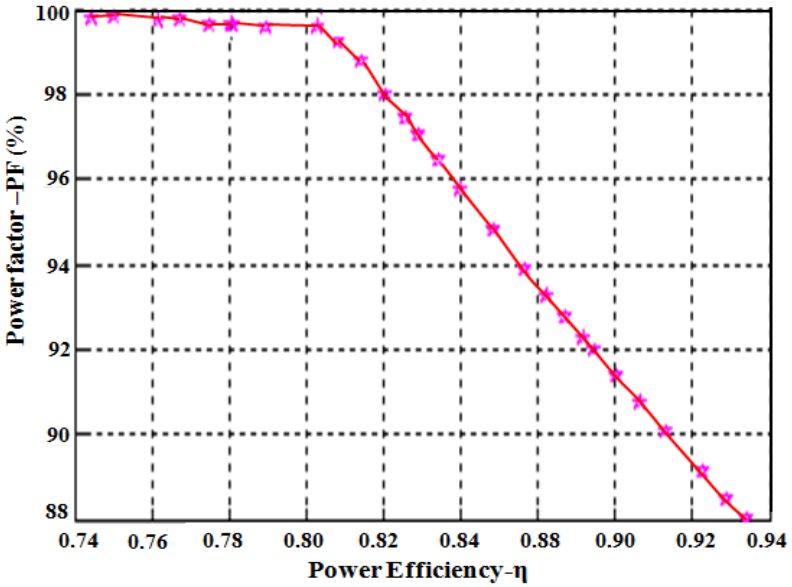


Figure 5.5: Optimal Values of Power Factor against Power Efficiency

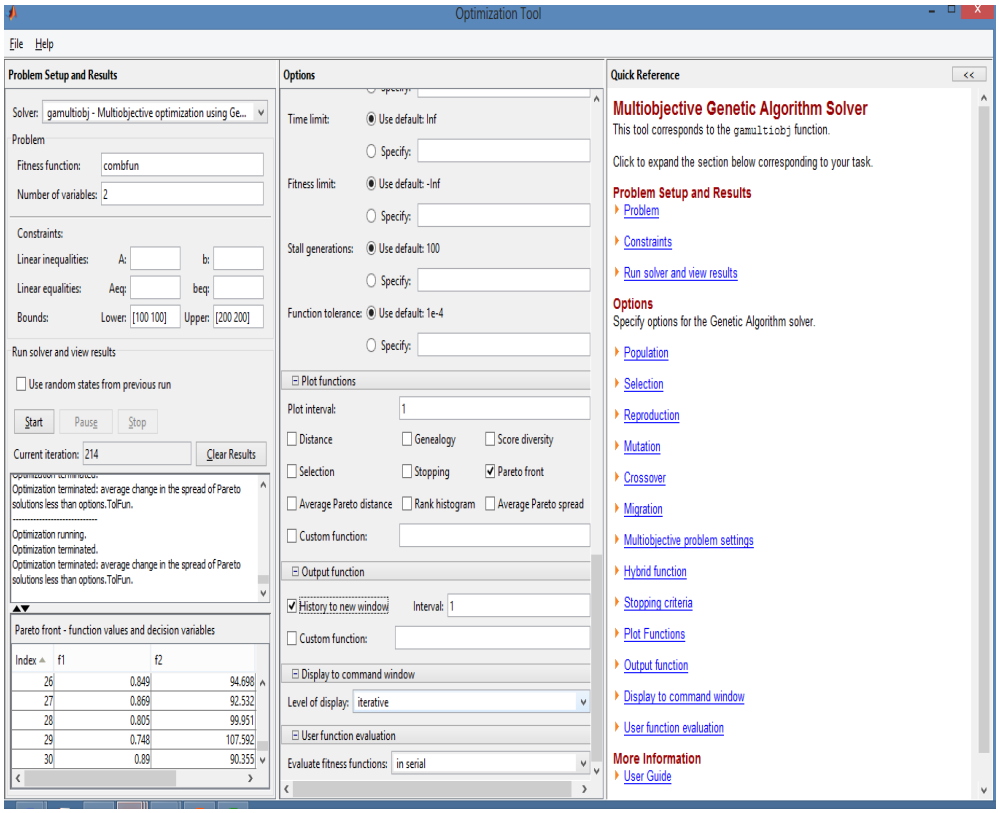


Figure 5.6: Screen Capture of GUI for the GA Optimization in MATLAB Environment

Table 5.5: Final Design DSWIM Values Based on ICD and ICD+GA Compared with 3-ϕ IM

Design Parameters	DSWIM		Standard 3-ϕ IM
	ICD	ICD+GA	
Core length, L_c	100 (mm)	100 (mm)	100 (mm)
Inside diameter of stator, D_{is}	150 (mm)	150 (mm)	150 (mm)
Outside diameter of rotor, D_{or}	149.2 (mm)	149.2(mm)	149.2(mm)
Outside diameter of stator, D_{os}	229 (mm)	229 (mm)	229 (mm)
Power factor (pf)	0.83	0.88	0.80
Efficiency (η)	89%	0.934	87%
Pole number (P)	8	8	8
Number of stator slot (S_s)	48	48	48
Number of skewed rotor bars (S_r)	42	42	42
Frequency (f)	50	50	50
Input Voltage (V_{L-L})	380 (rms)	380	380
Stator winding factor (k_w)	0.96	0.96	0.96
Number of Turns/Coil	60	53	120
Magnetic loading (B_g)	0.425	0.368	0.425
Electric Loading (ac)	30 000	27 000	52×10^4
Magnetizing Current (I_m)	0.67	0.56	1.33
Magnetizing Inductance (L_m)	0.12	0.16	0.347

5.2.3 Results of DSWIM parameter calculations based on winding function approach

Relying on the equations summarized in Table 2.6, applicable data extracted from Table 5.1 and Excel Spread sheet macros, the computed phase variable inductances for 8/8 pole DSWIM are presented in Table 5.6. Note that the winding function approach only allows the computations of inductances of DSWIM from the nature of its formulation and underlying assumptions delineated in Chapter Two.

Table 5.6: Calculated Parameters for a Test Case DSWIM

Inductance & Resistance Classifications	**Winding Set**		**Symbols used**	**Calculated Value (H)**
Self-Inductances	Stator	a-b-c x-y-z	$L_{asas}; L_{bsbs}; L_{cscs}$ $L_{xsxs}; L_{ysys}; L_{zszs}$	0.0138
	rotor	a-b-c	$L_{arar}; L_{brbr}; L_{crcr}$	0.049
Mutual Inductances	stator-stator	a-b-c ↔a-b-c x-y-z↔x-y-z	$L_{asbs}; L_{ascs}; L_{bscs}$ $L_{xsys}; L_{xszs}; L_{yszs}$	0.042
		a-b-c↔x-y-z	$L_{asys}; L_{aszs}; L_{aszs}$ $L_{bsys}; L_{bszs}; L_{bszs}$ $L_{csys}; L_{cszs}; L_{cszs}$	0.06428
	stator-rotor	as-bs-cs↔ar-br-cr xs-ys-zs↔ar-br-cr	$L_{asar}; L_{asbr}; L_{ascr}$ $L_{bsar}; L_{bsbr}; L_{bscr}$ $L_{csar}; L_{csbr}; L_{cscr}$	Depend on rotor position
Leakage Inductances	stator	a-b-c x-y-z	$L_{las}; L_{lbs}; L_{lcs}$ $L_{lxs}; L_{lys}; L_{lzs}$	0.0057
	rotor	ar-br-cr	$L_{lar}; L_{lbr}; L_{lcr}$	0.00347
Mutual leakage Inductances	stator-stator	a-b-c ↔a-b-c x-y-z↔x-y-z	$L_{lasbs}; L_{lascs}; L_{lbscs}$ $L_{lxsys}; L_{lxszs}; L_{lyszs}$	0.0027
		a-b-c↔x-y-z	$L_{asys}; L_{aszs}; L_{aszs}$ $L_{bsys}; L_{bszs}; L_{bszs}$ $L_{csys}; L_{cszs}; L_{cszs}$	0.00193
	stator-rotor	as-bs-cs↔ar-br-cr as-bs-cs↔ar-br-cr	$L_{lasar}; L_{lasbr}; L_{lascr}$ $L_{lbsar}; L_{lbsbr}; L_{lbscr}$ $L_{lcsar}; L_{lcsbr}; L_{lcscr}$	___

As can be inferred from Table 5.1, the equalities of all self inductances of, and all mutual inductances amongst, dual stator winding sets as well as all self and mutual inductances of rotor windings derive essentially from various windings symmetrical arrangements. However, all mutual and leakage inductances between stator winding sets on one hand and

rotor winding set on the other depend on the rotor position. With the additional knowledge of each winding set resistances, the mathematical model for DSWIM, can then be derived in phase variable form and subsequently transformed into arbitrary reference frame; as outlined in Chapter Two and finally accomplished in Chapter Four.

5.2.4 Results of FEMM model of DSWIM for parameter estimations

In this subsection, the results of FEMM modelling of DSWIM are presented. In the main, FEMM model of DSWIM has enabled the determination of its parameters as discussed in sequel.

5.2.4.1 Results of self inductances stator windings

Based on the procedure set forth in subsection 4.4.2, the results for the stator a-b-c and x-y-z windings self inductances are presented

$$L_{asas} = L_{bsbs} = L_{cscs} = L_{xsxs} = L_{ysys} = L_{zszs} = 13.8mH$$

5.2.4.2 Results of self inductances of rotor windings

In the case of the rotor (squirrel cage), the values of magnetic potentials are found from simulation using the program listed in Appendix G. The flux linkage when divided by the current of that phase gives the value of the self-inductance of the phase. Applying this technique to equivalent rotor a, b and c phases, the rotor self-inductances are found to be:

$$L_{arar} = L_{brbr} = L_{crcr} = 0.049\ H$$

5.2.4.3 Results of mutual inductances of intra-stator windings

The mutual inductances of interest here are those between phases of independent stator windings. Following the procedures outlined in subsection 4.4.3.3 anchored on FEMM simulations, the results of these computations are as presented below:

$$L_{asbs} = L_{bsas} = L_{ascs} = L_{csas} = L_{bscs} = L_{csbs} = L_{xsys} = L_{ysxs} = L_{xszs} = L_{zsxs} = L_{zsys} = L_{yz} = -42.3mH$$

The results obtained are in agreement with theory where, in this case, the mutual inductances expected to be approximately negative one-third of self-inductance of each winding. Expectedly, mutual inductances are equal due to winding spatial symmetry and their identical configurations.

5.2.4.4 Results of mutual inductances of inter-stator windings

The mutual inductances calculated are between phases of independent stator windings in contrast to that computed in the preceding subsection. Indeed, the procedures for the computations of these mutual inductances are fundamentally the same. Relying on the established technique, the results of these computations are presented below:

$$L_{ax} = L_{xa} = L_{by} = L_{yb} = L_{cz} = L_{zc} = 85.7mH$$

$$L_{ay} = L_{ya} = L_{bz} = L_{zb} = L_{cx} = L_{xc} = -86.4mH$$

$$L_{az} = L_{za} = L_{bx} = L_{xb} = L_{cy} = L_{yc} = 0.3mH$$

These values are within the range obtained by other researchers (Alberti et aL. 2008).

5.2.4.5 Results of mutual inductances of rotor windings

The inductances between rotor phases are computed in a similar manner as laid out in subsection 4.4.3.1. The results of the computations are:

$$L_{arbr} = L_{brar} = -0.27H$$

$$L_{arcr} = L_{crar} = 0.07H$$

$$L_{\quad} = L_{\quad} = -0.19H$$

It is worthy of mention that the computations of the above inductances are based on the FEMM simulations. Note that the mutual inductances of rotor windings are not equal due to asymmetric arrangements of the equivalent 'ar-br-cr' windings as captured in clock diagrams shown in Figures 4.12 to 4.14

5.2.4.6 Results of mutual inductances between stator and rotor windings

The flux distributions as obtained from FEMM model of DSWIM for some selected rotor angular positions are shown in Figure 4.16 enabled the calculations of mutual inductances between stator and rotor windings. The results which are then plotted in Figure 5.7 reveal that the rotor to stator mutual inductance varies sinusoidally with rotor position.

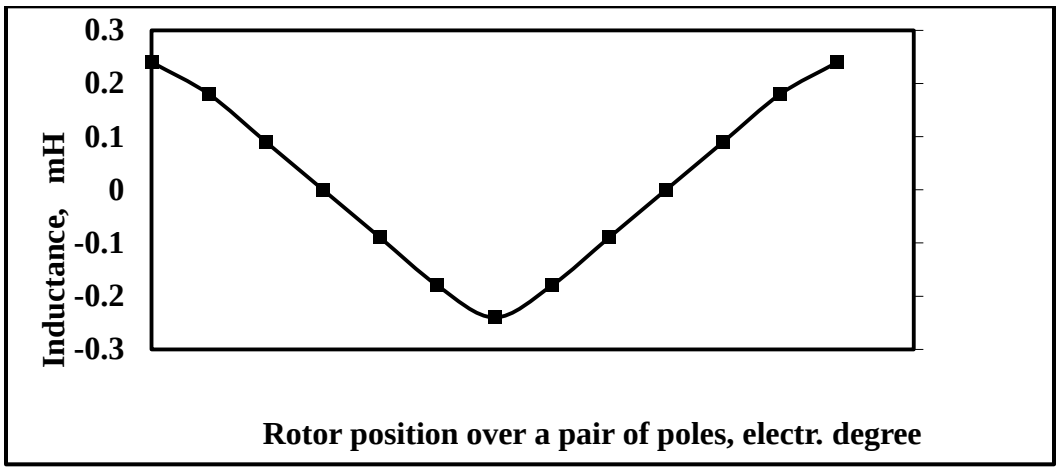


Figure- 5.7: Variation of Rotor-Stator Mutual Inductance with Rotor Position

The sinusoidal variation of the rotor-stator mutual inductances with rotor position signifies the symmetrical nature of the machines magnetic circuit. This means that for any given point on a north (south) pole, there exists a similar but opposite point on a south (north) pole with exactly the same magnetic characteristics. The peak value of the sinusoidal inductance extracted from Figure 5.7 is 0.26mH.

5.2.4.7 Results of equivalent Circuit Parameter Determinations from FEMM Model

As described in Subsection 4.5.2, three experiments were carried out on the FEMM model of DSWIM to emulate locked rotor tests at different angular positions of the rotor relative to the stator windings. A program has been written in "Luascript" listed in Appendix G and interfaced with FEMM model to automatically compute the flux linkages when the stator current is varied. The variation of the inductance with stator current is shown in Figure 5.8 along with the magnetization curve of the stator/rotor core utilized.

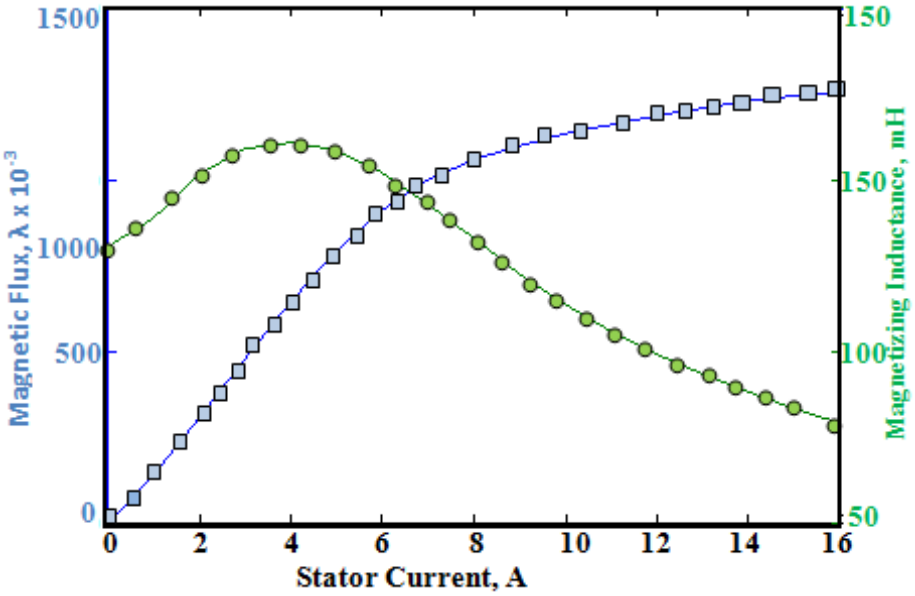


Figure 5.8: Variation of Magnetizing Inductance (L_m) with Stator Current

5.2.4.8 Analysis of FEMM simulation results

In order to support comprehensive discussion of FEMM simulation results, we present here again its complete implementation functional flow chart shown in Figure 5.9. From each finite element analysis based on the excitation current and frequency yielded the following computed quantities.

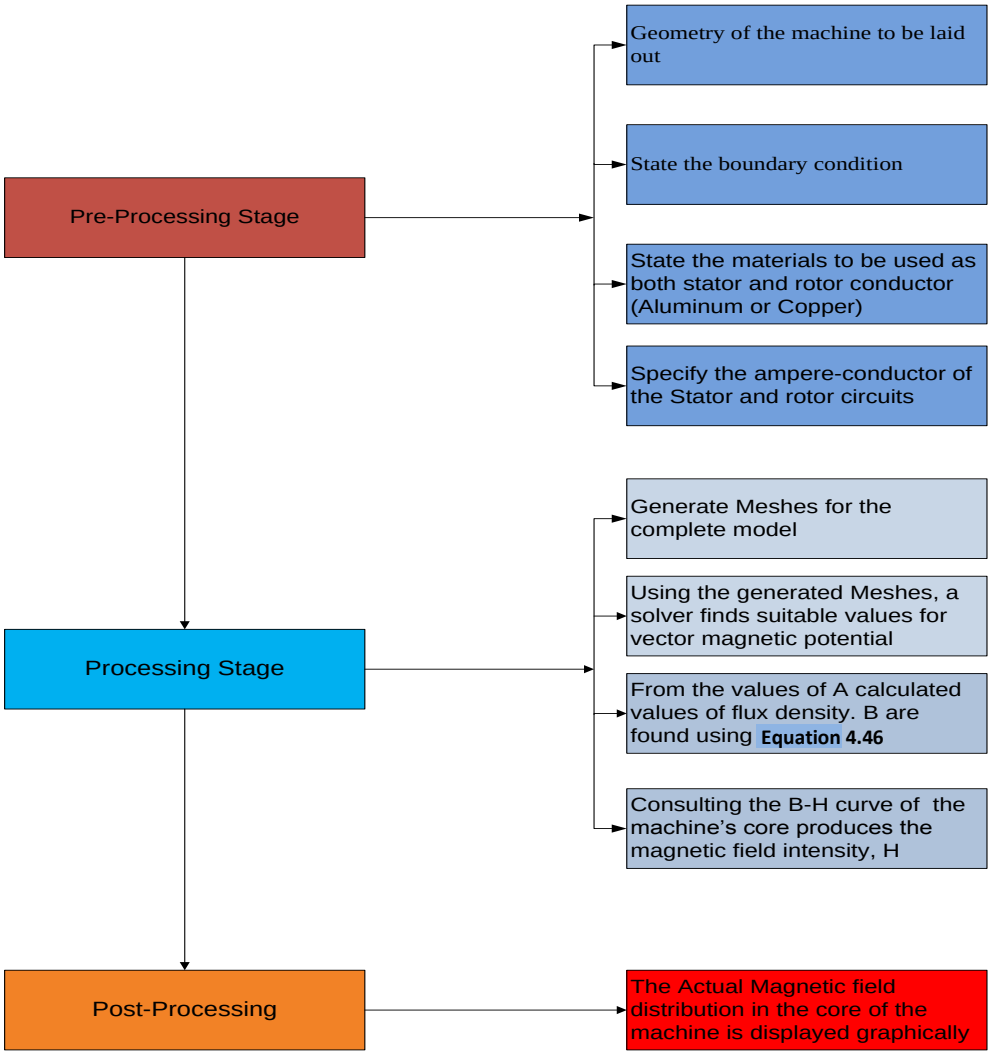


Figure: 5.9: A Detailed Functional Flow Chart Used in the Implementation of FEMM Model Development for DSWIM

1. Phase a/x flux linkage (real and imaginary part), $\lambda_{a/x}$; Vs
2. Phase b/y flux linkage (real and imaginary part), $\lambda_{b/y}$; Vs
3. Phase c/z flux linkage (real and imaginary part), $\lambda_{c/z}$; Vs
4. Torque computed from Maxwell stress tensor, T; Nm
5. Rotor Joule losses, P_{jr}; Watt
6. Magnetic energy, W_m; J
7. Magnetic co-energy, W_m; Joule

8. Integral of $A \cdot \boldsymbol{J}, W_{AJ}$; Joule

The foregoing quantities were then exported to MATLAB to enable calculations of fundamental DSWIM equivalent parameters, R_{eq} and L_{eq} and generate other far reaching results presented in graphical forms herein. The graphical presentations of results in Figures 5.10 to 5.112 essentially portray the parametric variations of some quantities of DSWIM for specified excitations versus different frequencies. They are further elaborated upon in what follows.

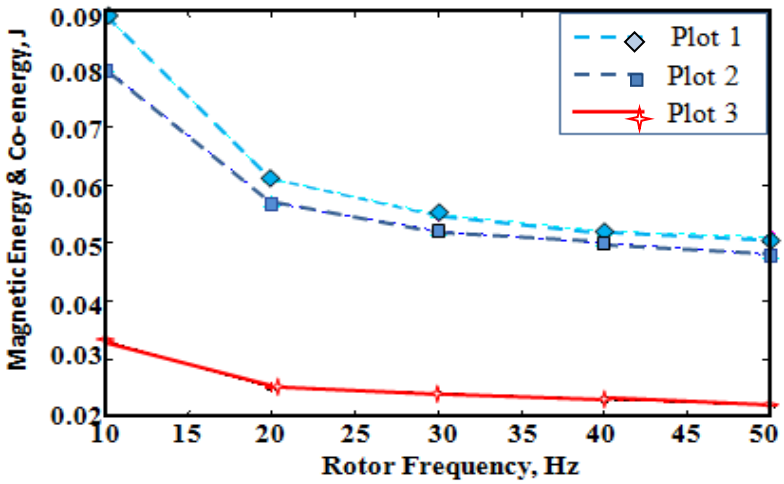


Figure 5.10: Magnetic Energy and Co-energy versus Rotor Frequency

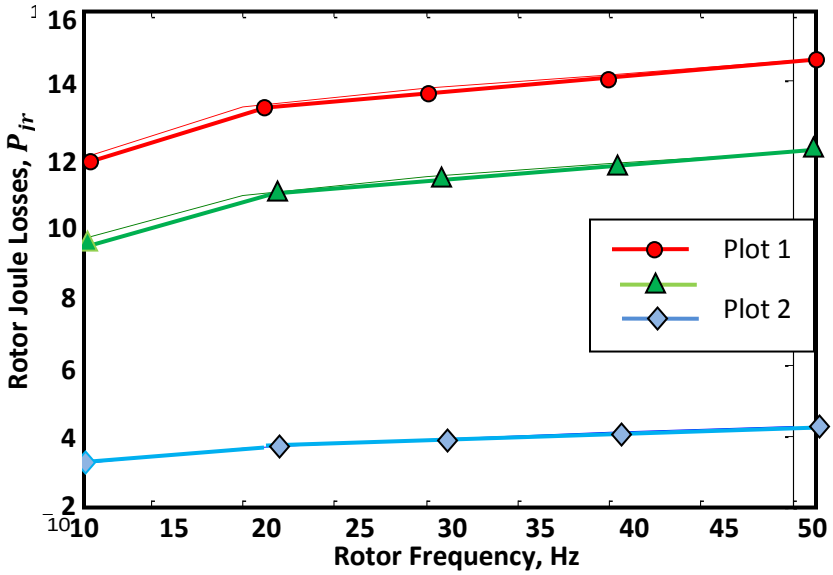


Figure 5.11: Rotor Joule Losses versus Rotor Frequency

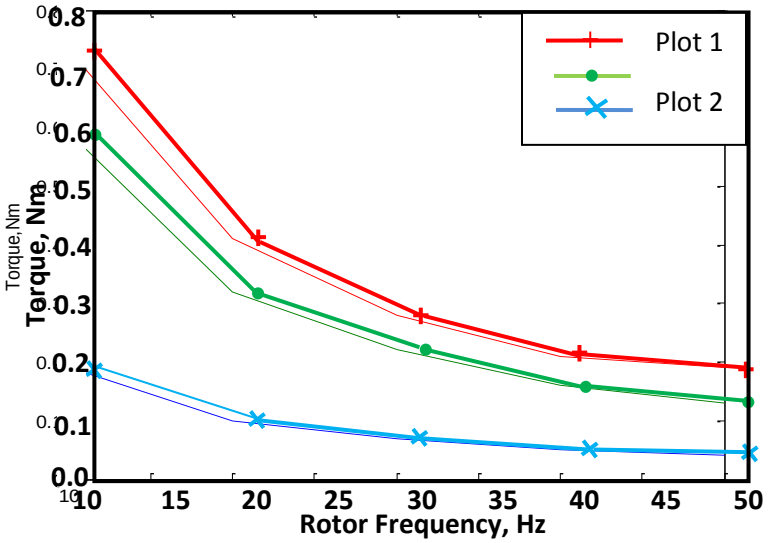


Figure 5.12: Torques from Maxwell Stress Tensor versus Rotor Frequency

Figure 5.10 shows the variations of magnetic energy and co-energy as a function of rotor frequency for three different operating conditions. The curve labelled plot 1 corresponds to a three phase (0^0 shift between 'a-b-c' and 'x-y-z' winding sets) operation of the DSWIM whilst the curve labelled plot 2 is for the six phase (30^0 shift) operation. In the third DSWIM operation, only 'a-b-c' winding set was excited implying that only half of the machine was operational. Note that both magnetic energy and co-energy plots are identical for each operation investigated. This can easily be attributed to the fact that the machine under locked rotor test is operating in the linear region of the magnetization curve due to application of relatively low voltage. In the case of the third operation corresponding to plot 3, the low values recorded for the magnetic energy/co-energy are to be expected for one winding set excitation only.

In Figure 5.10 there is no much variation of losses within the range of frequency investigated. This is an expected outcome. This is because the losses are a function of the resistivity of the rotor bar material and its cross sectional area. The small variation recorded may be due to skin effect (a phenomenon that tends to reduce the cross sectional area) at higher frequencies.

Referring to Figure 5.11, it is seen that the torque calculated from Maxwell stress tensor decays with frequency. It is vitally important to state that the torque computed here was based on a constant current source excitation fixed at 1.0 A throughout the simulation efforts. Relying on the data that underpinned the results portrayed in Figures 5.10 to 5.12, allowed also the equivalent parameters of DSWIM to be computed at selected rotor frequencies. Figure 5.13 shows composite plots of the equivalent parameters versus rotor frequency. Finally, following the approach similar to (Luigi, 2009), the referred rotor parameters for the DSWIM case study determined via 2-D FEMM analysis are presented in Table 5.4. Note again that DSWIM equivalent resistance R_{eq} (plot 1) is minimally affected by rotor frequency similar to Figure 5.11 on which its computational procedure depended and the same argument applies to L_{eq} (plot 2) in relation to Figure 5.10.

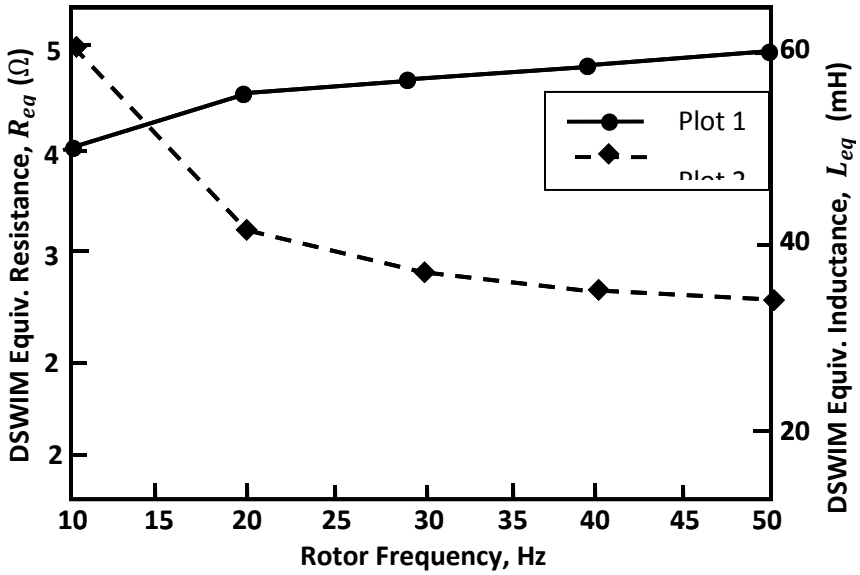


Figure 5.13: Composite Plots of DSWIM Equivalent Parameters versus Rotor Frequency

Table 5.7: Computed Rotor Referred Parameters from FEMM Model for DSWIM at Specified Frequencies

Rotor Frequency	Referred Rotor Parameters*

(Hz)	R_r' (Ω)	L_r' (H)
10	0.58	6.9×10^{-2}
20	0.6	6.5×10^{-2}
30	0.62	5.8×10^{-2}
40	0.62	5.3×10^{-2}
50	0.63	4.9×10^{-2}

*Equations used to compute referred rotor parameters (Luigi, 2009)

$$R_r'(f) = \frac{(\omega L_{eq})^2 R_{eq}}{R_{eq}^2 + (\omega L_m - \omega L_{eq})^2} \;\&\; L_r' = L_m \frac{\omega^2 L_{eq}(L_m - L_{eq}) - R_{eq}^2}{R_{eq}^2 + (\omega L_m - \omega L_{eq})^2}$$

Where: $\omega = 2\pi f$: All inductances are in Henries.

5.2.5 Comparison of DSWIM Inductance Values Computed Via Three Methods

In the preceding subsections, the results of various DSWIM inductances computed, by three different methods, were presented in accordance with their respective algorithmic computational framework. The DSWIM inductances calculated from hybrid ICD and GA approach have been chosen as the baseline inductance values against which inductance values other methods are to be compared. The basis for such selection has to do with the improved analytical tools developed that made use of fairly accurate measurements of the physical dimensions of the 3-D stator and rotor configurations in the computations of the various DSWIM inductances. The other two techniques are essentially model based solutions bearing inherent assumptions and/or approximations with expected lower computational accuracies than the baseline method.

Consequently, the hybrid ICD and GA approach based inductance values have been compared with those calculated using the winding function method as well as the finite element method. The results presented in Table 5.6 reveal, at a glance, that FEMM inductance values are much closer to the baseline values than the inductance values obtained via winding function method.

Table 5.8: Comparison of Computed DSWIM inductance Values by Three Different Methods

Type of Inductance	Major parts of DSWIM	Winding Group	Techniques Applied to Determine DSWIM Inductances (mH)		
			Winding Function	Finite Element	ICD+GA
Self	Stator	a-b-c	11.73	13.8	14.15
		x-y-z	11.73	13.8	14.15
	Rotor	a-b-c	40	49	51
Mutual	Stator	a-b-c	33.8	42.3	43.85
		x-y-z	33.8	42.3	43.85
		a-b-c/x-y-z	68.9	85.7	89.65
	Rotor	a-b-c	45	70	85
	Stator/Rotor	A harmonic function of the rotor position with respect to stator winding			

5.3 Results of DSWIM Simulation in MATLAB/Simulink Software

The Simulink models depicted in Figures 4.4-4.6, specifically developed for DSWIM drive system, has been implemented in MATLAB **7.6.0 (R2008a).** The parameters obtained from hybrid ICD and GA approach for the 8/8 similar pole DSWIM case study have been used in its simulation model implementation. For the sake of convenience, they are repeated in Table 5.7 amongst other vital simulation data presented therein. Note that the test machine is essentially a 6-hp, 380-V eight-pole dual stator winding induction machine. The main goal of this simulation effort is to demonstrate the efficacy of the model developed. Further, it ought to be capable of achieving simulation results of superior qualities than those found in the existing publications for different simulation scenarios envisioned in this research work.

In pursuit of this goal, the following output variables have been selected to facilitate model performance assessment.

i. Speed and Torque;

ii. Voltages;

iii. Currents;

iv. Fluxes; and

v. Rotor speed

The simulation scenarios considered include DSWIM start transient to its steady state speed with transient fault applied on phases 'a-b-c'. In addition, the effects of parameter variations on the test machine transient performance have also been investigated. Based on the simulation studies considered and with the Simulink model of the test machine excited by 3-ϕ sinusoidal voltage sources supplied to both a-b-c and x-y-z stator windings, the various simulation results obtained are shown in Figures 5.13 – 5.37. They are further characterized in the subsequent subsections.

Table 5.9: Parameter Specifications for the Simulation of Dual Stator Winding Induction Motor (DSWIM) in Simulink/MATLAB Environment

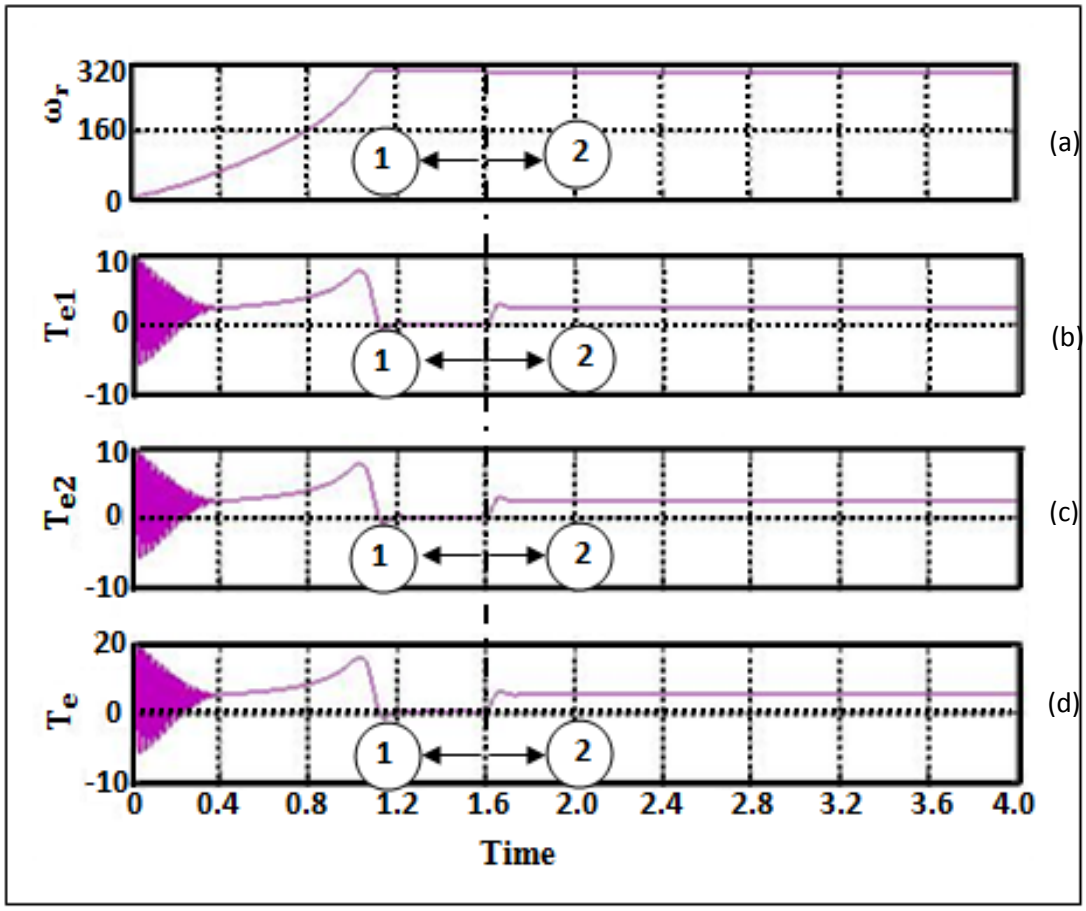
Description	Symbol	Unit	Stator Core		Rotor Cage
			a-b-c winding	x-y-z winding	$a_r - b_r - c_r$ winding
Number of Poles	p	-	8	8	8
Stator Resistance	R_s	Ω	1.5	1.5	3.8
Stator Leakage Inductance	L_{ls}	H	0.0138	0.0138	___
Rotor Resistance	R_r	Ω	___	___	0.63
Rotor Leakage Inductance	L_{lr}	H	___	___	0.049
Stator mutual Leakage Inductance	L_{lm}	H	0.00673		____
Magnetizing Inductance	L_m	H	0.12		
Rated Power Output	P_m	kW	6.0		

Line Voltage	V	Volts	380
Moment of Inertia	J_R	kg-m^2	0.045

5.3.1 Results of Starting process and fixed loading dynamic response of DSWIM

The no-load starting transients combined with fixed loading scenario response of similar pole DSWIM are depicted in Figure 5.13 with its 'a-b-c' and 'x-y-z' windings fed by balanced 3-ϕ voltage sources (380V line to line). During the no-load starting process of the similar pole DSWIM, its rotor speed increased steadily from zero to settle near synchronous speed within a period of approximately 1.2s and remaining at steady state for additional 0.4s according to Figure 5.13(a). The starting transients exhibited in the plots of the respective generated electrical torques (see (b), (c) & (d) of Figure 5.13) are typical signatures of any standard induction machine simulations of the existing publications.

Note that all the plots of Figure 5.14 have been partitioned into two sections labelled by circled 1 and 2, corresponding respectively to no-load and fixed load operating modes. The no-load steady state simulation period lasted for a total period of 1.6s whilst the remaining simulation period (i.e. from 1.6 to 4s) when a load of 3Nm is picked up by DSWIM. Figures 5.15 to 5.18 are plots of dq voltages and currents as well as their corresponding phase variable voltage and current quantities. In particular, current variable plots in Figure 5.18 carry the same information as previously described



s

Figure 5.14: Starting Process of 8/8 Pole Dual Stator Winding Induction Machine- (a) Speed Curve; (b) Torque Contribution by 'a-b-c' Winding; (c) Torque Contribution by 'x-y-z' Winding; & (d) Total Torque Developed

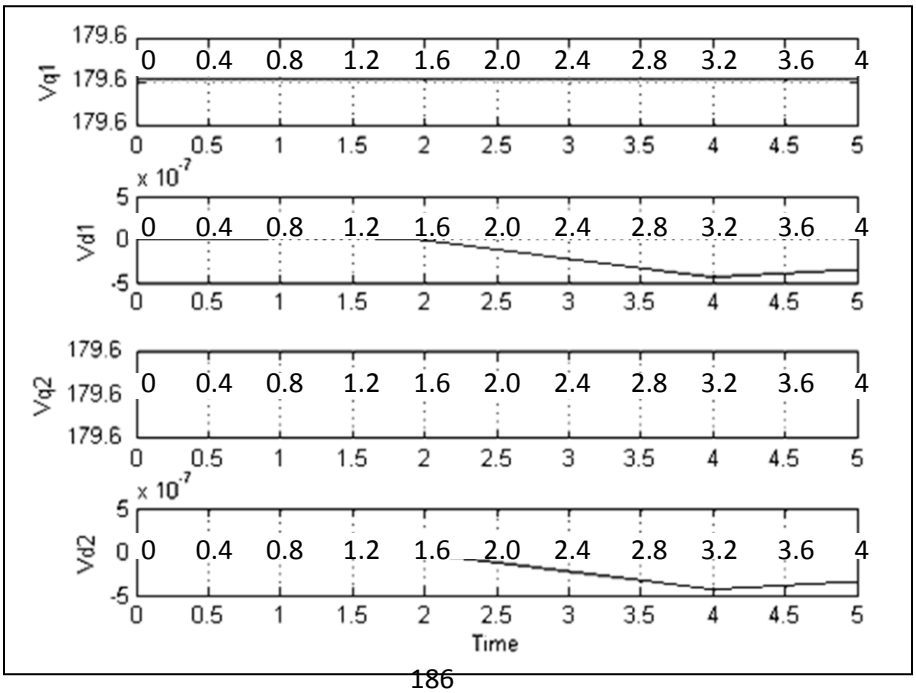


Figure 5.15: Quadrature and Direct Axis Voltages of the Two stator windings as a Function of Time

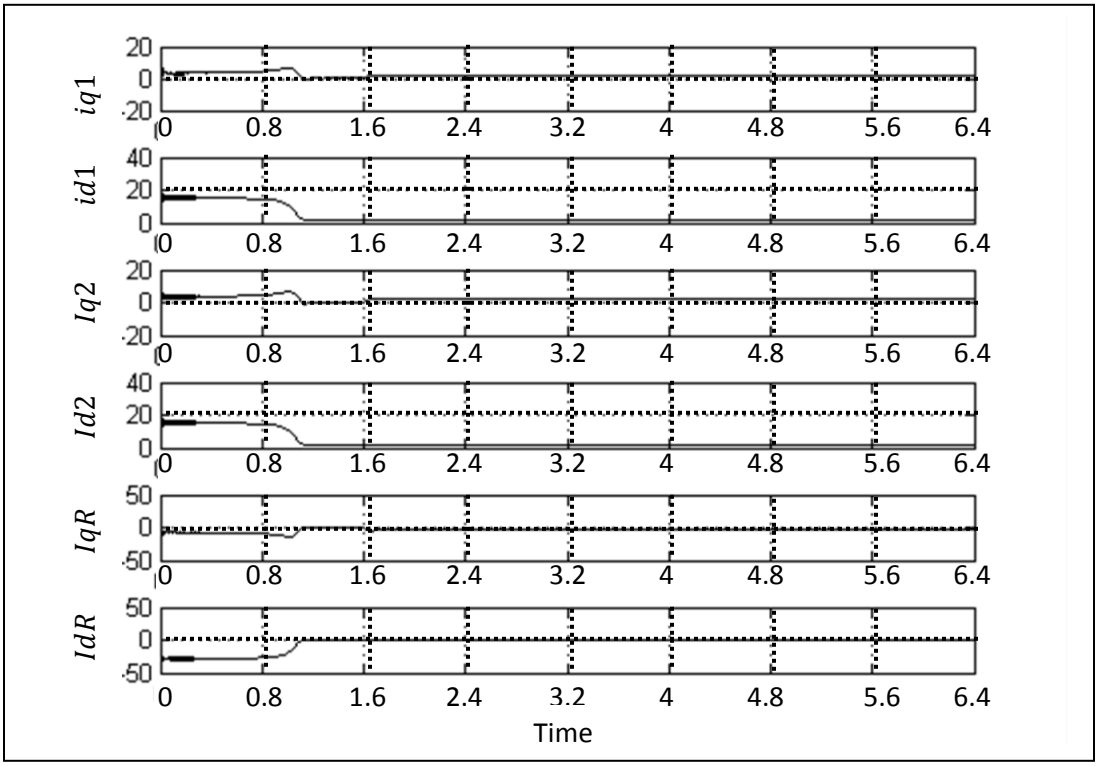


Figure 5.16: Currents of Two (a-b-c & x-y-z) Stator Windings and a-b-c Rotor Winding

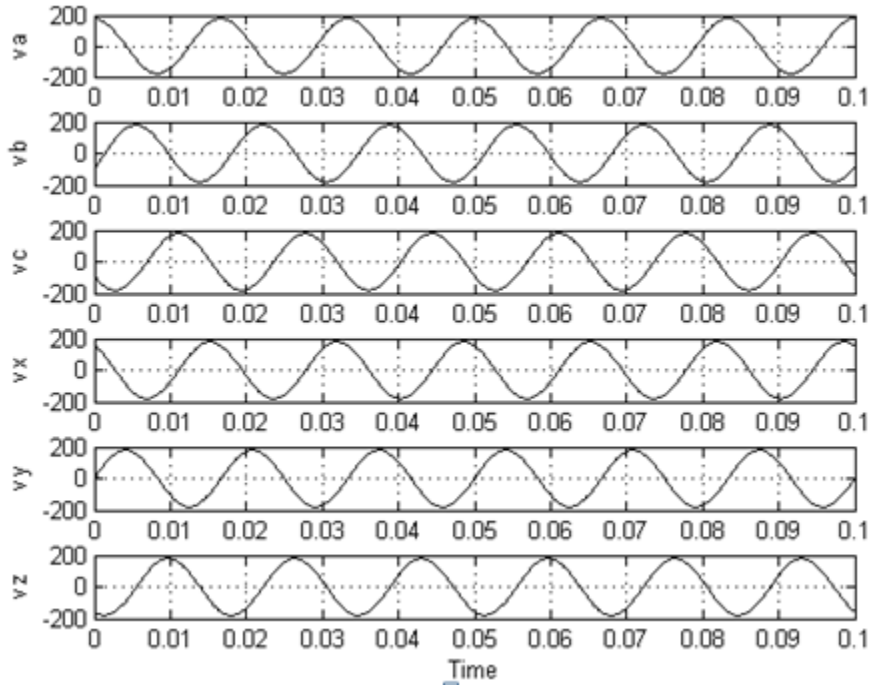


Figure 5.17: Stator Voltages in Phase (abc & xyz) Variables as a Function of Time

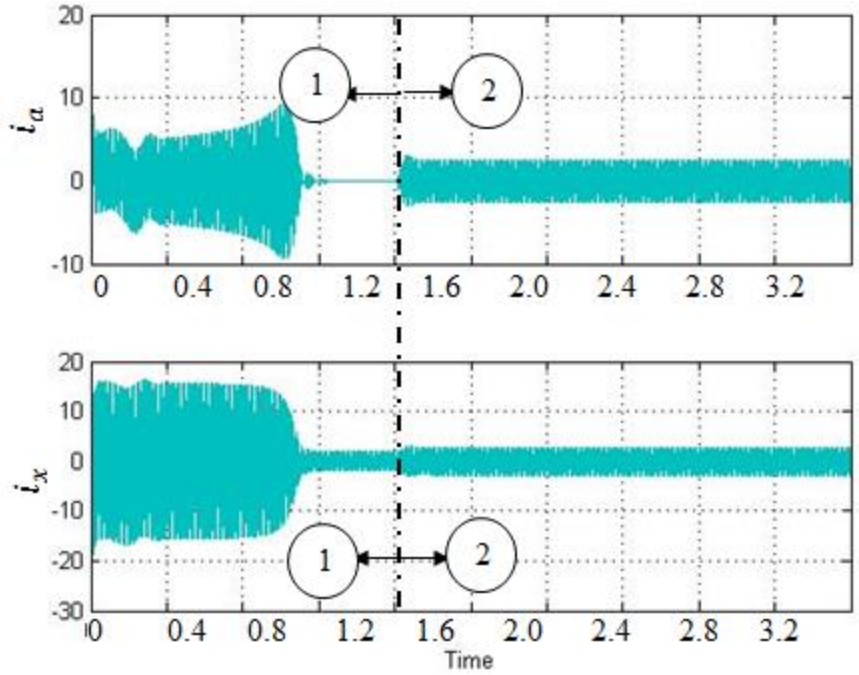


Figure 5.18: Stator Phase 'a' and Phase 'x' Currents as a Function of Time

5.3.2 Investigation of effects of mutual leakage inductance (L'_{ldq}) on the characteristics of similar pole DSWIM

Recall from Chapter Four that the equivalent circuits in dq0 reference frame were developed for similar ratio DSWIM. Therein, we considered mutual coupling between d and q axes of the stator windings via introduction of mutual leakage inductance ($\pm L'_{ldq}$**).** This subsection presents the simulation results showing the influence of the stator mutual leakage inductance L'_{ldq} on the DSWIM operational performance from the viewpoints of transient and steady state characteristic variations. Four case studies were considered as explained in sequel in accordance with each case study.

5.3.2.1 Case study I

In this case study, the value of mutual leakage inductance is assumed to be the same as that of either stator common or rotor leakage inductance. Consider the case in which the mutual leakage inductance is the same as the stator common leakage reactance (i.e. $L'_{ldq} = L_{lm}$), the

resulting performance of DSWIM simulation is shown in Figure 5.19. Figure 5.20 depicts the other case in which the mutual leakage inductance is set equal to rotor leakage reactance (i.e. $L'_{ldq} = L_{lr}$). In these two cases, the investigation is focused on the effects of the mutual inductance leakage consideration on the DSWIM electrical torque generation capabilities.

5.3.2.2 Case study II

In this case, the value of mutual leakage inductance was firstly set equal to stator leakage inductance ($\pm L'_{ldq} = L_{ls}$) and the simulation of DSWIM was run. Then mutual leakage, rotor and stator leakage inductances were assumed equal with ($L'_{ldq} = L_{lr} = L_{ls}$) implied. This was also implemented in the MATLAB/Simulink model for the similar pole ratio DSWIM. The outcome simulation results for both cases are depicted in Figures 5.21-5.32. The simulation results will be discussed later from the standpoints of their effects on DSWIM's dynamic and steady state performances. It is worthy of mention that most publications on simulation of DSWIM have not thoroughly investigated the effects of mutual leakage inductance as attempted in this dissertation.

5.3.2.3 Case study III

Finally, the value of mutual leakage inductance is assumed to be zero. i.e.L'_{ldq}=0. This is the widely modeled case in the literature and therefore for the baseline case against which other cases are compared in order to characterize conclusively, the effects of mutual leakage inductances on the operational performances of DSWIM. The similar pole ratio DSWIM simulation results for this case study are shown in Figures 5.33 to 5.38.

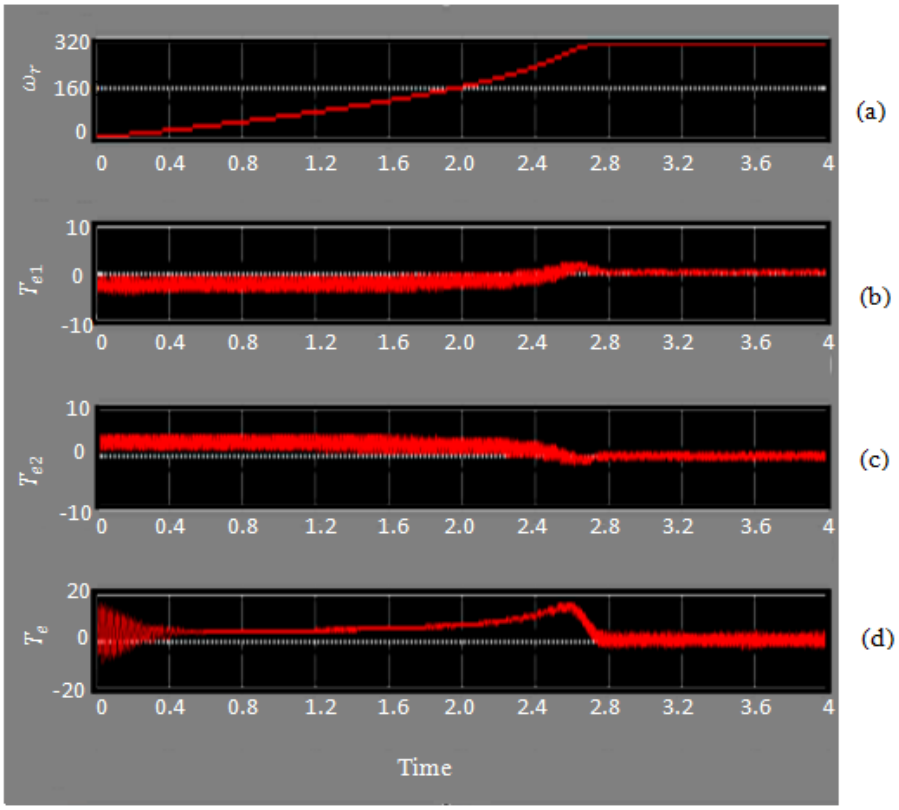


Figure 5.19: 8/8 Pole Ratio DSWIM Simulation Results with $\pm L'_{ldq} = L_{lm}$

(a) Speed Curve; (b) Torque Contribution by 'a-b-c' Winding; (c) Torque Contribution by 'x-y-z' Winding; & (d) Total Torque Developed

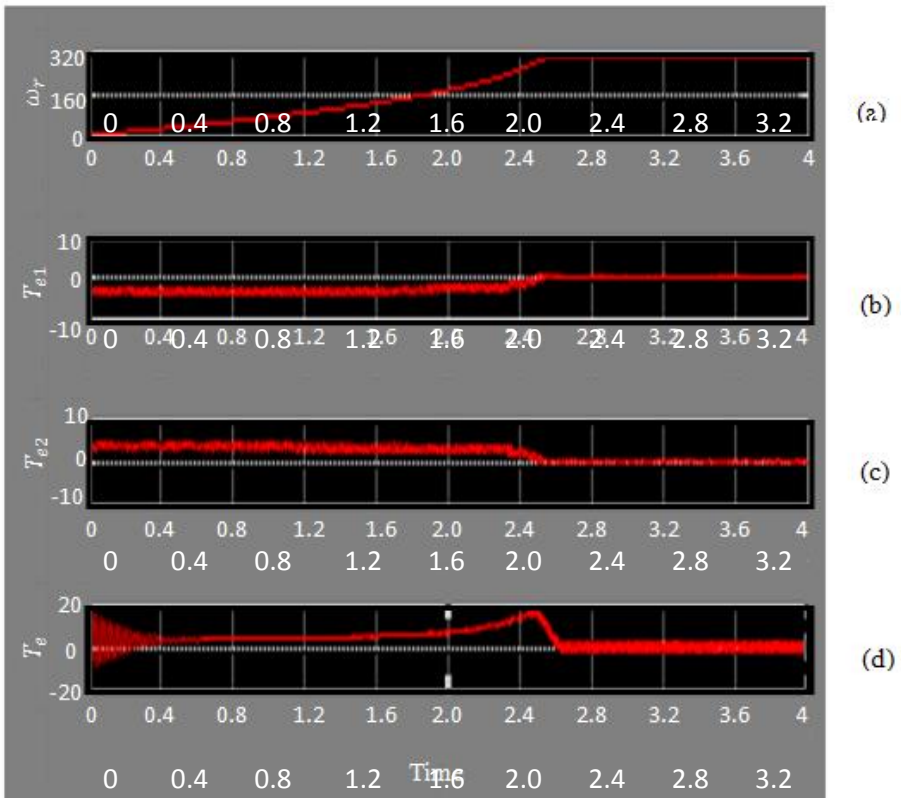


Figure 5.20: 8/8 Pole Ratio DSWIM Simulation Results with $\pm L'_{ldq} = L_{lr}$

(a) Speed Curve; (b) Torque Contribution by 'a-b-c' Winding; (c) Torque

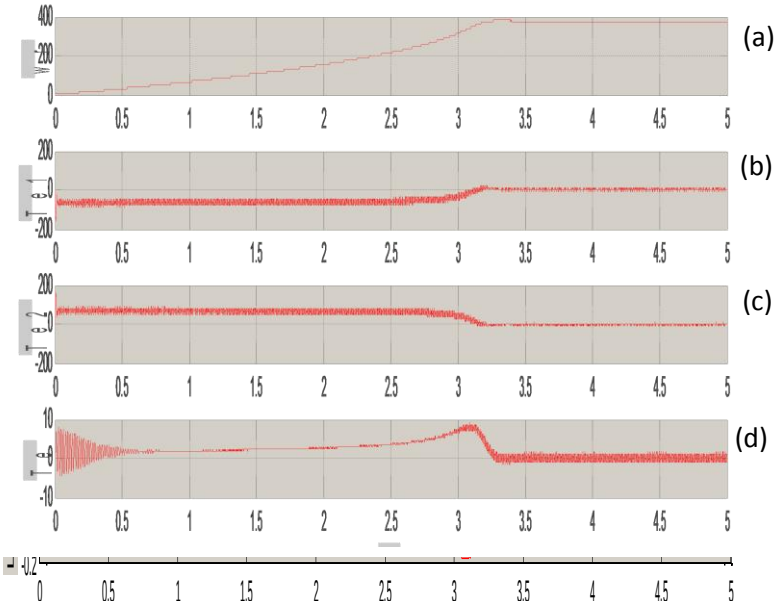


Figure 5.21: 8/8 Pole Ratio DSWIM Simulation Results with $\pm L'_{ldq} = L_{ls}$

(a) Speed Curve; (b) Torque Contribution by 'a-b-c' Winding; (c) Torque Contribution by 'x-y-z' Winding; & (d) Total Torque Developed

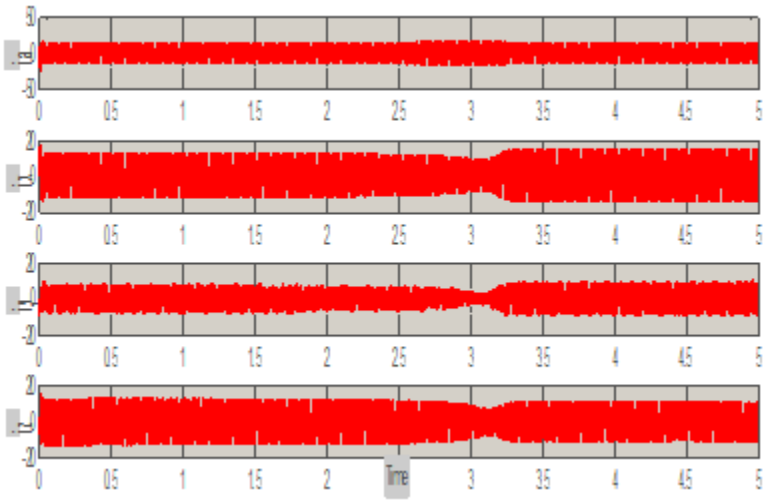


Figure 5.22: Stator Phases 'a' and' xyz' Winding Set Currents against Time

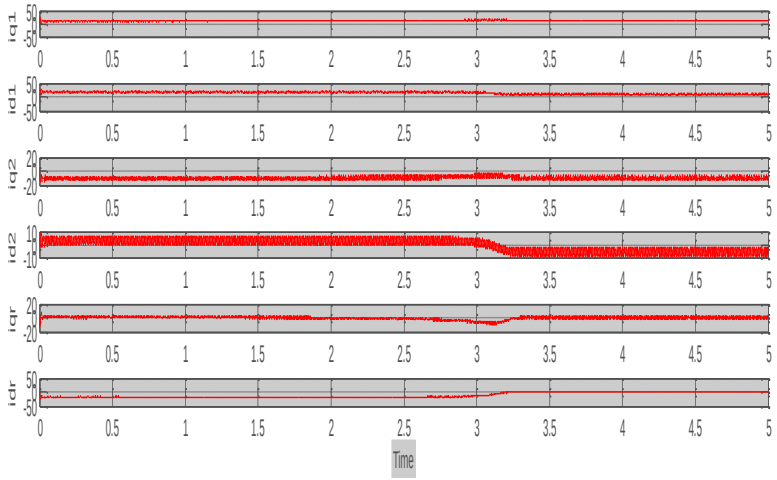


Figure 5.23: d-q currents of two (abc & xyz) stator windings and abc rotor winding

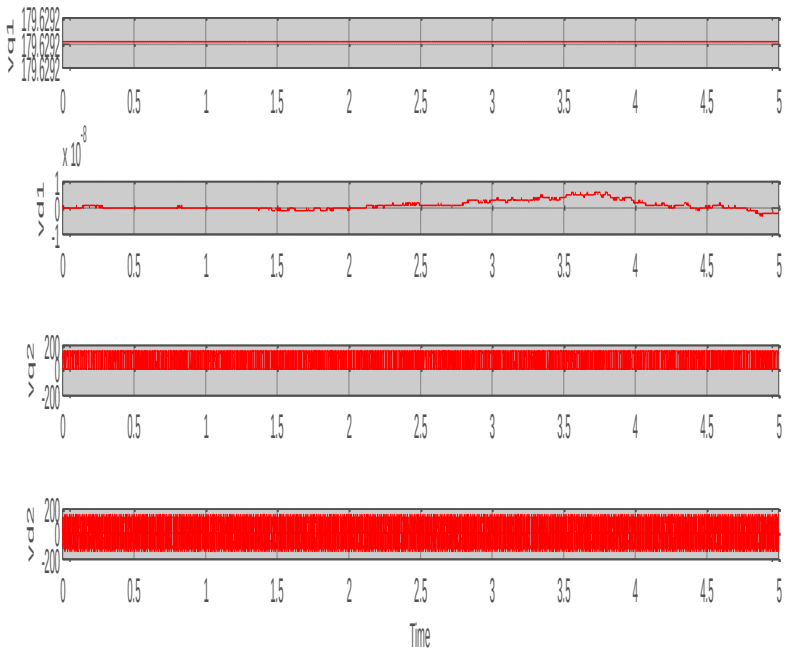


Figure 5.24: d-q voltages of the two (abc & xyz) stator windings as a function of time

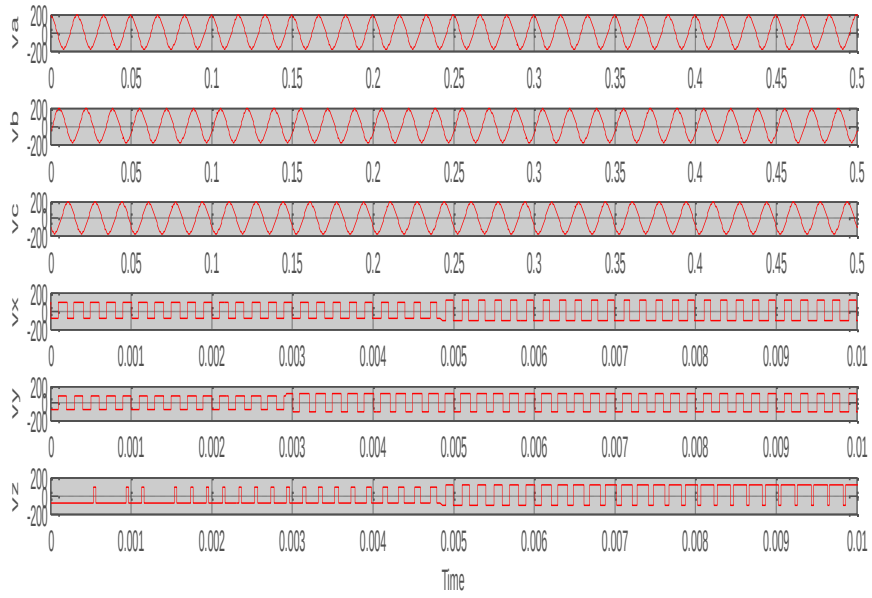


Figure 5.25: Stator voltages in natural (abc & xyz) variables as a function of time

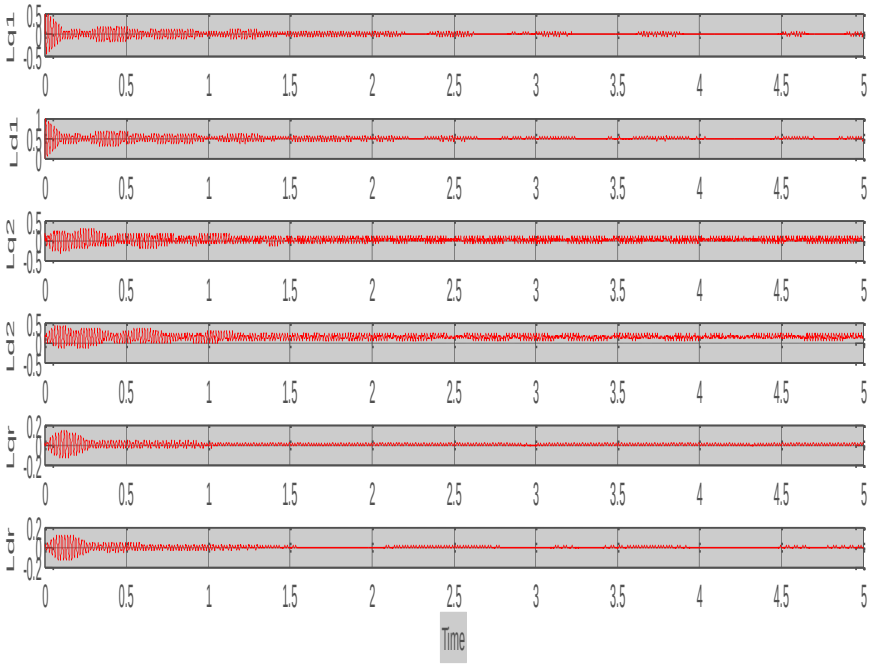


Figure 5.26: d-q axes flux linkages stator “abc”, ”xyz” and rotor“abc” winding sets against time

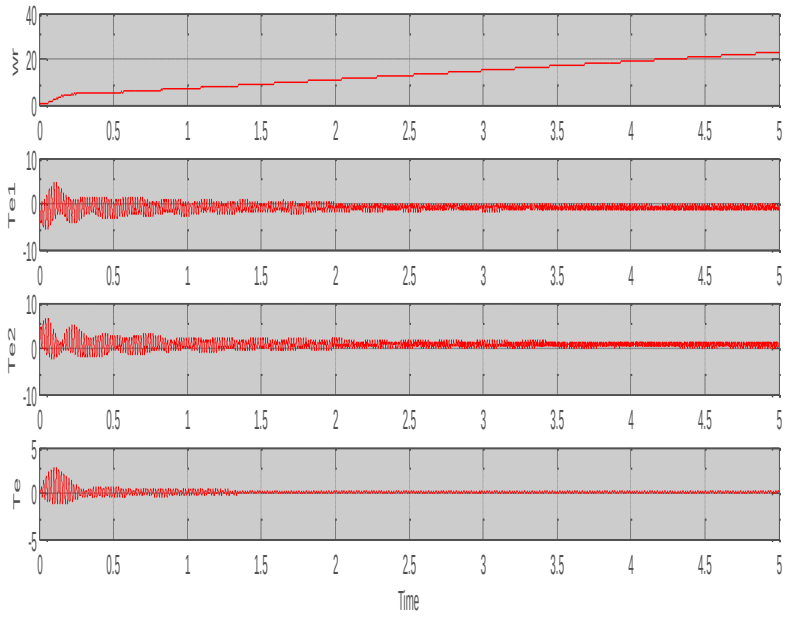


Figure 5.27: 8/8 Pole Ratio DSWIM Simulation Results with $\pm L'_{ldq} = L_{ls} = L_{lr}$

(a) Speed Curve; (b) Torque Contribution by 'a-b-c' Winding; (c) Torque Contribution by 'x-y-z' Winding; & (d) Total Torque Developed

.

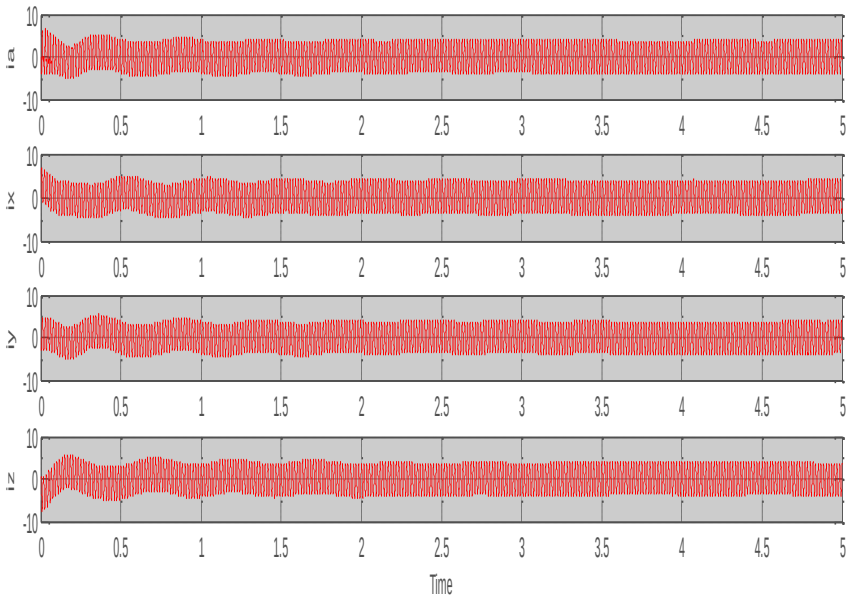


Figure 5.28: Stator Phases 'a' and 'xyz' Winding Sets Current against Time

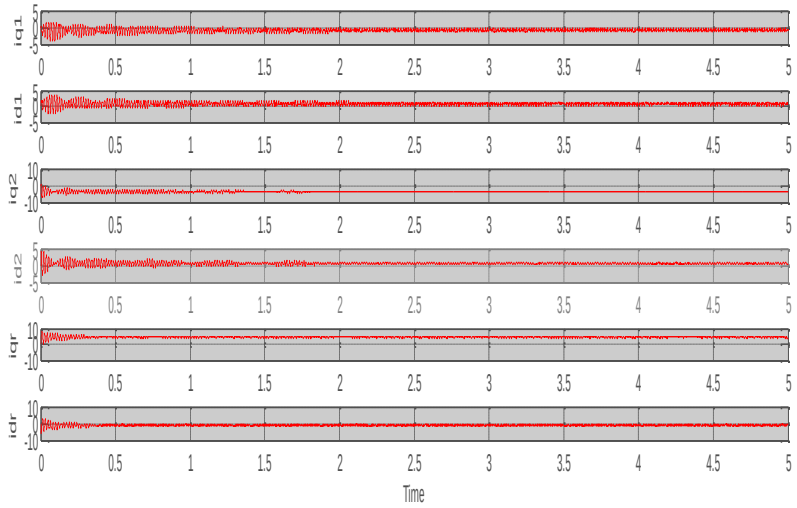


Figure 5.29: Quadrature and Direct Axis Currents of Two (‘a-b-c’ & ‘x-y-z’) Stator Winding and abc rotor winding

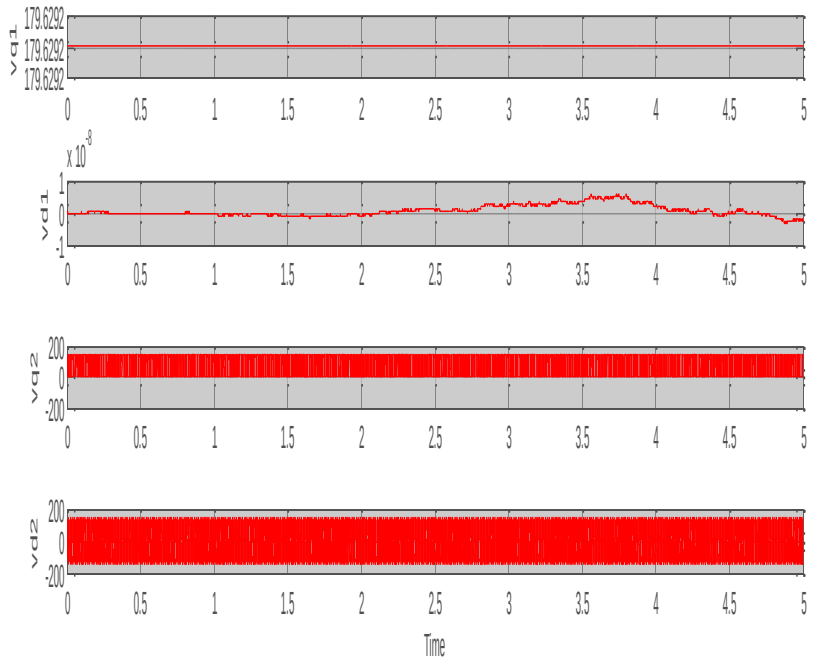


Figure 5.30: Quadrature and Direct Axis Voltages of the Two (abc & xyz) Stator Windings as a Function of Time

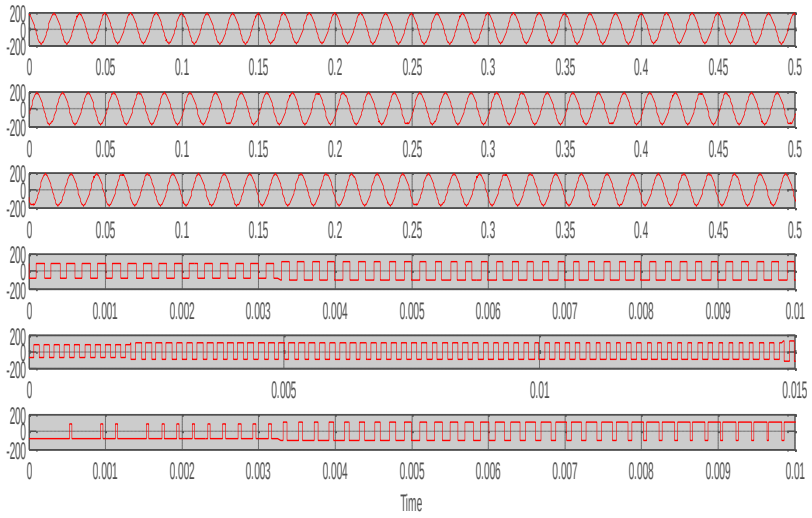


Figure 5.31: Stator Voltages in Phase (a-b-c & x-y-z) Variables as a Function of Time

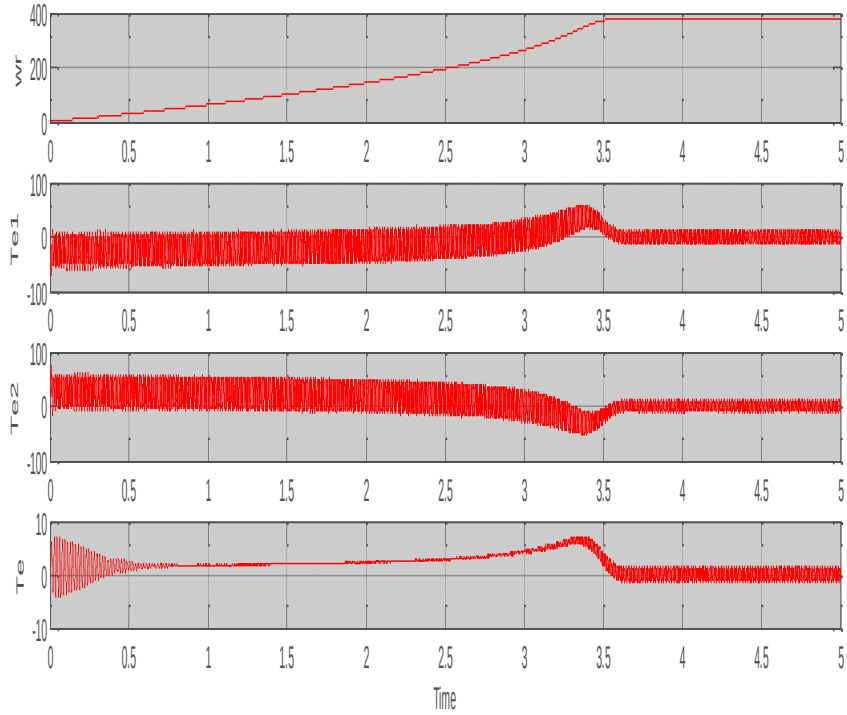


Figure 5.32: 8/8 Pole Ratio DSWIM Simulation Results with $\pm L'_{ldq} = 0$

(a) Speed Curve; (b) Torque Contribution by 'a-b-c' Winding; (c) Torque Contribution by 'x-y-z' Winding; & (d) Total Torque Developed

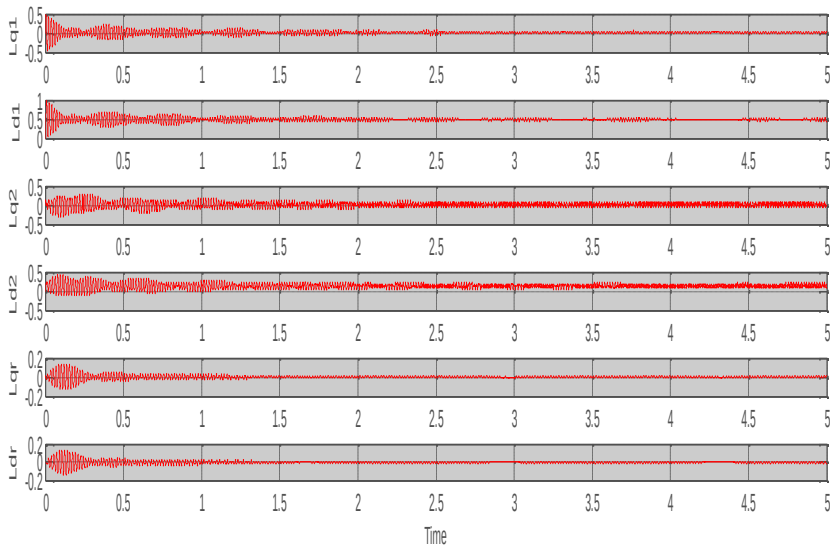


Figure 5.33: Quadrature and Direct Axis Flux Linkages Stator ‘a-b-c’, ‘x-y-z’ and Rotor ‘a-b-c’ Winding Sets against Time

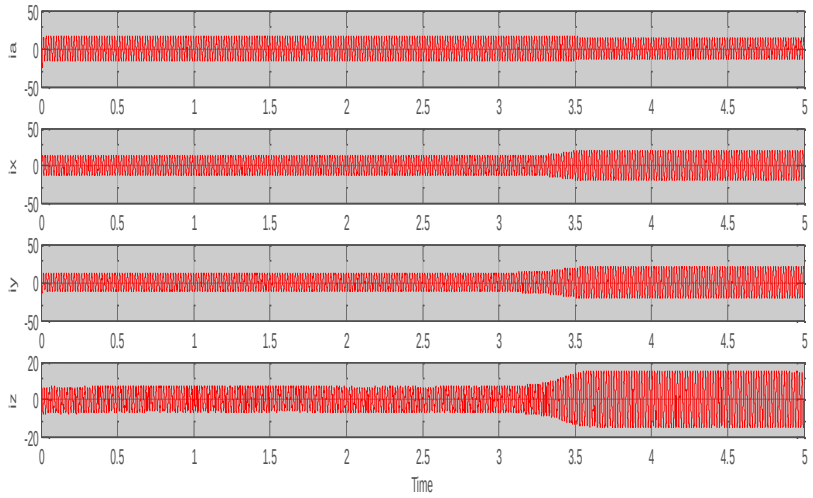


Figure 5.34: Stator Phases ‘a’ and ‘xyz’ Winding Set Currents against Time

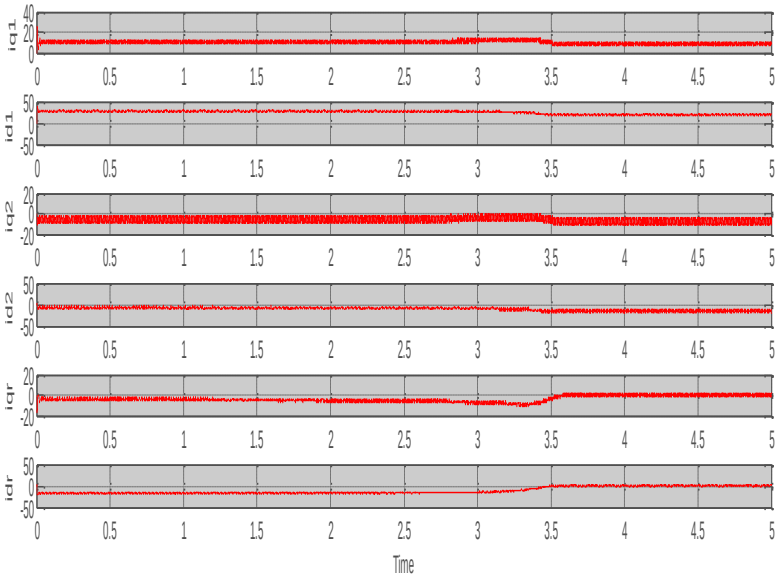


Figure 5.35: Quadrature and Direct Axis Currents of Two (‘a-b-c’ & ‘x-y-z’) Stator Windings and ‘a-b-c’ Rotor Winding

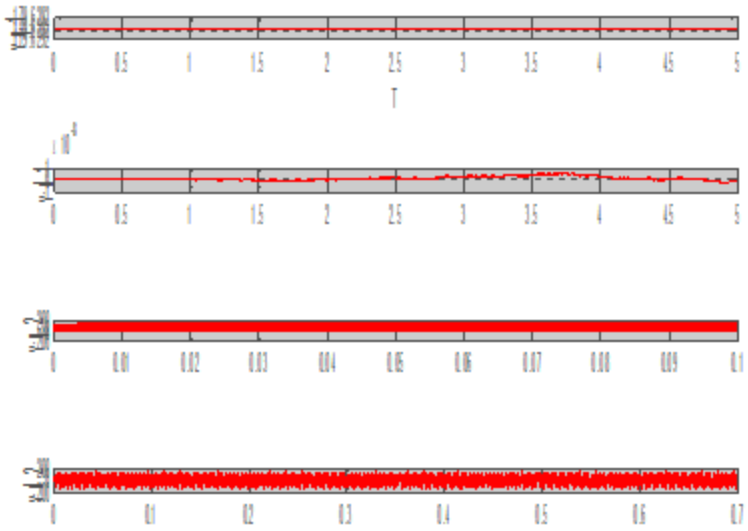


Figure 5.36: d-q Quadrature and Direct Voltages of the Two (a-b-c & x-y-z) Stator Windings as a Function of Time

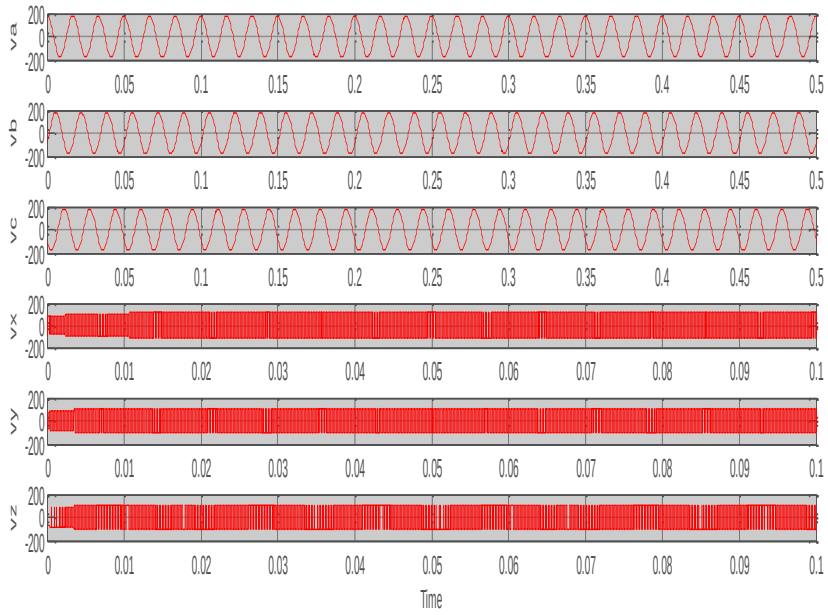


Figure 5.37: Stator Voltages in Phase ('a-b-c' & 'x-y-z') Variables as a Function of Time

5.3.3 Discussion of Simulink Model Results

In this section, various results presented in the preceding section are discussed from standpoints of test machine transient performances as revealed via its monitored output quantities. Indeed, induction machine speed transient torque behaviors captured over a short time frame are well known to exhibit standard characteristic signatures. The established benchmark results in the literature have been found to corroborate with the results presented in this dissertation.

Consistent with the benchmark simulation results, Figures 5.14; 5.19; 5.20; 5.22; 5.28 and 5.35 essentially show the dynamic simulation of rotor speed, segregated torque contribution by each stator winding and the total torque as appropriately conveyed in equations 2.169-2.171. These figures reveal that for a better dynamic response of the machine, the value of mutual leakage inductance must be kept minimal. Figures 5.16; 5.24; 5.30; 5.25 and 5.15; 5.22; 5.31; 5.38 further show the simulation results in d-q axes of currents and voltages in both windings respectively. Figure 5.29 is a simulation of the six phase voltages fed into the

two stator windings. In Figures 5.26; 5.33; 5.38 the simulations of the voltages are shown with a singular difference of 'x-y-z' winding set being fed via an inverter. Figure 5.18 shows the simulated currents in a-b-c reference frame for selected stator phases 'a' and 'x' only. Other phases were suppressed as they convey no additional information. It is noteworthy to mention again for the avoidance of doubt that the various results obtained are in agreement with similar results presented in relevant publications consulted in this research work.

Based on the results of the simulation obtained, it can be inferred that the dual winding machine exhibits similar, yet superior, characteristics to conventional three phase induction machine. In particular the six phase machine develops more torque per ampere than the three phase machine as also confirmed by other researchers. This desirable quality is attributable to the cumulative nature of the torque developed separately by each winding. Herein lies the superiority of dual stator winding induction machine over conventional induction machine such as fault tolerance and higher torque capability attributes as demanded by modern drive systems.

The effects of variations in mutual leakage inductances on the torque developed by each winding set were also briefly investigated as shown in Figures 5.19 and 5.20. Comparison of the peak torques extracted from these simulation results revealed insignificant variation in the torque outputs with change in mutual leakage inductance. Undoubtedly, further investigation is imperative in order to establish variational characteristics of DSWIM torque outputs with respect to changes in other parameters induced by temperature rise, eccentric rotor rotation, etc. This should ultimately lead to far reaching model simplification capable of quick prediction of DSWIM leading performance indices without any loss of accuracy.

5.4 Prototype Realization of DSWIM and Experimental Results

The algorithmic framework developed for redesign of a conventional 3-ϕ machine as a dual stator winding induction machine must be actualized for a specific case study. Towards

realizing this cardinal objective, a standard 8-pole, 6kW, 3-phase squirrel cage induction machine with 48 stator slots and 42 rotor slots is used as a case study in this research work. The 3-phase 8-pole stator winding of this machine has been modified to a 6-phase (dual 3-phase) each of 8-pole stator winding. The rotor of the original machine remains unaltered. The leading parameters of the machine being re-designed are presented in Table 5.1. Based on the design parameter specifications of Table 5.1 and DSWIM winding diagram offered in Chapter Three, we now proceed to achieve its practical realization in the next subsection.

5.4.1 Prototype realization of DSWIM

The calculated parameters have been applied in the realization of the prototype. The various phases of the prototype implementation are documented in Plates 5.1 to 5.5. More specifically, Plate 5.1 shows the stator with its coils inserted in stator slots bearing single layer and full pitch features. There are a total of 24 coils out of which the twelve belongs to the 'a-b-c' winding set whilst the remaining twelve belongs to the 'x-y-z' winding set. Plate 5.2 shows the rotor of the machine. Note that the rotor structure was not altered with 42 skewed slots. We reiterate again that the stator frame and rotor structure were carefully selected ab initio to satisfy the constraints on cogging, excessive vibrations and harmonics minimization. Plate 5.3 shows the squirrel cage rotor structure and the stator housing the dual windings side by side. Plate 5.4 shows the rotor of the machine inserted inside the wound cylindrical stator. Finally, Plate 5.5 depicts the assembled DSWIM prototype with all its terminals brought out for accessibility. Table 5.10 presents final design parameters and operating capabilities of the DSWIM prototype.



Plate 5.1: Stator coil in their respective slots



Plate 5.2 Squirrel cage rotor of the machine



Plate 5.3: Rotor and Wound Stator Side by Side



Plate 5.4: Inserted Rotor within the Stator Structure



Plate 5.5: Complete Prototype Machine

Table 5.10: Summary of Final Design Parameters and Operating Data for DSWIM Prototype

Design Parameter	Value	Remarks
Stator stack length	**100**	**Given**
Stator outer diameter	**206**	**Given**
Rotor outer diameter	**149**	**Given**
No of turns/coil	**60**	**Calculated**
Conductor diameter	**1.25**	**Calculated**
Air-gap	**0.05**	**Given**
Magnetic Loading	**0.425**	**Calculated**
Power factor	**0.88**	**Calculated**
Efficiency	**0.934**	**Calculated**
Rated Power	**6.0**	**Given**
Rated Speed	**743**	**Given**
Slip	**0.0093**	**Calculated**

5.4.2 Experimental results

The experimental work is of paramount importance and critically pivotal in the overall success of the research. The experimental test rig is equipped with very accurate measuring instruments and sensors so as to achieve reliable data and benchmark measurements with which to validate simulation activities on DSWIM. The schematic diagram of the prototype experimental setup depicted in Figure 5.39 has been deplored in different configurations to achieve the following:

i. Experimental determination of the equivalent circuit parameters of the newly designed stator winding machine using no-load and short-circuit tests to evolve its circle diagram;

ii. Accurate measurements of DSWIM performance characteristics indices (PCI) (torque, power factor, rotor speed, output power, and stator current) under varying loading conditions; and

iii. Experimental measurements of energy losses of DSWIM which will be segregated into their constituent components.

The complete experimental set up configured around the DSWIM prototype in the laboratory is shown in Plate 5.6 with the necessary drive system and digital meters. It is imperative to experimentally validate the theoretical design activities carried out. Therefore, the experimental investigations on the DSWIM prototype are so motivated to be presented in next subsections.

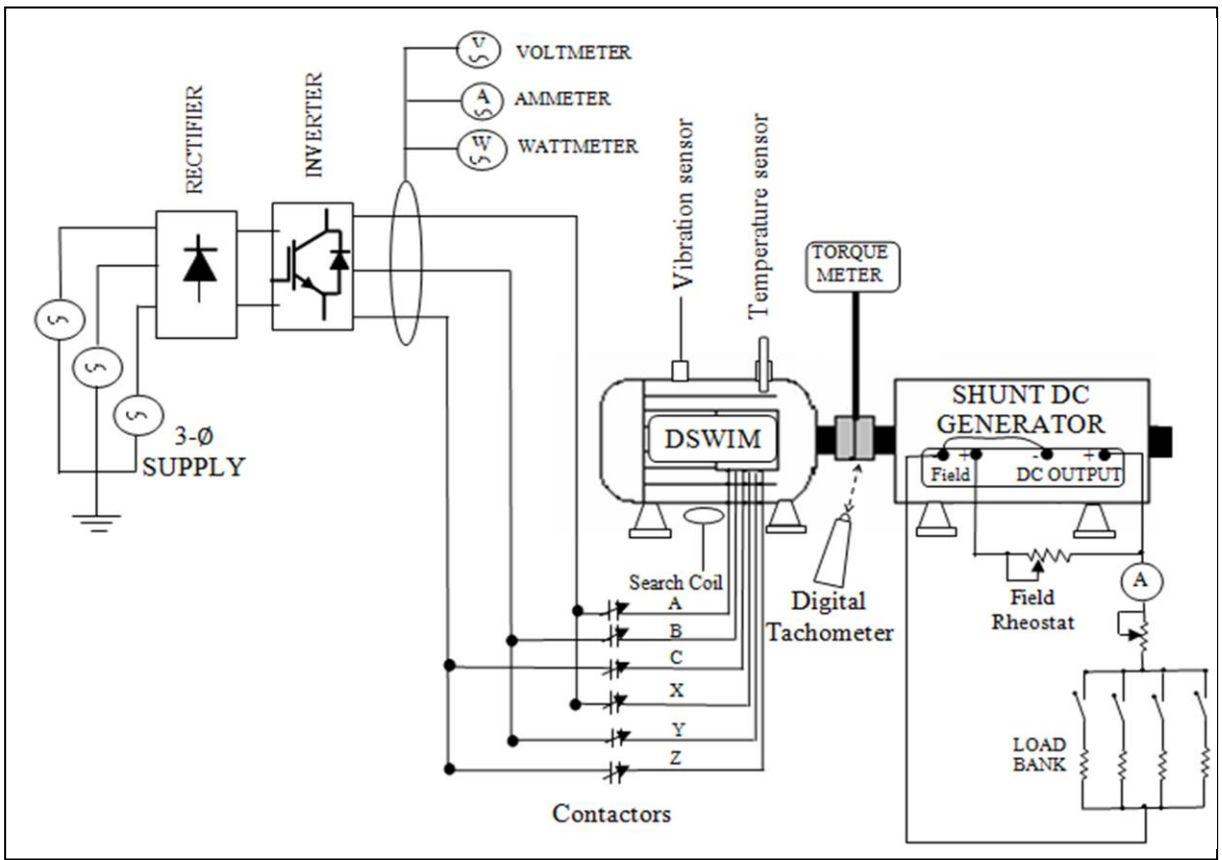


Figure 5.38: Schematic Representation of Experimental DSWIM Test Rig

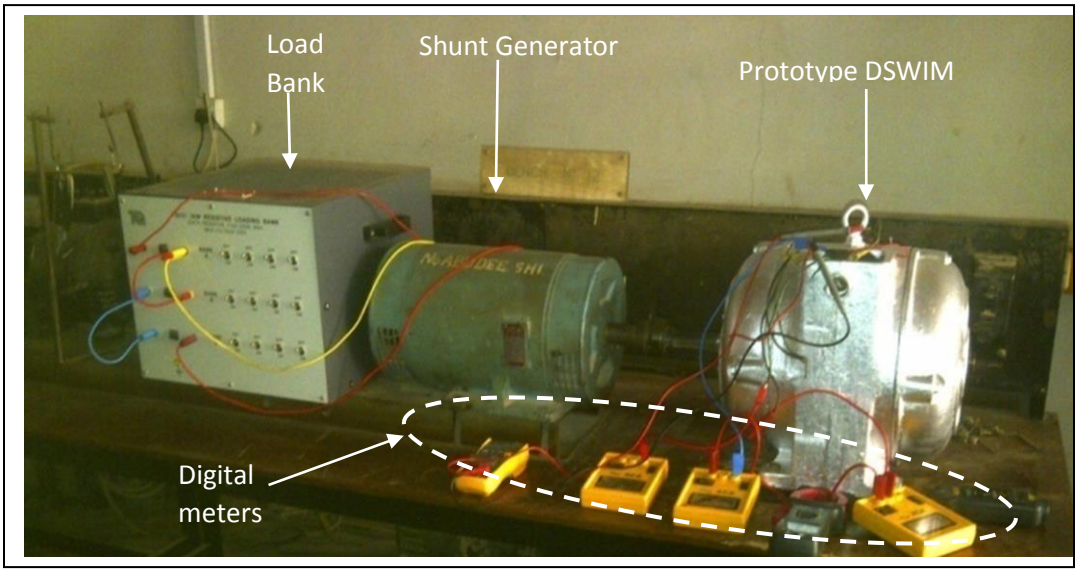


Plate 5.6: The Complete Laboratory Experimental Setup

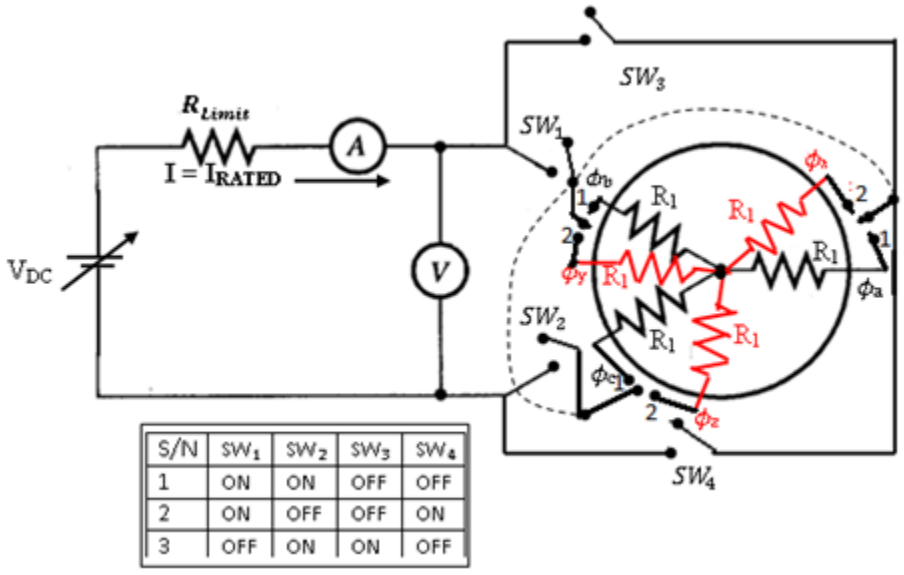
5.4.3 Determination of the induction machine parameters

Normally, all induction machines come with their parameters readily available from the manufacturers. However, the dual stator winding machine is modification of an existing three phase induction machine. It is therefore pertinent to determine its parameters before any analysis can be carried out on it. The parameters to be determined are: stator and rotor resistances, magnetizing, stator and rotor reactances. Three tests are usually performed for this purpose. They are DC resistance, no-load and locked rotor tests (Stephen, 1991).

5.4.3.1 DC resistance test

The purpose of the DC resistance test is to determine the stator resistance per phase for each winding set. This is accomplished by connecting any two stator leads, belonging to one winding set to a variable voltage DC source shown in Figure 5.40. This experimental set up

has made elaborate provisions via operations of ganged three phase toggled switch for winding set selection. Thereafter, the four normally-off (NO) single pole switches (SWs) incorporated are then switched (see switch selection table provided in Figure 5.40) to enable selection of all the possible winding combinations for their DC resistance measurements. The representative resistance per phase per winding set can then be determined by averaging the set of DC resistance measurements thus $R_s^{(a,x)} = (\sum_{j=1}^{3} R_{DC_j}^{(a,x)}/2)/3$. Note that the DC source is adjusted to provide approximately rated stator current for each winding set and the resistance between the two stator leads is determined from voltmeter and ammeter readings.



S/N	SW_1	SW_2	SW_3	SW_4
1	ON	ON	OFF	OFF
2	ON	OFF	OFF	ON
3	OFF	ON	ON	OFF

Figure 5.39: DC Resistance Measurement for each Stator Winding Set

5.4.3.2 Locked- rotor test

The locked- rotor test is used to determine x_{ls}^{a}, x_{ls}^{x} and x_{lr}. When combined with data from the DC test, it also determines r_2. The test is performed by locking the rotor so that it cannot turn and measuring the line voltages, line currents and three phase power inputs to 'a-b-c' stator winding set. The voltage is increased from zero in steps up to a value that gives rated currents in the stator windings. A voltmeter is also connected to the open 'x-y-z' winding set to measure its induced voltage. The procedure is repeated with 'x-y-z' winding set connected to the supply and 'a-b-c' winding set left open. Finally, the two stator winding sets were then supplied simultaneously with measurements taken as the 3-ϕ supply was gradually varied until the rated current circulated in the windings. The results of the measurements are as presented in Tables 5.11 & 5.12.

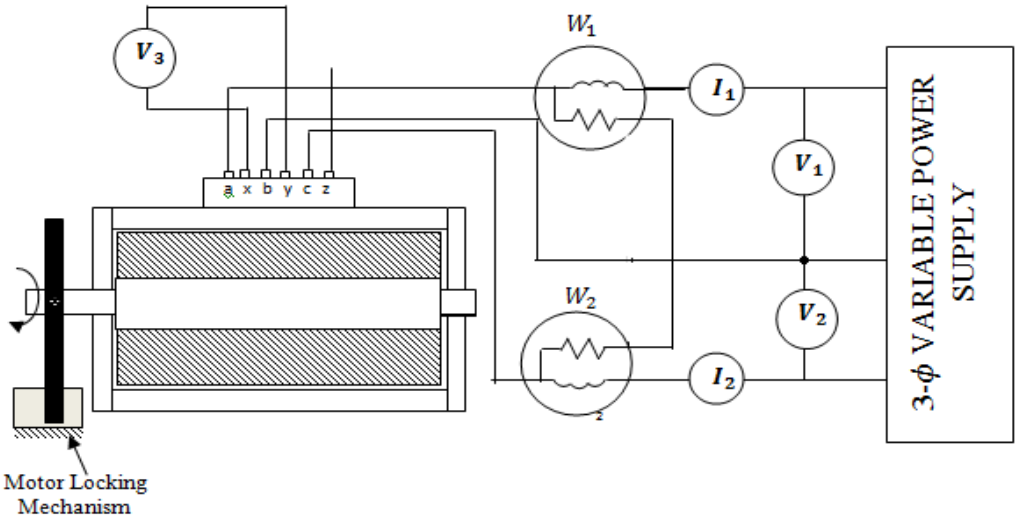


Figure 5.40: Connection Diagram for Locked Rotor Test on DSWIM Prototype

Table 5.11: Locked Rotor Test Results with x-y-z Winding Set Open

Meas. No	V_{ab} (Volts)	V_{bc} (Volts)	V_{xy} (Volts)	I_a (Amps)	P_{SC} (Watts)	Q_{sc} (Var)	S_{sc} (VA)	Speed (rpm)	$p.f.$ Cos(θ)

1	20	21	-	4.5	42	146	152	0	0.28
2	43	42	-	6.7	134	469	488	0	0.27
3	71	70	-	8.2	288	937	980	0	0.29
4	90	93	-	9.1	427	1305	1373	0	0.31
5	112	110	-	10.5	645	1874	1982	0	0.33
6	125	124	-	12	844	2364	2510	0	0.34

Table 5.12 Locked Rotor Test Results with 'a-b-c' Winding Set Open

Meas. No	V_{xy} (Volts)	V_{yz} (Volts)	V_{ab} (Volts)	I_x (Amps)	P_{SC} (Watts)	Q_{sc} (Var)	S_{sc} (VA)	Speed (rpm)	$p.f.$ Cos(θ)
1	19	22	-	3.8	44	117	125	0	0.35
2	45	41	-	5.6	153	409	437	0	0.35
3	74	76	-	7.3	346	869	935	0	0.37
4	93	90	-	8.8	553	1305	1417	0	0.39
5	115	112	-	10.2	813	1862	2032	0	0.40
6	120	123	-	11.7	1021	2207	2432	0	0.42

Since the no-load current (I_o) at locked rotor is considerably less than the rotor current (I_2), the no-load current may be neglected, enabling a simplification of the equivalent circuit. From the resulting simplified equivalent circuit, the relevant parameters of DSWIM (x_{ls}^{a}, x_{ls}^{x} , x_{lr} and r_r) are then computed with rotor parameters referred to stator side. Note that calculations are carried out with respect to each independent stator winding set so as to

enable their respective parameters to be determined. As a matter of fact, several of these calculations were performed and subsequently averaged to determine most representative DSWIM parameters based on locked rotor tests.

5.4.3.3 No- load test

The no-load test is used to determine the magnetizing reactance X_m and the combined core, friction, and windage losses. These losses are essentially known to be constant for all load conditions (Stephen, 1991). The connections for the no-load test are identical to those for the locked-rotor test, the only difference being in the operation of the test. For the no-load test, the rotor is unlocked and allowed to run unloaded at rated voltage and frequency. Rated voltage is applied and then gradually reduced until the slip approaches unity. As one ('a-b-c') winding set is connected to the supply a voltmeter is connected across two phases of the other ('x-y-z') winding set. Thus the voltmeter would measure an induced voltage due to transformer action.

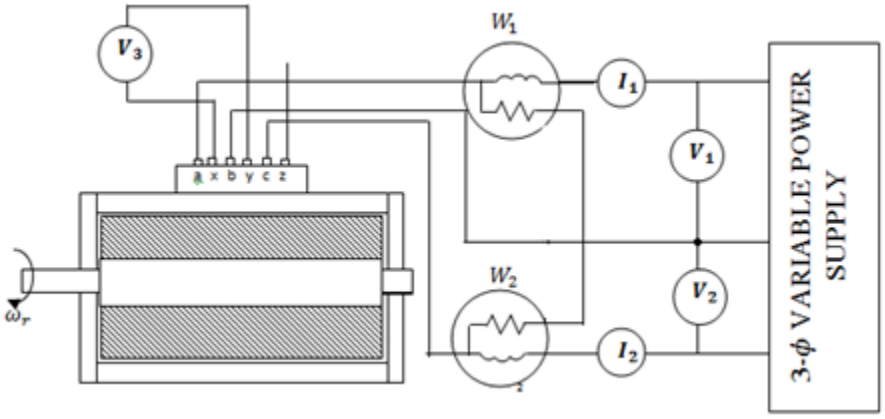


Figure 5.41: Connection Diagram for No-load Test on DSWIM Prototype

For each voltage measured the following were recorded:

i) Two line voltages;

ii) A phase current;

iii) One line voltage of the open winding set;

iv) Input power using two wattmeter method;

v) Rotor speed;

The same procedure is repeated with 'x-y-z' winding set connected to the supply while 'a-b-c' winding set is left open. Both stator winding sets are supplied from a variable 3-ϕ supply and same measurements carried out to generate credible results from which relevant DSWIM steady state parameters are estimated. The results of the various tests carried out are presented in Tables 5.13 and 5.14.

At no-load, the operating speed is very close to synchronous speed. Because the slip is very close to zero, the current flowing the in rotor circuit is very small. Consequently, the rotor circuit can be assumed to be open circuited, without any loss of accuracy, in the no-load current calculations. According to well established approach (Stephen, 1991), the separation of friction and windage losses from the no-load test may be accomplished by plotting the no-load power versus voltage squared for low values of voltages and then extrapolated to zero voltage. Note that the no-load data measured around the rated voltage were used to determine the DSWIM magnetizing branch elements (R_c and X_m). Table 5.15 presents the parameters of the DSWIM per phase determined from DC resistance, locked rotor and no-load tests carried out as facilitated by their respective computational procedures outlined in Appendix E.

Table 5.13: No Load Test Results with 'x-y-z' Winding Set Open

Meas. No	V_{ab} (V)	V_{bc} (V)	V_{xy} (V)	I_a (A)	I_b (A)	I_x (A)	P_0 (W)	Q_0 (Var)	S_0 (VA)	N_r (rpm)	$p.f.$ Cos(θ)
1	20	23	0	0.01	0.00	0	0	0	0	0	0
2	50	54	46	0.01	0.01	0	0	0	0	435	0
3	80	78	73	0.21	0.20	0	10	27	29	500	0.35
4	100	101	91	0.28	0.35	0	14	46	48	510	0.30
5	130	128	122	0.43	0.52	0	26	93	97	510	0.27

6	148	146	141	0.70	0.83	0	41	174	179	543	0.23
7	173	175	170	0.91	1.03	0	63	265	272	548	0.23
8	197	200	189	1.16	1.16	0	79	387	395	554	0.20
9	220	225	203	1.32	1.29	0	80	496	502	561	0.16
10	253	255	241	1.49	1.52	0	104	644	652	592	0.16
11	275	277	262	2.17	2.15	0	186	1017	1034	610	0.18
12	301	303	294	2.68	2.61	0	252	1375	1398	644	0.18
13	326	322	320	2.96	3.01	0	301	1644	1671	678	0.18
14	350	348	338	3.23	3.34	0	352	1927	1959	700	0.18
15	374	378	369	3.50	3.51	0	363	2238	2267	703	0.16

Table 5.14: No load Test Results with 'a-b-c' Winding Set Open

Meas. No	V_{xy} (V)	V_{yz} (V)	V_{ab} (V)	I_x (A)	I_y (A)	I_a (A)	P_0 (W)	Q_0 (Var)	S_0 (VA)	N_r (rpm)	$p.f.$ Cos(θ)
1	25	24	0	0	0	0	0	0	0	0	0
2	61	58	55	0.36	0.32	0	13	36	38	448	0.34
3	83	85	78	0.33	0.35	0	15	45	47	503	0.32
4	112	109	100	0.43	0.45	0	24	80	83	515	0.29
5	137	138	127	0.67	0.66	0	46	152	159	516	0.29
6	154	153	148	1.02	1.08	0	68	263	272	530	0.25
7	180	177	160	1.13	1.12	0	81	343	352	551	0.23
8	201	201	195	1.14	1.09	0	83	388	397	570	0.21
9	225	223	210	1.52	1.60	0	107	583	593	583	0.18
10	258	256	235	2.13	2.17	0	162	938	952	615	0.17
11	280	278	272	2.83	2.81	0	233	1352	1372	640	0.17
12	308	310	301	3.41	3.43	0	291	1806	1829	675	0.16
13	330	329	323	4.05	4.00	0	370	2256	2286	690	0.16
14	353	350	341	3.93	3.94	0	384	2372	2403	703	0.16
15	376	375	357	3.85	3.82	0	401	2475	2507	709	0.16

Table 5.15: Calculated DSWIM Parameters Based on Experimental Measurements

Parameter	'a-b-c' Winding	'x-y-z' Winding

Stator Resistance	$R_s^a = 1.5\Omega$	$R_s^x = 1.5\Omega$
Stator Leakage inductance	$L_{ls}^a = 14.3\text{mH}$	$L_{ls}^x = 14.4\text{mH}$
Stator Mutual Leakage Inductance	$L_{lm} = 46.7\text{mH}$	
Magnetizing Inductance	$L_m = 0.14\text{H}$	
Core Resistance	$R_c = 250\Omega$	
Rotor Resistance	$R_r' = 0.68\Omega$	
Rotor Leakage Inductance	$L_{lr}' = 38.5\text{mH}$	

5.4.4 Comparison of DSWIM simulation and prototype experimental results

Figure 5.42 depicts graphical comparisons of steady state torque speed characteristics of MATLAB/Simulink model of DSWIM and its prototype. Furthermore, Table 5.16 has offered comparisons between benchmark values obtained from DSWIM simulation results and their corresponding values returned from experimental measurements on the DSWIM prototype. Based on Figure 5.42and Table 5.16, and with DSWIM assumed as baseline values, it is seen that DSWIM simulation and experimental results closely match within maximum error band of $\pm 5\%$. The foregoing comparative analysis essentially gave effect to the validation of DSWIM model in MATLAB/Simulink environment. In the next subsection, the experimental results on DSWIM prototype and its standard 3-ϕ IM equivalent are compared comprehensively.

.

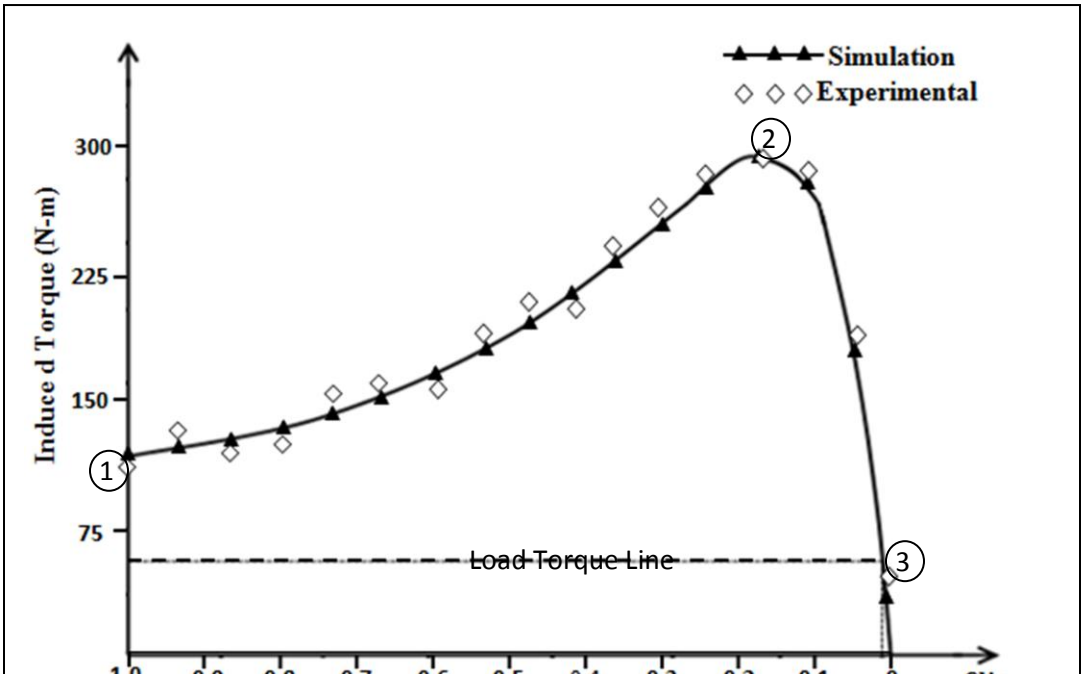


Figure 5.42: Comparison of DSWIM Simulated and Experimental Steady State Speed Torque Characteristics

Table 5.16: Comparison of Some Selected Parameters for DSWIM Model and Prototype

Parameter	**Dual Stator Winding Induction Machine (DSWIM)**		**Error Analysis (%)**
	Model	**Prototype**	
Starting Torque, τ_{start} (N-m)	105	101.33	-3.5
Max Torque,τ_{max} (N-m)	282	286.2	1.5
Rated Speed, n_r (rev/min)	713.4	737.88	3.2
Slip, $s = (n_s - n_r)/n_s$	0.05	0.053	2.8
Power factor, pf	0.88	0.902	2.5
Efficiency,η_{max} (%)	91	93.55	2.8
Starting Time, T_s (seconds)	1.25	1.29	3.2

5.4.5 Comparison of results for DSWIM and standard 3-ϕ IM

Figures 5.43-5.47 show the measured quantities torque, power factor, efficiency and motor current as a function of slip for DSWIM prototype and its original 3-ϕ induction machine equivalent ratings. Finally, Figure 5.48 depicts, at a glance, the dependence of these quantities on the output power specifically for DSWIM. Undoubtedly, the experimental results for the DSWIM are, prima facie, superior to those of the original 3-ϕ induction machine.

As can be seen in Figure 5.42, the power factor of the dual is higher than that of the single stator winding machine (by approximately 10%) at near synchronous speed, while their values are practically the same for both machines at rated speed. This observation may be attributed to the fact that on no-load the dual winding machine draws less magnetizing current than the single winding machine. As such, the dual winding machine will have an improved power factor in the vicinity of no-load. That is, near synchronous speed. Far more significant, is the improvement in the power efficiency of the DSWIM, as high as 10%, over the 3-ϕ single machine due to former's optimized electrical and magnetic loadings pursued in this research.

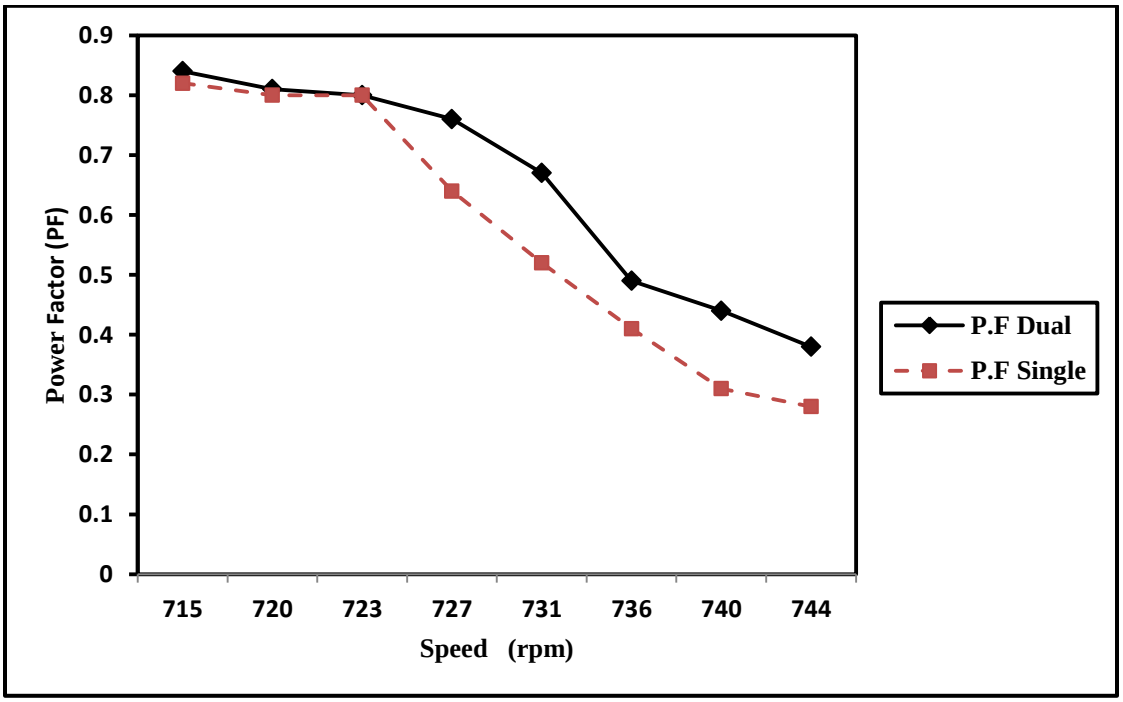


Figure 5.43: Comparison of Power Factor versus Speed for Dual and 3-ϕ Induction Machine

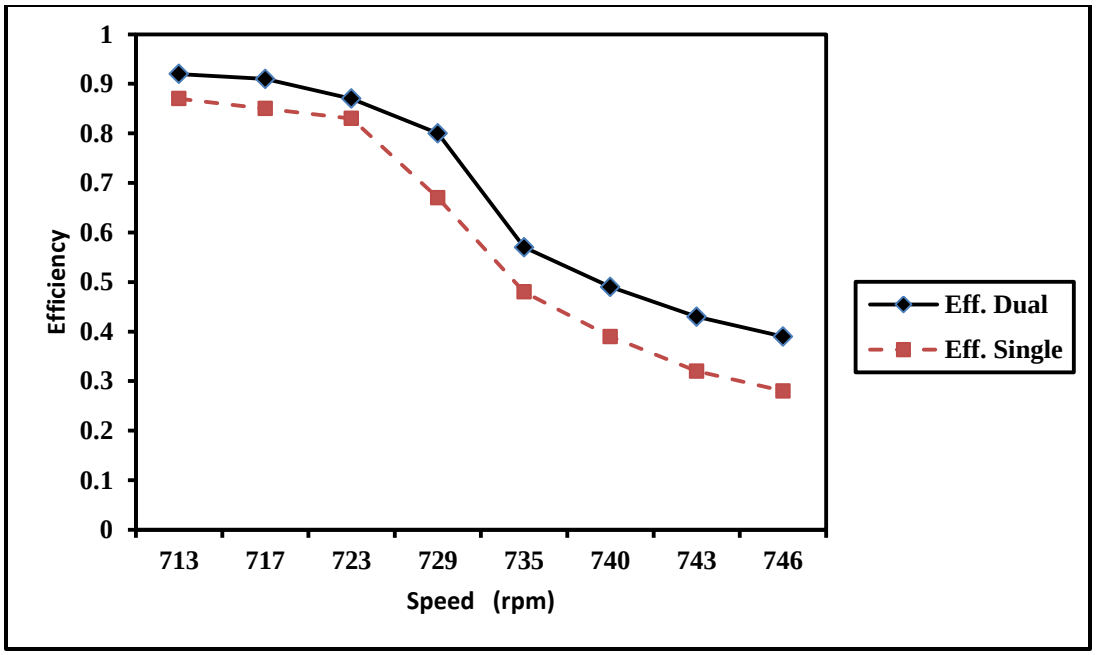


Figure 5.44: Comparison of Efficiency versus Speed for Dual and 3-ϕ Induction Machine

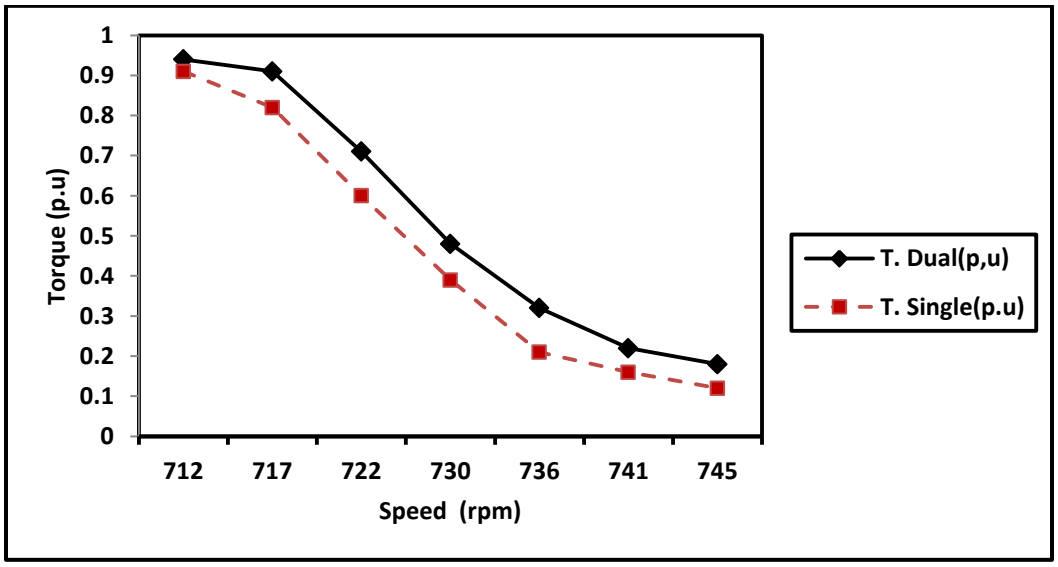


Figure 5.45: Comparison of Torque versus Speed for Dual and 3-ϕ Induction Machine

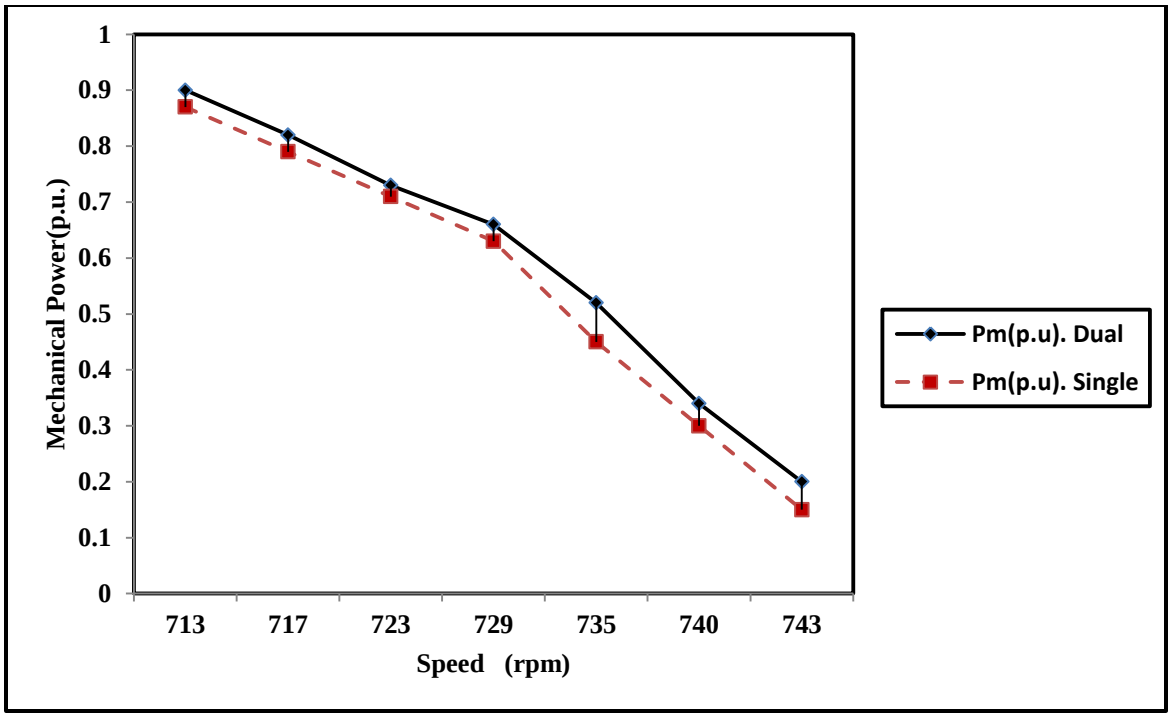


Figure 5.46: Comparison of Mechanical Power versus Speed for Dual and 3-ϕ Induction Machine

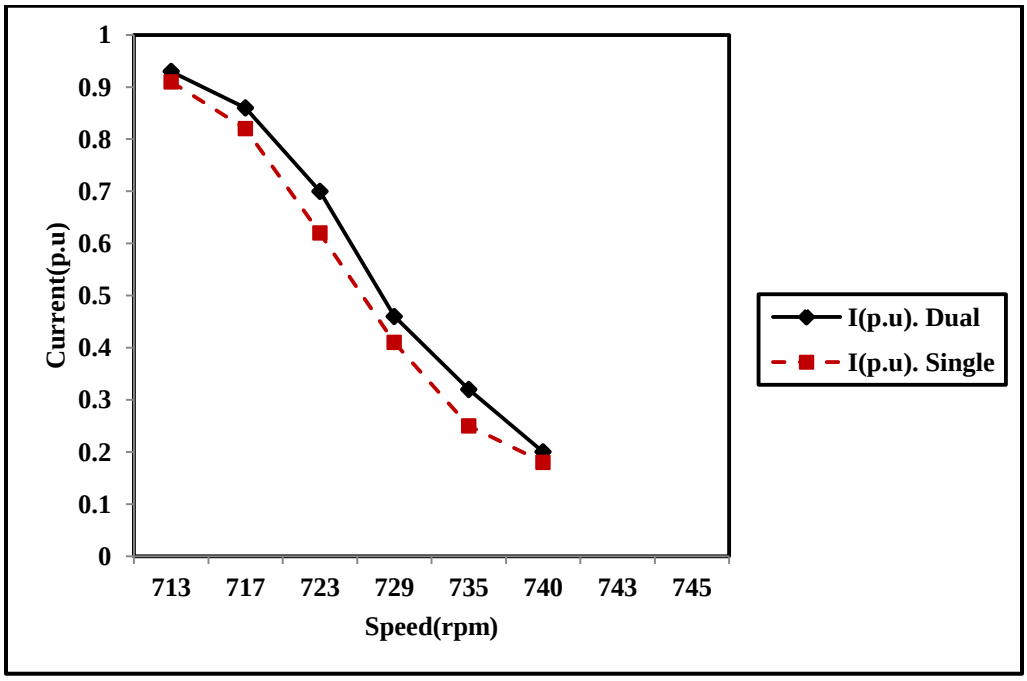


Figure 5.47: Comparison of Current versus Speed for Dual and 3-ϕ Induction Machine

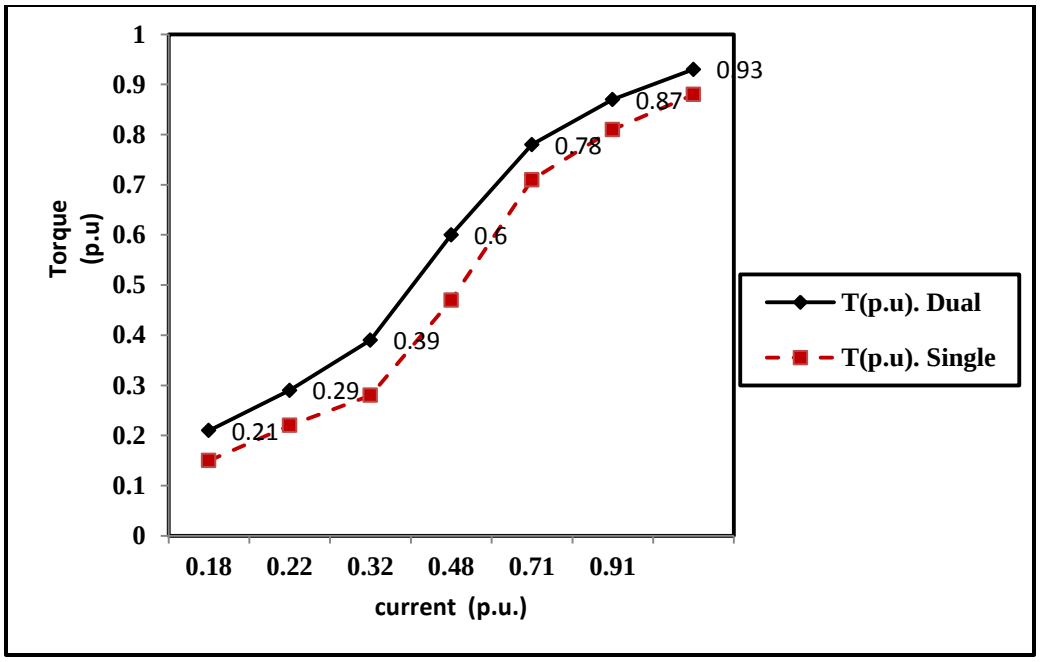


Figure 5.48: Comparison of Torque versus Current for Dual and 3-ϕ Induction Machine

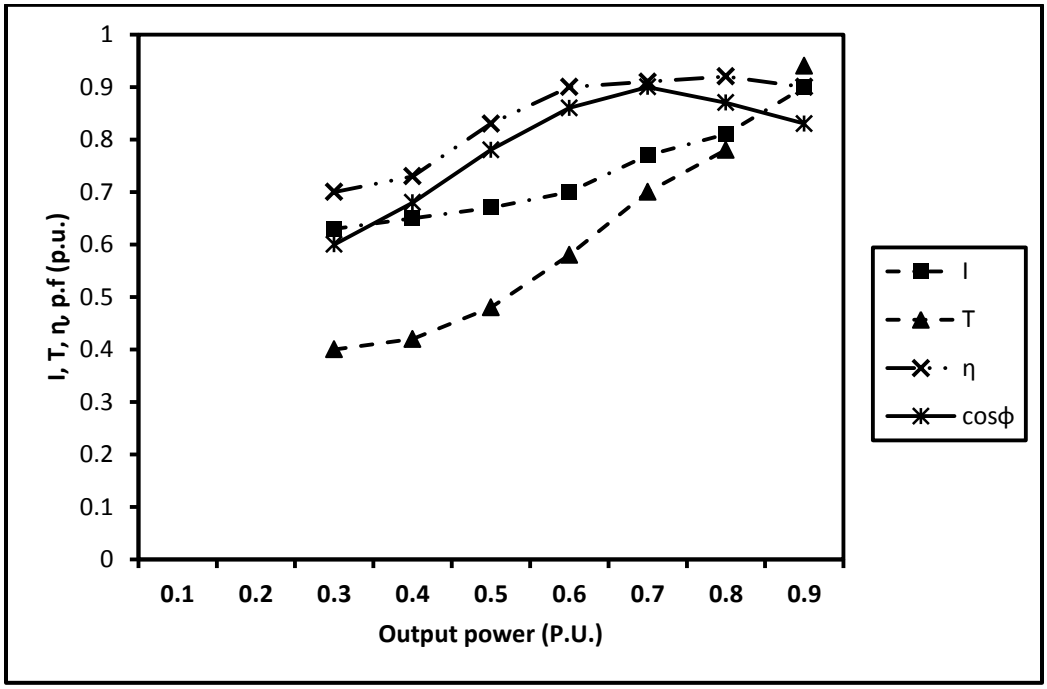


Figure 5.49: Key Performance Characteristics of the Dual Stator Machine

5.4.6 DSWIM circle diagram results

It is instructive to construct a representative circle diagram for DSWIM using parameters derived from its no-load and locked rotor tests. The import of circle diagram construction is to enable fairly accurate segregations of DSWIM losses at any given operating point.

Actually, the procedure for the construction of the circle diagram is not new with its salient constructional steps outlined in Appendix H; even though it was briefly introduced in Chapter Two as a tool embraced in the analysis of asynchronous machines. Relying on the locked and no-load test results presented in subsection 5.4.2, a circle diagram shown in Figure 5.50 has been constructed for the DSWIM prototype to aid its loss segregation determinations that will be tackled in the next subsection. It is noteworthy that the circle diagram so constructed, apply to both dual stator windings operating in steady state motoring mode. The foregoing is, of course, made possible due to the identical architecture of the two winding sets housed in the DSWIM case study. However, this is not applicable to the dissimilar pole DSWIM having different winding configuration where one winding is utilized as power winding and the other as control winding.

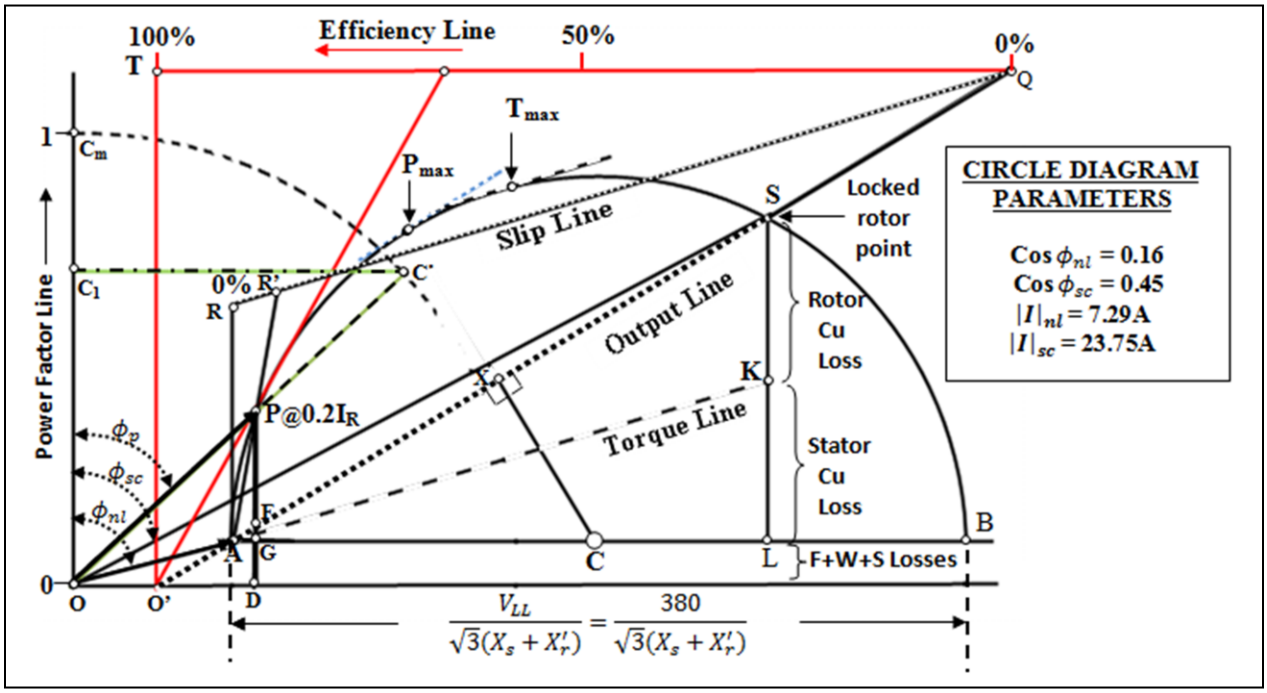


Figure 5.50: Constructed Circle Diagram for DSWIM Prototype

5.4.7 DSWIM loss segregation results

Figure 5.50 portrays in 3-D pie diagram in respect of the loss segregation analysis for the DSWIM prototype at full load. Due to measurement accuracy limitations, we have applied

loss percentage error applicable to the DSWIM rating recommended by IEEE, IEC, etc. and conveniently abridged in (Hsu, et al. 1998; Daut, et al. 2009). Table 5.17 presents summary of the computed losses at some selected DSWIM loading scenarios that made extensive use of the constructed DSWIM circle diagram of the preceding subsection. A cursory look at this table reveals that the stator and rotor copper losses decrease proportionately as should be expected and in conformity with the earlier experimental results of DSWIM prototype test rig; whilst the stray, core, windage and frictional losses remain constant.

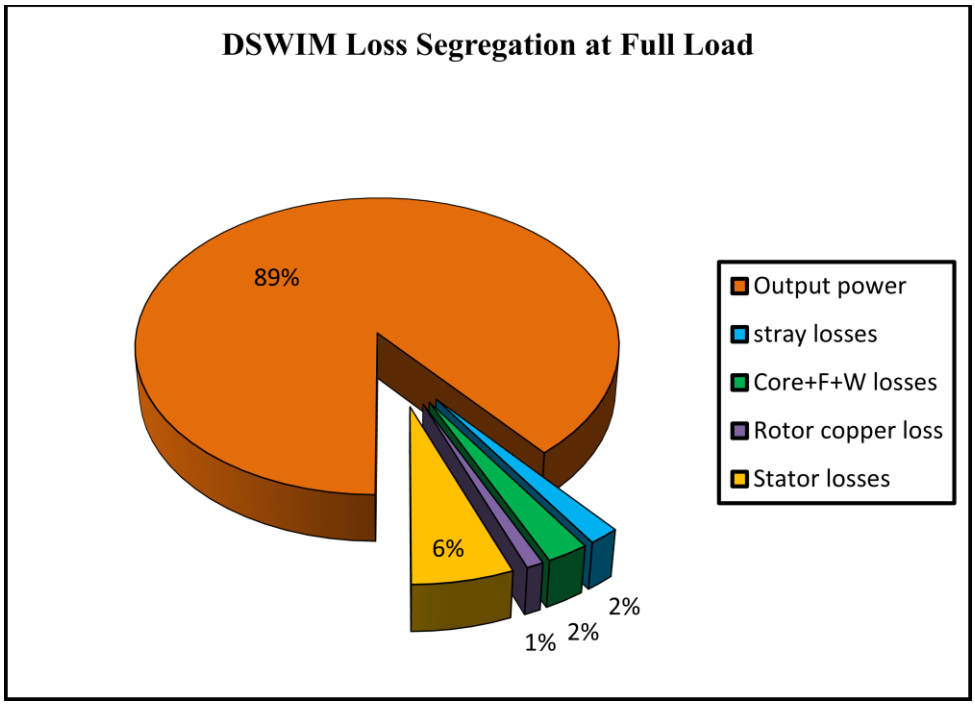


Figure 5.51: Full Load Loss Segregation Analysis for the Prototype DWSIM

Table 5.17: Summary of the computed losses at some selected DSWIM loading Scenarios

Segregated Loss Components (Watts)	DWSIM Loading Scenarios (Specified as percentage of full load current) and at rated speed								
	20	30	40	50	60	70	80	90	100
Stray Losses (Harmonic)	89.2	89.2	89.2	89.2	89.2	89.2	89.2	89.2	89.2
Core + Frictional + Windage Losses	89.2	89.2	89.2	89.2	89.2	89.2	89.2	89.2	89.2
Rotor Copper Loss	1.78	4.01	7.14	11.2	16.1	21.8	28.5	36.13	44.6

Stator copper Loss	10.74	10.7	43.0	67.3	96.7	132	172	217.6	268.6

5.5 Analyses of Experimental Results

The various far reaching experimental results obtained from the DSWIM prototype test rig were presented in the preceding subsections as found in Tables 5.11-5.17 and Figures 5.42-.5.51. This section seeks to further deepen and broaden the scope of analysis of some key results. Against this backdrop, empirical relations are developed which, even though emanated from the DWSIM prototype test rig results, are fundamentally valid with respect to induction machine motoring mode behavior in the neighbor of synchronous speed. More precisely, Figures 5.43-5.48 have clearly revealed higher operational performances of DSWIM prototype over standard 3-ϕ IM of the same rating. The various curves in Figures 5.43-5.47 corresponding to DSWIM have been fitted with polynomial functions using least squares techniques. The final describing equations recommended by the best $R^2 - \text{factor}$ are summarized in Table 5.18. Similar exercise has also been done with respect to Figure 5.49 and the equations developed are presented in Table 5.19. It is imperative to state that the various equations developed are valid within the range of values specified in Tables 5.18 and 5.19 respectively. In the subsequent subsections, some key features are revisited to shed light on their respective impacts on the operations of asynchronous machine family to which DSWIM belongs.

Table 5.18: Fitted Polynomial Equations for DSWIM Quantities Plotted in Figures 5.43-5.47

DSWIM Dependent variable	Model Equation with rotor speed (n_r) as Independent variable	Coefficient of fitness R^2
Power factor (PF< 1)	$PF = -0.01n_r^3 + 0.098n_r^2 + 0.386n_r + 0.06$	0.993
Efficiency ($\eta < 1$)	$\eta = 0.014n_r^4 - 0.15n_r^3 + 0.5n_r^2 + 0.74n_r + 0.64$	0.993
Torque (T p.u.)	$T = 0.01n_r^3 - 0.099n_r^2 + 0.163n_r + 0.49$	0.995

Mechanical (P_m p.u.)	$P_m = 0.001n_r^4 - 0.021n_r^3 + 0.12n_r^2 - 0.31n_r + 0.71$	0.993
Current (I p.u.)	$I = -0.001n_r^4 - 0.036n_r^3 + 0.23n_r^2 - 0.42n_r + 0.56$	0.997

Table 5.19: Fitted Polynomial Equations for DSWIM Quantities Plotted in Figure 5.48

DSWIM Dependent variable	Model Equation with Power Output (P_o) as Independent variable	Coefficient of fitness R^2
Power factor (PF< 1)	$PF = -0.015P_o^2 + 0.232P_o + 0.026$	0.977
Efficiency (η < 1)	$\eta = -0.009P_o^2 + 0.155P_o + 0.309$	0.957
Current (I p.u.)	$I = 0.006P_o^2 - 0.031P_o + 0.671$	0.993
Torque (T p.u.)	$T = 0.01P_o^2 - 0.028P_o + 0.385$	0.960

5.5.1 Rotor starting torque characterization

If the rotor is at rest, mechanical inertia prevents rotation at the instant voltage is applied to the stator; in effect, the motor behaves as though the rotor is locked. The torque developed at the locked rotor stage is the turning moment produced by the interaction of the rotor current and the stator flux when the shaft is at rest and a voltage applied to the stator winding. Recall that this torque was referred to as induction machine starting torque in Chapter 2 and it occurs at a slip $s = 1.0$. For the DSWIM prototype, its starting torque has been found to be 105N-m and identified by circled '1' in Figure 5.42. As a matter of fact, if the load torque on the shaft is greater or equal the starting torque, the motor will not start. Should this occur, and protective devices do not disconnect the machine from the line, the motor could suffer from insulation failure. One of the cardinal advantages of DSWIM is its fault tolerant feature.

Thus if the insulation failure affects only one winding set, the machine can still run on the healthy winding set but at reduced mechanical power output.

5.5.2 Acceleration of DSWIM from standstill

Assuming the load torque on the shaft of DSWIM is less than the starting torque, the rotor will accelerate. As the machine accelerates from its standstill position, the slip decreases causing the magnitude and phase angle of rotor current to decrease. Consequently, the active component of rotor current $I_r cos\theta_r$ will increase from its low value at DSWIM standstill to its maximum value referred to as breakdown value, and will decrease again with further acceleration. There is an observable correlation between developed torque (T_d) and $I_r \cos\theta_r$ which can be deduced from the DSWIM torque speed characteristics and its circle diagram of Figures 5.42 and 5.50 respectively.

5.5.3 Behavior of DSWIM near synchronous speed

If the DSWIM is lightly loaded, the rotor speed approaches that of the rotating flux. The current becomes quite small, and even though it is almost in phase with the induced $e.m.f$, the very low value of $I_r \cos\theta_r$ results in a very low T_D. If there is no load on the shaft, the rotor may sometimes lock in synchronism with the rotating flux. This becomes possible when the relative motion between the two is so small that the rotor iron becomes magnetized along some axis of minimum reluctance, and locks in synchronism with the rotating flux. This phenomenon is referred to reluctance motor action. Under such conditions, the machine no longer develops induction-motor torque; the slip is zero and no current appears in the rotor. The reluctance torque is very small, however, and a light load on the shaft will pull it out of synchronism.

5.5.4 DSWIM behavior during loading and breakdown

Consider DSWIM is operating at no load and for this condition; the load torque is essentially windage and friction. As shaft load is applied, the load torque becomes greater than the developed torque, and the motor slows down; the resultant increase in slip causes an increase in $I_r Cos\theta_r$, which in turn causes an increase in the developed torque. If rated load torque is applied to the shaft, the motor will decelerate until the increase in developed torque caused by the increase in slip equals the load torque on the shaft plus windage, friction and stay load. The motor will then operate at the steady-state speed identified by 'circled 3' of Figure 5.42. Further increase in shaft load (overload) causes additional deceleration, accompanied by increase in $I_r \cos\theta_r$, leading to increase in developed torque. If, however, the load torque on the shaft is increased to a value greater than the maximum torque that the machine can develop (circled 2), the machine will breakdown. This will be accompanied by increase in slip, due to increase in shaft load above the breakdown value; thereby causing rapid decrease in $I_r \cos\theta_r$ and attendant rapid decrease in developed torque. The machine will suffer a sharp drop in speed and could attract unintended braking action. The very high current associated with a high slip will burn out the motor windings, unless protective devices remove the machine from the line. The breakdown torque is defined as the maximum torque that a motor can developed while being loaded (at rated voltage and rated frequency) without suffering an abrupt drop in speed. A maximum torque of approximately 280N-m developed by DSWIM prototype was determined from Figure 5.42. Although an induction motor can be operated momentarily at overloads up to the breakdown point, it cannot do so continuously without overheating and causing severe damage to both the stator dual winding sets and squirrel cage rotor.

5.6 Summary

This chapter has provided an in-depth documentation of the numerous results generated and discussed them comprehensively in order to illuminate the far reaching accomplishments of

this research work. The results set forth encompass, first and foremost, the outcome of optimized design of dual stator winding induction machine involving improved classical design approach hybridized with GA tuning technique. The results of DSWIM parameter calculations based on improved design winding function and finite element techniques were then presented and discussed at length. In particular, Finite Element Analysis was used to analyze the field distribution pattern within the core and the air gap of the dual-stator winding machine. As a result of this analysis, the various windings inductances were calculated and some of the performance indices of the machine were predicted. The MATLAB/Simulink model developed for the DSWIM was successfully implemented with wide ranging results obtained. The DSWIM performance characteristics plotted were found to be in agreement with or superior to those published in the relevant literature.

Finally, the experimental DSWIM prototype was tested in the laboratory in order to validate the predicted results. The parameters of the experimental machine were then compared with the results of other techniques and found to be close within error bounds of $\pm$ 5%. The experimentally measured speed torque characteristics were found to be in close agreement with the MATLAB/Simulink model simulation results thus validating the efficacy of the model. More importantly, several performance characteristics plots based on experimental data obtained from the DSWIM prototype test rig and those of the original three phase machine were also established to be in agreement. Most interestingly, the DSWIM prototype returned 93.4% efficiency measurement at rated load compared with 87% obtained with respect to the standard three phase induction machine at full load and of the same rating. Indeed, at light loads the dual-stator winding machine exhibited superior characteristics. This could be attributed to the fact that, at light loads, the dual stator machine can be operated with only one winding set on. This is referred to as power segmentation. Power segmentation

brings about redundancy of the machine part, as a result of which the reliability of the machine increases.

CHAPTER SIX

SUMMARY, CONCLUSIONS AND RECOMMENDATIONS

6.1 Introduction

This chapter provides summary of tangible goals accomplished in this research work. Comprehensive conclusions are then drawn that essentially highlight the key findings reported in this dissertation. The contributions of this research work to the advancement of the existing knowledge base on dual stator winding induction machine are also included in this chapter. Finally, far-reaching recommendations and further research areas identified are also set forth to serve as dissertation's closure.

6.3 Summary

An improved re-design philosophy and detailed simulation model development for, as well as prototype realization of a dual-stator three phase induction machine constituted the main thrusts of the research work reported in this dissertation. Starting from its standard 3-ϕ stator frame and squirrel cage, a dual stator winding induction machine having similar pole ratio was designed using the developed hybrid improved design methodology and GA tuning scheme. The similar pole ratio DSWIM design philosophy and prototype realization were undertaken for the prime objective of investigating its operational superiorities over its three phase conventional machine of the same rating. The compendium of the overall research work is presented in the subsequent paragraphs that follow.

As a critical step to situating the main thrusts of this dissertation correctly, enjoined the need to provide the underlying theoretical characterization of induction machines based on winding function approach and extensive literature review on the extant development of dual stator winding induction machines. This has led to the pursuit of research in the design of dual stator winding induction machine with similar pole ratio and of its prototype realization. This arose chiefly from global trend towards efficient energy utilisation based on the

recognition that induction machines are the workhorses in modern industrial drive systems. For this reason, attention has been focused herein on the design philosophy of the new class of induction machines due to some advantages they possess over other machines. Such advantages include flexibility, ease of control, ruggedness and capability of generating mode at negative slip ($s < 0$).

The proposed analytical framework anchored on hybrid improved classical design (ICD) and genetic algorithm (GA) optimization process has been comprehensively outlined in accordance with its functional representation of Figure 3.1. Its efficacy has been demonstrated with respect to the design of two winding sets ('a-b-c' and 'x-y-z') having similar 8/8 pole ratio. More specifically, attention is focused on efficient calculations of its electric and magnetic loadings to meet imposed constraints by the a priori selected stator frame and squirrel cage rotor configuration. The paramount interest concerned efficient calculations of $mmfs$ in various magnetic paths of the DSWIM that enabled its modelling parameter determinations. The GA optimization process then secured optimum efficiency and operating power factor of DSWIM via parameter selections without violating any imposed magnetic and electric loading constraints. The winding diagram has also been developed specifically for a single layer implementation of 8/8 similar pole ratio two winding sets displaced electrically by 30^o to be housed in 48-slot stator frame.

The extensive simulation DSWIM has been made possible via its detailed modelling in MATLAB/Simulink environment using d-q-0 arbitrary reference frame. Additionally, 2-D finite element method has been employed to model DSWIM for the purpose of its steady state inductance calculations. The numerous results obtained are classified thus: Results of DSWIM design parameters using classical approach (Tables 5.1-5.7); Results of computed DSWIM inductance values using winding function and FEM modelling techniques (Tables 5.8-5.10 and Figures 5.8, 5.9 & 5.10-5.13); Results of wide ranging MATLAB/Simulink

simulations (Figures5.14-5.38) and finally results of in-depth experimental investigations on the DSWIM prototype test rig are to be found in Figures 5.42-5.49. Of noteworthy is the application of classical design approach in conjunction with GA tuning process, which has successfully optimized the efficiency and power factor of similar pole ratio dual stator winding induction machine. In support of the foregoing, Table 5.7 reveals optimized values of efficiency and power factor whilst Figures 5.45 and 5.46 are their respective experimentally measured values. Finally, this research work has therefore evolved a versatile multi-phase induction machine architecture that emerged from a new design concept and improved modelling strategy.

6.3 Conclusion

This research work has pursued rigorously an improved design philosophy and detailed mathematical modelling of a dual stator winding induction machine equipped with similar pole ratio. The following constitute the tangible goals achieved and concisely documented in this dissertation.

1. Implementation of pragmatic induction machine redesign philosophy to facilitate conversion of conventional induction machine into dual wound stator induction machine of identical or similar pole ratio has been accomplished. In this regard, an improved classical design approach hybridized with GA technique has been developed and successfully applied to design 8/8 pole ratio DSWIM with optimum efficiency of 93.4% and operating power factor of 0.88 at full load.
2. Generalized mathematical model in arbitrary d-q-0 reference frame and necessary equivalent circuit inductances to underpin performance analyses of dual stator winding induction machine have been calculated using winding function, improved classical design approach and 2D-FEM analysis. The various inductance values calculated by each method were then compared. It was conclusively established that

improved classical design approach inductance values agreed fairly well with those obtained from 2D-FEM values.

3. Investigation of redesigned dual stator wound induction machine model via simulations in MATLAB/Simulink software and validating such simulation results against equivalent experimental results for accuracy verifications. The torque-speed characteristics generated from DSWIM simulation model compared favourably with the experimentally measured torques from the 8/8 pole ratio DSWIM test rig.
4. A standard experimental test rig has been configured around the redesigned 8/8 pole ratio dual stator wound induction machine prototype as well as a conventional three phase induction machine of the same rating for comparative evaluations of key performance indices. The experimental results obtained have confirmed the 8/8 similar pole ratio DSWIM prototype operational superiorities over its equivalent standard 3-ϕ IM from the standpoints of torque output, efficiency and power factor variational studies.

Due to the rapidly growing demand for high power drive system and more flexible operation, multiphase machines will continue to attract serious research investigations. This research work has therefore laid sound foundation for further development of similar pole ratio dual stator winding induction machine so as to quicken its maturity and industrial drive penetration. The improvement in efficiency of similar pole ratio DSWIM over conventional 3-ϕ IM is particularly attractive as potential energy conversation strategy if and when widely adopted as rapidly penetrating new workhorses in ever expanding high power drive systems.

6.4 Contributions to Knowledge

This research work has made the following contributions to the existing knowledge base in the area of dual stator winding induction machine with special focus on the similar pole ratio dual machine induction machine.

1. **Developed generalized design algorithm for DSWIM**

   A generalized method of designing the dual stator winding machine has been developed. The proposed design concept is a premised on improved classical design approach hybridized with genetic algorithm (GA). Firstly, the improved classical design approach is employed to calculate the leading design parameters of DSWIM without violating the imposed electrical and magnetic loading constraints. Secondly, the GA is applied to tune the DSWIM design parameters with maximization of its efficiency and power factor as objective function. The effectiveness of proposed improved classical design approach has been demonstrated with respect to the design of 8/8 pole ratio DSWIM starting a proiri selected stator frame and squirrel cage rotor.

2. **Evolved accurate technique for DSWIM modelling parameter estimations**

   This research work has provided algorithmic procedures for computing critical inductance values associated with the two stator winding sets (‘a-b-c’ and ‘x-y-z’ windings), rotor winding (‘a_r-b_r-c_r’ rotor winding) inductance values, mutual and leakage inductances. In addition, stator winding and rotor winding resistances are also estimated accurately by relying on physical geometries of the stator and rotor configurations.

3. **Detailed mathematical modelling of DSWIM in arbitrary d-q-0 reference frame**

   A detailed mathematical model for dual stator winding has been developed in arbitrary d-q-0 reference frame considering the effects mutual leakage inductances between d and q axis. The dynamic simulation models of DSWIM that are available

in the literature have neglected such mutual leakage inductances. The incorporation of the leakage inductance has been shown to elongate starting times of the simulation by as much as 50% even though its effect on the peak torques produced by each winding is insignificant. The consideration of saturation can be taken care of in straight forward manner by introducing a saturation factor in the appropriate mutual inductances.

4. List of publications

The following publications emerged from this research work so far as evidence of the contribution to knowledge dissemination in the subject area.

i. **(2011). *"FEMM- based Analysis of the Magnetic Field Distribution Pattern of the Dual Stator Winding of an Induction Machine".*** Zaria Journal of Electrical Engineering Technology, A.B.U., Zaria, 1(1)|85-93.

ii. **(2010), *"Calculation of Inductances of a Dual-Stator Winding Induction machine using the finite element approach",*** Nigerian Journal of Engineering (NJE), A.B.U., Zaria, 16(2)|83–89.

iii. **(2010), *"Development of an equivalent circuit of a Dual-Stator Winding Induction machine",*** Nigerian Journal of Engineering (NJE), A.B.U., Zaria, 16(2)|90–97.

iv. **(2010) *"Operation of a Dual-Stator Winding Induction Generator at Unity Power Factor",*** 1^{s} International Conference IEEE NIGERCON 2010 (Emerging and Sustainable Technologies for Power and ICT in a Developing Society), Abuja, Nigeria,17th – 19thJune|207-212.

v. **(2009), *"Modelling and Simulation of a Dual-Stator Winding Induction Machine",*** 3rd International Conference on Power Systems and Telecommunications, University of Lagos, Lagos, Nigeria, 22nd-24th |71-78.

6.5 Recommendations

Although research activities in the area of dual stator winding induction machine are expanding rapidly in most industrialized countries, the same cannot be claimed in the developing countries. Indeed we are not aware, based on available literature survey at our disposal, of any on-going research work on the development of dual stator winding induction machine in Nigeria. Against this backdrop, the following recommendations are advanced to encourage sustainable research activities in this new class of induction machines to support the growth of its envisioned diverse applications in Nigeria's future industrial revolution road map.

a. There is need to introduce dual stator induction machine drive system in advanced ac machines courses at undergraduate and postgraduate levels to provoke students' research interests in high powered drive systems.
b. Research grants should be made available to researchers in institutions of higher learning to pursue research activities in advanced design and applications of dual stator winding induction machines in electric transportation system, wind energy harvest systems, electric hoist systems, etc.
c. Due to very large numbers of 3-ϕ induction machines currently in operations in Nigeria, call for programmed conversions of critical ones into dual stator winding induction machines so as to benefit maximally from their fault tolerance, ruggedness and energy saving attributes.
d. Technologists should be trained in the conversion of the existing standard 3-ϕ induction machines into their equivalent dual stator winding induction machines on the platform of the proposed design approach addressed in this dissertation.

6.6 Suggestions for further work

The following are suggested areas for further work to build on the foundation already laid in this research work:

i) The detailed modelling of dual stator winding induction machine developed in this research work should consider incorporating magnetic saturation, rotor eccentricity and harmonic effects to investigate their separate and combined influences on its overall dynamic and steady state performances. In particular third harmonic current injection has been reported to improve torque density and thus deserves investigation with respect to similar pole ratio DSWIM. The investigation should be extended to the possibility of reducing harmonic contents of inverter-fed multiphase machine drive system as well as high frequency core loss calculations.

ii) Although detailed mathematical formulation of the design of multiphase machine as a multi-objective function problem has been carried out in this dissertation, the pragmatic solution sought considered magnetic and electric loading constraints with maximization of efficiency and power factor as objective function. Assumed from on-set is the availability of a standard stator frame to house the two winding sets designed and squirrel cage rotor. As a follow up to this research work, the optimum solution to the multi-objective function should be pursued via application of meta-heuristic technique. This will essentially yield complete design specifications for the dual stator winding induction machine that include new stator frame and rotor leading dimension specifications. Herein, all the constraints must be met and also secure overall design cost minimization.

iii) The 2-D FEM modelling of DSWIM in this research work was restricted to magneto static problem formulation that facilitated computations of DSWIM leading parameters using FEMM software. Such restriction should be removed by adopting 2-D FEM modelling of DSWIM that allows transient magnetic analysis anchored on the solution of time varying Maxwell equations to enable high frequency core loss calculations and to achieve more accurate parameter determination for DSWIM.

REFERENCES

Abbas M. A., Christen R., Jahns T. M. (1984); Six-phase voltage source inverter driven induction motor. IEEE Transactions on Industry Applications, Vol. 20, pp 1251- 1259.

Alberti et aL. [2011], "Variable Speed Induction Machine performance Computed Using Finite Element," *IEEE Transactions on Industry Applications*, vol. 47, no. 2, pp. 789–797, Apr. 2011.

Alberti et aL. [2008],"A Very Rapid Prediction of IM Performance Combining Analytical and Finite-element Analysis," *IEEE Transactions on Industry Applications*, vol. 44, no. 5, pp. 1505–1512, Sep./Oct. 2008.

Alger P. L., Freiburghouse E. H. and Chase D. D. (1930).Double windings for turbine alternators.*AIEE Trans*., vol. 49, pp 226-244.

Alger P. L., "The Nature of Induction Machines", Gordon and Breach Publishers, 2nd Ed., 1970.

Anderson, O.W. 1967. Optimum design of electrical machines.*IEEE Transactions on Power Apparatus and Systems* PAS-86: 707-711.

Alfredo Munoz Garcia (1999). Analysis and control of a Dual stator winding squirrel cage induction machine drive. Ph. D Dissertation, University of Wisconson- Madison.

Alfredo M. and Thomas A. L. (1998) "Dual Stator Winding Induction Machine Drive", IEEE Transactions on Industry Applications, Vol. 25 (4), pp. 601-608.

Alfredo R. M. and Thomas A. L. (1999) "Complex Vector Model of the Squirrel-Cage Induction machine Including Instantaneous Rotor Bar Current", IEEE Transactions on Industry Applications, Vol. 35 (6), pp. 1332-1340.

Andriamalala R. N., Razik H., Didier G. and Sargos F. M. (2006) "A model of DSWIM in case f Stator and Rotor Faults for Diagnosis Purpose", IEEE Transactions on Energy Conversion, Vol. 11 (3), pp. 2340-2345.

Ammasaigouden N., Subbiah M and Krishnamurthy M. R. (1986). Wind-driven excited pole changing induction generators. Proc. Inst. Elect. Eng. B, vol. 133, no. 5, p 315 -321.

American Society for Metals, (1966), 'Metals Handbook,' 8th edition, Volume 1.

Applebanum, J., and M.S. Erlicki. 1964. A problem of economic optimization of electric equipment design. *IEEE Transaction of Communication and Electronic* 88:773.

Applebanum, J., and M.S. Erlicki. 1965. Optimized parameter analysis of an induction motor. *IEEE Transactions on Power Apparatus and Systems* 84: 1017-1024.

Apsley J. and Steve W. (2006) "Analysis of Multiphase Induction Machines with Winding Faults", IEEE Transactions on Industry Applications, Vol. 42 (2), pp. 465-471.

Barado Rodrigo J. A., and Munte X. [2013], "Design and Testing of a Dual Stator Winding Induction Generator", 10th International Multi-Conferences on Systems, Signals & Devices (SSD) Hammamet, Tunisia659-664, March 2013.

Basil M. S., and Ahmed J. A.,[2012] "Determination of Deep Bar Cage Rotor Induction Machine Parameters Based on Finite Element Approach," The First National Conference for Engineering Sciences FNCES'12, pp. 18–24, Nov.2012.

Bianchi, N. (2005) "*Electrical Machine Analysis using Finite Elements*," ser. Power Electronics and Applications Series, Boca Raton, FL: CRC Press, 2005.

Bharadwaj, D.G., K. Venkatesan, and R.B. Saxena.1979a. Induction motor design optimization using constrained Rosenbrock method (Hill algorithm), *Computer and Electrical Engineering* 5, pp.41-46.

Bansal R.C., Kothari D.P. and Bhatti T.S. (2004).A novel mathematical modelling of induction generator for reactive power control of isolated hybrid power systems.Int. J. modelling Simulation, vol.24, no.1, pp 1-7.

Basset E.D. and Potter F.M. (1935). Capacitor excitation for induction motors. AIEE Trans., vol. 54, pp 540-545.

Bakare, G. A., (2001), 'Removal of Overloads and Voltage Problems in Electric Power Systems Using Genetic Algorithms /Expert System Approaches,' PhD Thesis, Duisburg University.

Boldea, I., and Nasar, S. A., (2001), 'The Induction Machine Handbook,' 1 ed.: CRC Press.

Bonert R. and S. Rajakaruna (1998).Self-excited induction generator with excellent voltage and frequency control. Proc. Inst. Elect. Eng., pt C, vol. 145, no. 1, pp 33-39.

Bharadwaj, D.G., K. Venkatesan, and R. B. Saxena (1979b), Optimization techniques applied to induction motor design-A comparative study. *Computer and Electrical Engineering* 6:117-122.

Broadway A. R. W. and Ismail D. S., (1986), 'Phase modulated 3-phase pole changing winding,' Proceedings IEE, Vol. 133, pp.61-70.

BroadwayA. R. W., "Brushless cascade alternator," *Proceedings IEE,* Vol. 121, No. 12, Dec., 1974.

Brennen B. and A. Abbondanti (1977).Static exciters for induction generators. IEEE Trans. Ind. Applicat., vol. 1A-13, pp 422-428.

Chandrasekaran V. and Manigandan T. (2011)[a]"Design and Effective Operation of Double Winding Synchronous Reluctance Motor", International Journal of Computer and Electrical Engineering, Vol. 3 (3), pp. 432-438.

Chandrasekaran V. and Manigandan T. (2011)[b] "Double Winding Induction Motor-an Approach for Improvement of Power Factor and Efficiency", European Journal of Scientific Research, Vol. 66 (2) pp. 262-273.

Chapman S.J (1998). Electrical Machinery Fundamentals.2nd Ed. New York: McGraw-Hill.

Creedy F., "Some developments in multispeed cascade induction motors", Journal IEE,Vol.59, 1927, pp 511-532.

Djafar H. Hubert R. and Abdrrezak R (2004) "On the Modelling and Design of Dual-Stator Windings to Minimize Circulating Harmonic Currents for VSI Fed Machines", IEEE Transactions on industry Applications, Vol. 40 (2), pp. 506-515.

Dmitry S. W. and Yujing L. [2013] "Finite Element Analysis of End Ring Impedance in Squirrel cage Induction Machines," *IEEE Trans. Energy Convers.*, vol. 14, no. 4, pp. 411–416, Dec. 2013.

Elders J.M. , J. T. Boys, and J.L. Woodwards (1984). Self excited induction machine as a small low-cost generator. Proc. Inst. ELECT. Eng., pt. c, vol. 131, no. 2, pp 33-41.

Elder J.M.,Boys J.T. and Woodward J.L. (1983). The process of self-excitation in induction generators," Proc. Inst. Elect. Eng. B, vol. 130, no. 2, pp 103-108.

Faiz, J., and M. B. B Sharifian. 1995. Optimum design of a three-phase squirrel-cage induction motor based on efficiency maximization. *International journal of computers and Electrical Engineering* 21 (5): 367-373

Fiacco, A. V., and G. P McCormik. 1964a. The sequential unconstrained minimazation technique for nonlinear programming, a primal-dual method. *Management science* 10 (2) : 360-366

Fiacco, A. V., and G. P McCormik.1964b. Computational algorithm for the sequential unconstrained minimization technique for nonlinear programming. *Management science* 10(4) : 601-617.

Fireteanu V. and Romary R. [2013], "Finite Element Investigation of the Short-Circuit Fault in the Stator Winding of Induction Motors and Harmonics of the Neighboring Magnetic Field," *Elect. Mach. Power Syst.*, vol. 28, PP. 257-262.

Fitzgerald A., Kingsley C. Jr. and Kusco A. (1971).*Electric Machinery*.3rc Ed. New York: McGraw-Hill.

Fu J. ad Lipo T. A. (1994). Disturbance free operation of a multiphase current regulated motor drive. IEEE Transactions on Industry Applications, vol. 30, pp 1267 — 1274.

Fuchs E. F. and Rosenberg L. T. (1974). Analysis of an alternator with two displaced stator windings.*IEEE Trans. Power Apparatus and Systems,* vol. 93, pp. 1776-1786.

Fu, F., and Tang, X., (2002), Induction Machine Design Handbook, China Machine Press.

Goldberg, D. (1989), 'Genetic Algorithms in Search, Optimization and Machine Learning,' Reading, MA: Addison-Wesley.

Gopakumar K., Ranganathan T. and Bhat S. R. (1993).Split-phase induction motor operation from PWM voltage source inverter.IEEE Transactions on Industry Applications, vol. 29, pp 927- 932.

Gopakumar K., Ranganathan V. T. and Bhat S. R. (1994).Vector control of induction motor with split phase stator windings.Conf Rec. *IEEE-IAS* Annu. Meeting, pp 569-574.

Grantham C., Sutanto D. and Mismile B. (1993).Steady state and transient analysis of self excited induction generators. IEE Trans. Energy Conversion, vol. EC-8, no. 2, pp 304-311.

Gregor R., Barrero F., Toral S. And Duran M.J. (2011) "Realization of an Asynchronous Six-Phase-Phase Motor Drive Test-Rig", WWW.iceepq.com/icrepq-08/230-gregor.pdf.Assessed on 25th April, 2012.

Hadiouche D., Razik H. and Rezzoug A. (2000).Modelling of a double star induction motor with an arbitrary shift angle between its three phase windings, mt.

Han, G. J., and S. S. Shapiro. 1967. *Statistical models in engineering.* UK: John Wiley and Sons.

Harley, Ronald G. and Duan, Yao, (2009), 'Traditional Design of Cage Rotor Induction Motors,' Georgia Institute of Technology.

Holland, J. H. (1975), 'Adaption in Natural and Artificial Systems,' PhD thesis, University of Michigan Press

Hunt L. J , "A new type of induction motor". Journal IEE, Vol. 39, 1907, pp 648-677.

Idir.K., L. Chang, and H. Dai. 1997. A new global optimization approach for induction motor design. *Proceedings of the IEEE Canadian conference on electrical and computer engineering*.870-873

.

Jahns T. M. (1980). Improved reliability in solid-state ac drives by means of multiple independent phase-drive units. IEEE Trans. md.Appi. IA—16, pp. 321-331.

JinJ.M.,*The Finite Element Method in Electromagnetics*. NewYork, USA: John Wiley and Sons, 1992.

Juan M. G. and Ojo O. "Air-gap Flux Density Optimization in Dual Stator Winding Induction Machines", IEEE APEC 08, CD-ROM. Austin, USA, 2008.

Jones M., and Levi E. (2002). A literature survey of state-of-the-art in multi- phase ac drives. Proc. 36th *Univ. Power Eng. Conf UPEC*, Stafford, U.K., pp 505-510.

Kuphaldt, Tony R., (2007) 'Lessons in Electric Circuits, Volume II – AC,' Sixth Edition, last update July 25, 2007 *openbookproject.net/electricCircuits: accessed on 26th August, 2014.*

Klingshirn E. A. (1983) "High Phase Order Induction Motors," IEEE Transactions on Power Apparatus and Systems, Vol. 102 (1) pp. 47-51.

Kral C., Haumer A. and Grabner C. (2010) "Consistent Induction Motor Parameters for the Calculation of Partial Load Efficiencies by Means of an Advanced Simulation", Engineering Letters, Vol. 15(1), EL-18_1_04.

Levy D. (1986).Analysis of a double- stator induction machine used for a variable-speed /constant-frequency small-scale hydro/wind electric power generator.Electric power Systems research, vol.11, pp 205-223.

Liang F., Xu L., and Lipo T. A., "d-q Analysis of a variable speed doubly fed AC excited reluctance motor", Electric Machines and Power Systems, Vol. 19, No.2, 1991, pp 125-138.

Liwschitz-Garik and Whipple C. C. *"Electric Machinery, Vol. 2 AC Machines"*, Van Nostrad Publishers, 2nd Ed., 1961.

Lipo T. A. (1980). A q-d model for six phase induction machines. Proc. Int. Conf. Electric Machines, Athens, pp 860-867.

Lipo, T. A. (2004), Introduction to AC Machine Design, 2 ed.: University of Wisconsin-Madison.

Li G. J., Ojeda J., Hoang E. And Gabsi M. (2011) "Thermal-Electromagnetic Anaylsis of a Fault-Tolerant Dual Star Flux –Switching Permanent Magnet Motor for Critical Applications", IET Electric Power Applications, Vol. 5 (6), pp.503-513.

Mantero S., De Paola E. and Marina G. (1999). An optimized control strategy for double star motors configuration in redundancy operation mode. Proceedings of European Power Electronics and Applications Conference EPE, Lausanne, Switzerland, No. 013.

Mauljadi E. and T.A. Lipo (1994). Series compensated PWN inverter with battery supply applied to an isolated induction generator. IEEE Trans. Ind. Applicat., vol. 30, pp 1073-1082.

Mohan N., T.M. Undeland, and W.P. Robbings (1995).Power Electronics, Converters, Applications and Design. New York: Wiley.

Mohapatra K.K., Gopakumar K., Somasekhar V.T., Umanand L. (2003). A harmonic elimination scheme for an open-end winding induction motor drive.IEEE Trans. md. Electron, 50 pp 1187-1198.

Munoz-Garcia A., and T.A. Lipo (1998). Stator winding induction machine drive.Conf. Rec. IEEE-IAS Annu. Meeting, pp 601-608.

Moreira J. C. and Lipo T. A. (1992) "Modeling Saturated ac Machines Including Air Gap Flux Harrmonic Components", IEEE Trans on Industry Applications, Vol. 28 (2), pp. 343-349.

Munoz A. R. and Lipo T. A. (2000) "Dual Stator-Winding Induction Machine Drive", IEEE Trans. IAS.Vol. 36 (5), pp.1369-1379.

Nagrath I.J. and Kothari D. P. (1997). Electrical machines, 2nd Ed. New York: Tata Mcgraw-Hill.

Nelson R. H. and Krause P. C. (1974).Induction machine analysis for arbitrary displacement between multiple windings.IEEE Transactions on Power Apparatus and Systems, vol. 93, pp 841- 848.

Ojo O. and I.E. Davidson (2000).PWM-VSI inverter-assisted stand-alone dual stator winding generator. IEEE *Transactions on Industry Applications* Vol. 36, No. 6 pp 1604-1611.

Ojo O., O. Obasohan, and A. Jimoh (1998).Expanding the operating range of a single-phase induction generator with a PWM inverter.Conf. Rec. IEEE-IAS Annu. Meeting, pp 205-212

Quazene L. and Mcpherson Jr. G. (1983).Analysis of an isolated induction generator.IEEE Trans. Power App. Syst., vol. 102, no.PAS-8, pp 2793-2798.

Pereira L. ,Pereira L. F. A., Scharlan C. C., Ricardo S.D. R. and Haffner S. (2010) "Analysis of the Influence of Saturation on the Airgap Induction Waveform of Five Phase Induction Machines", XVIII Congresso Brasileiro Automatica/12 16-Setembro-2010, Bonito-MS, pp. 4904-4910.

Pramanic A. [2013], "Electromagnetism Theory and Applications" Parentice-Hall of India ltd., 2nd Ed.

Pyrhonen, J., Jokinen, T., and Hrabovcova, V. (2008), Design of Rotating Electrical Machines, John Wiley & Sons, Ltd.

Ramarathnam, R., and B. G. Desai. 1971. Optimazation of polyphase induction motor design: A nonlinear programing approach. *IEEE Transaction on Power Apparatus and systems PAS-90 (2): 570-578.*

Ramarathnam, R., B. G. Desia, and V. Subba Rau. 1973. A comparative study of minimisation techniques for the optimazation of induction motor design. . *IEEE Transaction on Power Apparatus and systems PAS-92 (5): 1448-1454.*

Rangarajan M. T., Thomas G. H. and Ronald G. H(2002) "Transient Model for Induction Machines with Stator Winding Turn Faults," IEEE Transactions on Industry Applications, Vol. 35 (3), pp. 632-637

Razik H. (2003) "Modelling of Double Star Induction Motor for Diagnosis Purpose," IEEE Transactions on Industry Applications, Vol. 40 (2), pp. 908-911

Raj, C. Thanga , Scivastava, S. P. and Agarwal, Pramod, (2009), 'Energy Efficient Control of Three-Phase Induction Motor-A Review,' International Journal of Computer and Electrical Engineering, Vol. 1, No. 1, April 2009, pp. 61-70.

Raj, C. Thanga, Srivastava, S.P and Agarwal, Pramod, (2009), 'Energy Efficient Control of Three-Phase Induction Motor–A Review,' International Journal of Computer and Electrical Engineering,Vol.1, pp. 61 – 70.

Raj, C. T., Thangaraj, R., Pant M., Bourvy, P. and Abraham, A. (2012), 'Design Optimization of Induction Motors with Differential Evolution Algorithms with Application in Textile Spinning,' Applied Artificial Intelligence, 26:809–831, 2012 Copyright # 2012 Taylor & Francis Group, LLCISSN: 0883-9514 print=1087-6545 online DOI: 10.1080/08839514.2012.721696 Downloaded by [Indian Institute of Technology Roorkee] at 07:42 15 October 2012.

Roberts,P. C. "**A Study of Brushless Doubly-Fed (Induction) Machines**," Ph.Ddissertation, University of Cambridge, 2005.

Roberts P. C. McMahon R. A., Tavner P. J. Maciejowski J. M and Flack T. J. (2005) "Equivalent Circuit for the Brushless Doubly Fed Machine (BDFM) including Parameter Estimation and Experimental Verification", IEEE Proc.-Electrical Power Application, Vol. 152 (4) pp. 933-942

Rochelle P., Spee R. and Wallace A., "The effect of stator winding configuration on the performance of brushless doubly-fed machines in adjustable speed drives", IEEE Industrial Application Society Annual Meeting, Seatle October 1990, pp. 331-337.
or connections. *MS. thesis*, Purdue Univ., West Lafayette.

Salon S. J., *Finite Element Analysis of Electrical Machine*. USA: Kluwer Academic Publishers, 1995.

Soong W. L., StatonD.A., and MillerT. J. E.[1990], "Validation of lumped circuit and finite-element modelling of axially-laminated brushless motors," in *Proc. Inst. Elec. Eng. 6th Int. Conf. Electrical Machines and Drives, EMD'93*, 1993, pp. 85–90.

Stephen J. C., [1991] "Electric Machinery Fundamentals" McGraw-Hill, Inc., 2nd Ed.

Stermecki et al., "Calculation of load-dependent equivalent circuit parameters of squirrel cage induction motors using time-harmonic FEM," in *Electrical Machines,2008. ICEM 2008. 18th International Conference on*, Vilamoura, Sep. 2008, pp. 1–6.

Schiferl R. (1982). Detailed analysis of a six-phase synchronous machine with AC and DC stat

Say, M. G., (1970), Performance and Design of AC Machines: Pitman, London.

Sawhney, A. K. (1991): A Course in Electrical Machine Design, Dhanpat Rai & Sons.

Sedighizadeh, Davoud and Masehian, Ellips, (2009), 'Particle Swarm Optimization Methods, Taxonomy and Applications,' International Journal of Computer Theory and Engineering, Vol. 1, No. 5, pp. 486-502.

Sharifian, M. B. B., Feyzi, M. R., Farrokhifar, M., Shaarbafi, K., and Mohammadi, R. (2009), 'Slot Fringing Effect on the Magnetic Characteristics of Electrical Machines,' Journal of Electrical Engineering, Vol. 60 , No. 1, pp. 16-23.

Sivaraju, S. S., and Devarajan, N. (2011), 'GA Based Optimal Design of Three Squirrel Cage Inductiom Machine for Enhancing Performance,' International Journal of Advanced Engineering Technology (IJAET), Vol. II, Issue IV, October-December, pp. 202-206.

Singh G. K. (2002). Multi-phase induction machine drive research — a survey. Electric Power Systems Research, vol. 61, pp 139-147.

Singh G. K. (1998). High horse power ratings in ac drives by means of phase- redundancy technique-Some experimental investigations. Proc. *IEEE TECNCON'98*, vol. 2, pp 580-583.

Singh G. K., Pant V. and Singh Y. P. (2003). Voltage source inverter driven multi-phase induction machine.*Comput.Elect. Eng*., vol. 29, pp. 8 13-834.

Singh G. K. and Pant V. (2001).Analysis of multi-phase induction machine under fault condition in a phase-redundant ac drive system.*Elect.Mach. Power Syst.*, vol. 28, pp 577-50.

Singh G. K., Nam K. and Lim S. K. (2000) "A Simple Indirect Field Oriented Control Scheme for Multiphase Induction Machine", IEEE Trans. Industrial Electronics, Vol. 54(4), pp. 1177-1185.

ThangaRal C., RadhaThangaraj, Millie Pant, Pascal Bonvry, Ajith Abraham, 2012 "Design Optimazation of Induction Motors with Different Evolution Algorithms with an application in Textile spinning" Applied Artificial Intelligence. Pp 809-831.

Toliyat H.A. (1998). Analysis and simulation of five-phase variable speed induction motor drives under asymmetrical connections. *IEEE Trans. Power Elec.,* vol. 13, no. 4, pp 748-756.

Toliyat H.A., Xu L., Lipo T.A. (1992). A five-phase reluctance motor with high specific torque.*IEEE Trans. Industry Applications*, vol. 28, no. 3, pp 659-667.

Vas P. (1992). Electrical Machines and Drives, A Space-Vector Theory Approach. Oxford, U.K: Oxford Univ. press

Vaseghi B., Takorabet, N., and Meibody-Tabar, F. (2009), 'Transient Finite Element Analysis of Induction Machines with Stator Winding Turn Fault,' Progress in Electromagnetics Research, PIER 95, pp.1-18.

Virgiliu F. and Marcel S. [2013], "Finite Element Analysis and Diagnosis of the one Broken Bar Fault in the Squirrel Cage Induction Motors," *IEEE Trans. Industry Applications*, vol. 28, no. 3, pp.411-416.

Wang L. and Deng R. Y. (1999).Transient performance of an isolated induction generator under unbalanced excitation capacitors.*IEEE Trans. Energy Conversion*, vol. 14, no. 4, pp 887-893.

Ward E.E. and Harer H. (1969).Preliminary investigation of an inverter-fed 5- phase induction motor. Proc. IEE 116 (6), pp 980-984.

WexlerA. [1973], "Finite element field analysis of an inhomogeneous, anisotropic, reluctance machine rotor," *IEEE Trans. Power App. Syst.*,pp. 145–149.

White D.C., Woodson H.H. (1959); E*lectromechanical energy conversion* New York: John Wiley and Sons.

Willaimson S., A.C Ferreira, and A.K. Wallacxe (1997). Generalized theory of the brushless doubly-fed machine-Part I: Analysis. Proc. IEE-Elect Power Applicat, vol. 144, no. 2 pp 111-121.

Williamson S. and Smith S. (2003).Pulsating torque and losses in multiphase induction machines.IEEE Trans. md. App, vol. 39, no. 4, pp. 986-993.

Wu Z. and O. Ojo (2006).Coupled circuit model simulation and air gap field calculation of a dual stator winding induction machine. IEE *Proceedings –Electric power Applications*, Vol.153, No.3, pp 387-400.

Wu Z. and O. Ojo and J. Sastry (2005).Control of a dual stator winding induction machine as a source of DC power.Conference record of IEEE *Industry Applications Conference*, Vol. 2, pp 1089-1096.

Wu Z. and O. Ojo (2006). High performance of a dual winding induction generator with series connected boost rectifiers. Conference of 37th IEEE *Power Electronics Specialists Conference*, pp 18-22.

Wu Z. (1998). Modeling, simulation and application of a doubly-fed reluctance electrical machine. Ph.D. Dissertation, Tennessee Technol. Uni., Cookeville.

www.icrepq.com/icrepq-08/230-gregor.pdf: *Accessed on September, 24th 2014.*

Xu L. and Tang Y. (1992). A novel wind-power generating system using field orientation controlled doubly-excited brushless reluctance machine. Conf Rec. *IEEE-IAS Annu*, pp 408-413.

Yong-le A. (2006) "Novel Direct Field and Torque Control of Six-phase Induction Machine with Special Phase Current Waveform", PhD Dissertation, University of Stellenbosch.

Zhao Y. and Lipo T. A. (1995).Space vector PWM control of dual three-phase induction machine using vector space decomposition.IEEE Transactions on Industry Applications, vol. 31, pp. 1100- 1109.

Zhao Y. and Lipo T. A. (1996) "Modelling and Control of a Multi-Phase Induction Machine with Structural Unbalance," IEEE Transactions on Energy Conversion, Vol. 11 (3), pp. 570-577

APPENDIX A

Specific permeance

The reactance (or leakage inductance) of a coil is proportional to the square of the number of turns, and the specific permeance. Knowledge of permeance is necessary in the calculation of leakage fluxes mentioned above (or their leakage inductances). Thus the next step in this design is the calculation of permeances associated with the leakage fluxes.

(i) slot leakage permeance

It is necessary to know the various dimensions of the slot so as to be able to calculate the slot leakage permeance. Fig.A1shows the type of slot used in the machine under consideration.

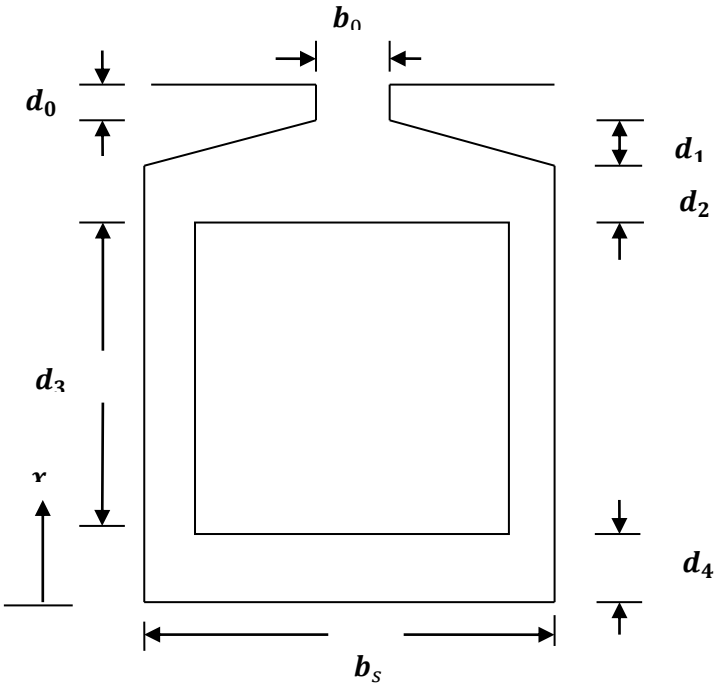


Figure A1 : Semi-closed slot with parallel sides (semi-closed slot) with b_0 as the slot opening.

The lengths d_0, d_2, and d_4 are potions along the depth of the slot covered by insulation while d_3 is the actual space covered by the conductors.

As shown in fig.A1 the permeance of the flux paths can be found by summing up all tubes of flux of cross-sectional area $l_e\ d_x$ (l_e being the effective core length).if a flux line 1 and 2 having a constant value of H within the slot shown in fig. A2 is considered then Ampere's law states

$$\int_1^2 \mathrm{H.\,dl} = n(x)I \qquad \text{A1}$$

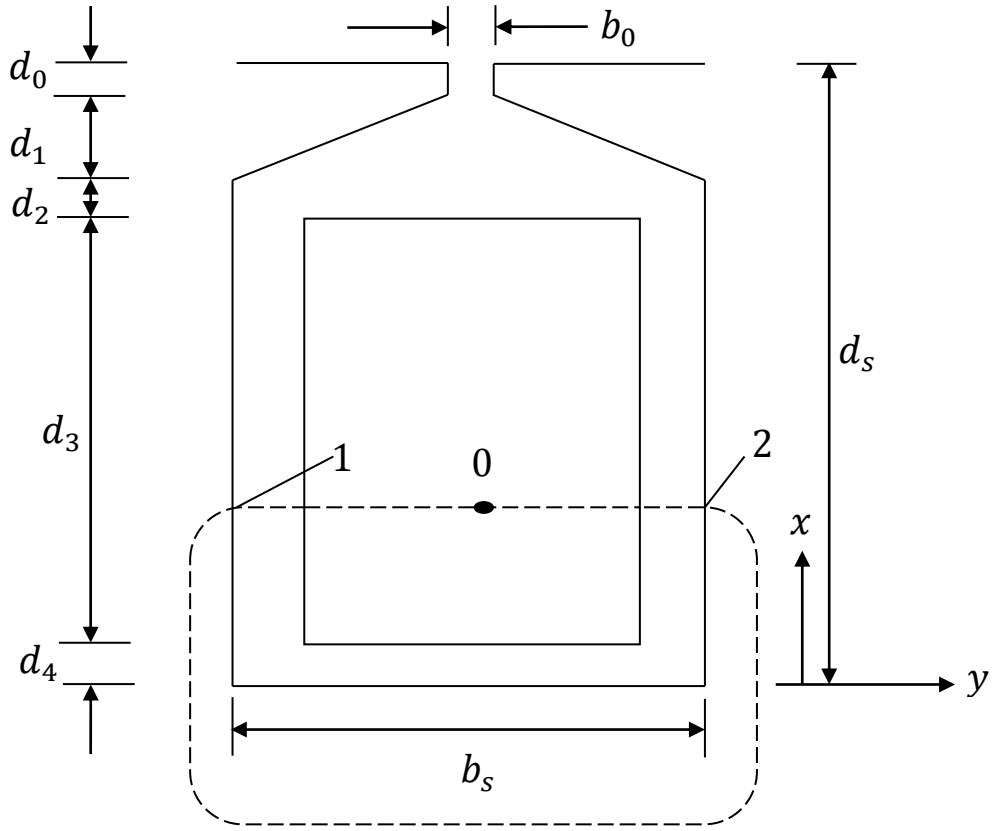


Figure A2: Flux path used in applying Ampere's law

Where n(x) is the number of conductors carrying current I enclosed within the path of integration. Since H is constant along the path 1-2 then;

$$H_y\ y = n(x)\ I \qquad \text{A2}$$

Or in terms of flux density

$$\frac{By\ y}{\mu 0} = n(x)\ I \qquad \text{A3}$$

An incremental flux dø passing through an incremental area $l_e\ dx$ within the path 1-2 is;

$$d\phi = B_y l_e dx = \mu_0 \frac{n(x)\, I\, ledx}{y} \quad \text{A4}$$

Then the flux linkage enclosed by the incremental flux is

$$d\lambda = n(x)d\phi = \mu_0 [n(x)]^2 I \frac{ledx}{y} \quad \text{A5}$$

Or

$$d\lambda = \mu_0 n_s^2 I [\frac{n(x)}{ns}]^2 \frac{ledx}{y} \quad \text{A6}$$

Where n_s is the total number of conductors in the slot. The incremental inductance associated with the path under consideration is

$$dL = \frac{d\lambda}{I} = \mu_0 n_s^2 [\frac{n(x)}{ns}]^2 \frac{ledx}{y} \quad \text{A7}$$

Since inductance by definition is the product of number of conductors n_s carryingI and the permeance then

$$dL = n_s^2 dP \quad \text{A8}$$

then the incremental permeance dP is found by combining the above two equations.

$$dP = \mu_0 [\frac{n(x)}{ns}]^2 \frac{ledx}{y} \quad \text{A9}$$

Equation A9 reveals that the calculation of permeance is a three dimensional problem. However the problem can be reduced to a two dimensional one if instead of permeance the term specific permeance is used. Since the permeance does not change along Z-axis(in the direction of l_e) then equation A9 is divided by l_e to get the specific permeance. Hence

$$dP = \mu_0 [\frac{n(x)}{ns}]^2 \frac{dx}{y} \quad \text{A10}$$

When equation A10 is integrated over the entire slot depth (i.e in the x direction) the value for the total specific slot permeance is obtained. Thus;

$$p = \mu_0 \int [\frac{n(x)}{ns}]^2 \frac{dx}{y} \quad \text{A11}$$

Equation A11 is used to determine the specific permeance of the various sections shown in figure 1.16.

Hence, for

(i)$0 < x < d_4$

The specific permeance for this section is zero since no current is enclosed in the space below the conductors. Thus;

$P_4 = 0$

(ii)$d_4 < x < (d_3 + d_4)$

The specific permeance in this section is found as

$$P_3=\mu_0\int_{d4}^{(d3+d4)} \frac{x-d4}{d3}\frac{dx}{bs} =\mu_0\frac{d3}{bs} \quad \text{A12}$$

(iii) $(d_4 + d_3) < x < (d_4 + d_3 + d_2)$

The value of specific permeance in this case is;

$$P_2=\mu_0\int_{d4+d3}^{(d4+d3+d2)} \frac{[x-(d4+d3)]}{d3}\frac{dx}{bs}= \mu_0\frac{d2}{bs} \quad \text{A13}$$

(iv) $(d_4 + d_3 + d_2) < x < (d_4 + d_3 + d_2 + d_1)$

Owing to the slanting nature of this section, an empirical relationship is used in getting the specific permeance. Thus;

$$P_1 = \frac{\mu 0 d1}{bs-b0}\log_e\left(\frac{bs}{b0}\right) \quad \text{A14}$$

(v) Finally, for the slot opening section the specific permeance is;

$$P_0 = \mu_0\frac{d0}{bo} \quad \text{A15}$$

Using the actual dimensions of the slot all the four permeances can be found. Since they are all connected in parallel the total specific slot permeance is the sum of all the individual permeances. Hence;

$$p_s = p_0 + p_1 + p_2 + p_3 \quad \text{A16}$$

APPENDIX B

Estimation of stator resistance

The average length of a coil is found as;

$$L_c = 2l_c + 4l_{c2} + 4l_{c3} \quad \text{B1}$$

Where, l_s is the effective length of the stator conductor, l_{c2} and lc_3 are as shown in fig. B1. These two lengths represent the dimension of overhang. With reference to the figure, lc_3 is found as;

$$l_{c3} = \frac{\text{pTp(ave)}}{2} \frac{\text{pTs(ave)}}{\sqrt{\text{pTp(ave)}^2 - (bc+te)^2}} \quad \text{B2}$$

Where all the symbols used are as indicated on the figure.

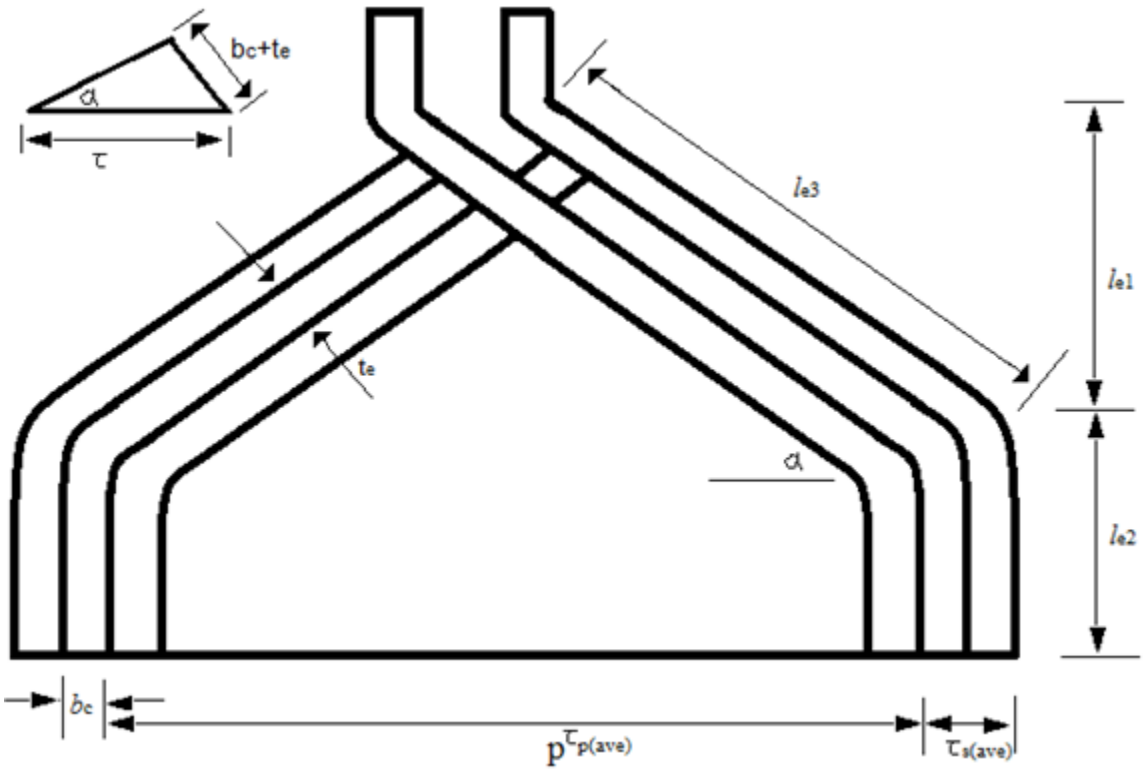


Figure B1. The stator end winding arrangement.

The resistance of one coil is therefore

$$r_c = \frac{\rho n_c l_c}{Ac} \qquad \text{B3}$$

Where ρ is the resistivity of the conductor and A_c is the cross-sectional area of a conductor in the coil. Since C_u conductor is used, $\rho_{cu} = 2.1 \times 10^{-6} \Omega cm$. The resistance per phase of all the coils connected in series within a pole pitch is;

$$r_p = \frac{Q1}{3p} r_c \qquad \text{B4}$$

Where Q_1 is the number of slots in the stator and P is the total number of poles. The resistance of one parallel path for ac parallel path machine is;

$$r_b = \frac{P}{C} r_p = \frac{Q1}{3C} r_c \quad \text{B5}$$

The net resistance per phase is then the resistance of the C circuit connected in parallel. Thus;

$$r_s = \frac{r_b}{C} = \frac{Q1}{3C\text{^}2} r_c = \frac{N_s}{C} \rho \frac{l_c}{A_c} \quad \text{B6}$$

APPENDIX C

DETERMINATION OF ROTOR PARAMETERS

Structurally, the rotor of induction machines are of two types: the wound rotor and the squirrel cage rotor. The difference is basically due to the architectural design of the rotor windings. In wound rotor machines the winding is designed in the same way as the stator winding and thus the parameter determination in such winding will be similar to that explained in section 3.10.

However, the squirrel cage induction machine has its rotor made up of conducting bars which run axially in the rotor slots. The bars are effectively shorted at both ends by another conducting material called end-rings. The portion of the end-ring between two bars is termed end ring segment. The physical connections between the bars and the end-rings are as shown in fig. C1.

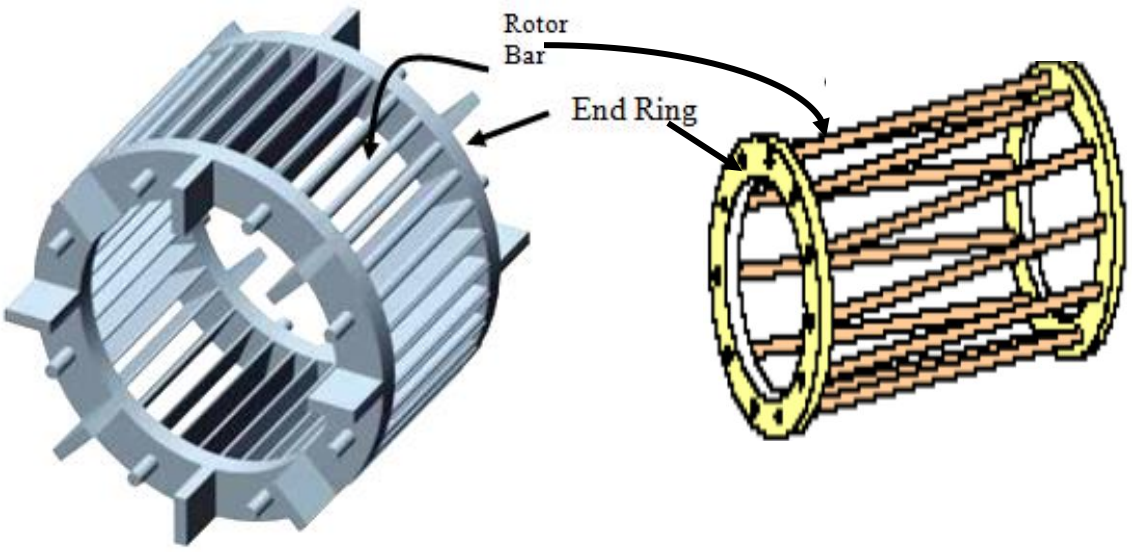


Figure C1: Schematic Representation of Rotor cage of induction motor

The parameter determination is set forth in this section.

Figure C2 represents the meshes formed by the squirrel cage rotor. Where;

R_b ,L_b are the resistance and inductance of each bar respectively;

R_e , L_e are the resistance and inductance of each end ring segment;

i_{bn} is the current flowing in the n^{th} bar;

i_{en} is the current flowing in the n^{th} end ring segment;

e_{bn} is the induced voltage in the n^{th} bar;

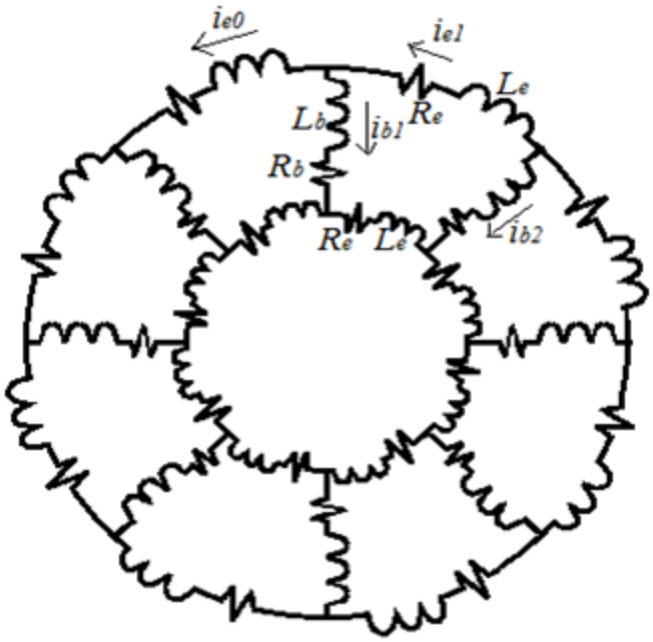


Figure C2: Meshes Formed by a Squirrel Cage Rotor

Applying KVL to the mesh formed by bar 1, end ring segment, bar 2 and the other end ring segment we get;

$$e_{b1} - e_{b2} = R_b(i_{b1} - i_{b2}) + L_b\frac{d}{dt}(i_{b1} - i_{b2}) + 2R_e i_{e1} + 2L_e\frac{d}{dt}(i_{e1}) \quad \text{C1}$$

And by KCL;

$$i_{b1} + i_{eo} = i_{e1} \quad \text{C2}$$

The induced voltages and currents can as well be represented in phasor form as;

$$E_{b2} = E_{b1}e^{(j\pi p)/Q_2} \quad \text{C3}$$

$$I_{b2} = I_{b1}e^{(j\pi p)/Q_2} \quad \text{C4}$$

$$I_{e1} = I_{eo}e^{(j\pi p)/Q_2} \quad \text{C5}$$

Combining equation C2 and C5 yields;

$$I_{e1} = \frac{I_{b1}}{1-e^{(j\pi p)/Q_2}} \quad \text{C6}$$

Also from C3 and C4 we get;

$$E_{b1} - E_{b2} = E_{b1}\left(1 - e^{(j\pi p)/Q_2}\right) \quad \text{C7}$$

And;

$$I_{b1} - I_{b2} = I_{b1}\left(1 - e^{(j\pi p)/Q_2}\right) \quad \text{C8}$$

Putting equations C3 to C7 in the equivalent vector form of equation C1 yields;

$$E_{b1}\left(1 - e^{(j\pi p)/Q_2}\right) = I_{b1}\left(1 - e^{(j\pi p)/Q_2}\right)(R_b + j\omega L_b) + \frac{2I_{b1}}{1 - e^{(j\pi p)/Q_2}}(R_e + j\omega L_e) \quad \text{C9}$$

Where ω denotes the angular frequency induced in the rotor meshes (slip frequency);

$$\omega = s\omega_e \quad \text{C10}$$

Where $\omega_e$the angular frequency of the stator current and s is the slip.

Making E_{b1} the subject of equation C9 yields;

$$E_{b1} = I_{b1}(R_b + j\omega L_b) + \frac{2I_{b1}}{\left(1 - e^{(j\pi p)/Q_2}\right)\left(1 - e^{(-j\pi p)/Q_2}\right)}(R_e + j\omega L_e) \quad \text{C11}$$

From the identity,

$$\left(1 - e^{j\propto}\right)\left(1 - e^{-j\propto}\right) = e^{j\propto}\left(e^{-j\propto} - e^{j\propto}\right)\left(e^{-j\propto}\right)\left(e^{j\alpha} - e^{-j\propto}\right) = 4sin^2\alpha \quad \text{C12}$$

The denominator of equation C11 reduces to $4sin^2\left(\frac{\pi p}{2Q_2}\right)$

Equation C9 thus becomes

$$E_{b1} = I_{b1}(R_b + j\omega L_b) + I_{b1}\left[\frac{R_e + j\omega L_e}{2sin^2\left(\frac{\pi p}{2Q_2}\right)}\right] \quad \text{C13}$$

From equation C13, it can be deduced that the equivalent bar resistance and inductance respectively are;

$$R_{be} = R_b + \frac{R_e}{2sin^2\left(\frac{\pi p}{2Q_2}\right)} \quad \text{C14}$$

And

$$L_{be} = L_b + \frac{L_e}{2sin^2\left(\frac{\pi p}{2Q_2}\right)} \quad \text{C15}$$

Where, L_b and R_b are found as follows:

The bar is assumed to be confined within the rotor slot as such the specific rotor slot permeance can be computed using the relationship similar to that of the stator slot (Appendix A). Thus;

$$P_{rsl} = \mu_o \left[\frac{d_{3r}}{3b_{rs}} + \frac{d_{1r}}{(b_{rs}-b_{or})} log_e \left\{\frac{b_{rs}}{b_{or}}\right\} + \frac{d_{or}}{b_{or}}\right] \quad \text{C16}$$

With reference to equation 3.45, the slot leakage/rotor bar is

$$L_b = n_{rs}^2 l_{er} P_{rsl} \quad \text{C17}$$

Where all dimensions are as defined in Appendix A.

The bar resistance R_b can be computed from the known dimensions of the bar. Let;

Actual bar length be l_b ,

Effective stator and rotor length be l_{es}= l_{er},

Bar width b; Bar depth d,

End ring width t_{be}; End ring depth d_{be}

Rotor bar extension l_{be},

Average rotor pole pitch $\tau_{p2.}$

The resistance of one rotor bar is

$$r_b = \frac{l_b \rho_{cu}}{bd} \quad \text{C18}$$

The resistance of the end ring portion over one rotor slot pitch is

$$r_e = \frac{\tau_{r2} \rho_{cu}}{t_{be} d_{be}} \quad \text{C19}$$

The effective bar resistance is thus

$$r_{be} = r_b + \frac{r_e}{2sin^2\left(\frac{\pi P}{2Q_2}\right)} \quad \text{C20}$$

The resistance per rotor mesh is

$$r_r = 2r_{be} \quad \text{C21}$$

The rotor resistance referred to the stator is obtained from

$$r_r' = \frac{12k_1^2 N_s^2}{Q2} r_r$$ C22

Appendix D

Estimation of Iron Losses

Corresponding to flux density in tooth $B_{t\frac{1}{3}h_t}$ determine iron loss per Kg from the graph shown in Figure D1. Thus

$$B_{t\frac{1}{3}h_t} \Rightarrow p_{it} \quad W/Kg$$

D1

Iron loss in teeth

= p_{it}* density * volume of iron in teeth

= p_{it}* 7600 * volume of iron in teeth

Total iron losses P_i = Iron loss in teeth + Iron loss in yoke

So $$I_C = \frac{P_i}{3V_{Ph1}}$$

D2

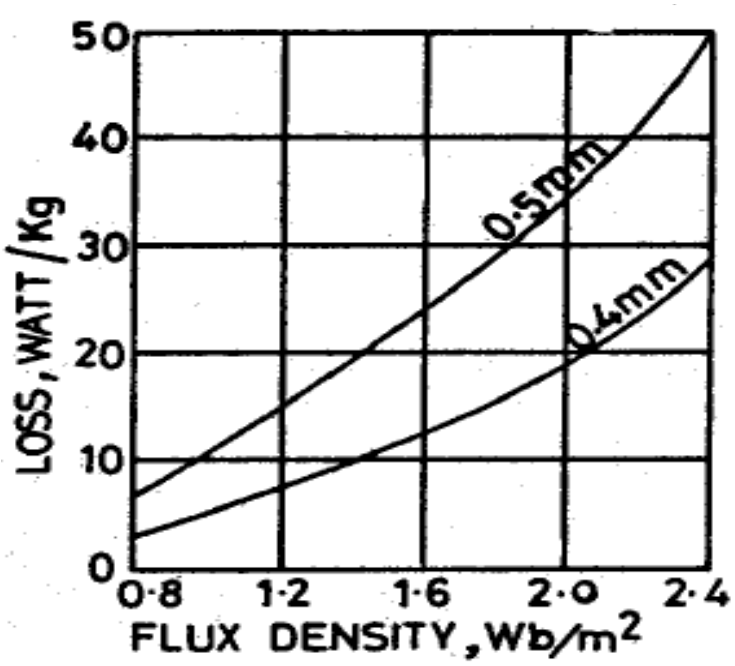


Figure D1:

Based on the design data of the stator and rotor of an induction motor, performance of the machine has to be evaluated. The parameters for performance evaluation are iron losses, no load current, no load power factor, leakage reactance etc. Based on the values of these parameters design values of stator and rotor can be justified.

Iron losses: Iron losses are occurring in all the iron parts due to the varying magnetic field of the machine. Iron loss has two components, hysteresis and eddy current losses occurring in the iron parts depend upon the frequency of the applied voltage. The frequency of the induced voltage in rotor is equal to the slip frequency which is very low and hence the iron losses occurring in the rotor is negligibly small. Hence the iron losses occurring in the induction motor is mainly due to the losses in the stator alone. Iron losses occurring in the stator can be computed as given below.

(a) Losses in stator teeth:

The following steps explain the calculation of iron loss in the stator teeth

(i) Calculate the area of cross section of stator tooth based on the width of the tooth at $1/3^{rd}$ height and iron length of the core as $A'_{ts} = b'_{ts} \times l_i \ m^2$

(ii) Calculate the volume all the teeth in stator $V_{ts} = A'_{ts} \times h_{ts} \times S_s \ m^3$

(iii) Compute the weight of all the teeth based on volume and density of the material as $W_{ts} = V_{ts} \times$ density. (density of the material can be found in DDH) $(7.8 \times 10^{-3} \ kg/m^3)$

(iv) Corresponding to the operating flux density in the stator teeth of the machine iron loss per kg of the material can be found by referring to the graph on pp179 of DDH.

(v) Total iron losses in teeth= Iron loss /kg x weight of all teeth W_{ts} ie result of (iii) x (iv)

(c) Losses in stator core

Similar to the above calculation of iron loss in teeth, iron loss in stator core can be estimated.

(i) Calculate the area of cross section of the core as $A_{cs} = d_{cs} \times l_i \ m^2$

(ii) Calculate the mean diameter of the stator core below the slots as $D_{mcs} = D + 2\ h_{ts} + d_{cs}$ m

(iii) Compute the volume of stator core as $V_{cs} = A_{cs} \times \pi \ D_{mcs} \ m^3$

(iv) Calculate the weight of the stator core as $W_{cs} = V_{cs} \times$ density

(v) Corresponding to the operating flux density in the stator core of the machine iron loss per kg of the material can be found by referring to the graph on pp 179 of DDH.

(vi) Total iron losses in core = Iron loss /kg x weight of core W_{cs} ie result of (iv) x (v)

Total iron losses in induction motor = Iron loss in stator core + iron losses in stator teeth.

In addition friction and windage loss can be taken into account by assuming it as 1- 2 % of the out put of the motor.

Hence total no load losses = Total iron losses + Friction and windage loss.

APPENDIX E

DEERMINATION OF THE INDUCTION MACHINE PARAMETERS

Normally, all induction machines come with their parameters readily available from the manufacturers. However, the dual stator winding machine is modification of an existing three phase induction machine. It is therefore mandatory to determine its parameters before any analysis can be carried out on it. The parameters to be determined are: stator and rotor resistances, magnetizing, stator and rotor reactances. Three tests are usually performed for this purpose. They are DC resistance, no-load and blocked rotor tests (Stephen, 1991).

E.1 DC resistance Test

The purpose of the DC resistance test is to determine the stator resistance per phase, r_1. This is accomplished by connecting any two stator leads, belonging to one winding set to a variable voltage DC source as shown in Figure E1. The DC source is adjusted to provide approximately rated stator current, and the resistance between the two stator leads is determined from voltmeter and ammeter readings.

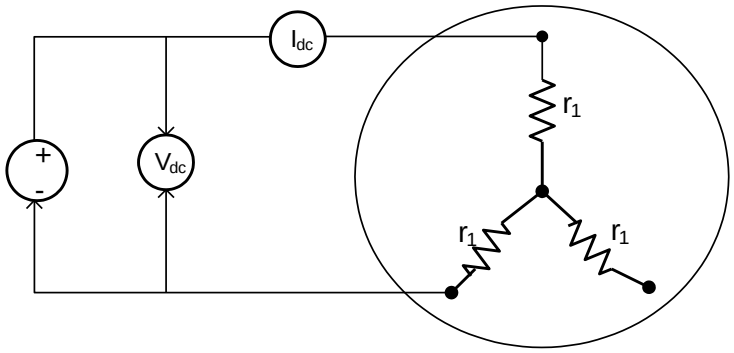


Figure E1: Circuit Diagram for DC Resistance Test

Thus from figure E1,

$$R_{DC} = \frac{V_{DC}}{I_{DC}} \quad \text{E1}$$

Since the stator is wye connected,

$$r_1 = \frac{R_{DC}}{2} \quad \text{E2}$$

E.2 Blocked- Rotor Test

The blocked- rotor test is used to determine X_1 and X_2. When combined with data from the DC test, it also determines r_2.

The test is performed by blocking the rotor so that it cannot turn and measuring the line voltages, line currents and three phase power inputs to 'a-b-c' stator winding set. The voltage is increased from zero in steps up to a value that gives rated currents in the stator windings. A voltmeter is also connected to the open 'x-y-z' winding set to measure the induced voltage in the winding. The procedure is repeated with xyz winding set connected to the supply and 'a-b-c' winding set left open.

Since the no-load current (I_o) at blocked rotor is considerably less than the rotor current (I_2), the no-load current may be neglected, enabling a simplification of the equivalent circuit. This is shown in Figure E2, where X_m and r_{h+e} are drawn with dotted lines and omitted when making blocked rotor calculations.

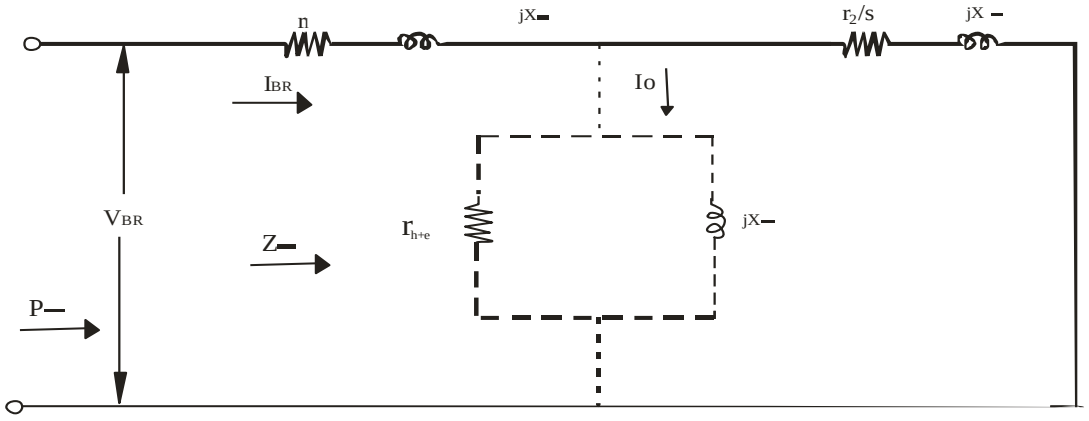


Figure E2: Equivalent Circuits per Phase for Blocked Rotor Test

Thus referring to Figure E2 where all values are per phase.

$$r_1 + r_2 = R_{BR} \quad \text{E3}$$

$$Z_{BR} = \frac{V_{BR}}{I_{BR}} \quad \text{E4}$$

$$R_{BR} = \frac{P_{BR}}{I^2_{BR}} \quad \text{E5}$$

Resistance r_2 is obtained from R_{BR} by substituting r_1 from the DC resistance test into equation E3 Hence,

$$r_2 = R_{BR} - r_1 \quad \text{E6}$$

From Figure E2,

$$X_1 + X_2 = \sqrt{Z^2_{BR} - R^2_{BR}} \quad \text{E7}$$

Using NEMA design letter, the blocked rotor reactance can be divided into its stator and rotor components X_1 and X_2

4.3.3 No- Load Test

The no-load test is used to determine the magnetizing reactance X_m and the combine core, friction, and windage losses. These losses are essentially constant for all load conditions (Stephen, 1991).

The connections for the no-load test are identical to those shown in Figure E3 for the blocked-rotor test the only difference is in the operation of the test. For the no-load test, the rotor is unblocked and allowed to run unloaded at rated voltage and frequency.

Rated voltage is applied and then reduced gradually until the slip is becoming high.

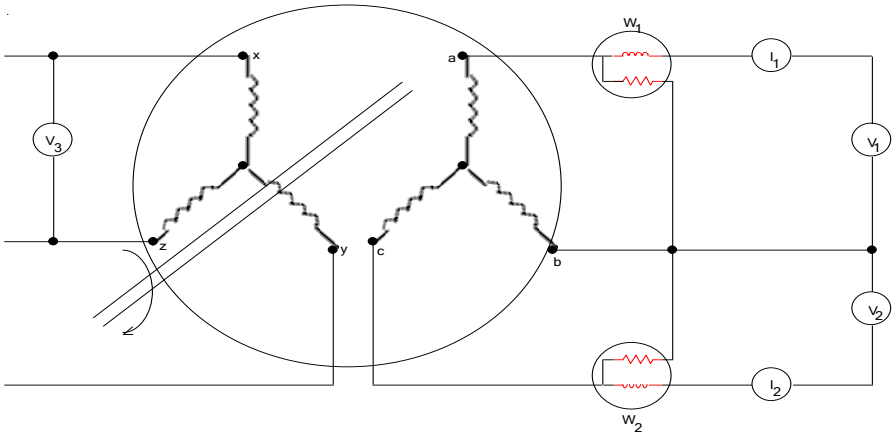


Figure E3: Connection for No-Load Test

As one 'a-b-c' winding set is connected to the supply a voltmeter, V_3 is connected across two phases of the other 'x-y-z' winding set. Thus V_3 measures an induced voltage due to transformer action. On no-load, the operating speed is very close to synchronous speed; the slip is very close to zero, causing the current in the r_2/s branch to be very small. For this reason, the r_2/s branch is drawn with dotted lines, as shown in Figure E3, and omitted from the no-load current calculations. Furthermore, since I_{μ} is by far greater than I_{h+e}, then I_o will approximately be the same as I_{μ}, thus, the r_{h+e} branch is also drawn with dotted lines, as in figure 4.6, and omitted from the no-load current calculations.

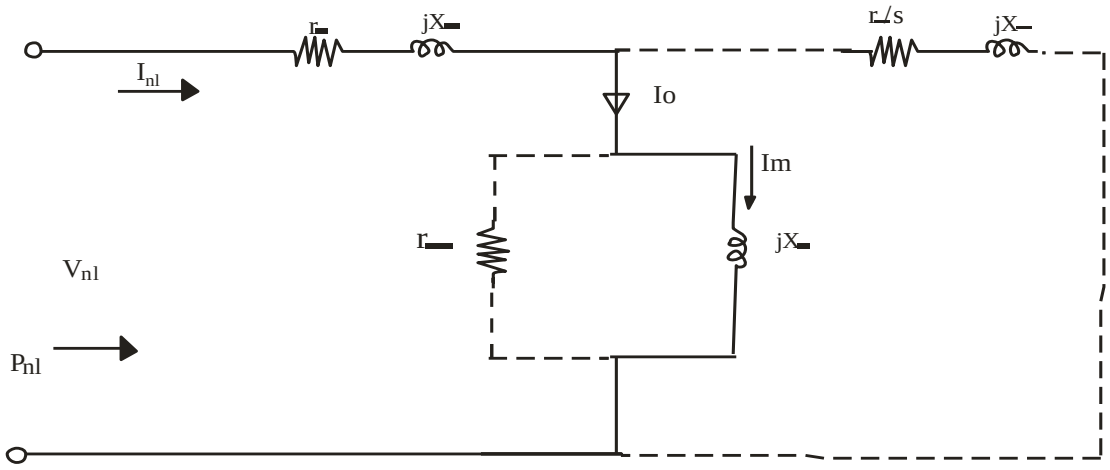


Figure E3: Equivalent circuits per phase for no-load test.

Referring to the approximate equivalent circuit shown in figure 4.6 for the no-load test, the apparent power input per phase is

$$S_{nl} = V_{nl} * I_{nl} \quad \text{E8}$$

The reactive power per phase is determined from

$$S_{nl} = \sqrt{P_{nl}^2 + Q_{nl}^2} \quad \text{E9}$$

Expressing the reactive power in terms of current and reactance, and solving for the equivalent reactance at no-load, yields:

$$X_{nl} = \frac{Q_{nl}}{I_{nl}^2} \quad \text{E10}$$

Where, as indicated in Figure E3

$$X_{nl} = X_1 + X_m \quad \text{E11}$$

Substituting X_1 as determined from the blocked-rotor test, into equation E11 permits the determination of X_m.

The input power per phase at no-load includes the core loss, stator copper loss, windage loss, and friction loss. That is,

$$P_{nl} = I_{nl}^2 * (r_1 + r_c) + P_{pf} \quad \text{E12}$$

Separation of friction and windage losses from the no-load may be accomplished by plotting the no-load power versus voltage squared for low values of voltage and then extrapolating to zero voltage (Stephen, 1991).

APPENDIX F

MATLAB CODES FOR G.A OPTIMIZATION

```
%%%%%%%%%%%%%%%%%%%%%%%%%%%%%%%%%%%%%%%%%%%%%%%%%%%%%%%%%%%%%%%%%%%%%%%%%%%%%%%%
%%%%%
JIBRIL YUSUF
PhD/ENG/14582/2011-2012
Department of Electrical and Computer Engineering
Ahmadu Bello University, Zaria
%%%%%%%%%%%%%%%%%%%%%%%%%%%%%%%%%%%%%%%%%%%%%%%%%%%%%%%%%%%%%%%%%%%%%%%%%%%%%%%%
%%%%%
Title: Multi-objective Genetic Algorithm Optimization of Power
Factor and Power Efficiency
%%%%%%%%%%%%%%%%%%%%%%%%%%%%%%%%%%%%%%%%%%%%%%%%%%%%%%%%%%%%%%%%%%%%%%%%%%%%%%%%
%%%%%

Program Code of the Power Efficiency Objective function
function y = P_Eff(x)
Dis = 0.15; %
Le = 0.1;
K1 = 0.96;
Ws = 25*pi;
Ks = 3*1e4;
Bg = 0.63;
Pmech1 = 3.0*1e4;
L = 0.00673;
Lm =0.276;
f = 50;
xr = 2*pi*f*L;
xm = 2*pi*f*Lm;
xt = (xr + xm)^2;
y(:,1) =
(Pmech1/(((sqrt(2)*pi^2)/120)*Ws*K1*(Dis^2)*Le*Bg*Ks*x(:,1)/sqrt(xt
+ x(:,1)^2)));
end

%%%%%%%%%%%%%%%%%%%%%%%%%%%%%%%%%%%%%%%%%%%%%%%%%%%%%%%%%%%%%%%%%%%%%%%%%%%%%%%%
%%%%%%%%%

Program Code of the Power Factor Objective function
```

```
function y = P_factor(x)
L = 0.00673;
Lm =0.276;
f = 50;
xr = 2*pi*f*L;
xm = 2*pi*f*Lm;
xt = (xr + xm)^2;
y(:,1) = (x(:,1)/sqrt(xt + x(:,1)^2));
end

%%%%%%%%%%%%%%%%%%%%%%%%%%%%%%%%%%%%%%%%%%%%%%%%%%%%%%%%%%%%%%%%%%%%%%
%%%%%%%%%
```

```
%%%%%%%%%%%%%%%%%%%%%%%%%%%%%%%%%%%%%%%%%%%%%%%%%%%%%%%%%%%%%%%%%%%%%%
%%%%%%%%
Main Program Code of the Multi-objective functions

clc
f1 = @(x) P_factor(x); %Power Factor as the first Objective Function
      f2 = @(x) P_Eff(x);% Power Factor as the second Objective
Function

%      % Combine two objectives 'f1' and 'f2'
combfun = @(x) [f1(x) f2(x)];
% Bound constraints on X
lb = [100 100]; ub = [200 200];
%      % Specify the initial range for population
options = gaoptimset('PopInitRange',[lb;ub]);
%      % Minimize using GAMULTIOBJ
      [x,fval] = gamultiobj(combfun,2,[],[],[],[],lb,ub,options)
%
%    Display Pareto fronts and rank of individuals while GAMULTIOBJ
%    minimizes
% options = gaoptimset('PopInitRange',[lb;ub]);
options = gaoptimset(options,'PlotFcns',{@gaplotpareto});
      [x,fval,exitflag,output] =
gamultiobj(combfun,2,[],[],[],[],lb,ub,options)
```

APPENDIX G

Lua-Script for FEM

```
[Format]     =  3.3
[Frequency]  =  0
[Precision]  =  1.000000119209296e-08
[Depth]      =  100
[LengthUnits] =  millimeters
[ProblemType] =  planar
[Coordinates] =  cartesian
[Comment]    =  "Motor for test in Padova"
[PointProps]  = 0
[BdryProps]  = 5
  <BeginBdry>
    <BdryName> = "Az0"
    <BdryType> = 0
    <A_0> = 0
    <A_1> = 0
    <A_2> = 0
    <Phi> = 0
    <c0> = 0
    <c1> = 0
    <Mu_ssd> = 0
    <Sigma_ssd> = 0
  <EndBdry>
  <BeginBdry>
    <BdryName> = "AntiPeriodica1"
    <BdryType> = 4
    <A_0> = 0
    <A_1> = 0
    <A_2> = 0
    <Phi> = 0
    <c0> = 0
    <c1> = 0
    <Mu_ssd> = 0
    <Sigma_ssd> = 0
  <EndBdry>
  <BeginBdry>
    <BdryName> = "AntiPeriodica2"
    <BdryType> = 4
    <A_0> = 0
    <A_1> = 0
    <A_2> = 0
    <Phi> = 0
```

<c0> = 0
<c1> = 0
<Mu_ssd> = 0
<Sigma_ssd> = 0
<EndBdry>
<BeginBdry>
<BdryName> = "AntiPeriodica3"
<BdryType> = 4
<A_0> = 0
<A_1> = 0
<A_2> = 0
<Phi> = 0
<c0> = 0
<c1> = 0
<Mu_ssd> = 0
<Sigma_ssd> = 0
<EndBdry>
<BeginBdry>
<BdryName> = "AntiPeriodica4"
<BdryType> = 4
<A_0> = 0
<A_1> = 0
<A_2> = 0
<Phi> = 0
<c0> = 0
<c1> = 0
<Mu_ssd> = 0
<Sigma_ssd> = 0
<EndBdry>
[BlockProps] = 51
<BeginBlock>
<BlockName> = "Copper1"
<Mu_x> = 1
<Mu_y> = 1
<H_c> = 0
<H_cAngle> = 0
<J_re> = 0
<J_im> = 0
<Sigma> = 0
<d_lam> = 0
<Phi_h> = 0
<Phi_hx> = 0
<Phi_hy> = 0
<LamType> = 0
<LamFill> = 0
<BHPoints> = 0
<EndBlock>
<BeginBlock>
<BlockName> = "Copper2"
<Mu_x> = 1
<Mu_y> = 1
<H_c> = 0
<H_cAngle> = 0
<J_re> = 0

<J_im> = 0
<Sigma> = 0
<d_lam> = 0
<Phi_h> = 0
<Phi_hx> = 0
<Phi_hy> = 0
<LamType> = 0
<LamFill> = 0
<BHPoints> = 0
<EndBlock>
<BeginBlock>
<BlockName> = "Copper3"
<Mu_x> = 1
<Mu_y> = 1
<H_c> = 0
<H_cAngle> = 0
<J_re> = 0
<J_im> = 0
<Sigma> = 0
<d_lam> = 0
<Phi_h> = 0
<Phi_hx> = 0
<Phi_hy> = 0
<LamType> = 0
<LamFill> = 0
<BHPoints> = 0
<EndBlock>
<BeginBlock>
<BlockName> = "Copper4"
<Mu_x> = 1
<Mu_y> = 1
<H_c> = 0
<H_cAngle> = 0
<J_re> = 0
<J_im> = 0
<Sigma> = 0
<d_lam> = 0
<Phi_h> = 0
<Phi_hx> = 0
<Phi_hy> = 0
<LamType> = 0
<LamFill> = 0
<BHPoints> = 0
<EndBlock>
<BeginBlock>
<BlockName> = "Copper5"
<Mu_x> = 1
<Mu_y> = 1
<H_c> = 0
<H_cAngle> = 0
<J_re> = 0
<J_im> = 0
<Sigma> = 0
<d_lam> = 0

<Phi_h> = 0
<Phi_hx> = 0
<Phi_hy> = 0
<LamType> = 0
<LamFill> = 0
<BHPoints> = 0
<EndBlock>
<BeginBlock>
<BlockName> = "Copper6"
<Mu_x> = 1
<Mu_y> = 1
<H_c> = 0
<H_cAngle> = 0
<J_re> = 0
<J_im> = 0
<Sigma> = 0
<d_lam> = 0
<Phi_h> = 0
<Phi_hx> = 0
<Phi_hy> = 0
<LamType> = 0
<LamFill> = 0
<BHPoints> = 0
<EndBlock>
<BeginBlock>
<BlockName> = "Copper7"
<Mu_x> = 1
<Mu_y> = 1
<H_c> = 0
<H_cAngle> = 0
<J_re> = 0
<J_im> = 0
<Sigma> = 0
<d_lam> = 0
<Phi_h> = 0
<Phi_hx> = 0
<Phi_hy> = 0
<LamType> = 0
<LamFill> = 0
<BHPoints> = 0
<EndBlock>
<BeginBlock>
<BlockName> = "Copper8"
<Mu_x> = 1
<Mu_y> = 1
<H_c> = 0
<H_cAngle> = 0
<J_re> = 0
<J_im> = 0
<Sigma> = 0
<d_lam> = 0
<Phi_h> = 0
<Phi_hx> = 0
<Phi_hy> = 0

<LamType> = 0
<LamFill> = 0
<BHPoints> = 0
<EndBlock>
<BeginBlock>
<BlockName> = "Copper9"
<Mu_x> = 1
<Mu_y> = 1
<H_c> = 0
<H_cAngle> = 0
<J_re> = 0
<J_im> = 0
<Sigma> = 0
<d_lam> = 0
<Phi_h> = 0
<Phi_hx> = 0
<Phi_hy> = 0
<LamType> = 0
<LamFill> = 0
<BHPoints> = 0
<EndBlock>
<BeginBlock>
<BlockName> = "Copper10"
<Mu_x> = 1
<Mu_y> = 1
<H_c> = 0
<H_cAngle> = 0
<J_re> = 0
<J_im> = 0
<Sigma> = 0
<d_lam> = 0
<Phi_h> = 0
<Phi_hx> = 0
<Phi_hy> = 0
<LamType> = 0
<LamFill> = 0
<BHPoints> = 0
<EndBlock>
<BeginBlock>
<BlockName> = "Copper11"
<Mu_x> = 1
<Mu_y> = 1
<H_c> = 0
<H_cAngle> = 0
<J_re> = 0
<J_im> = 0
<Sigma> = 0
<d_lam> = 0
<Phi_h> = 0
<Phi_hx> = 0
<Phi_hy> = 0
<LamType> = 0
<LamFill> = 0
<BHPoints> = 0

<EndBlock>
<BeginBlock>
<BlockName> = "Copper12"
<Mu_x> = 1
<Mu_y> = 1
<H_c> = 0
<H_cAngle> = 0
<J_re> = 0
<J_im> = 0
<Sigma> = 0
<d_lam> = 0
<Phi_h> = 0
<Phi_hx> = 0
<Phi_hy> = 0
<LamType> = 0
<LamFill> = 0
<BHPoints> = 0
<EndBlock>
<BeginBlock>
<BlockName> = "Copper13"
<Mu_x> = 1
<Mu_y> = 1
<H_c> = 0
<H_cAngle> = 0
<J_re> = 0
<J_im> = 0
<Sigma> = 0
<d_lam> = 0
<Phi_h> = 0
<Phi_hx> = 0
<Phi_hy> = 0
<LamType> = 0
<LamFill> = 0
<BHPoints> = 0
<EndBlock>
<BeginBlock>
<BlockName> = "Copper14"
<Mu_x> = 1
<Mu_y> = 1
<H_c> = 0
<H_cAngle> = 0
<J_re> = 0
<J_im> = 0
<Sigma> = 0
<d_lam> = 0
<Phi_h> = 0
<Phi_hx> = 0
<Phi_hy> = 0
<LamType> = 0
<LamFill> = 0
<BHPoints> = 0
<EndBlock>
<BeginBlock>
<BlockName> = "Copper15"

<Mu_x> = 1
<Mu_y> = 1
<H_c> = 0
<H_cAngle> = 0
<J_re> = 0
<J_im> = 0
<Sigma> = 0
<d_lam> = 0
<Phi_h> = 0
<Phi_hx> = 0
<Phi_hy> = 0
<LamType> = 0
<LamFill> = 0
<BHPoints> = 0
<EndBlock>
<BeginBlock>
<BlockName> = "Copper16"
<Mu_x> = 1
<Mu_y> = 1
<H_c> = 0
<H_cAngle> = 0
<J_re> = 0
<J_im> = 0
<Sigma> = 0
<d_lam> = 0
<Phi_h> = 0
<Phi_hx> = 0
<Phi_hy> = 0
<LamType> = 0
<LamFill> = 0
<BHPoints> = 0
<EndBlock>
<BeginBlock>
<BlockName> = "Copper17"
<Mu_x> = 1
<Mu_y> = 1
<H_c> = 0
<H_cAngle> = 0
<J_re> = 0
<J_im> = 0
<Sigma> = 0
<d_lam> = 0
<Phi_h> = 0
<Phi_hx> = 0
<Phi_hy> = 0
<LamType> = 0
<LamFill> = 0
<BHPoints> = 0
<EndBlock>
<BeginBlock>
<BlockName> = "Copper18"
<Mu_x> = 1
<Mu_y> = 1
<H_c> = 0

<H_cAngle> = 0
<J_re> = 0
<J_im> = 0
<Sigma> = 0
<d_lam> = 0
<Phi_h> = 0
<Phi_hx> = 0
<Phi_hy> = 0
<LamType> = 0
<LamFill> = 0
<BHPoints> = 0
<EndBlock>
<BeginBlock>
<BlockName> = "Copper19"
<Mu_x> = 1
<Mu_y> = 1
<H_c> = 0
<H_cAngle> = 0
<J_re> = 0
<J_im> = 0
<Sigma> = 0
<d_lam> = 0
<Phi_h> = 0
<Phi_hx> = 0
<Phi_hy> = 0
<LamType> = 0
<LamFill> = 0
<BHPoints> = 0
<EndBlock>
<BeginBlock>
<BlockName> = "Copper20"
<Mu_x> = 1
<Mu_y> = 1
<H_c> = 0
<H_cAngle> = 0
<J_re> = 0
<J_im> = 0
<Sigma> = 0
<d_lam> = 0
<Phi_h> = 0
<Phi_hx> = 0
<Phi_hy> = 0
<LamType> = 0
<LamFill> = 0
<BHPoints> = 0
<EndBlock>
<BeginBlock>
<BlockName> = "Copper21"
<Mu_x> = 1
<Mu_y> = 1
<H_c> = 0
<H_cAngle> = 0
<J_re> = 0
<J_im> = 0

<Sigma> = 0
<d_lam> = 0
<Phi_h> = 0
<Phi_hx> = 0
<Phi_hy> = 0
<LamType> = 0
<LamFill> = 0
<BHPoints> = 0
<EndBlock>
<BeginBlock>
<BlockName> = "Copper22"
<Mu_x> = 1
<Mu_y> = 1
<H_c> = 0
<H_cAngle> = 0
<J_re> = 0
<J_im> = 0
<Sigma> = 0
<d_lam> = 0
<Phi_h> = 0
<Phi_hx> = 0
<Phi_hy> = 0
<LamType> = 0
<LamFill> = 0
<BHPoints> = 0
<EndBlock>
<BeginBlock>
<BlockName> = "Copper23"
<Mu_x> = 1
<Mu_y> = 1
<H_c> = 0
<H_cAngle> = 0
<J_re> = 0
<J_im> = 0
<Sigma> = 0
<d_lam> = 0
<Phi_h> = 0
<Phi_hx> = 0
<Phi_hy> = 0
<LamType> = 0
<LamFill> = 0
<BHPoints> = 0
<EndBlock>
<BeginBlock>
<BlockName> = "Copper24"
<Mu_x> = 1
<Mu_y> = 1
<H_c> = 0
<H_cAngle> = 0
<J_re> = 0
<J_im> = 0
<Sigma> = 0
<d_lam> = 0
<Phi_h> = 0

<Phi_hx> = 0
<Phi_hy> = 0
<LamType> = 0
<LamFill> = 0
<BHPoints> = 0
<EndBlock>
<BeginBlock>
<BlockName> = "Copper25"
<Mu_x> = 1
<Mu_y> = 1
<H_c> = 0
<H_cAngle> = 0
<J_re> = 0
<J_im> = 0
<Sigma> = 0
<d_lam> = 0
<Phi_h> = 0
<Phi_hx> = 0
<Phi_hy> = 0
<LamType> = 0
<LamFill> = 0
<BHPoints> = 0
<EndBlock>
<BeginBlock>
<BlockName> = "Copper26"
<Mu_x> = 1
<Mu_y> = 1
<H_c> = 0
<H_cAngle> = 0
<J_re> = 0
<J_im> = 0
<Sigma> = 0
<d_lam> = 0
<Phi_h> = 0
<Phi_hx> = 0
<Phi_hy> = 0
<LamType> = 0
<LamFill> = 0
<BHPoints> = 0
<EndBlock>
<BeginBlock>
<BlockName> = "Copper27"
<Mu_x> = 1
<Mu_y> = 1
<H_c> = 0
<H_cAngle> = 0
<J_re> = 0
<J_im> = 0
<Sigma> = 0
<d_lam> = 0
<Phi_h> = 0
<Phi_hx> = 0
<Phi_hy> = 0
<LamType> = 0

<LamFill> = 0
<BHPoints> = 0
<EndBlock>
<BeginBlock>
<BlockName> = "Copper28"
<Mu_x> = 1
<Mu_y> = 1
<H_c> = 0
<H_cAngle> = 0
<J_re> = 0
<J_im> = 0
<Sigma> = 0
<d_lam> = 0
<Phi_h> = 0
<Phi_hx> = 0
<Phi_hy> = 0
<LamType> = 0
<LamFill> = 0
<BHPoints> = 0
<EndBlock>
<BeginBlock>
<BlockName> = "Copper29"
<Mu_x> = 1
<Mu_y> = 1
<H_c> = 0
<H_cAngle> = 0
<J_re> = 0
<J_im> = 0
<Sigma> = 0
<d_lam> = 0
<Phi_h> = 0
<Phi_hx> = 0
<Phi_hy> = 0
<LamType> = 0
<LamFill> = 0
<BHPoints> = 0
<EndBlock>
<BeginBlock>
<BlockName> = "Copper30"
<Mu_x> = 1
<Mu_y> = 1
<H_c> = 0
<H_cAngle> = 0
<J_re> = 0
<J_im> = 0
<Sigma> = 0
<d_lam> = 0
<Phi_h> = 0
<Phi_hx> = 0
<Phi_hy> = 0
<LamType> = 0
<LamFill> = 0
<BHPoints> = 0
<EndBlock>

<BeginBlock>
<BlockName> = "Copper31"
<Mu_x> = 1
<Mu_y> = 1
<H_c> = 0
<H_cAngle> = 0
<J_re> = 0
<J_im> = 0
<Sigma> = 0
<d_lam> = 0
<Phi_h> = 0
<Phi_hx> = 0
<Phi_hy> = 0
<LamType> = 0
<LamFill> = 0
<BHPoints> = 0
<EndBlock>
<BeginBlock>
<BlockName> = "Copper32"
<Mu_x> = 1
<Mu_y> = 1
<H_c> = 0
<H_cAngle> = 0
<J_re> = 0
<J_im> = 0
<Sigma> = 0
<d_lam> = 0
<Phi_h> = 0
<Phi_hx> = 0
<Phi_hy> = 0
<LamType> = 0
<LamFill> = 0
<BHPoints> = 0
<EndBlock>
<BeginBlock>
<BlockName> = "Copper33"
<Mu_x> = 1
<Mu_y> = 1
<H_c> = 0
<H_cAngle> = 0
<J_re> = 0
<J_im> = 0
<Sigma> = 0
<d_lam> = 0
<Phi_h> = 0
<Phi_hx> = 0
<Phi_hy> = 0
<LamType> = 0
<LamFill> = 0
<BHPoints> = 0
<EndBlock>
<BeginBlock>
<BlockName> = "Copper34"
<Mu_x> = 1

<Mu_y> = 1
<H_c> = 0
<H_cAngle> = 0
<J_re> = 0
<J_im> = 0
<Sigma> = 0
<d_lam> = 0
<Phi_h> = 0
<Phi_hx> = 0
<Phi_hy> = 0
<LamType> = 0
<LamFill> = 0
<BHPoints> = 0
<EndBlock>
<BeginBlock>
<BlockName> = "Copper35"
<Mu_x> = 1
<Mu_y> = 1
<H_c> = 0
<H_cAngle> = 0
<J_re> = 0
<J_im> = 0
<Sigma> = 0
<d_lam> = 0
<Phi_h> = 0
<Phi_hx> = 0
<Phi_hy> = 0
<LamType> = 0
<LamFill> = 0
<BHPoints> = 0
<EndBlock>
<BeginBlock>
<BlockName> = "Copper36"
<Mu_x> = 1
<Mu_y> = 1
<H_c> = 0
<H_cAngle> = 0
<J_re> = 0
<J_im> = 0
<Sigma> = 0
<d_lam> = 0
<Phi_h> = 0
<Phi_hx> = 0
<Phi_hy> = 0
<LamType> = 0
<LamFill> = 0
<BHPoints> = 0
<EndBlock>
<BeginBlock>
<BlockName> = "Copper37"
<Mu_x> = 1
<Mu_y> = 1
<H_c> = 0
<H_cAngle> = 0

<J_re> = 0
<J_im> = 0
<Sigma> = 0
<d_lam> = 0
<Phi_h> = 0
<Phi_hx> = 0
<Phi_hy> = 0
<LamType> = 0
<LamFill> = 0
<BHPoints> = 0
<EndBlock>
<BeginBlock>
<BlockName> = "Copper38"
<Mu_x> = 1
<Mu_y> = 1
<H_c> = 0
<H_cAngle> = 0
<J_re> = 0
<J_im> = 0
<Sigma> = 0
<d_lam> = 0
<Phi_h> = 0
<Phi_hx> = 0
<Phi_hy> = 0
<LamType> = 0
<LamFill> = 0
<BHPoints> = 0
<EndBlock>
<BeginBlock>
<BlockName> = "Copper39"
<Mu_x> = 1
<Mu_y> = 1
<H_c> = 0
<H_cAngle> = 0
<J_re> = 0
<J_im> = 0
<Sigma> = 0
<d_lam> = 0
<Phi_h> = 0
<Phi_hx> = 0
<Phi_hy> = 0
<LamType> = 0
<LamFill> = 0
<BHPoints> = 0
<EndBlock>
<BeginBlock>
<BlockName> = "Copper40"
<Mu_x> = 1
<Mu_y> = 1
<H_c> = 0
<H_cAngle> = 0
<J_re> = 0
<J_im> = 0
<Sigma> = 0

<d_lam> = 0
<Phi_h> = 0
<Phi_hx> = 0
<Phi_hy> = 0
<LamType> = 0
<LamFill> = 0
<BHPoints> = 0
<EndBlock>
<BeginBlock>
<BlockName> = "Copper41"
<Mu_x> = 1
<Mu_y> = 1
<H_c> = 0
<H_cAngle> = 0
<J_re> = 0
<J_im> = 0
<Sigma> = 0
<d_lam> = 0
<Phi_h> = 0
<Phi_hx> = 0
<Phi_hy> = 0
<LamType> = 0
<LamFill> = 0
<BHPoints> = 0
<EndBlock>
<BeginBlock>
<BlockName> = "Copper42"
<Mu_x> = 1
<Mu_y> = 1
<H_c> = 0
<H_cAngle> = 0
<J_re> = 0
<J_im> = 0
<Sigma> = 0
<d_lam> = 0
<Phi_h> = 0
<Phi_hx> = 0
<Phi_hy> = 0
<LamType> = 0
<LamFill> = 0
<BHPoints> = 0
<EndBlock>
<BeginBlock>
<BlockName> = "Copper43"
<Mu_x> = 1
<Mu_y> = 1
<H_c> = 0
<H_cAngle> = 0
<J_re> = 0
<J_im> = 0
<Sigma> = 0
<d_lam> = 0
<Phi_h> = 0
<Phi_hx> = 0

<Phi_hy> = 0
<LamType> = 0
<LamFill> = 0
<BHPoints> = 0
<EndBlock>
<BeginBlock>
<BlockName> = "Copper44"
<Mu_x> = 1
<Mu_y> = 1
<H_c> = 0
<H_cAngle> = 0
<J_re> = 0
<J_im> = 0
<Sigma> = 0
<d_lam> = 0
<Phi_h> = 0
<Phi_hx> = 0
<Phi_hy> = 0
<LamType> = 0
<LamFill> = 0
<BHPoints> = 0
<EndBlock>
<BeginBlock>
<BlockName> = "Copper45"
<Mu_x> = 1
<Mu_y> = 1
<H_c> = 0
<H_cAngle> = 0
<J_re> = 0
<J_im> = 0
<Sigma> = 0
<d_lam> = 0
<Phi_h> = 0
<Phi_hx> = 0
<Phi_hy> = 0
<LamType> = 0
<LamFill> = 0
<BHPoints> = 0
<EndBlock>
<BeginBlock>
<BlockName> = "Copper46"
<Mu_x> = 1
<Mu_y> = 1
<H_c> = 0
<H_cAngle> = 0
<J_re> = 0
<J_im> = 0
<Sigma> = 0
<d_lam> = 0
<Phi_h> = 0
<Phi_hx> = 0
<Phi_hy> = 0
<LamType> = 0
<LamFill> = 0

<BHPoints> = 0
<EndBlock>
<BeginBlock>
<BlockName> = "Copper47"
<Mu_x> = 1
<Mu_y> = 1
<H_c> = 0
<H_cAngle> = 0
<J_re> = 0
<J_im> = 0
<Sigma> = 0
<d_lam> = 0
<Phi_h> = 0
<Phi_hx> = 0
<Phi_hy> = 0
<LamType> = 0
<LamFill> = 0
<BHPoints> = 0
<EndBlock>
<BeginBlock>
<BlockName> = "Copper48"
<Mu_x> = 1
<Mu_y> = 1
<H_c> = 0
<H_cAngle> = 0
<J_re> = 0
<J_im> = 0
<Sigma> = 0
<d_lam> = 0
<Phi_h> = 0
<Phi_hx> = 0
<Phi_hy> = 0
<LamType> = 0
<LamFill> = 0
<BHPoints> = 0
<EndBlock>
<BeginBlock>
<BlockName> = "Air"
<Mu_x> = 1
<Mu_y> = 1
<H_c> = 0
<H_cAngle> = 0
<J_re> = 0
<J_im> = 0
<Sigma> = 0
<d_lam> = 0
<Phi_h> = 0
<Phi_hx> = 0
<Phi_hy> = 0
<LamType> = 0
<LamFill> = 1
<BHPoints> = 0
<EndBlock>
<BeginBlock>

<BlockName> = "Aluminum"
<Mu_x> = 1
<Mu_y> = 1
<H_c> = 0
<H_cAngle> = 0
<J_re> = 0
<J_im> = 0
<Sigma> = 25
<d_lam> = 0
<Phi_h> = 0
<Phi_hx> = 0
<Phi_hy> = 0
<LamType> = 0
<LamFill> = 1
<BHPoints> = 0
<EndBlock>
<BeginBlock>
<BlockName> = "1010 Steel"
<Mu_x> = 902.60000000000002
<Mu_y> = 902.60000000000002
<H_c> = 0
<H_cAngle> = 0
<J_re> = 0
<J_im> = 0
<Sigma> = 0
<d_lam> = 0
<Phi_h> = 0
<Phi_hx> = 0
<Phi_hy> = 0
<LamType> = 0
<LamFill> = 1
<BHPoints> = 16
<EndBlock>
[CircuitProps] = 2
<BeginCircuit>
<CircuitName> = "positive"
<VoltGradient_re> = 0
<VoltGradient_im> = 0
<TotalAmps_re> = 240
<TotalAmps_im> = 0
<CircuitType> = 0
<EndCircuit>
<BeginCircuit>
<CircuitName> = "negative"
<VoltGradient_re> = 0
<VoltGradient_im> = 0
<TotalAmps_re> = -240
<TotalAmps_im> = 0
<CircuitType> = 0
<EndCircuit>
[NumPoints] = 998

```
-- Post computations

-- load the motor data
dofile('motordata.lua')


--Lunghezza in metri
Lstk=Lstk/1000

-- inizializzo i flussi concatenati

  flussoA_re=0
  flussoB_re=0
  flussoC_re=0
  flussoA_im=0
  flussoB_im=0
  flussoC_im=0

  flussoX_re=0
  flussoY_re=0
  flussoZ_re=0
  flussoX_im=0
  flussoY_im=0
  flussoZ_im=0

groupselectblock(1001)
  Sup = blockintegral(5)
clearblock()

for q = 1, Qsim ,1 do

groupselectblock(1000+q)    -- le cave sono 1001, 1002, ...
    Areal, Aimag = blockintegral(1)
clearblock()

    Areal = Areal / Sup
    Aimag = Aimag / Sup

    flussoA_re = flussoA_re + Areal * ka[q]
    flussoB_re = flussoB_re + Areal * kb[q]
    flussoC_re = flussoC_re + Areal * kc[q]
    flussoX_re = flussoX_re + Areal * kx[q]
    flussoY_re = flussoY_re + Areal * ky[q]
    flussoZ_re = flussoZ_re + Areal * kz[q]

    flussoA_im = flussoA_im + Aimag * ka[q]
    flussoB_im = flussoB_im + Aimag * kb[q]
    flussoC_im = flussoC_im + Aimag * kc[q]
    flussoX_im = flussoX_im + Aimag * kx[q]
```

```
    flussoY_im = flussoY_im + Aimag * ky[q]
    flussoZ_im = flussoZ_im + Aimag * kz[q]

end

  flussoA_re = flussoA_re * Lstk * nc
  flussoB_re = flussoB_re * Lstk * nc
  flussoC_re = flussoC_re * Lstk * nc
  flussoX_re = flussoX_re * Lstk * nc
  flussoY_re = flussoY_re * Lstk * nc
  flussoZ_re = flussoZ_re * Lstk * nc

  flussoA_im = flussoA_im * Lstk * nc
  flussoB_im = flussoB_im * Lstk * nc
  flussoC_im = flussoC_im * Lstk * nc
  flussoX_im = flussoX_im * Lstk * nc
  flussoY_im = flussoY_im * Lstk * nc
  flussoZ_im = flussoZ_im * Lstk * nc

-- coppia e perdite

groupselectblock(10)
  Torque = blockintegral(22)
  RotLosses = blockintegral(6)
clearblock()

-- energia
groupselectblock()
  Energy = blockintegral(2)
  Coenergy = blockintegral(17)
  AJintrg = blockintegral(0)

-- Callcolo il massimo modulo dell'induzione nei denti di statore
--Calcolo il modulo lungo un percorso e ne tengo il valore massimo
Bmaxs=0
for k = 0, 360 ,1 do
  x=Rs*cos(k)
  y=Rs*sin(k)
  Are, Aim, B1re, B1im, B2re, B2im, Sig, E, H1re, H1im, H2re, H2im, Jere, Jeim,Jsre,Jsim,
Mu1re, Mu1im, Mu2re, Mu2im, Pe, Ph = getpointvalues(x,y)
  B=sqrt((B1re^2+B1im^2)+(B2re^2+B2im^2))
if B>Bmaxs then
  Bmaxs=B
end
end

-- Callcolo il massimo modulo dell'induzione nei denti di rotore
--Calcolo il modulo lungo un percorso e ne tengo il valore massimo
Bmaxr=0
for k = 0, 360 ,1 do
  x=Rr*cos(k)
  y=Rr*sin(k)
  Are, Aim, B1re, B1im, B2re, B2im, Sig, E, H1re, H1im, H2re, H2im, Jere, Jeim,Jsre,Jsim,
Mu1re, Mu1im, Mu2re, Mu2im, Pe, Ph = getpointvalues(x,y)
```

```
  B=sqrt((B1re^2+B1im^2)+(B2re^2+B2im^2))
if B>Bmaxr then
  Bmaxr=B
end
end

-- Callcolo il massimo modulo dell'induzione nella corona di statore
--Calcolo il modulo lungo un percorso e ne tengo il valore massimo
Bmaxc=0
for k = 0, 360 ,1 do
  x=Rc*cos(k)
  y=Rc*sin(k)
  Are, Aim, B1re, B1im, B2re, B2im, Sig, E, H1re, H1im, H2re, H2im, Jere, Jeim,Jsre,Jsim,
Mu1re, Mu1im, Mu2re, Mu2im, Pe, Ph = getpointvalues(x,y)
  B=sqrt((B1re^2+B1im^2)+(B2re^2+B2im^2))
if B>Bmaxc then
  Bmaxc=B
end
end

-- scrittura su file

handle=openfile('Result.txt',"a")
write(handle,
              flussoA_re, "  ",
              flussoA_im, "  ",
              flussoB_re, "  ",
              flussoB_im, "  ",
              flussoC_re, "  ",
              flussoC_im, "  ",
              flussoX_re, "  ",
              flussoX_im, "  ",
              flussoY_re, "  ",
              flussoY_im, "  ",
              flussoZ_re, "  ",
              flussoZ_im, "  ",
              Torque, "  ",
              RotLosses, "  ",
              Energy, "  ",
              Coenergy, "  ",
              AJintrg, "  ",
              Bmaxs, "\t",
              Bmaxr, "\t",
              Bmaxc, "\t",
              "\n")
closefile(handle)

exitpost()
```

Appendix H.

Salient Steps for the Construction of a Circle Diagram.

Step 1: Obtain equivalent circuit parameters.

Step 2: Obtain a short circuit I_{sc} and open circuit I_o currents and their corresponding power factors $\cos\phi_{sc}$ and $\cos\phi_o$ respectively.

Note: The above two steps can readily be obtained from no load and blocked rotor tests.

With reference to figure 5.50 on page 221, the remaining steps are as outlined below:

Step 3: Draw 2 vertical axes intersecting at point O.

Step 4: Draw **OO'**= I_0 at angle ϕ_o to the vertical axis.

Step 5: Draw **O'E** parallel to X-axis.

Step 6: Draw **OB**=I_{sc} at angle ϕ_{sc} to the vertical axis.

Step 7: Join O' with B.

Step 8: Construct the perpendicular bisector of **O'B** intersecting the line **O'D** at C. point C is the center of the circle having radius O'C.

Step 9: Draw the circle **O'BD**.

Step 10: Draw a perpendicular line to **O'D** at point F from B.

Step 11: Draw a line from O' to cut **BF** at G. such that:

$$\frac{\boldsymbol{BG}}{\boldsymbol{GF}} = \frac{rotor\ resistance\ refered\ to\ stator}{stator\ resistance} = \frac{r_r'}{r_s}$$

Note: the line **O'G** is known as torque line and line **O'B** as output line. The diagram can be used to determine the characteristics of the machine at any load current.